Development of acyclic chelates for incorporation into theranostic radiopharmaceuticals for cancer

by

Imma Carbo Bague

M.Sc. (*cum laude*), Universiteit Leiden, 2018

Thesis Submitted in Partial Fulfillment of the
Requirements for the Degree of
Doctor of Philosophy

in the
Department of Chemistry
Faculty of Science

SIMON FRASER UNIVERSITY
Fall 2023

Declaration of Committee

Name:	**Imma Carbo Bague**
Degree:	**Doctor of Philosophy (Chemistry)**
Title:	**Development of acyclic chelates for incorporation into theranostic radiopharmaceuticals for cancer**
Committee:	**Chair: Loren Kaake** Associate Professor, Chemistry
	Caterina Ramogida Supervisor Assistant Professor, Chemistry
	Tim Storr Committee Member Professor, Chemistry
	Daniel Leznoff Committee Member Professor, Chemistry
	Hua Yang Examiner Adjunct Professor, Chemistry
	Lynn Francesconi External Examiner Professor, Chemistry Hunter College

Ethics Statement

The author, whose name appears on the title page of this work, has obtained, for the research described in this work, either:

a. human research ethics approval from the Simon Fraser University Office of Research Ethics

or

b. advance approval of the animal care protocol from the University Animal Care Committee of Simon Fraser University

or has conducted the research

c. as a co-investigator, collaborator, or research assistant in a research project approved in advance.

A copy of the approval letter has been filed with the Theses Office of the University Library at the time of submission of this thesis or project.

The original application for approval and letter of approval are filed with the relevant offices. Inquiries may be directed to those authorities.

Simon Fraser University Library
Burnaby, British Columbia, Canada

Update Spring 2016

Abstract

Radioactive metals possess various chemical and physical properties (e.g., half-life, radioactive decay), making them aptly suited for the diagnosis and treatment (theranostics) of cancer. Securing the radiometal in a drug complex for safe delivery into the tumor site is crucial for the successful clinical application of these radioactive drugs called radiopharmaceuticals. A fundamental component of a radiopharmaceutical is the chelate, a ligand that tightly binds the radiometal forming a stable radioactive complex, which is then covalently attached to a disease targeting molecule such as a peptide or an antibody through a linker. In the past two decades, intense research efforts have expanded the production of radiometals suitable for radiopharmaceutical applications such as titanium-45 (^{45}Ti) and actinium-225 (^{225}Ac), among many others. To this end, some of these radiometals have shown excellent preclinical and clinical results. However, the stable chelation in vivo of these radiometals remains a challenge resulting in the need to develop novel chelates tailored to the properties of each radioisotope.

This work focuses on developing novel acyclic chelates for the stable chelation of the cutting-edge first-row transition metals scandium-44/47 ($^{44/47}$Sc) and ^{45}Ti, the radiolanthanides lanthanum-135 (^{135}La) and terbium-155/161 ($^{155/161}$Tb), and the radioactinides ^{225}Ac and thorium-227 (^{227}Th). For this purpose, we exploited the oxophylic 1,2-hydroxypyridinone (1,2-HOPO) moiety through a pentaamine backbone on a decadentate chelate (HOPO-O_{10}) for the larger radiometals and on a tripodal backbone for a hexadentate chelate (HOPO-O_6-C4) along with its catechol amide version (CAM-O_6-C4) for the smaller radiometals. These three chelates were synthesized, their coordination chemistry was characterized using the corresponding non-radioactive complexes, and they were evaluated in radiolabeling studies to determine their potential for incorporation into radiopharmaceuticals. HOPO-O_{10} was found to be an excellent candidate for ^{161}Tb and ^{227}Th with high in vitro stability. A simpler version of HOPO-O_{10}, HOPO-O_8, was used for incorporation into a radiopharmaceutical for which a novel tetrazine-containing bifunctional chelate analogue (HOPO-O_8-Me-Tz) was prepared and evaluated in a preclinical animal study with encouraging results for zirconium-89 (^{89}Zr), a possible imaging pair for ^{227}Th. Moreover, HOPO-O_6-C4 showed excellent affinity for ^{47}Sc and promising complex stability in vivo.

Keywords: radiometal; chelate; radiopharmaceutical; cancer; imaging; therapy

Dedication

To my family and close friends.

Acknowledgements

I must first acknowledge my supervisor Dr. Caterina Ramogida for her guidance and continuous support during my Ph.D. She gave me the freedom to design my projects and explore my scientific interests from synthetic chemistry to preclinical studies. She also encouraged me, supported my collaborations, and funded my attendance at international conferences.

I would also like to thank all of the amazing people in the Ramogida group and others I had the pleasure to work with and learn from over the past 4.5 years. In particular, Parmissa Randhawa and Brooke McNeil, my fellow Ph.D. students, for their unconditional support and the many hours of research and fun spent together. Dr. Anthony McDonagh for being an excellent organic chemistry teacher and sharing all his synthetic advice with me. Dr. Gang Chen for teaching me how to operate and maintain all our lab instrumentation (HR-MS, HPLC, etc.). From TRIUMF, I would like to thank Dr. Valery Radchenko for his advice and support, for connecting me with other research scientists via email or at international conferences, and for funding my attendance at International Symposium on Trends in Radiopharmaceuticals (ISTR 2023). Dr. Hua Yang for sharing her radiochemistry knowledge and giving me access to ^{227}Th. The friendly and helpful staff from SFU and TRIUMF are also acknowledged and thanked. To our collaborators at CCM, Dr. Cristina Rodriguez-Rodriguez and Maryam Osooly for performing our in vivo studies and helping with all the data processing. To Shelbie Cingoranelli from the Lapi group for her hard work on the ^{47}Sc radiolabeling, to Dr. Angus Koller and Owen Glaser for the ^{45}Ti studies, and Dr. Kondappa Naidu Bobba from the Flavell group for his advice on ^{89}Zr radiolabeling and for taking on the pretargeting project (chapter 4). Thank you to SFU and NSERC for funding. Thank you to my Ph.D. committee members Dr. Tim Storr and Dr. Daniel Leznoff for their advice in my yearly committee meetings and for taking time out of their schedules to read my thesis and/or attend my committee meetings. I would also like to extend this acknowledgement to the other committee members Prof. Lynn Francesconi and Dr. Hua Yang.

Last, to the infinite support and understanding of my husband Albert, my parents Julia i Ramon, my sister Anna, and my friends here, in the Netherlands and Catalonia.

Table of Contents

List of Tables

List of Figures

List of Schemes

List of Acronyms and Abbreviations

%ID/g	Percentage of injected radioactive dose per gram of tissue
®	Trademark
°C	Degrees Celsius
2D	Two dimensions
3D	Three dimensions
Å	Angstrom (10^{-10} m)
AAZTA	1,4-bis(carboxymethyl)-6-[bis(carboxymethyl)]amino-6-methylperhydro-1,4-diazepine
ACC	Animal care committee
ADF	Amsterdam density functional
A_m	Molar activity
AML	Acute myeloid leukemia
A_s	Specific activity
ATSM	diacetyl-bis(N-methylthiosemicarbazone)
B3-DJ	Becke-Johnson damping
B3LYP	Becke, 3-parameter, Lee-Yang-Par
BAPTA	1,2-bis(o-aminophenoxy)ethane-N,N,N', N'-tetraacetic acid
BFC	Bifunctional chelate
Bn	Benzyl
Boc	tert-Butyloxycarbonyl
Bq	Becquerel
BR	Branching ratio
cal	calorie
CAM	Catechol amide
CCAC	Canadian Council on animal care
CE	Conversion electrons
CHX-A''-DTPA	2,2'-((2-(((1S,2S)2bis(carboxymethyl)amino)cyclohexyl)-(carboxymethyl)amino)ethyl)-azanediyl)diacetic acid
CK	Coster-Kroning electrons
CN	Coordination number

Crown	2,2',2'',2'''-(1,10-dioxa-4,7,13,16-tetraazacyclooctadecane-4,7,13,16-tetrayl)-tetraacetic acid
CT	Computed tomography
d	Doublet
DEPA	7-[2-(bis-carboxymethyl-amino)-ethyl]-4,10-bis-carboxymethyl-1,4,7,10-tetraaza-cyclododec-1-yl-acetic acid
DFO	Deferoxamine
DFT	Density functional theory
DIPEA	*N,N*-Diisopropylethylamine
DMAP	4-(Dimethylamino)pyridine
DMF	Dimethylformamide
DMSO	Dimethyl sulfoxide
DNA	Deoxyribonucleic acid
DOTA	1,4,7,10-tetraazacyclododecane-1,4,7,10-tetraacetic acid
DSB	Double strand break
DTPA	Diethylenetriaminepentaacetic acid
EC	Electron capture
EDA	Energy density analysis
EDTA	Ethylenediaminetetraacetic acid
EGTA	ethylene glycol-bis(2-aminoethylether)-N,N,N’,N’-tetraacetic acid
eV	electronvolt
FA	Formic acid
FDG	Fluorodeoxyglucose
g	gram
G	Giga (10^9)
h	Hour
H_2bispa	6,6’-({9-hydroxy-1,5-bis(methoxycarbonyl)-2,4-di(pyridin-2-yl)-3,7-diazabicyclo[3.3.1]nonane-3,7-diyl}bis(-methylene))dipicolinic acid
H_2macropa	N,N′-bis[(6-carboxy-2-pyridyl)methyl]- 1,7-diaza-18-crown-6
H_4octapa	N,N′-bis(6-carboxy-2-pyridylmethyl)-ethylenediamine-N,N′-diacetic acid
HEPES	4-(2-hydroxyethyl)-1-piperazineethanesulfonic acid

HOPO	Hydroxypyridinone
HPGe	High-purity germanium
HPLC	High-Performance Liquid Chromatography
HR	High resolution
HSAB	Hard and soft acid and base
HSQC	Heteronuclear single quantum coherence
HYNIC	Hydrazinonicotinic acid
Hz	Hertz
I	Ionic strength
IC	Internal conversion
ICP	Inductively coupled plasma
IEDDA	Inverse electron demand [4+2] Diels -Alder
Ig	Immunoglobulin
K	Degree Kelvin
k	Kilo (10^3)
LAC	Library and Archives Canada
LEHR	Low energy high resolution
LET	Linear energy transfer
M	Molar or mega (10^6)
m	Milli (10^{-3}) or multiplet
m/z	Per unit charge
mAb	Monoclonal antibody
MAE	Meitner-Auger electrons
MALDI	Matrix-assisted laser desorption/ionization
mCRPC	Metastatic castration-resistant prostate cancer
Me	methyl
mIBG	Meta-iodobenzyl-guanidine
min	Minute
MM	Molecular mechanics
mol	Mole
MS	Mass spectrometry

MSD	Mass selective detection
MSH	Melanocyte stimulating hormone
n	Nano (10^{-9})
NET	Neuroendocrine tumour
NETA	(2-(4,7-biscarboxymethyl[1,4,7]triazacyclonona-1-yl-ethyl)carbonyl-methylamino]acetic acid)
NHS	N-hydroxysuccinimide
NMR	Nuclear magnetic resonance
NOTA	1,4,7-Triazacyclononane-1,4,7-triacetic acid
OAc	Acetate (CH_3CO_2)
p	Para substituent or pico (10^{-12})
p.i.	Post injection
PBS	Phosphate buffered saline
Pd/C	Palladium on carbon
PEG	Polyethylene glycol
PEPA	1,4,7,10,13-pentaazacyclopentadecane-N,N',N'',N''',N''''-pentaacetic acid
PET	Positron emission tomography
pH	-log [H^+]
pM	-log [free metal]
POSEM	Pixel-ordered subset expectation maximization
ppm	Parts per million
PRRT	Peptide receptor radionuclide therapy
PSI	Pound per square inch
PSMA	Prostate-specific membrane antigen
PTSM	pyruvaldehyde-bis(N4-methylthiosemicarbazone
RCY	Radiochemical yield
RES	Reticuloendothelial system
RGD	Arg-Gly-Asp cyclic peptide
RIBE	Radiation-induced bystander effect
RIT	Radioimmunotherapy
RMSD	Root mean square deviation

ROI	Region of interest
ROS	Reactive oxygen species
RP	Reverse phase
rpm	Rotation per minute
rt	Room temperature
s	Second or singlet
SA	Silicic acid
Sar	sarcophagine
sCK	Super Coster-Kroning electrons
SEC	Size exclusion chromatography
SFU	Simon Fraser University
SG	Silica gel
SP	Substance P
SPECT	Single photon emission computed tomography
SSB	Single strand break
SST	Somatostatin
SUV	Standardized uptake value
T	Temperature
t	Time
$t_{1/2}$	Half-life
TAT	Target alpha therapy
TATE	(Tyr$_3$-Thr^8)-octreotate
TCMC	2-(4-isothiocyanatobenzyl-1,4,7,10-tetraaza-1,4,7,10-tetra-(2-carbamonylmetyl)-cyclododecane
TCO	Trans-cyclooctene
TETA	1,4,8,11-tetra-azacyclotetradecane- 1,4,8,11-tetraacetic acid
TFA	Trifluoracetic acid
TLC	Thin layer chromatography
TOC	Tyr^3-octeotride
ToF	Time-of-flight
t_R	Retention time

TRT	Target radionuclide therapy
TSP	3-(trimethylsilyl) propionic acid
TTHA	triethylenetetra-amine-N,N',N'',N'''-hexaacetic acid
Tz	Tetrazine
Tz	Tetrazine
TZ2P	triple-ζ plus two polarization
Tzmb	Trastuzumab
UV-vis	Ultraviolet-visible
VDD	Voronoi deformation density
VEGF	Vascular endothelial growth factor
VT	Variable temperature
XAFS	X-ray absorption fine structure
y	Year
ZORA	Zeroth-order regular approximation
α	Alpha particle
β^-	Beta particle
β^+	Positron
γ	Gamma-ray
ΔG	Change in Gibbs free energy
λ	Wavelength
λ_{max}	Maximum absorption wavelength
μ	Micro (10^{-6})

Preface

Chapter 1 is an adaptation of published work, and is reproduced in part, with permission from Imma Carbo-Bague, and Caterina F. Ramogida, Emerging Therapeutic Radiopharmaceuticals and Their Theranostic Pairs. **2021**, *Encyclopedia of Inorganic and Bioinorganic Chemistry* R.A. Scott (Ed), DOI: 10.1002/9781119951438.eibc2763, Copyright 2021 John Wiley & Sons, Inc. Imma Carbo-Bague wrote the manuscript with input and editing from Dr. Caterina Ramogida.

Chapter 2 is an adaptation of published work, and is reproduced in part, with permission from Imma Carbo-Bague, Cen Li, Brooke L. McNeil, Yang Gao, Anthony W. McDonagh, Michiel Vande Voorde, Maarten Ooms, Peter Kunz, Hua Yang, Valery Radchenko, Georg Schreckenbach, and Caterina F. Ramogida, Comparative Study of a Decadentate Acyclic Chelate, HOPO-O_{10}, and Its Octadentate Analogue, HOPO-O_8, for Radiopharmaceutical Applications. *Inorganic Chemistry* **2023**. DOI: 10.1021/acs.inorgchem.2c03671, Copyright 203 American Chemical Society. Imma Carbo-Bague performed the synthesis and coordination chemistry and the radiochemistry experiments at TRIUMF. DFT calculations were performed by Cen Li. This project was supervised by Dr. Caterina F. Ramogida and Dr. Georg Schreckenbach. Imma Carbo-Bague wrote the manuscript except for the DFT section which was written by Cen Li.

Chapter 3 is an adaptation of a manuscript in preparation from Imma Carbo-Bague, Shelbie Cingoranelli, Shefali Saini, Angus Koller, Owen Glaser, Marianna Tosato, Patrick Davey, Eszter Boros, Suzanne E. Lapi, Caterina F. Ramogida. Imma Carbo-Bague performed the synthesis and received some assistance for the coordination chemistry from Marianna Tosato. The ^{47}Sc radiochemistry and in vivo evaluation was done by Shelbi at the University of Alabama and the ^{45}Ti radiochemistry was performed by Dr. Angus Koller and Owen Glaser at the University of Wisconsin-Madison. DFT calculations were performed by Patrick Davey. This project was supervisor by Dr. Caterina F. Ramogida, Dr. Suzanne Lapi, and Dr. Eszter Boros.

Chapter 4 is an adaptation of a manuscript in preparation from Imma Carbo-Bague, Lucas London, Milena Colovic, Michiel Van der Voorde, Cristina Rodriguez-Rodriguez, Marten Ooms, François Bénard, Hua Yang, Caterina F. Ramogida. The synthesis was performed by Imma Carbo-Bague who also performed the radiochemistry at TRIUMF. Immunoreactivity assays were performed by Milena Colovic at TRIUMF. All animal experiments were performed by Cristina Rodriguez-Rodriguez with assistance from Imma Carbo-Bague at the Centre for Comparative Medicine (CCM) and the protocol used was approved by the Institutional Animal Care Committee (IACC) of the University of British Columbia (protocol #A20-0132 (Sossi)) and was performed following the Canadian Council on Animal Care Guidelines. This project was supervised by Dr. Caterina F. Ramogida. Imma Carbo-Bague wrote the manuscript.

Chapter 1.

Introduction

1.1. Background

Targeted radionuclide therapy (TRT) has emerged as a highly promising alternative to traditional cancer therapies (e.g., chemotherapy or biologically targeted therapy) due to its ability to non-invasively treat disease by selectively depositing a radiation payload to the damaged cells while sparing the nearby healthy tissue. The specificity of TRT results in very little off-target toxicity and fewer side effects, significantly increasing the quality of life of patients during and after treatment.[1] The cytotoxic radiation is delivered to the tumor site by radioactive nuclides incorporated in a drug complex known as a radiopharmaceutical. The decay properties of the isotope will determine its use. Therapeutic radionuclides are those that decay via the emission of alpha (α) or beta (β^-) particles or Meitner-Auger electrons (MAEs). In contrast, radioisotopes used for nuclear imaging emit photons (gamma (γ-rays)) either directly or indirectly.

The synchrony of therapy and imaging is key to the successful application of nuclear medicine. Indeed, one clear advantage of TRT is the possibility to assess the therapeutic efficacy and monitor the disease progression using nuclear imaging tools. Single photon emission computed tomography (SPECT) and positron emission tomography (PET) are the most common imaging modalities. The main difference between SPECT and PET is the type of radionuclides used. While SPECT imaging requires the use of a γ-emitting radionuclide (e.g., technetium-99m (^{99m}Tc), indium-111 (^{111}In)), PET scans are based on the coincidence detection of 511 keV photons produced during positron (β^+) annihilation, which are emitted by radionuclides such as fluorine-18 (^{18}F) or gallium-68 (^{68}Ga) to create a 3D image.[2–5] SPECT imaging has been traditionally used more extensively than PET due to its availability and lower cost. However, current trends in nuclear imaging are moving towards the use of PET because of its higher resolution and sensitivity. SPECT and PET scans are usually performed along with CT scans (3D x-rays) to obtain a more detailed biological representation.

1.1.1. Radiopharmaceutical design

How a radionuclide is incorporated into a drug complex depends on the nature of the radionuclide. Generally, ‘organic’ or non-metallic isotopes (e.g., ^{18}F, iodine-131 (^{131}I), carbon-11 (^{11}C)) can be incorporated via covalent bond linkages, while ‘inorganic’ or metallic radioisotopes (e.g., ^{68}Ga, ^{111}In) can be attached to a disease delivery vehicle via coordinate bonds through a chelating ligand. Often, the preparation of organic radiopharmaceuticals can involve a complex and lengthy radiosynthesis which requires the production of large amounts of radioactivity to compensate for the short half-life. Metallic radionuclides (aka radiometals) have emerged as excellent candidates to expand the nuclear toolbox as they are extremely flexible in terms of radiological half-life, decay emissions, and chemical properties making them amenable for incorporation into radiopharmaceuticals for imaging and therapy. Consequently, the vast majority of emerging radionuclides being investigated for TRT are radiometals.

1.1.1.1. The bifunctional chelate (BFC) strategy

The most common approach to building an inorganic radiopharmaceutical is the bifunctional chelate (BFC) strategy (**Figure 1.1**). The purpose of this design is to use a chelate that can both sequester the radiometal and offer a conjugation point for the incorporation of a disease-targeting moiety (e.g., antibody, peptide). Employing this strategy, a typical radiopharmaceutical will have four components: (i) a radiometal with physical properties relevant for medical applications (type of decay and half-life), (ii) a chelate for metal binding and functionalization, (iii) a targeting vector that ensures drug accumulation in damaged cells, and (iv) a linker to connect the chelate and targeting vector. An advantage of this strategy is the possibility to tune each component individually to optimize the radiopharmaceutical performance.[5–8] Despite the apparent simplicity of this strategy, many considerations must be accounted for when designing a radiopharmaceutical. Some of the most important are the availability and accessibility of the radionuclide, matching of the physical and biological half-life of the radionuclide and targeting vector, the influence that the linker can have in the biodistribution of the drug complex (e.g., lipophilicity), and selectivity of the targeting vector for receptors that are overexpressed in cancer cells with minimal expression in neighbouring healthy cells. In this thesis, we are focusing on the basic component of this strategy, the bifunctional chelate. In general, the ideal BFC will have the following properties: fast complexation (<1

h) at low temperatures (<40 °C) and mild conditions (buffered solutions compatible with biological systems), thermodynamic stability and kinetic inertness to avoid demetallation in vivo and high selectivity for the desired radiometal to reduce the binding competition of metal impurities present in solution.

BFC design

When a new chelate is developed, it is essential to know the chemical properties of the desired radiometal including oxidation state, hard-soft acid-base (HSAB) character, preferred coordination number(s), redox chemistry, or the affinity to bind endogenous proteins to rationally design a BFC that will have all the ideal properties for radiopharmaceutical elaboration. However, this knowledge is not always available especially for radiometals that do not have stable isotopes (e.g., actinium-225 (^{225}Ac)). In these cases a surrogate metal is chosen that has similar chemical properties (e.g., La^{3+} for Ac^{3+}) for which comparisons can be drawn. Once this information is gathered, the next question is the choice of a macrocyclic or an acyclic chelate. Historically, macrocycles are more kinetically inert than acyclic chelates even if their thermodynamic stabilities are comparable. Macrocycles also benefit from a lower entropic loss upon metal coordination compared to acyclics, due to the so-called macrocyclic effect. In contrast, acyclics tend to have faster coordination kinetics. However, with the recent enormous effort on developing highly efficient chelates, both macrocyclic and acyclic chelates have demonstrated excellent radiolabeling properties with a variety of radiometals, for example, the macrocycle H$_2$macropa with ^{225}Ac or the acyclic Me-3,2-HOPO with thorium-227 (^{227}Th) which can both label the corresponding isotopes at room temperature in 30 min. Lastly, it is important to design a synthetic route for the BFC that is relatively simple and modular to incorporate various bifunctional handles (e.g., p-SCN-benzyl, maleimide group) for conjugation to different targeting vectors. To reduce the synthetic workload and optimize time and resources, it is common to design a route for the BFC but first synthesize the simpler version without the bifunctional handle. If preliminary radiolabeling results are promising, then attaching the bifunctional handle should be straightforward.

BFC evaluation

Once the chelate or the BFC is synthesized, preliminary radiolabeling screening is used to determine the suitability for use with the radiometal(s) of interest: binding affinity to the radiometals and conditions required to achieve high yields. If the radiometal-chelate complex fulfills the requirements of a BFC (*vida supra*) including high yields at low concentrations then the complex can be further characterized using the non-radioactive metal (or surrogate) through the standard inorganic chemistry characterization techniques including NMR, MS, UV-vis, etc. Structural information of the complex in solution can be obtained by NMR spectroscopy or in the solid state by X-ray crystallography. Thermodynamic stability constants or formation constants (K_{ML}) and pM values (-log $[M]_{free}$) – independent of the ligand protonation constants – are usually determined by potentiometry or spectrometric titrations and are useful values to compare the binding affinity of the same or different chelates with multiple metals. The kinetic inertness can be measured through acid dissociation constants or through competition assays with other metals that can compete in vivo with the radiometal of interest (e.g., Ca^{2+}, Fe^{3+}).[8] It is important to note that all these characterization data are obtained in the metal concentration range of 0.01-1 mM which is a few orders of magnitude higher than the radiometal concentration in the radiolabeling experiments which is typically in the pM to nM range. Thus, all this information is not directly relatable to the experimental radiochemistry data although it is extremely helpful in the design of future chelates.

Before conducting in vivo studies as an ultimate test of the radiometal-chelate complex stability, the complex is usually incubated in vitro in a mixture of biologically relevant mixtures such as human serum or blood serum and monitored over time via standard radioactive techniques (radio-thin layer chromatography (TLC) or radio-HPLC) to determine the amount of intact complex. This assay is a more pertinent way to estimate the stability and kinetic inertness of the radiometal complex in vivo. Failure to remain >80% intact over a reasonable time frame (~1 half-life) can indicate a low in vivo performance.

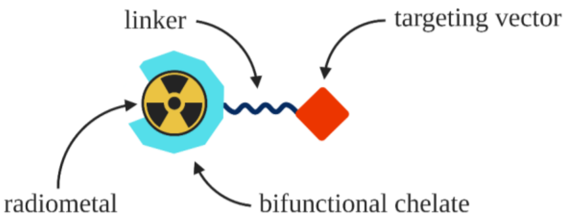

Figure 1.1. Depiction of the bifunctional chelate (BFC) strategy used for the radiopharmaceutical design.

Besides the BFC strategy, other radionuclide delivery approaches that have been investigated include unconjugated radionuclide compounds (e.g., radium-223

[^{223}Ra]RaCl$_2$), nanoconstructs, and microspheres (e.g., yttrium-90 (^{90}Y-microspheres)).[9–11] However, in this introduction we only describe the radiopharmaceuticals designed via the BFC model. For further information, the reader is redirected to the following reviews.[1,12]

1.1.2. Radiotheranostics

Theranostics (aka theragnostics) is an emerging medical technique that couples imaging and therapy of disease. Radiotheranostics is the term used in nuclear medicine that describes the use of one or two radiopharmaceuticals for theranostic purposes, typically one radiopharmaceutical which emits particulate radiation for therapy, and a second drug which emits photons for imaging/diagnosis (**Figure 1.2**). The success of radiotheranostics lies on the identical or very similar chemical and biological properties (i.e., biodistribution, pharmacokinetics, etc.) of the radiopharmaceutical pair in use. Choosing the wrong theranostic pair can lead to the use of inappropriate therapeutic strategies ultimately leading to detrimental effects in treatment accuracy.[13–15] Theranostic pairs can generally be divided into three categories: (i) same-element isotope pairs, (ii) different-element pairs, and (iii) different-radiopharmaceutical pairs.[15] In an ideal situation, a same-element theranostic pair would be chosen due to the intrinsically identical chemical properties of the two radioisotopes with the only difference being the number of neutrons, for example, ^{124}I/^{131}I, or yttrium-86 and yttrium-90 (^{86}Y/^{90}Y).[16–18]

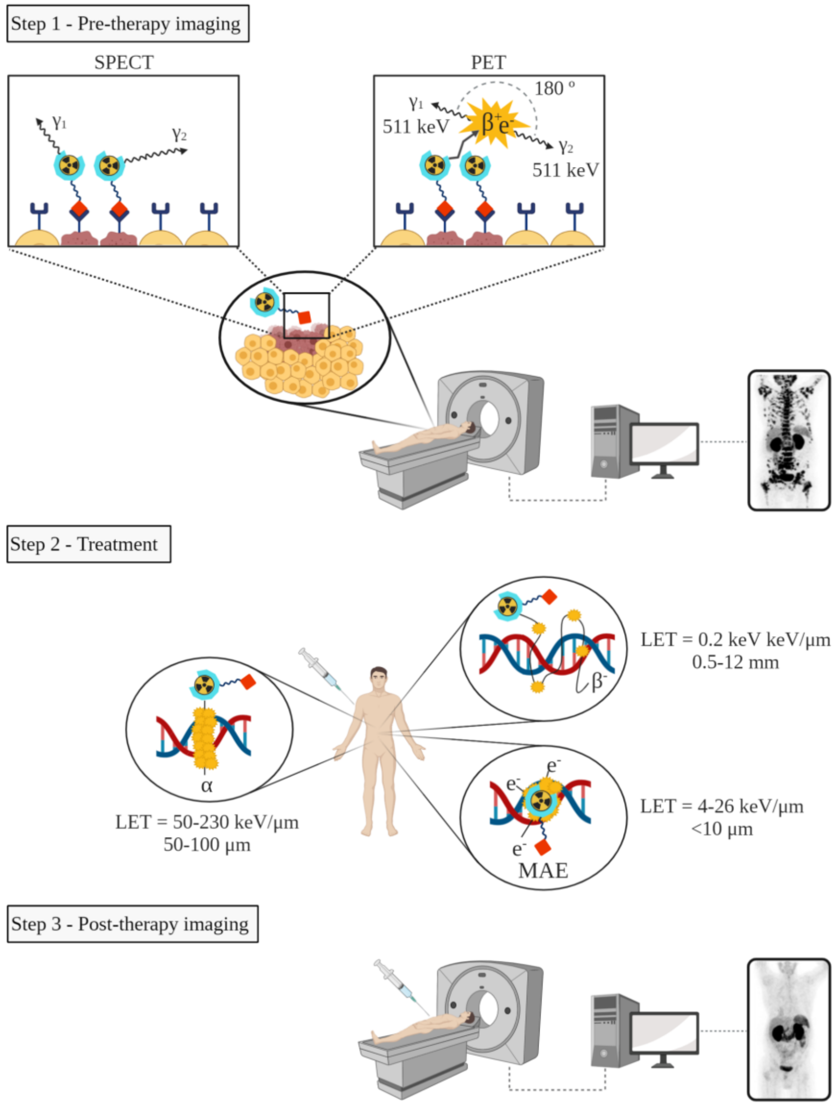

Figure 1.2. Depiction of a typical radiotheranostic treatment process.
Step 1 – the patient is administered a β^+-emitting radiopharmaceutical for PET or SPECT imaging, respectively. Acquired images can be used to diagnose and stage disease and predict response to therapy. Representative PET/CT scan shows widely spread metastatic disease indicated by accumulation of radioactivity (black regions) throughout the skeletal structure, and normal excretion of radiotracer through the kidneys. *Step 2* – the patient is administered one or more cycles of a radiopharmaceutical that emits particulate radiation (α, β^-, or Meitner-Auger electrons) that can cause DNA damage and cell death. *Step 3* – the patient is administered with the same imaging radiopharmaceutical as in step 1, and the response to therapy is visualized through image acquisition. Representative PET/CT scan shows the image of the same patient after treatment; metastatic disease is gone, and only normal renal excretion of the radiotracer remains. In all steps, following administration, the radiopharmaceutical circulates the body and primarily accumulates at the diseased cells (e.g., a targeting vector covalently attached to the radiation payload binds to over expressed surface receptors on diseased cells). Representative PET/CT images were originally published in JNM: Kratochwil, C., et al. J. Nucl. Med. 2018:59:795-802 ©SNMMI

The different radioisotopes are bound to the same delivery system and the resulting radiopharmaceuticals are generally accepted to have the same biological behaviours. Unfortunately, there are very few elements that have a therapeutic radioisotope and an imaging analogue with decay characteristics relevant to nuclear medicine. Different-element pairs labeled to the same drug complex are the preferred choice when the same-element isotope pair is not possible. In this case, the therapeutic and imaging isotope must have very similar chemical properties. The evaluation of the suitability of this type of theranostic pair is not straightforward and often chemically similar isotopes are assumed to have similar biological properties when this is usually not the case. Most of the theranostic pairs in current clinical use are different-element pairs which are chosen based on their complimentary decay properties and ease of access and availability rather than their chemical similarities and characteristics. The most remarkable pair is ^{68}Ga and lutetium-177 ([^{68}Ga]Ga-DOTATOC/[^{177}Lu]Lu-DOTATOC) (1,4,7,10-tetraazacyclododecane-1,4,7,10-tetraacetic acid (DOTA)-Tyr^{3}-octreotide (TOC)) used for PET imaging and TRT, respectively.[19,20] The last and most complex group is the different-radiopharmaceutical pairs. A wide range of options arises from the combination of different-element isotopes and different radiopharmaceuticals (e.g., [^{99m}Tc]Tc-HYNIC-TOC (hydrazinonicotinic acid (HYNIC)) and [^{18}F]-FDG (fluorodeoxyglucose)).[21] The assessment of each pair is highly challenging and thus will not be taken into account here. Only the same- and different-element isotope pairs will be discussed here.

1.1.3. General considerations of radiotheranostics

1.1.3.1. Radiobiology

Radiobiology studies the biological response of cells to ionizing radiation and the resulting cellular consequences.[22] DNA is the main target of radiation-induced damage. The incident radiation produces a variety of direct DNA lesions including single-strand and double-strand breaks (SSBs, DSBs) or base pair modifications and indirect mechanisms such as water dissociation leading to the production of reactive oxygen species (ROS) or hydroxyl radicals. These clusters of DNA damage activate a large number of cellular pathways (apoptosis, cell-cycle arrest, etc.) ultimately leading to cell death. Although the cell has mechanisms to repair small lesions such as SSBs, the accumulation of many unrepaired lesions or a few highly cytotoxic events (namely DSBs) is lethal. The biological response of cells is dependent on many factors including the total dose, absorbed rate, type of tissue, volume of the irradiated area or the linear energy transfer (LET), which measures the energy released by radiation per unit of length (keV/µm). At equal absorbed doses, radiation with high LET is more cytotoxic than low LET.[22–25]

The DNA-centered approach has changed over the years with the discovery of alternative radiation-induced biological effects that cannot be explained by this simplistic view. The new paradigms include extra-nuclear targets (cell membrane and mitochondria) and non-targeted effects, also known as the radiation-induced bystander effect (RIBE)[23]. The RIBE is the production of signals from irradiated cells which induce responses to non-irradiated cells in the vicinity. A complete understanding of the RIBE effect can significantly impact the design of novel TRTs by incorporating a non-targeted effect model in dose assessment. Detailed descriptions of these effects are out of the scope of this introduction and the reader is directed to the following articles.[22,23,26]

1.1.3.2. Dosimetry

Radiation dosimetry is the measurement of the absorbed dose delivered by ionizing radiation to healthy and damaged tissue.[25] Dosimetry studies are highly important because they provide an understanding of the effects and efficacy of various radiation treatments and are essential for the determination of the correlation between treatment doses and patient response. Dosimetry calculations are currently obtained by analyzing quantitative PET and SPECT images of the radiopharmaceuticals after injection. This approach only provides information at a macroscopic scale (organs and large tumors) and dosimetry calculations at a microscopic level still remain a challenge.[1,22] Profound research efforts are currently aimed at developing novel methodologies for the accurate quantification of absorbed dose. These findings will have a large implication in the clinical implementation of novel radiopharmaceuticals for TRT. In this context, radiotheranostics are believed to be the future of nuclear medicine by establishing the basis of personalized precise treatment. Detailed information on the dosimetry of radiotheranostics can be found elsewhere.[15]

The development and clinical investigations of novel radiopharmaceuticals is a rapidly evolving research field. Besides the widely used FDA-approved drugs, the recent incorporation of a novel radionuclide-based therapy, lutetium-177 [^{177}Lu]Lu-DOTATATE ((Tyr$_3$-Thr^8)-octreotate (TATE)) (Lutathera®),[27] is an important milestone in TRT that is encouraging further development of radiotracers based on rare medical isotopes. We envision that the clinical implementation of these emerging drugs will have an enormous impact on cancer treatment in the coming years. In this review, we have selected some of the most prominent radioisotopes that we believe will be part of an increasing catalogue of available radiopharmaceuticals.

This introduction chapter presents some of the most promising and emerging radionuclides for TRT for cancer treatment. The radioisotopes are classified according to their type of emission (α, β^- and MAE) and each section includes a brief description of the type of therapeutic particle followed by the chemistry, production, and biological studies of the corresponding radionuclide. This introduction chapter intends to give an overview of the cutting-edge radionuclides which the authors believe have immense potential for clinical TRT applications. We also present a discussion of the possible theranostic pairs of each radionuclide and the advantages and disadvantages of each. The commonly used therapeutic radionuclides are not described here and the reader is referred to other reviews on the topic.[1,4–6]

1.2. α-particle-emitters

An alpha (α) particle is a nucleus of helium-4 $(^{4}He)^{2+}$ consisting of two protons and two neutrons. Due to the high positive charge and heavy mass, alpha particles are a source of highly powerful ionizing radiation (LET 50-230 keV/µm) (**Figure 1.2**).[22] Their high energy (5-9 MeV) and short tissue range (50-100 µm, <10 cell diameters) make α particles very suitable for the treatment of small metastatic tumors or circulating malignant cells (blood or bone marrow). In addition to their highly toxic intrinsic nature, some of the most up-and-coming α-emitters (^{225}Ac or ^{227}Th) decay via the emission of multiple α particles which drastically increases the potency of such radioligands.

Although it has been clinically demonstrated that alpha particles are extremely powerful tools for tumor eradication, a few challenges must be addressed before targeted alpha therapies (TATs) can be translated into the clinic: (i) the fate of the daughter isotope after an α decay, particularly for multiple α-emitting radionuclides, is a general concern surrounding TAT. Each α emission has an associated recoil energy of about 100-200 keV that will break coordination bonds (~5 eV) causing the detachment of daughter isotope from chelate thus resulting in the “free” circulation of potentially radiotoxic radionuclides that might cause undesired harm. For example, in the case of ^{225}Ac with four α-particle emissions, the longest-lived daughter isotope bismuth-213 (^{213}Bi, $t_{1/2}$ = 46.6 min) is known to accumulate in kidneys when circulating "freely". Cell internalization of the radiopharmaceutical may be a way to overcome the recoiling daughter issue although there is yet no solid evidence of the daughter radionuclides' retention inside cells;[25,28] (ii) radiation dosimetry is another impediment to the development of TAT. High LET, short-range and complex decay schemes with multiple α emissions make the dosimetry methods of α-emitters highly demanding.[25,29,30] A promising tool for TAT dosimetry is the α-camera developed by Bäck et al.[31] This revolutionary bioimaging technique provides quantitative data to detect α-particles in tissues ex vivo on a near-cellular scale. Despite the difficulties associated with the clinical implementation of alpha-emitters, there are currently already three FDA approved α-particle emitting agents. A non-targeted drug used to treat skeletal metastases, [^{223}Ra]RaCl$_2$ (Xofigo®), and two targeted ^{177}Lu radiopharmaceuticals, [^{177}Lu]Lu-DOTATATE to treat neuroendocrine tumours and [^{177}Lu]Lu-PSMA-617 (Pluvicto®) for metastatic prostate cancer.[27,32]

Despite the aforementioned issues which are currently being addressed by many research groups, α-emitters are of high interest due to their increased potency compared to the commonly used β$^-$-emitters. There are some clinical reports where an excellent response to α-therapy has been observed in patients that were resistant to β$^-$ therapy.[33–35] The immense potential of α-emitters as therapeutic agents in nuclear medicine is undeniable; this promising group of radiopharmaceuticals is expected to become part of routine hospital treatments. The most prominent and emerging alpha-emitting isotopes will be presented next (summarized in **Table 1.1**); other clinically relevant α-emitters have not been described here but can be found elsewhere (e.g., astatine-211 (^{211}At) or ^{212}Bi).[4,6,36]

Table 1.1 α-emitting radionuclides discussed in this chapter with relevant physical decay data, chelates of interest, targeting vectors employed in previous biological studies, and previously used or proposed (blue) theranostic pairs.

Isotope	Half-life	Decay	E_{avg} (keV)	Chelates	Targeting vectors			Theranostic Pair used/proposed
					mAb	Peptides	Small molecules	
^{149}Tb	4.1 h	α (17%)	4000	CHX-A"-DTPA	rituximab[37]			^{149}Tb (SPECT)[38]
				DOTA			PSMA-617[38] cm09[39,40]	^{152}Tb (17.5 h, PET)[41,42] ^{155}Tb (5.32 d, SPECT)[43]
^{212}Pb	10.6 h	$β^-$ α (36%)[a]	100 6300[a]	DOTA		αMSH[44] TATE[45]	PSMA-targeting[46]	^{203}Pb (51.9 h, SPECT)[47]
				TCMC	trastuzumab[48,49]		PSMA-617[50] NG001[50] PSMA-targeting[46] CA012[47]	
				Crypt[51]				
				Cyclen-4py[52]				
^{225}Ac	10.0 d	α	5800	DOTA	lintuzumab[53]	Substance-P[54] TOC[55,56]	PSMA-617[33,57]	^{68}Ga (67.7 min, PET)[57] ^{111}In (2.80 d, SPECT)[58]
				H_2macropa	trastuzumab[59]		RPS-070[59]	^{132}La (4.59 h, PET)
				H_2bispa^{2} [60]				^{133}La (3.91 h, PET)
				crown		αMSH[61]		^{134}Ce (3.16 d, PET)
				H_4py4pa	trastuzumab[62]			^{226}Ac (29.4 h, SPECT)
^{227}Th	18.7 d	α	6000	DOTA	trastuzumab[63]			^{89}Zr (78.4 h, PET)
				$(Me\text{-}3,2\text{-}HOPO)_4$	Mesothelin-targeting[64] PSMA-targeting[65]			^{134}Ce (3.16 d, PET)

Branching ratios in parentheses if not 100%. [a]Decay daughter

1.2.1. Terbium-149

Terbium is a unique element with four clinically relevant isotopes (^{149}Tb, ^{152}Tb, ^{155}Tb, ^{161}Tb) with nuclear properties suitable for all types of imaging and therapeutic applications. Terbium-149 (^{149}Tb) is a low-branching alpha-emitting radionuclide with a half-life of 4.1 h (E(α) = 4.0 MeV, branching ratio (BR) = 17%)[1] (**Figure 1.3**).

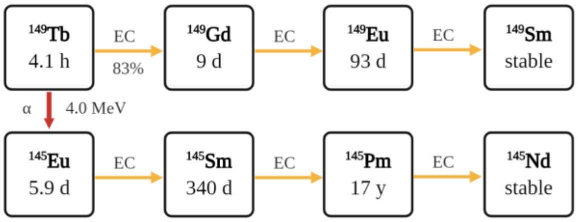

Figure 1.3. ^{149}Tb decay scheme

1.2.1.1. Production of ^{149}Tb

Obtention of high specific activity ^{149}Tb has proven to be challenging. In general, the production of all terbium radionuclides with interest in nuclear medicine is not easily accessible and is dependant on mass separation facilities. There are currently only a few facilities with the capability to produce ^{149}Tb: ISOLDE facility at CERN (Geneva, Switzerland) is among the most active research centers. To date, the most efficient production route is the proton-induced spallation of tantalum targets on a zinc-covered gold foil via a ^{nat}Ta(p,x)^{149}Tb nuclear reaction followed by online mass separation.[38–40]

Alternative methods were previously described using light particle-induced (p or ^{3,4}He) reactions on ^{152}Gd or heavy ion induced nuclear reactions by direct or indirect methods such as ^{141}Pr(^{12}C, 4*n*)^{149}Tb or ^{142}Nd(^{12}C, 5*n*)^{149}Dy→^{149}Tb.[66,67] However, the easy availability of tantalum and the obtention of highly pure ^{149}Tb using an online mass separation technology have made this methodology the preferred pathway to obtain small amounts of clinical-grade ^{149}Tb. The large-scale production of this rare isotope is currently being developed.

---

[1] Physical-decay data (half-life, energies, intensities, branching ratios) for all radioisotopes were obtained from the National Nuclear Data Center (nndc.bnl.gov) unless otherwise noted.

1.2.1.2. Chemistry of terbium

Terbium has only one naturally occurring stable isotope (^{159}Tb). It is commonly found in the 3+ oxidation state with an ionic radius of 1.04 Å in coordination number (CN) = 8 and as a lanthanide member, it has a high binding affinity for oxygen donor ligands. In the context of nuclear medicine, Tb^{3+} is chemically very similar to $^{90}Y^{3+}$ (1.16 Å in CN = 8) and $^{177}Lu^{3+}$ (1.12 Å in CN = 8).[68]

1.2.1.3. Chelates of interest

DOTA (N_4O_4; **Table 1.2**) forms highly stable complexes with Tb (log K_{ML} = 23.5-28.6) and it is the preferred choice for terbium chelation; however, radiolabeling reactions require high temperature (95 ºC) which is incompatible with temperature-sensitive biomolecules.[41,69] On the other hand, diethylenetriaminepentaacetic acid (DTPA, N_3O_5, **Table 1.3**) forms equally robust complexes (log K_{ML} ≈ 23) and its derivative 2,2'-((2-(((1S,2S)2bis(carboxymethyl)amino)cyclohexyl)-(carboxymethyl)amino)ethyl)-azanediyl)diacetic acid) (CHX-A''-DTPA) (N_3O_5, **Table 1.3**) has been used in heat-sensitive reactions as it can achieve quantitative radiolabeling at room temperature.[43] With the successful Tb chelation using commercially available chelates, the development of terbium tailored chelates has not been needed urgently, while research efforts have prioritized the scale-up of isotope production.

1.2.1.4. Biological studies with ^{149}Tb

The low availability of ^{149}Tb has resulted in a limited number of studies on the therapeutic efficacy of ^{149}Tb radiopharmaceuticals (**Table 1.1**). [^{149}Tb]Tb-CHX-A''-DTPA-rituximab was the first radiotracer of this isotope investigated in a preclinical study in animal models.[37] Additionally, encouraging results have been obtained with the prostate-specific membrane antigen (PSMA) PSMA-617 and cm09 (**Table 1.4**), a low molecular-weight DOTA-folate conjugate with an albumin binding entity to enhance blood circulation time.[38–40] Tumor growth delay and increased survival times with no signs of acute toxicity were observed in treated mice in both studies.

Table 1.2. Selected macrocyclic chelates discussed in this chapter.

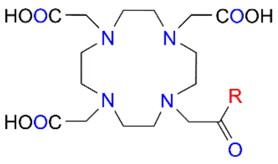 **DOTA** Pb^{2+}, Ac^{3+}, Th^{4+}, Tb^{3+}, Sc^{3+}	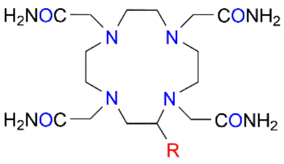 **TCMC** Pb^{2+}	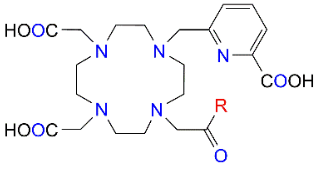 **DO3Apic** La^{3+}
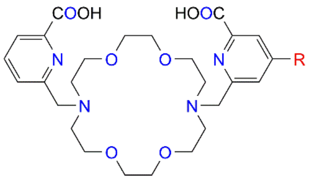 **H_2macropa** Ac^{3+}	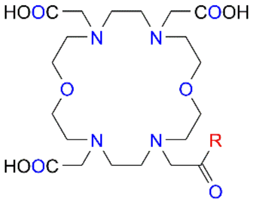 **crown** Ac^{3+}	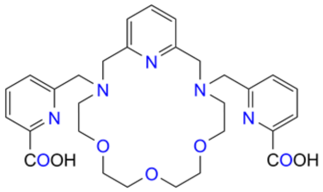 **py-macrodipa** Sc^{3+}
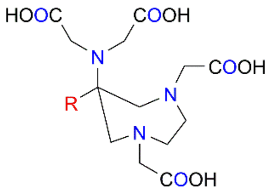 **AAZTA** Sc^{3+}	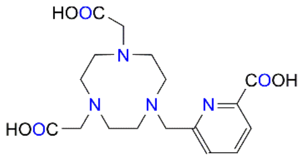 **H_3mpatcn** Sc^{3+}	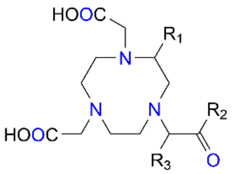 **NOTA** - R_1 = H, R_2 = R, R_3 = H **MANOTA** - R_1 = CH_2NH-R, R_2 = OH, R_3 = H **NODAGA** - R_1 = H, R_2 = OH, R_3 = CH_2CH_2CO-R Cu^{2+}, Sc^{3+}
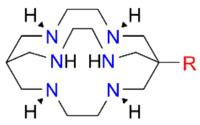 **Sar** Cu^{2+}	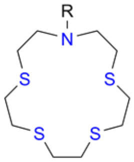 **NS_4** – R = H **NS_4-CA** – R = CH_2COOH **NS_4-BA** – R = N-benzylacetamide Hg^{2+}	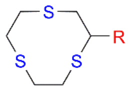 **trithiamacrocycle** Hg^{2+}

Potential (radio)metal coordinating atoms highlighted in blue. R (red) represents atom position for conjugation to targeting vectors or integration of a linker to create a bifunctional chelate (BFC).

1.2.1.5. ^{149}Tb theranostic pairs

^{149}Tb stands as a therapeutic isotope itself with the emission of γ rays (E(γ) = 165 and 359 keV, I = 26 and 29%) with energies suitable for SPECT imaging, respectively. The suitability of in vivo tumor localization with ^{149}Tb radiotracers in tumor xenografts has been demonstrated in two different studies.[38,70] Although the quality of the images was very high, it has been noted that the required dose for in-human visualization is not known yet and further investigations are needed to translate the imaging possibilities into clinics.[70]

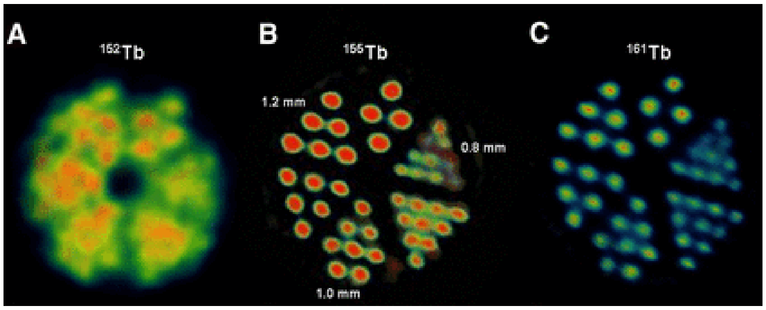

Figure 1.4. (A) PET image of Derenzo Phantoms (~ 1.9 MBq of ^{152}Tb). (B) SPECT images of Derenzo Phantoms (~ 0.6 MBq of ^{155}Tb). (C) SPECT images of Derenzo Phantoms (~ 50 MBq of ^{161}Tb).

Adapted from Müller C, Zhernosekov K, Köster U, et al. A unique matched quadruplet of terbium radioisotopes for PET and SPECT and for α-andβ- radionuclide therapy: an in vivo proof-of-concept study with a new receptor-targeted folate derivative. J Nucl Med. 2012;53:1951–9.[40]

In addition, there are two more terbium isotopes with decay properties suitable for imaging, ^{152}Tb ($t_{1/2}$ = 17.5 h, E(β^{+}_{avg}) = 1.14 MeV, I = 20%) for PET and ^{155}Tb ($t_{1/2}$ = 5.32 d, E(γ) = 86.5 and 105.3 keV, I = 32 and 25%) for SPECT. The feasibility of ^{152}Tb and ^{155}Tb was first demonstrated in phantom studies by Müller et al. (**Figure 1.4**).[40] Despite the lower resolution, ^{152}Tb has already been tested as the imaging surrogate of ^{149}Tb in two different in-human studies using DOTATOC and PSMA-617 in substitution of the routine imaging isotope ^{68}Ga ($t_{1/2}$ = 67.7 min, E(β^{+}_{avg}) = 829.5 keV, I = 89%).[41,42] The use of ^{152}Tb has a clear advantage over ^{68}Ga due to its longer half-life which would allow for imaging at late time points. Regarding the imaging potential of ^{152}Tb, there is currently only one study on its use as the diagnostic pair for ^{177}Lu instead of the imaging radionuclide ^{111}In ($t_{1/2}$ =2.80 d, E(γ) = 171.3 and 245.3 keV, I = 91 and 94%), which can be radiolabeled to the same chelates as ^{177}Lu but has very different chemical behaviour and pharmacokinetics to radio-lanthanides.[43]

1.2.2. Lead-212

Even though lead-212 (^{212}Pb) is a pure beta emitter ($t_{1/2}$ = 10.6 h, E(β^-_{avg}) = 100 keV, intensity (I) = 100%), it is commonly investigated in alpha therapy as it can be used as an α particle generator through its decay daughter ^{212}Bi ($t_{1/2}$ = 60.5 min, E(α) = 6.3 MeV, 36%) and the very short-lived polonium-212 (^{212}Po, $t_{1/2}$ = 0.51 s, E(α) = 7.4 MeV) (**Figure 1.5**). One of the benefits of ^{212}Pb labeled radiopharmaceuticals is extending the short half-life of ^{212}Bi which allows increased sample preparation time.

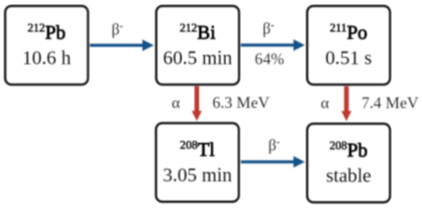

Figure 1.5. ^{212}Pb decay scheme

1.2.2.1. Production of ^{212}Pb

^{212}Pb is obtained with high yields from a ^{224}Ra generator that can be used for on-site production of clinical grade ^{212}Pb and ^{212}Bi. The production and separation methods for the obtention of highly pure ^{212}Pb and ^{212}Bi have been well described before.[71] In brief, ^{224}Ra is obtained by eluting with 1 M HCl a generator column containing actinide resin with immobilized ^{228}Th. Then a solution of ^{224}Ra in equilibrium with its progeny in 0.1M HCl and 0.5 M NH_4OAc is used for radiolabeling.[72]

1.2.2.2. Chemistry of lead

^{208}Pb is the most abundant natural lead isotope (52.4%). Pb exists in two different oxidation states, 2+ and 4+, although Pb^{2+} is more stable. Pb^{2+} is classified as an intermediate/soft Lewis acid according to the hard-soft acid-base (HSAB) theory and thus can form stable complexes with a variety of compounds bearing N, S or P atoms. Lead compounds are found in a vast variety of coordination numbers (1-12) and geometries and it has a large ionic radius that ranges from 1.19-1.49 Å (CN 6-12).[68,73]

Table 1.3. Selected acyclic chelates discussed in this chapter.

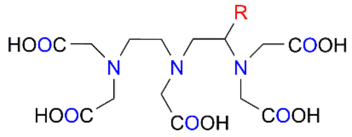

DTPA

Ac^{3+}, Tb^{3+}, Sc^{3+}

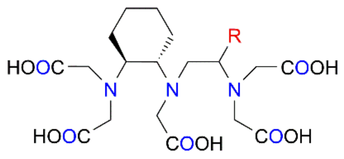

CHX-A"-DTPA

Tb^{3+}

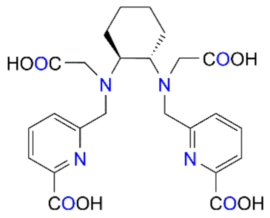

H_4CHXoctapa

Ac^{3+}

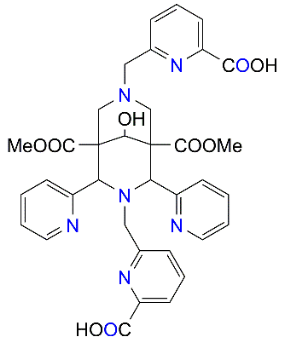

H_2bispa2

Ac^{3+}

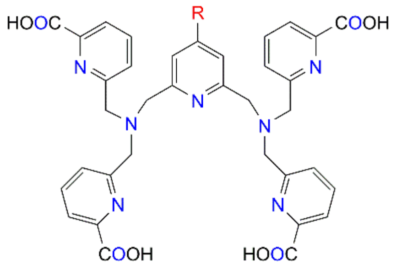

H_4py$_4$pa

Ac^{3+}

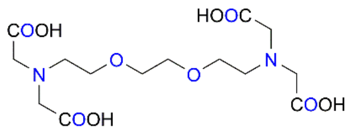

EGTA

Sc^{3+}

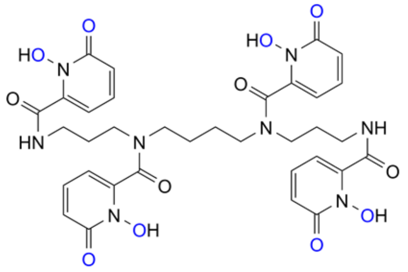

HOPO-O$_8$

Sc^{3+}, Th^{4+}

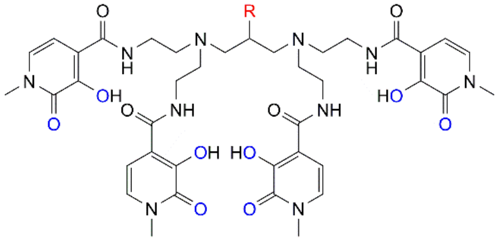

Me-3,2-HOPO

Th^{4+}

Potential (radio)metal coordinating atoms highlighted in blue. R (red) represents atom position for conjugation to targeting vectors or integration of the linker to create a bifunctional chelate (BFC).

1.2.2.3. Chelates of interest

Chelation of the ^{212}Pb radioisotope has been explored with mainly two chelates, the multi-purpose macrocycle DOTA and the Pb^{2+} specifically designed 2-(4-isothiocyanatobenzyl-1,4,7,10-tetraaza-1,4,7,10-tetra-(2-carbamonylmetyl)-cyclododecane (TCMC, N_4O_4; **Table 1.2**).[50,74] Even though Pb-DOTA complexes are stable at biological pH, this macrocyclic ligand is only able to retain about 65% of the progeny isotope generating off-target toxicity that can be fatal in vivo.[75] Moreover, DOTA is susceptible to acidic conditions which can result in the acid-catalyzed dissociation of Pb^{2+} after cell internalization or during metabolic processing of proteins. These low concentrations of "free" lead have been demonstrated to be transported by red blood cells to the bone causing bone marrow toxicity.[76,77]. TCMC, a DOTA derivative bearing four amide pendant arms, has to date been the most effective lead chelate.[71,78] ^{212}Pb radiolabeling of TCMC can be easily achieved in a short time at mild temperatures (30 min, 37 ºC).[50] The coordination of the lead ion in the Pb-TCMC complex is very favourable and results in a full encapsulation of the metal ion in an eight-coordinate complex which enhances the stability of the complex and lowers the acidic lability of the metal ion. Unfortunately, the destabilization of the decay daughter from the TCMC complex remains a challenge.[46] The Ramogida group has recently reported the development of a cryptand BFC (Crpyt, N_2O_4) with similar radiolabeling affinity to TCMC and an evaluation of the effect of the macrocyclic ring size on ^{212}Pb complexes.[51,52] Among the studied structures, two pyridyl-based macrocycles (Crown-4py, N_8O_2 and Cyclen-4py, N_8) showed higher specific activities to the TCMC analog complexes.

1.2.2.4. Biological studies with ^{212}Pb

^{212}Pb mAb (monoclonal antibody)-conjugates have been investigated extensively for radioimmunotherapy despite the seemingly incompatible physical half-life of the isotope and biological half-life of the targeting vector (typically 3-4 weeks for mAbs).[48,79,80] Among them, [^{212}Pb]Pb-TCMC conjugated to trastuzumab (tzmb, Herceptin®), which targets the human epidermal growth factor receptor 2 (HER2) overexpressed in many breast cancers, has shown the most promising therapeutic results.[48,49,81]

With a better matching biological and physical half-life, ^{212}Pb radiopharmaceuticals have also been investigated for peptide receptor radionuclide therapy (PRRT) (the biological half-life of radiolabeled peptides is generally on the order of hours to days).[82]

Multiple targeting vectors such as derivatives of the melanocyte-stimulating hormone (MSH; **Table 1.4**) or TATE (**Table 1.4**) have been conjugated to a [^{212}Pb]Pb-DOTA construct for preclinical studies.[44,45,83,84] The encouraging preclinical data of [^{212}Pb]Pb-DOTAMTATE (DOTAM = TCMC) supported the initiation of a phase I clinical trial (NCT03466216).

^{212}Pb-labeled TCMC and DOTA have also been investigated in the context of PSMA ligands.[46,47,50] While both radiopharmaceuticals seem to have similar biodistribution profiles and tumor uptake, a 2.5-fold decrease in kidney uptake was observed for [^{212}Pb]Pb-TCMC-PSMA compared to [^{212}Pb]Pb-DOTA-PSMA. High stability of the radiotracers in vivo was determined by the absence of detectable ^{213}Bi activity outside of the tumor region after 24 h.[50]

1.2.2.4. ^{203}Pb theranostic pairs

^{203}Pb ($t_{1/2}$ = 51.9 h, E(γ) = 279.1 keV, I = 81%) is a gamma-emitting radioisotope and the ideal theranostic pair for ^{212}Pb suitable for SPECT imaging. Besides, ^{203}Pb is a very unique theranostic match because of its readily commercial cyclotron production and long half-life that accounts for four half-lives of ^{212}Pb.[85] Garmestani et al. performed pioneering work on the purification of ^{203}Pb and in vitro and in vivo evaluation of ^{203}Pb radioimmunoconjugates with [^{203}Pb]Pb-C-DOTA-trastuzumab.[85] The similar biochemical behaviour of ^{203}Pb and ^{212}Pb labeled peptides and small molecules has been examined in preclinical studies with animal models.[46,86] Strikingly, the clinical potential of [^{203}Pb]Pb-TCMC-PSMA image-based dosimetry in patients has recently been evaluated in two patients with metastatic castration-resistant prostate cancer (mCRPC).[47] This report highlights the importance of being cautious when extrapolating dosimetry studies from ^{203}Pb to ^{212}Pb due to the inherent different decay properties. Therapeutic studies with the ^{212}Pb analogue are warranted.

Table 1.4. Selected targeting vectors discussed in this chapter.

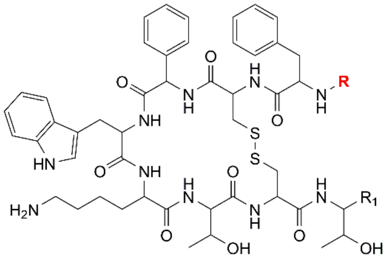

TATE[a] - R1 = COOH / TOC[b] - R1 = OH

TATE - ^{212}Pb, ^{67}Cu / TOC - ^{213}Bi, ^{225}Ac

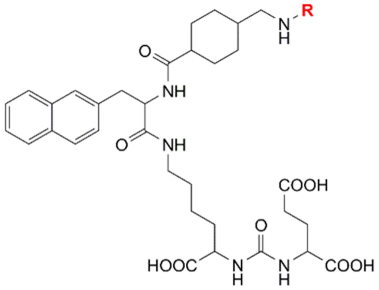

PSMA-617[c]

^{212}Pb, ^{213}Bi, ^{225}Ac, $^{149/161}$Tb

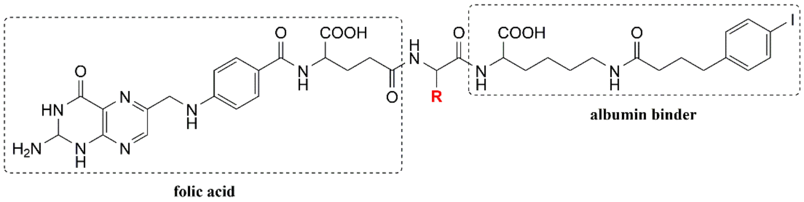

cm09

$^{149/161}$Tb

cm10

^{47}Sc

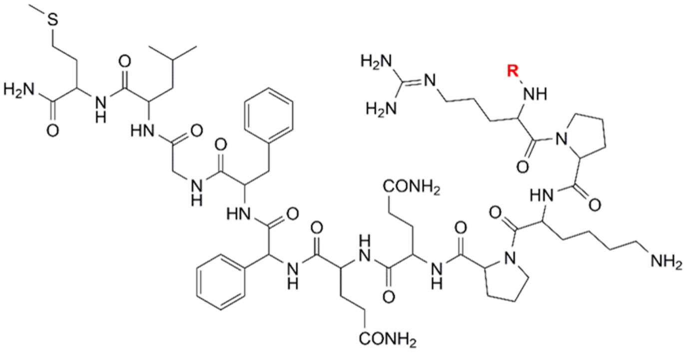

Substance P

^{225}Ac

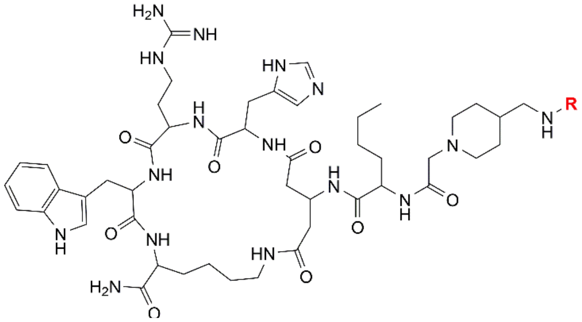

α-MSH[d]

^{212}Pb, ^{225}Ac

R (red) represents atom position for integration of the linker and chelate. [a]Tyr3-octreotate; [b]Tyr3-octreotide; [c]prostate-specific membrane antigen; [d]alpha-melanocyte stimulating hormone.

1.2.3. Actinium-225

^{225}Ac ($t_{1/2}$ = 10.0 d, E(α) = 5.8 MeV), with four powerful alpha particle emissions, is among the most promising isotopes for TAT. The decay chain of ^{225}Ac generates a cascade of six progeny isotopes with a total emission of four α and three β^- particles (**Figure 1.6**). The predominant decay path includes the two short-lived isotopes ^{221}Fr ($t_{1/2}$ = 4.80 min, E(α) = 6.3 MeV) and ^{217}At ($t_{1/2}$ = 32.3 ms, E(α) = 7.1 MeV) followed by ^{213}Bi ($t_{1/2}$ = 45.6 min, E(α) = 5.8 MeV, BR = 2%), which has been evaluated as a therapeutic isotope itself. However, there is a growing preference to use the longer-lived parent isotope ^{225}Ac for the optimal distribution and therapeutic efficiency of the tracer in larger tumors.

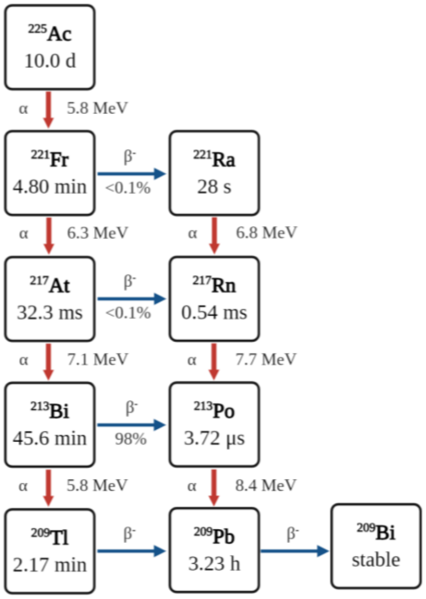

Figure 1.6. ^{225}Ac decay scheme

1.2.3.1. Production of ^{225}Ac

The global ^{225}Ac supply comes from stockpiles of ^{229}Th ($t_{1/2}$ = 7340 y), a daughter nuclide from ^{233}U that was produced via neutron irradiation of ^{232}Th as a component of the U.S. molten salt breeder reactor program for nuclear weapons development.[87] There are currently three main worldwide sources of ^{229}Th that provide clinical-grade ^{225}Ac: Oak Ridge National Laboratory (U.S.), Institute for Transuranium Elements (Germany) and Leipunskii Institute for Physics and Power Engineering (Russia). The standard procedure to separate carrier-free ^{225}Ac is achieved via a four-step chemical process consisting of anion and cation exchange chromatography in concentrated HNO_3.[88,89] The current annual worldwide production of ^{225}Ac is estimated to be ~63 GBq[90] which is sufficient for research and initial pre-clinical evaluations yet not enough to perform large clinical trials or to incorporate ^{225}Ac radiopharmaceuticals in routine treatments. Thus, much effort has been put towards the development of novel methods to produce ^{225}Ac at a large scale and reduced costs. Most of the production alternatives involve target irradiation of its parent nuclide ^{226}Ra. Among the various routes proposed,[91,92] the proton irradiation of ^{226}Ra in a cyclotron via the reaction ^{226}Ra[p,2n] shows potential; however, the use of ^{226}Ra targets is complex due to the low availability and the safety hazards associated with this isotope.[88] Spallation of ^{232}Th with high energetic protons has also been suggested to obtain significant amounts of pure ^{225}Ac [28,61,93]. For more details on the production of ^{225}Ac, readers are directed to the review by Radchenko et al.[28]

1.2.3.2. Chemistry of actinium

Little is known about the coordination chemistry of actinium as this element has no stable isotopes. It is a low polarizable ion classified as a "hard"/intermediate acid according to HSAB theory which is likely to form stable complexes with hard bases, such as O or N atoms.[94] ^{225}Ac has a very large ionic radius of 1.12 Å (CN = 6) and will, therefore prefer large coordination numbers (CN > 8).[6,68,94] Ac is found almost exclusively as Ac^{3+}. Characterization of Ac^{3+} complexes is extremely challenging due to the electronic configuration of the ion ($5f^0 6d^0$), which makes the isotope silent to the most common spectroscopic techniques (UV-vis, EPR, etc.), and the low branching ratios of the γ emissions of ^{225}Ac and ^{227}Ac and their daughters, which result in poorly resolved gamma spectroscopy spectra.[95]

Lanthanum (La^{3+}) is commonly used as an Ac surrogate metal to perform coordination chemistry studies due to its similar chemical properties. However, this methodology has some limitations and the fundamentals of Ac chemistry remain virtually unexplored to date.[94] The exceptionally promising results of ^{225}Ac radiopharmaceuticals for TAT have motivated researchers to explore new technologies to elucidate many aspects of actinium coordination chemistry. In 2016, Ferrier et al. characterized for the first time the Ac-aquo ion using XAFS revealing that the Ac^{3+} ion is coordinated to 10.9 ± 0.5 water molecules with an Ac-O_{H2O} distance of 2.63(1) Å.[96] Aldrich et al. recently reported the development of a ^{228}Ac generator, a short-lived actinium isotope (^{228}Ac, $t_{1/2}$ =

6.15 h) with intense and well-defined gamma emissions suited for γ spectroscopy offering a new perspective to the characterization of Ac complexes and their chemical behaviour.[97]

1.2.3.3. Chelates of interest

Predicting the chemical structure of a ligand that can form stable Ac^{3+} complexes in vitro and in vivo is extremely challenging when considering the current poor understanding of actinium chemical behaviour. Initial complexation studies involved the evaluation of both the common acyclic ethylenediaminetetraacetic acid (EDTA, N_2O_4), DTPA and cyclic ligands (1,4,7,10,13-pentaazacyclopentadecane-N,N',N'',N''',N''''-pentaacetic acid (PEPA, N_5O_5), 1,4,8,11-tetra-azacyclotetradecane- 1,4,8,11-tetraacetic acid (TETA, N_4O_4), DOTA.[98,99] The only one that showed quantitative labeling and stability in vivo was DOTA[100,101] yet, the stability of [^{225}Ac]Ac-DOTA has been questioned several times thereafter.[98,102] Moreover, DOTA has suboptimal ^{225}Ac labeling conditions requiring high temperatures (95 ºC), long reaction times and low specificity for the Ac^{3+} ion.[33]

The inefficiency of [^{225}Ac]Ac-DOTA has led to the development of novel high-denticity ligands. One of the most promising ^{225}Ac chelates is the macrocycle N,N′-bis[(6-carboxy-2-pyridyl)methyl]- 1,7-diaza-18-crown-6 (H_2macropa, N_4O_6; **Table 1.2**) investigated by Thiele et al.[59] This 18-membered macrocyclic ligand can radiolabel ^{225}Ac at sub-micromolar concentrations in 5 min at RT and remains intact after 7 days when challenged with an excess of La^{3+} ions or in human serum. Inspired by the performance of this macrocycle, Yang et al. recently reported the synthesis and evaluation of a crown chelate (2,2',2'',2'''-(1,10-dioxa-4,7,13,16-tetraazacyclooctadecane-4,7,13,16-tetrayl)-tetraacetic acid) consisting of a macrocycle with four nitrogen and two oxygen donor atoms and four carboxylic acid pendant arms (crown, N_4O_6; **Table 1.2**).[61] In radiolabeling studies, the crown chelate binds ^{225}Ac quantitatively at RT in less than 10 min.

Two acyclic ligands, 6,6'-({9-hydroxy-1,5-bis(methoxycarbonyl)-2,4-di(pyridin-2-yl)-3,7-diazabicyclo[3.3.1]nonane-3,7-diyl}bis(-methylene))dipicolinic acid (H_2bispa^2, N_6O_2; **Table 1.3**) and H_4py4pa (N_7O_4; **Table 1.3**) have recently been investigated as efficient ^{225}Ac chelators. H_2bispa^2,[60] an octadentate bispidine chelate bearing two picolinic acid pendant arms, was successfully radiolabeled by ^{225}Ac at RT under 30 min giving radiochemical yields (RCYs) of 94% at a ligand concentration of 10^{-5} M, and [^{225}Ac]Ac-bispa^2 showed improved stability over the [^{225}Ac]Ac-DOTA complex in human serum and La^{3+} competition studies. H_4py4pa,[62] an undecadentate chelate with a partially preorganized cavity consisting of four picolinate arms and a pyridyl cap, similarly complexes ^{225}Ac in less than 30 min at RT with ~97% RCY and is stable in serum over 9 days. Additionally, the evaluation of a small library of polydentate picolinic acid acyclic chelates revealed high RCY for ^{225}Ac radiolabeling with a N,N′-bis(6-carboxy-2-pyridylmethyl)-ethylenediamine-N,N′-diacetic acid (H_4octapa) chiral derivative, H_4*CHX*octapa (CHX = cyclohexyl) (N_4O_4; **Table 1.3**).[103]

1.2.3.4. Biological studies with ^{225}Ac

The unprecedented clinical results of ^{225}Ac radiopharmaceuticals have led to a surge in interest in ^{225}Ac TAT.[33,55,57,104] However, the clinical development of such drugs is being hampered by the low availability, high cost of the isotope, and lack of suitable chelates. Although the radiolabeling properties of DOTA are not optimal for ^{225}Ac chelation, [^{225}Ac]Ac-DOTA complexes have so far been the most exploited bioconjugates in preclinical studies and the only ones evaluated in a clinical setup.

Radioimmunotherapy is the preferred TAT type for a long-lived isotope like ^{225}Ac because of their matching biological and physical half-lives. Several mAbs have been tested in preclinical studies against a variety of cancer cell lines such as E4G10 targeting the vascular endothelial growth factor (VEGF) in colon cancer xenograft models,[105] 3F8 an IgG3 antibody for neuroblastoma treatment,[106] anti-CD33 for acute myeloid leukemia (AML),[53,107] the well-known anti-HER2/neu Trastuzumab for breast cancer therapy.[59,62,108] Among them, Hum195 (Lintuzumab), an anti-CD33 antibody for AML, has shown the highest performance and the promising results have supported the development of a solid clinical plan for ^{225}Ac-lintuzumab.[107]

The interest in [^{225}Ac]Ac-DOTA constructs conjugated to small peptides grew after the successful clinical studies of ^{213}Bi bioconjugates in PRRT. The longer half-life and higher potency of the parent isotope ^{225}Ac can overcome the challenges associated with using the short-lived radionuclide ^{213}Bi. Compared to mAbs, small peptides have faster circulation and clearance times which can be advantageous for ^{225}Ac therapy, particularly if the radiopharmaceutical is internalized to prevent the free circulation of recoiling daughters. [^{225}Ac]Ac-Substance P (**Table 1.4**) for therapy of glioblastoma and [^{225}Ac]Ac-DOTATOC for treatment of NETs are two of the most promising candidates for PRRT that have been investigated in patients in dose-escalation studies.[54–56]

Remarkably, [^{225}Ac]Ac-PSMA-617 has had the most significant impact on the development of ^{225}Ac radiopharmaceuticals for clinical implementation in TAT. The clinical potential of the PSMA-617 ligand was first evaluated with ^{177}Lu and based on the demonstrated superior activity of alpha emitters over beta emitters. In 2016, the first clinical experience with [^{225}Ac]Ac-PSMA-617 was reported in two patients with late-stage mCRPC. These unprecedented clinical results motivated further development of this radiotracer which has to date been evaluated in a large number of patients with mCRPC (**Figure 1.7**).[57,104,109] Despite the enduring responses, xerostomia is a concern for [^{225}Ac]Ac-PSMA-617 therapy and it is the main reason for treatment discontinuation, which highlights the need to optimize the treatment regimen for better therapies with lower side effects.

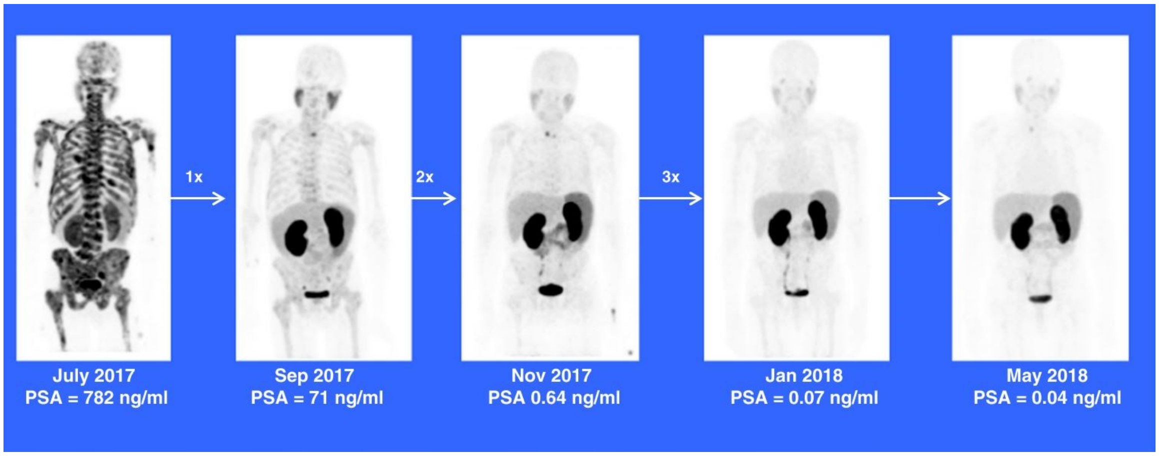

Figure 1.7. A treatment-naïve patient who presented with extensive bone metastasis at primary diagnosis achieved complete remission after three cycles of [^{225}Ac]Ac-PSMA-617 with de-escalating activities of 8/7/6 MBq. PET/CT scans were obtained with [^{68}Ga]Ga-PSMA-11.

Adapted from M. Sathekge, F. Bruchertseifer, O. Knoesen, F. Reyneke, I. Lawal, T. Lengana, C. Davis, J. Mahapane, C. Corbett, M. Vorster and A. Morgenstern, Eur. J. Nucl. Med. Mol. Imaging, 2019, 46, 129–138. Licensed under CC BY 4.0

1.2.3.5. ^{225}Ac theranostic pairs

Two daughter isotopes of ^{225}Ac emit gamma rays with energy suitable for SPECT imaging, ^{221}Fr (E(γ) = 218 keV) and ^{213}Bi (E(γ) = 440 keV).[110] While there is a limited number of studies on patient imaging with ^{213}Bi,[34] there are currently no reports on imaging in humans with the decay daughters of ^{225}Ac. It is worth noting the first investigation on the feasibility of simultaneous quantitative imaging ^{221}Fr and ^{213}Bi in vivo using a VECTor microSPECT/PET/CT system.[110] However, this imaging modality may be limited to preclinical in vivo models because the small amount of ^{225}Ac injected in a patient would require very long acquisition times to obtain quantitative data. Cerenkov luminescence imaging (CLI) has also been proposed as an alternative technique to perform in vivo visualization with ^{225}Ac radiopharmaceuticals.[111]

To date, clinical imaging of ^{225}Ac therapy relies on the widely used positron emitter ^{68}Ga although significant progress has been made on the use of the imaging surrogate ^{177}Lu ($t_{1/2}$ = 6.64 d, $E(\beta^{+}_{avg})$ = 133.6 keV, I = 100%).[57,109] An issue with this isotope is the enormous difference in injected activity of the ^{177}Lu analogue (7.4 GBq/cycle)[27] which can be up to 1000 times higher than that of ^{225}Ac (safe at 100 kBq/kg);[109] the effect that this can have in the biodistribution and the data accuracy is not yet well understood.[15] In 2020, cerium-134 (^{134}Ce, $t_{1/2}$ = 3.16 d, electron capture (EC) (100%)), an in vivo generator of the PET imaging isotope lanthanum-134 (^{134}La, $t_{1/2}$ = 6.45 min, $E(\beta^{+}_{avg})$ = 1217 keV, I = 64%) was proven to be an excellent imaging pair in its lower oxidation state.[112] Other La isotopes of interest recently produced include the two positron emitters lanthanum-132 ($t_{1/2}$ = 4.59 h, $E(\beta^{+}_{avg})$ = 1.29 MeV, I = 42%, $E(\gamma)$ = 464.5 keV, I = 76 %) or lanthanum-133 ($t_{1/2}$ = 3.91 h, $E(\beta^{+}_{avg})$ = 462 keV, I = 7.2%, $E(\gamma)$ = 278.8 keV, I = 3%). ^{133}La would be the preferred isotope with lower positron energies and less energetic and abundant concomitant γ rays.[113,114]

Furthermore, we propose ^{226}Ac ($t_{1/2}$ = 29.4 h, β^{-} (83%), EC (17%)) is an unexplored medically-relevant radioisotope with two SPECT-compatible gamma rays ($E(\gamma)$ = 230 keV, I = 27%; $E(\gamma)$ = 158 keV, I = 17.5%), which presents the possibility for chemically-matched Ac-radiopharmaceuticals; isotope production is possible via ISOL (isotope separation on-line) techniques.[103,110]

1.2.4. Thorium-227

^{227}Th ($t_{1/2}$ = 18.7 d, $E(\alpha)$ = 6.0 MeV) is the parent nuclide of ^{223}Ra – the first-in-class alpha-emitting radiopharmaceutical – which decays via the emission of five α particles with a total energy of ~ 33 MeV and two β^{-} particles (**Figure 1.8**). This radionuclide is of high interest due to the powerful long decay chain which could be greatly beneficial for the treatment of small metastatic tumors.

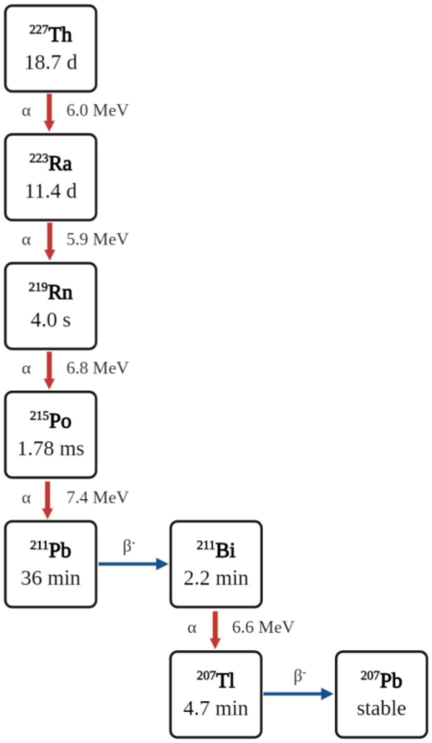

Figure 1.8. ^{227}Th decay scheme

1.2.4.1. Production of ^{227}Th

^{227}Th is produced from the β^- decay (98.6%) of its parent isotope ^{227}Ac (21.8 years); the two are commonly separated using ion-exchange or extraction chromatography.[115] ^{227}Ac is accessible via legacy material of ^{231}Pa stockpiles, a decay product of ^{235}U. An f-element selective extraction chromatographic material TRU-resin is used to isolate ^{227}Ac in 1M HCl.[116] Alternatively, large scale production of ^{227}Th can be achieved by irradiation of ^{226}Ra with thermal neutrons via ^{226}Ra(n,γ)^{227}Ra→^{227}Ac.[115,117,118]

1.2.4.2 Chemistry of thorium

Despite being the most abundant radioactive element in nature, thorium chemistry remains quite unexplored. It is mostly found in the 4+ state however 3+, 2+, and 1+ are also available. Th^{4+} is a strong Lewis acid with a high binding affinity for oxygen donor atoms and commonly forms octa- and nonacoordinate compounds.[119] The ionic radii of such Th^{4+} compounds are 1.05-1.09 Å.[68] Just like actinium, the absence of non-radioactive isotopes is a big challenge for the development of ^{227}Th tailored chelates.

1.2.4.3. Chelates of interest

The multipurpose macrocycle DOTA is known to form stable complexes with Th^{4+}; however, like in many other cases (^{225}Ac or ^{212}Pb), radiolabeling with ^{227}Th occurs in suboptimal conditions (>60 ºC) incompatible with radioimmunoconjugates. Two-step radiolabelling procedures requiring first forming the ^{227}Th-BFC complex and then coupling the targeting vector are inefficient. This process was recently improved by Ramdahl et al. with the development of an alternative chelate for fast (30 min) one-step reaction radiolabeling at RT.[120] The specifically designed chelate is an octadentate acyclic molecule with four hydroxypyridinone moieties attached to a branched symmetric polyamine scaffold with a carboxylic group for the conjugation of various biomolecules Me-3,2-HOPO O_8; **Table 1.3**). The high affinity of this ligand for large tetravalent metal ions has been demonstrated in thermodynamic and kinetic studies in conjunction with spectroscopic techniques.[121] Chapter 2 and chapter 4 present my work on the development and evaluation of ^{227}Th chelates with similar specific activities to that of Me-3,2-HOPO.

1.2.4.4. Biological studies with ^{227}Th

The long half-life of ^{227}Th makes this isotope very suitable for targeted radioimmunotherapy (RIT) to treat various cancer types such as lymphomas, breast, and ovarian cancers.[63,122–124] The DOTA conjugates [^{227}Th]Th-rituximab and [^{227}Th]Th-trastuzumab have been the focus of most in vitro and in vivo studies before the development of Me-3,2-HOPO.[63,124–126] The successful complexation of ^{227}Th to Me-3,2-HOPO chelate opened the door to exploring other targeting vectors such as mAb targeting CD70 against B cell lymphoma, and CD33 to treat AML.[123,127] Among the most relevant preclinical data, [^{227}Th]Th-mesothelin and a PSMA-targeting antibody conjugate, [^{227}Th]Th-PSMA, have shown excellent antitumor potency against lung and patient-derived prostate cancer xenograft models in mice.[64,65] The positive results reported have supported the initiation of two clinical trials NCT03507452 and NCT03724747, respectively. A more detailed analysis of all the ^{227}Th based radiopharmaceuticals can be found elsewhere.[128]

1.2.4.5. ^{227}Th theranostic pairs

Zirconium-89 (^{89}Zr, $t_{1/2}$ = 78.4 h, E(β^+_{avg}) = 396 keV, I = 23%) and ^{68}Ga have been evaluated as theranostic pairs to ^{227}Th. However, the $^{134}Ce^{4+}$ and ^{134}La in situ imaging pair was proposed as a more suitable theranostic pair better matching its electronics and size.[112,129] We believe this novel imaging pair along with its lower oxidation state for ^{225}Ac will play a key role in the future development of α-emitting theranostic pairs.

1.3. β^--particle-emitters

A β^- particle is an electron emitted from the nucleus of a radioactive atom during decay. β^- particles have intermediate energies (0.1-2.3 MeV) and long tissue ranges (0.5 - 12 mm) resulting in the lowest LET (0.2 keV/µm) of all therapeutic particles (**Figure 1.2**).[22] β-emitters are the most investigated and commonly used radionuclides for internal radiotherapy.[1] The intrinsic properties of β^- particles make them very appropriate for the treatment of mid- to large size tumors. Due to their long path-length, the cytotoxicity of beta particles is strictly related to the crossfire effect. This effect occurs when the irradiation reaches cells that are not directly targeted by the radiopharmaceutical. However, crossfire irradiation can result in undesired damage to healthy cells if the targeted cell cluster is too small. Additionally, the bystander effect must also be accounted for (see 1.3.1).[22]

Low LET radiation faces another challenge. The low energy deposited per cell produces few and scattered irradiation events which lead to partial DNA damage, such as single-strand DNA breaks or modifications on the base pairs, and each of them can be easily repaired. The sub-lethal damage caused by such particles requires extremely high doses of radiopharmaceutical to have a therapeutic effect on patients. Typically, β^--therapy consists of various cycles of high activity doses with up to several GBq/cycle,[130,131] which is approximately 100-fold larger than the experimental doses used for α-emitters presented in the previous section (typically 1-100 MBq/cycle)[57] except for ^{213}Bi (up to 3 GBq/cycle).[132]

Biodistribution and dosimetry studies are more accessible for β^--emitters compared to α-emitters. Most of the beta-emitters used in nuclear medicine have either a diagnostic pair from the same element (copper-64/67 (^{64}Cu/^{67}Cu)) or the therapeutic isotope itself co-emits imageable γ-rays (e.g., ^{177}Lu) or β^+ (e.g., ^{64}Cu) that allows for the obtention of good quality images for dose quantification and localization. Additionally, these β^--emitting radionuclides have simpler decay schemes with only one β^- particle emission per atom and very low recoil energies (~10 eV) associated with the daughter nuclide minimizing the likelihood of a nuclide-loss event. In the case of radiometal release, the range of the recoil energy is only a few interatomic spaces and can be neglected.[24]

^{131}I ($t_{1/2}$ = 8.02 d, E(β^-_{avg}) = 191.6 keV, I = 89.6%) is the more frequently used β^- emitter with two commercially available drugs, [^{131}I]NaI for thyroid cancer and [^{131}I]meta-iodobenzyl-guanidine (mIBG) for adrenergic receptor-positive tumors. Other popular β^--emitting radionuclides include the high-energy β^--emitter yttrium-90 (^{90}Y, $t_{1/2}$ = 64.0 h, E(β^-_{avg}) = 934 keV, I = 100%) and ^{177}Lu.[6] In the following section, we will describe four emerging β^--emitters which hold great promise for the future of therapeutic radiopharmaceuticals (summarized in **Table 1.5**), some of them have made their way into clinical trials while others are still in the development phase.

Table 1.5. β^-- emitting radionuclides discussed in this chapter with relevant physical decay data, chelates of interest, targeting vectors employed in previous biological studies, and previously used or proposed theranostic pairs.

Isotope	Half-life	Decay	E_{avg} (keV)	Chelates	Targeting vectors			Theranostic Pair used/proposed
					mAb	Peptides	Small molecules	
^{47}Sc	3.35 d	β^-	162.0	DOTA			cm10[133]	^{44}Sc (3.97 h, PET)[133]
				EGTA[134]				
				AAZTA			c(RGDfK)[135]	
^{67}Cu	61.8 h	β^-	141	DOTA	Anti-IGSF4[136]			^{64}Cu (12.7 h, PET)[137]
				cyclam			-c(-RGDfK)$_4$[138]	
				NOTA	panitumumab[139]			
				MANOTA[140]				
				Sar		TATE[141]		
^{161}Tb	6.9 d	β^-	154	DOTA			cm09[40,142]	^{161}Tb (SPECT)[40,69]
		IC	5.1[a]/0.9[b]				PSMA-617[69]	^{152}Tb (17.5 h, PET)[41,42]
								^{155}Tb (5.32 d, SPECT)[43]

[a] keV/decay for MAEs emitted following internal conversion (IC); [b] MAEs/decay

1.3.1. Scandium-47

Scandium-47 (^{47}Sc, $t_{1/2}$ = 3.35 d) is a pure low-energy β^- particle emitter (E(β^-_{avg}) = 162.0 keV, I = 100%). The short half-life of this isotope makes it attractive for its clinical use as a substituent for the longer-lived ^{177}Lu in PRRT.

1.3.1.1. Production of ^{47}Sc

Numerous pathways have been studied for the production of ^{47}Sc via nuclear reactors or accelerators;[143–147] however, the current availability of ^{47}Sc is limited. High activities of ^{47}Sc can be obtained in a nuclear reactor by fast neutron irradiation of enriched $^{47}TiO_2$ or $^{nat}TiO_2$ targets via a ^{47}Ti(n,p)^{47}Sc reaction.[148] Alternatively, ^{47}Sc can be indirectly produced by thermal neutron irradiation of enriched calcium-46 (^{46}Ca) targets via a ^{46}Ca(n,γ)^{47}Ca→^{47}Sc reaction.[133] After two consecutive chromatographic columns, highly pure ^{47}Sc is obtained in a mixture of CH_3COONH_4 and HCl solution at pH 4.5. This method is more advantageous because it uses more accessible thermal neutrons and a ^{47}Ca/^{47}Sc generator to supply ^{47}Sc activity (^{47}Ca, $t_{1/2}$ = 4.53 d). On the other hand, highly enriched ^{46}Ca is currently only available at 30% enrichment which makes the target very costly.[149]

1.3.1.2. Chemistry of scandium

Scandium has been traditionally classified as a rare-earth element along with the lanthanides and yttrium, and thus it exhibits similar chemical properties to them. ^{45}Sc is the only naturally stable scandium isotope. The trivalent oxidation state, Sc^{3+}, is the most common form and preferably forms hexadentate complexes with an ionic radius of 0.745 Å although three to nine coordination numbers have been reported.[68,150] Like other M^{3+} ions, Sc^{3+} forms stable complexes with some of the most common O-donor multidentate ligands. For example, the Sc complexes with polyamino-carboxylic acid ligands EDTA (an eight-coordinated complex $[Sc(EDTA)(H_2O)_2] \times 3H_2O$) and DTPA ($[Sc(DTPA)]^{2-} \times 4\,H_2O$) have been known for a long time.[150–152] These octadentate complexes reflect the tendency of Sc^{3+} to adopt coordination spheres between first-row transition metals and lanthanides.

1.3.1.3. Chelates of interest

Based on the reported stability of the aforementioned organometallic complexes and the chemical similarity to Y^{3+} and Lu^{3+}, the widely used macrocycles DOTA and DTPA and their bifunctional chelates were a good starting point, with log K_{ML} = 27.43 (DTPA) and 30.79 (DOTA).[153] Despite the formation of highly stable complexes, the kinetics of Sc complexation with DOTA is slow at RT and requires high temperatures (70-90 ºC) to occur in a short time.[152,154] Acyclic ligands are very suitable alternatives to DOTA with comparable stability constants and higher rate constants. The evaluation of various acyclic polyamino-polycarboxylate ligands revealed that 1,2-bis(o-aminophenoxy)ethane-N,N,N',N'-tetraacetic acid (BAPTA, N_2O_4), ethylene glycol-bis(2-aminoethylether)-N,N,N',N'-tetraacetic acid (EGTA, N_2O_6; **Table 1.3**) and triethylenetetra- amine-N,N',N'',N'''-hexaacetic acid (TTHA, N_2O_8) quantitatively label scandium at mild temperatures in less than 10 min; however, only Sc-EGTA is stable in PBS buffer.[134] 1,4-bis(carboxymethyl)-6-[bis(carboxymethyl)]amino-6-methylperhydro-1,4-diazepine (AAZTA, N_3O_4; **Table 1.2**), a readily available mesocyclic chelate used in the preparation of ^{68}Ga conjugates,[155] was reported to radiolabel ^{44}Sc very efficiently forming a highly thermodynamically stable and kinetically inert complex, [^{44}Sc][Sc(AAZTA)]$^-$.[156] X-ray analysis of single crystals revealed that the Sc^{3+} forms an octadentate complex with the seven donor atoms of the ligand and an oxygen atom of a water molecule.[135] Seeking to develop a more lipophilic complex for improved tumor accumulation, Vaughn et al. very recently studied a small library of triaza-macrocycle-based picolinate-functionalized chelators that exhibit excellent chelation properties for Sc^{3+}; H_3mpatcn (N_4O_3; **Table 1.2**) was identified as the leading structure.[157] Another efficient macrocyclic chelate with a larger backbone size is py-macrodipa (N_4O_2; **Table 1.2**) with high specific activities and excellent serum stability. 3,4,3-(1,2-HOPO) (1,2-hydroxypyridinone, O_8; **Table 1.3**), a highly efficient chelate for ^{89}Zr radiolabeling, was very recently evaluated as a suitable scaffold for Sc-radiopharmaceuticals.[158]

1.3.1.4. Biological studies with ^{47}Sc

The lack of a reliable supply is the limiting factor for the preclinical evaluation of ^{47}Sc radiopharmaceuticals. There is only one preclinical pilot study in the literature that examines its therapeutic potential.[133] Müller et al. developed the [^{47}Sc]Sc-cm10 (**Table 1.4**) radiotracer, with the same functionalities as cm09 but lacking the tetrazine moiety in the linker, that showed similar therapeutic effects to those of [^{177}Lu]Lu-cm09 and [^{161}Tb]Tb-cm09.[142]

1.3.1.5. ^{47}Sc theranostic pairs

^{47}Sc could stand alone as a theranostic radioisotope with the emission of an imageable γ-ray (E(γ) = 159.3 keV, I = 68%). However, the same-element PET imaging radionuclide ^{44}Sc ($t_{1/2}$ = 3.97 h, E(β^+_{avg}) = 632 keV, I = 94%) is a more suitable candidate. ^{44}Sc PET imaging agents are of interest in nuclear medicine as they can be a longer-lived imaging surrogate of other commonly used trivalent cations such as ^{68}Ga. Strikingly, the promising potential of the $^{44/47}$Sc matching pair has been demonstrated for the first time in a preclinical setup with the small drug complex [$^{44/47}$Sc]Sc-DOTA-cm10.[133]

1.3.2. Copper-67

^{67}Cu ($t_{1/2}$ = 61.8 h) is the longest-lived isotope of all medically relevant copper radionuclides. ^{67}Cu decays via the emission of one beta particle (E(β^-_{avg}) = 141 keV, I = 100%) to stable ^{67}Zn.

1.3.2.1. Production of ^{67}Cu

The challenges associated with producing a reliable and large quantity of high specific activity ^{67}Cu are well known.[159] The most commonly used procedures to obtain small amounts of medical-grade ^{67}Cu are by high energy proton irradiation of zinc targets via a ^{68}Zn(p,2p)^{67}Cu or ^{70}Zn(p,α)^{67}Cu reaction in a cyclotron or by bombardment with fast neutrons through a ^{67}Zn(*n*,p)^{67}Cu nuclear reaction in high flux reactors.[160–163] Other currently investigated methods include nuclear reactions induced by alpha particles, via ^{64}Ni(α,p)^{67}Cu, or deuterons, via ^{68}Zn(d,2pn)^{67}Cu.[164–166] ^{67}Cu production via the (p, 2p) reaction has gained more interest due to the possibility to use a cyclotron, which is more accessible than a nuclear reactor. This reaction requires the use of enriched ^{68}Zn to increase the yield and specific activity of ^{67}Cu. To make this pathway economically feasible, the recovery of the expensive target material is necessary. The major drawback of this reaction is the simultaneous production of ^{64}Cu which is extremely challenging to isolate and remains in the solution for several days.[162,167] Several methods have been reported for the radiochemical separation of Cu from Zn target material and coproduced Ga.[168] Among them, ion exchange extraction chromatography is becoming the most popular method due to its simplicity and reliability.[162,169]

1.3.2.2. Chemistry of copper

Copper is an essential trace metal for all living systems and it plays a key role in the active sites of enzymes involved in a wide range of biochemical processes such as O_2 transport electron transfer.[170,171] Copper has very rich coordination chemistry and can be found in nature in its metallic form (Cu^0) or as a monovalent (Cu^{1+}) or divalent (Cu^{2+}) cation. The monovalent ion has a d^{10} electron configuration and is classified as a soft metal ion that interacts strongly with ligands bearing soft donor atoms (e.g., thiols). Cu^{1+} complexes can adopt linear, trigonal planar or tetrahedral geometries. In contrast, Cu^{2+} is a d^9 ion with a borderline acid character that preferentially forms stable complexes with borderline bases such as amines. Cu^{2+} can form coordination compounds with four to six ligands, square planar and octahedral with Jahn-Teller distortion are the usual geometries.[172] The ionic radius of copper can range from 0.6 Å in Cu^{1+} (CN = 4) to 0.76 Å in Cu^{2+} (CN = 6).[68]

1.3.2.3. Chelates of interest

Cu^{2+} is the prevalent cation for the development of radiopharmaceuticals. The formation of highly inert copper complexes is extremely important to avoid in vivo reduction of Cu^{2+} to Cu^{+1} which can be transchelated by copper-binding proteins (e.g., superoxide dismutase) and transported to off-target sites, namely the liver.[173,174] In this respect, kinetic inertness is more important than thermodynamic stability in the design of Cu radiopharmaceuticals. The only compounds that required in situ copper reduction were the first copper radiotracers based on the small molecules bis(thiosemicarbazones), Cu-PTSM (pyruvaldehyde-bis(N4-methylthiosemicarbazone) and Cu-ATSM (diacetyl-bis(N-methylthiosemicarbazone)).[175–177]

Copper radiopharmaceuticals have been widely investigated for clinical implementation with the PET radionuclide ^{64}Cu. A wide variety of acyclic and cage-type chelates are reported for the stable complexation of Cu^{2+} in radiotracers. A brief description of the recent advances in the novel copper-based chelates is presented here; an exhaustive review on this topic can be found elsewhere.[177–180] The next-generation of copper radiopharmaceuticals is moving away from the use of the multipurpose tetraaza-macrocyclic ligands, such as DOTA, TETA and derivatives or cyclams,[181–185] towards employing the smaller size triaza-macrocycle 1,4,7-triazacyclononane-1,4,7-triacetic acid (NOTA; N_3O_3; **Table 1.2**) and derivatives (e.g., MANOTA, NODAGA (**Table 1.2**)) and the macrobicyclic sarcophagine caging ligand (sarcophagine = sar = 3,6,10,13,16,19-

hexaaza-bicyclo[6.6.6]icosane, N_6) (**Table 1.2**).[137,140,186,187] These chelates emerged as promising alternatives due to their remarkably fast complexation kinetics and excellent in vivo stability, particularly for Cu-Sar complexes.[188–190]

It is interesting to mention the different opinions on the suitability of copper radiolabeling with DOTA. While this chelate is known to bind copper with high affinity, Cu-DOTA complexes have demonstrated susceptibility to reduction in vivo resulting in Cu transchelation and undesired high copper uptake in the liver.[191] In general, experts in the field seem to agree on the suboptimal in vivo performance of such compounds; however, preclinical and clinical investigations are still pursuing this chemistry.[136,192]

1.3.2.4. Biological studies with ^{67}Cu

The physical half-life of ^{67}Cu makes this isotope a versatile choice for both RIT and PRRT applications. Therapy with ^{67}Cu radioimmunoconjugates was actively investigated in the 1990s and early 2000s for clinical treatment of Non-Hodgkin's lymphoma, colorectal tumors and bladder cancer.[193–195] Despite the positive outcome of the clinical studies, the low availability of the radionuclide and the increasing interest in ^{64}Cu led to a substantial decrease in the therapeutic investigations of ^{67}Cu. It was not until recently with the innovative approaches to produce ^{67}Cu that research efforts continued to investigate the anticancer properties of such compounds.

In 2015, Mastren et al. demonstrated in a proof-of-concept study the antitumor efficacy of [^{67}Cu]Cu-NOTA-Panitumumab, targeting the human epidermal growth factor receptor, in mice bearing colon cancer xenografts.[139] Another example of ^{67}Cu radioimmunoconjugates are the [^{67}Cu]Cu-DOTA constructs conjugated to albumin and anti-IGSF4 mAb that were prepared using a novel one-pot three-component double-click method for practical and efficient Cu^{2+} radiolabeling.[136]

Furthermore, ^{67}Cu radiotracers are gaining attention in PRRT as alternative candidates to the currently used ^{177}Lu radiopharmaceuticals which are not ideally suited for peptide radiolabeling due to mismatching radiological and biological half-lives. An initial investigation was performed using the peptide conjugate cyclam-RAFT-c(-RGDfK-)$_4$, which selectively targets $\alpha_v\beta_3$ integrin.[138] Culliane et al. have developed a novel [^{67}Cu]Cu-Sar-TATE radiotracer to treat NETs with a therapeutic efficacy comparable to that of the FDA-approved [^{177}Lu]Lu-DOTATATE.[196] The enduring responses supported the initiation of two clinical studies in patients with meningioma (NCT03936426) and pediatric patients with high-risk neuroblastoma (NCT04023331).

1.3.2.5. ^{67}Cu theranostic pairs

Although the radioactive decay of ^{67}Cu involves the emission of three γ-rays with energies suitable for SPECT imaging (E(γ) = 91.2, 93.3 and 184.5, I = 7, 16 and 49%), the existence of a well-studied same-element PET imaging radionuclide (^{64}Cu, $t_{1/2}$ = 12.7 h, $E(\beta^+_{avg})$ = 278 keV, I = 19%) makes ^{64}Cu the most reasonable theranostic pair.[180,186,192] Some of the advantages of using ^{64}Cu for imaging are the easy production in a biomedical cyclotron and the emission of low-energy positrons for the obtention of high-resolution images.[197,198]

Recent studies on ^{67}Cu radiotracers for PRRT have already exploited the theranostic potential of the $^{64/67}$Cu matching pair for in vivo biodistribution and dosimetry estimates.[138,196] Additionally, Kelly et al. demonstrated similar pharmacokinetics and tumor uptake of the Sar-containing PSMA ligand [$^{64/67}$Cu]Cu-RPS-085 in a preclinical setting.[137]

1.3.3. Terbium-161

Terbium-161 (^{161}Tb, $t_{1/2}$ = 6.9 d) has two emissions suitable for therapeutic applications, low energy β^- particles ($E(\beta^-_{avg})$ = 154 keV, I = 101 %) and MAEs (0.9 MAE/decay, average of 5.1 keV/decay).[199] The co-emission of MAEs and β^- particles is a very unique feature to identify this isotope as a promising radionuclide for the treatment of disseminated cancers with large metastatic cell clusters.

1.3.3.1. Production of ^{161}Tb

^{161}Tb is the only medically relevant terbium isotope that is not produced via proton-induced spallation of tantalum targets. Instead, Lehenberger et al. suggested to indirectly obtain ^{161}Tb by neutron irradiation of enriched gadolinium targets (^{160}Gd) via the $^{160}\mathrm{Gd}(n,\gamma)^{161}\mathrm{Gd}\rightarrow{}^{161}\mathrm{Tb}$ reaction.[200] Experimental data showed the possibility to irradiate massive ^{160}Gd targets in nuclear reactors and chemically isolate large quantities of high specific activity ^{161}Tb in the form of [^{161}Tb]$TbCl_3$ using cation exchange chromatography.

1.3.3.2. Chemistry of terbium

For the chemistry of Tb please refer to section 1.2.1.2.

1.3.3.3. Chelates of interest

For Tb chelation please refer to section 1.2.1.3.

1.3.3.4. Biological studies with ^{161}Tb

Besides one preliminary study with [^{161}Tb]Tb-DTPA-octreotide reported by de Jong et al. in 1995,[201] ^{161}Tb was not in the spotlight of therapeutic isotope research until recently. In particular, ^{161}Tb TRT has garnered attention due to the similar decay properties to ^{177}Lu; however, the radioactive decay of ^{161}Tb simultaneously emits a significant number of MAEs that are expected to enhance the therapeutic effect.[200,202]

[^{161}Tb]Tb-cm09 has been the focus of the investigations on the anticancer properties of ^{161}Tb radiopharmaceuticals.[40,142,200,203] Müller et al. first demonstrated the therapeutic efficacy in an in vivo proof-of-concept study.[40] A follow-up experiment was performed to directly compare the antitumor activity of [^{161}Tb]Tb-cm09 and [^{177}Lu]Lu-cm09.[142] Equal pharmacokinetics and biodistribution profiles were reported for both radiotracers. However, higher absorbed doses in tumor tissues and longer survival times were found for [^{161}Tb]Tb-cm09 treated mice suggesting that ^{161}Tb might be a more potent alternative to ^{177}Lu. Concerns about increased renal toxicity due to the emission of MAEs have been dispelled with a long-term study on nude mice injected with high activities of [^{161}Tb]Tb-cm09.[204]

Very recently, the small molecule PSMA-617 has also been examined for ^{161}Tb therapy. A comparison study revealed higher anticancer efficacy than the ^{177}Lu analogue.[69] Moreover, theoretical studies employing Monte Carlo simulations also show evidence of the higher dose deposition of ^{161}Tb compared to over ^{177}Lu, ^{90}Y, ^{67}Cu, and ^{47}Sc.[205,206]

1.3.3.5. ^{161}Tb theranostic pairs

Like its α-emitting analogue (^{149}Tb), terbium-161 can stand itself as a theranostic isotope with the emission of three low-energy γ rays (E(γ) = 48.9 and 74.5 keV, I= 17 and 10%) imageable through SPECT. The feasibility of ^{161}Tb imaging using the 74.5 keV γ-emission has been examined in phantom studies and in a preclinical setting with excellent in vivo tumor visualization (**Figure 1.4**).[40,69] Furthermore, ^{152}Tb and ^{155}Tb can also be used as theranostic true match pairs (see section 1.2.1.5 for more information).

1.4. Meitner-Auger electron (MAE)-emitters

The Meitner-Auger effect describes the emission of a series of low-energy atomic electrons as a secondary process following radionuclides that decay by EC or internal conversion (IC). In EC, depending on the energy level the electron originates from, three different types of electrons can be emitted: Meitner-Auger electrons (MAE), Coster-Kroning (CK) or super Coster-Kroning (sCK) electrons. For convenience, these electrons are usually referred all together as MAEs. In IC, an excited unstable nucleus transfers the energy directly to an orbital electron which escapes from the atom with high kinetic energy leaving an inner orbital vacancy; these electrons are known as conversion electrons (CE). This section will only focus on MAEs although CEs also have therapeutic effects.[199]

MAEs have low energies, typically 1-10 keV, and can travel very short distances, a few micrometres (<10 μm, 1-2 cell diameters), which makes them extraordinarily powerful for localized treatment of micro metastatic tumors or single cancer cells (**Figure 1.2**).[207] Compared to α- and β^--particles, MAEs have an intermediate LET of 4-26 keV/μm.[22] However, a unique feature of MAEs is that the decay of a single atom produces a cascade of electrons (up to 50 MAE/decay depending on the radionuclide) resulting in a high radiation density in the vicinity of the decay site. If the radiation payload is specifically delivered to the target cancer cells, the damage to the nearby healthy tissue is minimal. To maximize the lethality of MAEs, research efforts initially focused on the internalization of the radiotracers to deliver radiation close to the nuclear DNA of cancer cells. It was later demonstrated that this is indeed not required and MAE-emitters can produce cytotoxicity effects when bound to the cell surface through alternative mechanisms such as oxidative stress.[199,208,209] The radiotoxicity effects are certainly not the same in both situations; internalized radiotracers display a cytotoxicity profile resembling that of high LET radiations (i.e. alpha particles) compared to non-internalized constructs whose effects are closer to that of low-LET particles (β^- particles).

The short distances travelled by MAEs make dosimetry calculations complex as cellular dosimetry becomes an important aspect to understand the effects of the radiation on the different cell targets (e.g., cytoplasm, nucleus, etc.) and to study the energy deposition in each of them. The determination of this factor has to be performed in in vivo animal models as this information is not possible to obtain from patient-based dosimetry. Thus, more extensive investigations are required to comprehend the dose-effect relationships of MAE-emitters in different tumor environments before this class of radionuclides can be implemented in the clinics.[199,210,211]

MAE emitting radionuclides are less investigated among the three types of therapeutic radiation. While there is a significant number of successful preclinical investigations,[142,212–214] reports of clinical studies are very limited.[215,216] The most investigated MAE-emitters include the common imaging and therapy radionuclides ^{99m}Tc, ^{123}I, ^{125}I, ^{111}In or ^{67}Ga.[199,217,218] However, this is not an indication of the suitability of these radionuclides for MAE therapy as their choices were based on easy accessibility rather than optimal decay schemes. Next, we will describe three cutting-edge MAE-emitters that have been identified as very promising candidates with ideal physical properties (summarized in **Table 1.6**).

Table 1.6. MAE-emitting radionuclides discussed in this chapter with relevant physical decay data, chelates of interest, targeting vectors employed in previous biological studies, and previously used or proposed (blue) theranostic pairs.

Isotope	Half-life	Decay	E_{avg} (keV/decay) MAE/decay	Chelates	Targeting vectors			Theranostic Pair used/proposed
					mAb	Peptides	Small molecules	
^{135}La	19.5 h	EC	6.45	H_2macropa			DUPA[219]	^{132}La (4.59 h, PET)
			10.9	DO3Apic			DUPA[219]	^{133}La (3.91 h, PET)
								^{134}Ce (3.16 d, PET)
^{197g}Hg	2.67 d	EC	16.1	Trithiamacrocycle	IgG[221]			^{197g}Hg (SPECT)
			23.2	NS_4[220]				
^{197m}Hg	23.8 h	IT[b] (91%)	13.5					^{197g}Hg (SPECT)
		EC (9%)	19.4					

Branching ratios in parentheses if not 100%. [a]EC= electron capture; [b]IC = internal conversion

1.4.1. Lanthanum-135

Amongst the other MAE-emitting isotopes presented here, ^{135}La is the most recently introduced radionuclide for nuclear medicine applications, and surprisingly, the first one to have available biological data.[219] The interest in this radionuclide not only lies in the suitability of its decay properties (^{135}La, $t_{1/2}$ = 19.5 h, 100% EC) but also in its chemical similarity to the α-emitter ^{225}Ac. The total energy released through the MAE per decay is 6.45 keV with an average of 10.9 MAE per decay (>97% of total) that have energies less than 4 keV.[222]

1.4.1.1. Production of ^{135}La

Small amounts of ^{135}La can be readily obtained from proton irradiation of natural barium (^{nat}Ba) targets through a ^{nat}Ba(p,n)^{135}La nuclear reaction in a cyclotron.[114,223] The radiochemical separation of ^{135}La was described by Fonslet et al., where purified ^{135}La is obtained in 0.1 M HCl[223]. Aluicio-Sarduy et al. reported a different procedure to obtain a mixture of $^{132/135}$La^{3+} suitable for preliminary imaging and therapy studies.[114] In this case, a combination of precipitations and chromatographic separation was used to obtain a solution of mainly ^{135}La with 2.47% of ^{132}La. The possibilities to upscale this production method and the obtention of high specific activity ^{135}La have not been discussed yet.

1.4.1.2. Chemistry of lanthanum

Lanthanum is a naturally occurring rare earth metal mainly composed of ^{139}La. La is commonly found in the +3 oxidation state and its ionic radius ranges from 1.03-1.27 Å in a six to ten-coordinate complex.[68] As expected for a lanthanide, La^{3+} is an oxophylic cation that will form strong coordination compounds with ligands bearing multiple oxygen donor atoms.[150] Chemically, La^{3+} is very similar to the therapeutic isotope ^{225}Ac^{3+} and it has been used as its surrogate metal for coordination chemistry studies. As a result, the thermodynamic stability of La^{3+} complexes with some of the most investigated ^{225}Ac chelates is known, e.g. $K_{DOTA\text{-}La}$ = 22.86 or $K_{macropa\text{-}La}$ = 14.99.[224,225]

1.4.1.3. Chelates of interest & biological studies with ^{135}La

The first in vivo proof-of-concept study of radiolanthanum was published very recently.[219] The therapeutic potential of ^{13x}La in TRT was examined using two previously reported chelates, H$_2$macropa and a DOTA derivative, DO3Apic (N_5O_4, **Table 1.2**), conjugated to the PSMA-targeting agent DUPA.[59,225] Excellent tumor-to-normal tissue ratios and in vivo stability in mice xenografts were observed for [^{13x}La]La-macropa-DUPA and [^{13x}La]La-DO2Apic-DUPA radiotracers; however, macropa was identified as the more suitable chelate due to a higher maximum apparent molar activity.

Another important contribution to the development of La^{3+} radiopharmaceuticals was the evaluation of the in vivo and ex vivo biodistribution of "free" $^{132/135}$La^{3+} in healthy mice.[114] The results revealed that unchelated ^{13x}La accumulates mainly in bones and liver, 30.45 ± 2.62 %IA g^{-1} and 6.65 ± 0.42 %IA g^{-1}, respectively, 20 h post-injection.

1.4.1.4. ^{135}La theranostic pairs

The three positron emitters ^{132}La, ^{133}La, and ^{134}La are all ideal chemically matched pairs for the therapeutic isotope ^{135}La (section 1.2.4.5). The accuracy of PET imaging with ^{132}La has been validated with ex vivo data in a preliminary study with "free" ^{13x}La.[114] Furthermore, in vivo tumor localization was also feasible in the [^{13x}La]La-macropa-DUPA and [^{13x}La]La-DO2Apic-DUPA preclinical study.[219] Although the production of all imaging pairs of ^{135}La is still under development, these theranostic pairs hold great promise for future clinical investigations not only for ^{135}La tracers but also as diagnostic pairs for the promising α-emitter ^{225}Ac^{3+}.

1.4.2. Mercury-197m/g

There are two isomers of mercury-197 with potential for diagnosis and therapy: the ground state mercury-197g (^{197g}Hg, $t_{1/2}$ = 2.67 d) and the metastable mercury-197m (^{197m}Hg, $t_{1/2}$ = 23.8 h) separated by an energy difference of 299 keV. The decay process of ^{197g}Hg and ^{197m}Hg states emits 23.2 MAE and 19.4 MAE per decay with an average energy of 16.1 keV and 13.5 keV, respectively.[199]

1.4.2.1. Production of $^{197m/g}$Hg

The mercury radioisotopes ^{197}Hg and ^{203}Hg with low specific activity were first produced from neutron reactions on natural Hg in the 1950s for brain scanning and cancer imaging.[226,227] The medical application of such compounds was rapidly cancelled due to the long half-life and the high toxicity of the radiotracers observed in vivo. In recent years, there has been a resurgence of interest in finding alternative production pathways with higher specific activities in large quantities for the theranostic application of $^{197m/g}$Hg.[228]

The most effective way to produce medical-grade $^{197m/g}$Hg is by proton or deuteron irradiation of natural gold (^{nat}Au) in cyclotrons, which does not require target enrichment lowering the overall production cost. Deuteron bombardment of gold targets via a ^{197}Au(d,2n)$^{197m/g}$Hg reaction has a higher cross section although its application is restricted to fewer cyclotrons due to the use of high energy deuterons.[229] Alternative production routes include platinum foils irradiation via ^{194}Pt(α,n)$^{197m/g}$Hg or ^{195}Pt(α,2n)$^{197m/g}$Hg[230] or by spallation of lead targets.[231]

Method development for the separation of mercury from the gold target material is on-going, with liquid-liquid extraction and chromatographic separation under investigation.[228,230,232–235] The latter is preferred for large-scale productions. To date, the highest efficiency has been reported using a stepwise elution with 6 M HCl on an LN-resin to obtain highly pure mercury in the form of $HgCl_2$.[236]

1.4.2.2. Chemistry of mercury

Mercury is a very low abundance naturally occurring metal, with ^{202}Hg being the most abundant at 29.9%. Hg can be found in two oxidation states, Hg^{1+} or Hg^{2+}, and in its metallic form, Hg^0; although only Hg^{2+} is relevant for radiopharmaceutical applications.[237] Mercury is toxic in all its forms and in particular, Hg^{2+} produces toxicity in humans by transchelation to sulphur-rich endogenous biomolecules.[238–240] However, mercury toxicity is not a concern for nuclear medicine because of the extremely low concentrations of radiometal used (nanomolar range), well below the body's threshold exposure limit.[241]

The divalent oxidation state is classified as a soft acid according to the HSAB theory and it forms stable complexes with soft bases like sulphur and phosphorous. Despite the hard-acidic character of nitrogen atoms, Hg^{2+} can also form strong covalent bonds with nitrogen-containing ligands.[242–244] In terms of coordination chemistry, Hg^{2+} is a very flexible cation as there is no evidence of a strong preference for certain coordination numbers, such compounds range from simple linear geometries to more complex multidentate highly distorted structures (0.69 to 1.14 Å, CN = 2-8).[68,237]

1.4.2.3. Chelates of interest

$^{197m/g}$Hg bifunctional chelate chemistry is virtually unexplored. To date, there are only two examples available in the literature of a BFC labeled with ^{197}Hg. The first one was reported by Blower et al. in 1992 and consisted of a nine-membered trithiamacrocycle

(S_3, **Table 1.2**) conjugated to an immunoglobulin (rabbit IgG) which proved to be unstable in serum after 24 h.[221] The second study has just been published by Randhawa et al. in our group and it explored a sulfur-rich macrocyclic backbone (NS_4, **Table 1.2**) with two different bifunctional handles (a carboxylic acid (CA) and a benzyl amide (BA)) and presented a standardized radiolabeling protocol for ^{197}Hg. The NS4-BA showed significantly increased radiolabeling affinity compared to DOTA and its radioactive complex was kinetically inert in a human serum assay over 24 h.[220] More detailed information on mercury ligands can be found in this review.[235]

1.4.2.4. Biological studies with $^{197m/g}$Hg

The therapeutic effect of $^{197m/g}$Hg has been compared to the β^--emitter ^{177}Lu in theoretical studies. It was found that due to the higher number of MAEs, the dose per decay is ten times higher in $^{197m/g}$Hg compared to ^{177}Lu in a 1 μm sphere.[228] These results indicate that $^{197m/g}$Hg therapy should be more effective; however, this radionuclide also emits a gamma-dose six times higher than ^{177}Lu, which must be accounted for in clinical applications. No $^{197m/g}$Hg biological studies are present in the literature yet.

1.4.2.5. $^{197m/g}$Hg theranostic pairs

The ground and metastable state of Hg emit multiple γ-rays (^{197g}Hg, E(γ) = 191.4, I = 0.6 %; ^{197m}Hg, E(γ) = 133.8, and 278.7, I = 34 and 4%) imageable through SPECT.[229,245] Freudenberg et al. recently examined for the first time the imaging possibilities of the theranostic pair $^{197m/g}$Hg.[246] Phantom studies and Monte Carlo simulations revealed that quantitative images can be obtained with the commercially available low energy high resolution (LEHR) collimators. The favourable decay properties of $^{197m/g}$Hg (e.g., number of MAE per emission) are key features for the emerging interest in this theranostic pair which brings a new attractive prospective for the clinical application of MAE-targeted therapy.

1.5. Concluding remarks

The future of disease treatment (particularly in oncology) is leaning towards a personalized approach, indeed nuclear medicine is aptly suited to both image and treat disease at the cellular and molecular levels. Therapeutic radiopharmaceuticals are extremely powerful tools that offer the possibility to selectively deliver potent radiation to diseased cells. Besides the traditionally investigated radiometals, a wide variety of novel rare medical isotopes (e.g., ^{225}Ac, $^{149/161}$Tb, or ^{135}La) have been introduced in the development of innovative radiopharmaceuticals for TRT. These emerging radiometals have been successfully incorporated in a variety of radiopharmaceuticals and are currently in various development phases from preliminary preclinical studies to advanced clinical trials. Moreover, radiotheranostics (therapy and diagnosis) is attracting the attention of researchers due to the unique opportunity to assess and monitor the disease progression for personalized patient treatment. Intense research efforts and subsequent recent advances in radionuclide production, chelate development and biological studies with these next-generation therapeutic radiopharmaceuticals and their theranostic pairs highlight the potential of these drugs. It is expected that (radio)theranostic treatments will be incorporated into routine clinical settings in the coming years, leading to revolutionized cancer treatments and improved quality of life for patients.

1.6. Thesis overview and aims

After writing an overview of the most promising radiometals for incorporation into radiopharmaceuticals to treat cancer, we sought to develop novel chelates for the formation of stable radiometal complexes and to evaluate their performance in preclinical studies. This thesis focuses on the synthesis, characterization, radiolabeling and in vivo evaluation of novel acyclic chelates based on the 1,2-HOPO ligand. As the first Ph.D. student in the Ramogida group, I started a new research area based on the chelation of radiolanthanides and actinides (e.g., ^{225}Ac) and as the group grew, I also expanded the chelate development to first-row transition metals (e.g., ^{47}Sc) with the increased availability of isotopes at TRIUMF. Besides the research efforts, I have also built productive relationships to foster a collaborative environment with all team members through these 4.5 years.

Inspired by the excellent performance of [^{89}Zr]Zr-HOPO-O$_8$, we decided to investigate the potential of the 1,2-HOPO ligand for the chelation of oxophylic radiometals through different backbones with variable lengths and degrees of flexibility. Herein, the aims of this work are:

- Rationally design large multidentate chelates for radiolanthanides and actinides with CN > 8 and smaller chelates with CN = 6 for the first-row transition radiometals which can be readily made bifunctional.
- Synthesize and fully characterize the novel chelates.
- Characterize their corresponding non-radioactive complexes to gain insight into the coordination chemistry.
- Perform radiolabeling studies to evaluate their efficiency with the radiometals of interest.
- Synthesize the bifunctional analog of the most promising structures and conjugate them to a disease targeting vector.
- Evaluate the radiopharmaceuticals in preclinical studies.

Chapter 2 explores the effect of adding one extra 1,2-HOPO ligand to HOPO-O_8 to make a decadentate chelate, HOPO-O_{10}, on the coordination of larger radiolanthanides and actinides, i.e., ^{135}La, ^{161}Tb, ^{225}Ac and ^{227}Th. In chapter 3, I moved away from linear backbones to investigate the coordination of small radiometals such as ^{47}Sc with branched amine-based backbones containing 1,2-HOPO or an amide catechol ligand that can form hexacoordinate complexes. Chapter 4 focuses on the most promising results from chapter 2 and modifies HOPO-O_8 with a tetrazine (Tz) bifunctional handle for click chemistry applications. After conjugation to the mAb trastuzumab, the ^{161}Tb and ^{89}Zr radioimmunoconjugates are assessed in vivo. Lastly, chapter 5 summarizes and concludes all the work presented here, suggests future projects to continue the research areas explored in this thesis and ends with an outlook on the future of the development of acyclic chelates for radiopharmaceutical applications.

Chapter 2.

A comparative study of a decadentate acyclic chelate, HOPO-O_{10}, and its octadentate analogue, HOPO-O_8, for radiopharmaceutical applications

2.1. Introduction

Radiolanthanides and radioactinides, often referred to as exotic radiometals, have emerged as promising candidates to expand the use of therapeutic isotopes and find new theranostic pairs for the current clinical imaging agents (section 1.1.2). With remarkably diverse radiological and chemical properties, exotic radiometals are particularly interesting for the development of novel therapeutic and theranostic pairs to complement the numerous imaging radiopharmaceuticals that are available for routine clinical diagnosis such as ^{68}Ga or technetium-99m (^{99m}Tc, $t_{1/2}$= 6.0 h, IT (100%)). Currently, ^{177}Lu is the only radiometal approved by the FDA for TRT with neuroendocrine tumors, [^{177}Lu]Lu-DOTATATE ((Tyr3) octreotide (TATE) (Lutathera®), and metastatic prostate cancer, [^{177}Lu]Lu-PSMA-617 (Pluvicto®).[27,32] This marked milestone has put exotic radiometals with α and MAE emissions (e.g., ^{225}Ac, $t_{1/2}$= 9.9 d, α (100%), $E_α$ = 5.8 MeV; and ^{135}La, $t_{1/2}$= 19.5 h, EC (100%)) in the spotlight to develop novel therapeutic agents. Moreover, some of these isotopes have same-element theranostic pairs, like ^{149}Tb/^{155}Tb suitable for α therapy and SPECT, while others can form different-element theranostic agents with higher chemical similarity than the generally accepted ones, such as ^{225}Ac/^{132}La (^{132}La; $t_{1/2}$ = 4.59 h, $β^+$(42%)) instead of ^{225}Ac/^{68}Ga. The unprecedented clinical results obtained with some α-emitting radionuclides (e.g., ^{225}Ac or ^{227}Th, $t_{1/2}$= 18.7 d, α (100%)), have increased the demand for novel chelators specifically designed for the chemistry of these exotic radiometals.[33,55,65,104,247]

Four medically relevant radiolanthanides and actinides were chosen for the work in this chapter: ^{135}La, ^{155}Tb, ^{225}Ac and, ^{227}Th (**Table 2.1**), all of which conventionally have been described as relatively-hard to hard Lewis acids and exhibit large ionic radii with a preference for large coordination numbers (≥ 8). The study of the thermodynamics and kinetics of the lanthanides with a large variety of multidentate chelates including the well-known 8-coordinate macrocycle DOTA (**Table 2.2**) and the acyclic DTPA started more than 30 years ago.[248–250] However, these data are not easily correlated with the radiometal chelation for radiopharmaceutical development due to the difference in the experiment conditions (solvents, concentration, etc.). While some of these chelates show promising complexation and stability results, they are not ideal for nuclear medicine applications.

A clear example is DOTA which is highly effective for smaller radiometals such as ^{177}Lu and ^{111}In, it is far from ideal for larger radiolanthanides (e.g., ^{135}La) or radioactinides (e.g., ^{225}Ac) as it requires high temperatures (>80 °C) for their incorporation and lacks selectivity. When preparing tracers for clinical studies, metal selectivity becomes crucial since the presence of small metal impurities can significantly affect the specific activity (A_s) of the tracer. Despite this, the majority of the preclinical and clinical studies with radiolanthanides and actinides rely on DOTA chelation.[42,57] Intense research efforts are currently focused on developing novel highly specific chelates for some of the most promising exotic radiometals such as ^{225}Ac or ^{135}La.[61,62,251,252] To date, the stable chelation of ^{225}Ac is the most explored of all the medically relevant radiolanthanides and actinides. Thiele et al. investigated the medical application of an 18-membered macrocycle (H_2bp18c6) reported by Roca-Sabio earlier with excellent binding affinity for large lanthanides.[225] It was renamed H_2macropa (**Table 2.2**) and it is to date the ^{225}Ac chelate with the highest performance, observed as high ambient temperature Ac^{3+} incorporation at low concentrations and highly stable to transmetallation and transchelation in vivo.[59,253] Close competitors include the crown chelate (**Table 2.2**) developed by Yang et al. and the acyclic H_4py4pa (**Table 2.2**) investigated by Li et al.[61,62] H_2macropa was also demonstrated to have superior radiolabeling properties compared to the DOTA derivative DO2Apic (**Table 2.2**) with the novel theranostic pair $^{132/135}$La in a unique proof-of-concept study of this matched pair.[219] Py-macrodipa (**Table 2.2**) is a recently investigated novel chelate that is capable of efficiently radiolabeling ^{135}La in 15 min at 25 °C, and surprisingly, it is also efficient at labeling the much smaller radiometal scandium-44 (^{44}Sc, $t_{1/2}$= 3.94 h, β^+ (94%)).[252]

Table 2.1. Radiometals of interest studied in this chapter with their chemical and physical properties relevant to radiopharmaceutical development.

	Chemical properties				Physical properties			Nuclear medicine properties	
Isotope	Oxidation state	Stable isotopes?	Ionic radius[a] (Å)	HSAB[b] character	Half-life	Decay emission	Energy	Use	Theranostic pair
^{135}La	3+	Yes	1.032	hard	19.5 h	MAE[c]	6.45 keV/decay	therapy	^{132}La ^{133}La ^{134}La
^{155}Tb	3+	Yes	0.923	hard	5.32 d	γ	85 and 105 keV (32 and 25%)	imaging	
^{161}Tb	3+	Yes	0.923	hard	6.9 d	β^-	154 keV[d] (101%)	therapy/ imaging	^{152}Tb/^{155}Tb
^{225}Ac	3+	No	1.12	hard	9.9 d	α	5.8 MeV(~25 MeV)[e]	therapy	^{132}La/^{226}Ac
^{227}Th	4+	No	0.94	hard	18.7 d	α	6.0 MeV(~33 MeV)	therapy	^{89}Zr/^{134}Ce

[a] All ionic radii are referring to coordination number 6. [b] HSAB: hard soft acid base theory. [c] MAE: Meitner−Auger electrons. [d] Average energy. [e] Total energy emitted through α decay along the decay chain.

The scarcely available α-emitter ^{227}Th is one of the few exotic radiometals with an extremely low binding affinity for DOTA, requiring heat to obtain significant labeling. Ramdahl et al. developed (Me-3,2-HOPO) (**Table 2.2**), a Th^{4+} tailored chelate for fast complexation at ambient temperatures, which has become the gold standard.[120] This intrinsic BFC has been linked to various disease-targeting vectors and is transitioning to clinical phase I programs in mesothelioma and ovarian cancer patients (NCT035074252).[64]

Tb^{3+} is a rare earth metal that has an exceptional matching quadruplet of medically relevant radioisotopes ^{149}Tb, ^{152}Tb ($t_{1/2}$= 17.5 h, β^+ (17%)), ^{155}Tb, and ^{161}Tb ($t_{1/2}$= 6.89 h, β^- (100%)). DOTA and CHX-A''-DTPA (**Table 2.2**) have been the chelates of choice for Tb^{3+} despite its incompatibility with temperature-sensitive targeting molecules which require 90 °C for quantitative labeling. However, this year Wharton et al. presented the first preclinical study with the crown chelate, [$^{155/161}$Tb]Tb-crown-TATE. [41,70,254]

Hydroxypyridinone (HOPO) is a well-known bidentate ligand that forms 5-membered chelate rings with high affinity for trivalent and tetravalent cations such as Fe^{3+} and Pu^{4+}. Three types of HOPO moieties are available for chelation: 1-hydroxy-2(1H)-pyridinone (1,2-HOPO), 3-hydroxy-2(1H)-pyridinone (3,2-HOPO), and 3-hydroxy-4(1H)-pyridinone (3,4-HOPO). Chelating agents containing HOPO moieties have been investigated to treat human iron toxicity or as actinide decorporation agents.[255–257] The Abergel group is leading investigations on the solution thermodynamics of lanthanide and actinide complexes with the octadentate ligand 3,4,3-LI(1,2-HOPO), referred to herein as HOPO-O_8, first reported by Gorden et al.[121,258,259] Their studies have demonstrated that this ligand forms highly stable complexes with Ln^{3+} with thermodynamic stability constants ranging from 16.8 – 22.2 in aqueous solution across the series. More importantly, HOPO-O_8 showed exceptionally high thermodynamic stability constants for tetravalent ions such as Th^{4+} and Zr^{4+} with stability constants of 40.1 or 43.1, respectively, the highest reported for a Zr^{4+} complex. As such, HOPO-O_8 is a highly promising candidate for the PET imaging agent zirconium-89 (^{89}Zr, $t_{1/2}$ = 3.27 d, β^+ (23%)). Deri et al. reported the first study of a [^{89}Zr]Zr-HOPO-O_8 radiopharmaceutical with demonstrated superior affinity over the commonly used deferoxamine B (DFO).[260,261] A synthetic route to functionalize the chelate was successfully developed without altering its radiolabeling properties and was conjugated to the mAb trastuzumab showing encouraging in vivo results.[44] Recently, Bailey et al. investigated the novel radiolanthanide ^{134}Ce ($t_{1/2}$ = 3.16 d, EC (100%)) as PET agent for ^{225}Ac and ^{227}Th through its daughter ^{134}La ($t_{1/2}$ = 6.45 min, β^+ (62%)). HOPO-O$_8$ provided successful chelation and protected Ce^{4+} from biological reduction.[112]

Table 2.2. Chemical structures of the most relevant chelates discussed in this chapter.

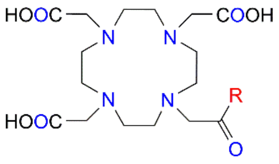 **DOTA** Ac^{3+}, Tb^{3+}, Th^{4+}	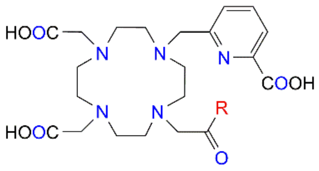 **DO2Apic** La^{3+}	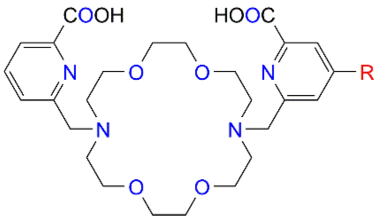 **H$_2$macropa** Ac^{3+}
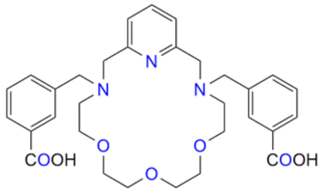 **py-macrodipa** La^{3+}	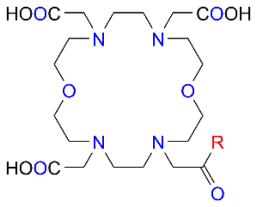 **crown** Ac^{3+}, Tb^{3+}	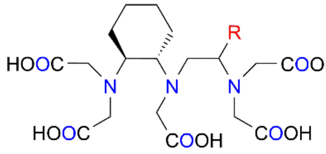 **CHX-A”-DTPA** Tb^{3+}
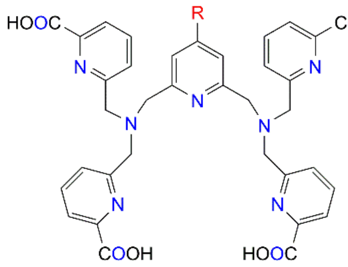 **H$_4$py4pa** La^{3+}	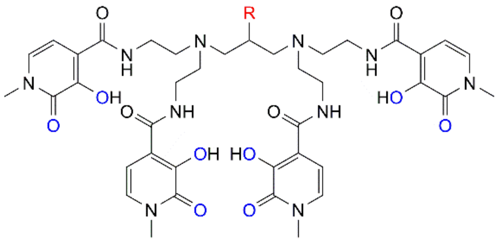 **Me-3,2-HOPO** Th^{4+}	
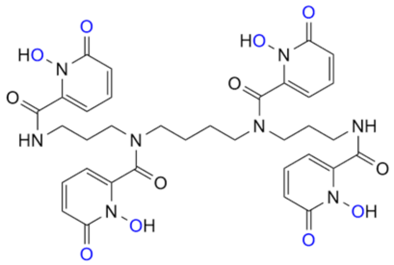 **HOPO-O$_8$** Zr^{4+}	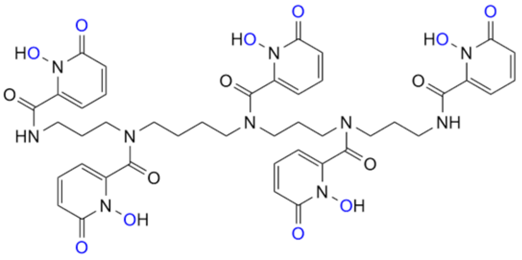 **HOPO-O$_{10}$** This work	

Coordinating atoms labeled in blue and conjugation site labeled in red.

Inspired by the exceptional binding affinity of HOPO-O_8 towards tetravalent ions, we sought to explore the effect of increased denticity on the formation of a series of radioactive lanthanide and actinide complexes including ^{135}La, $^{155/161}$Tb, ^{225}Ac and, ^{227}Th via the preparation of a novel 10-coordinate acyclic 1,2-HOPO chelator. The novel 3,4,3,3-(LI-1,2-HOPO) chelator, referred to herein as HOPO-O_{10} (**Table 2.2**), was designed keeping in mind the properties of the ideal bifunctional chelate described in chapter 1 (section 1.1.1.1). Compared to HOPO-$O_{8,}$ HOPO-O_{10} has an extended pentaamine backbone with the capacity of incorporating an extra 1,2-HOPO moiety to a total of five units, offering 10 oxygen coordination atoms instead of 8. We hypothesized that this potentially decadentate ligand would form more stable complexes than the octadentate HOPO-O_8 with the series of radioactinides/lanthanides tested, given their large ionic radii and propensity to form coordination complexes with high denticity. Herein, we report the synthesis and characterization of the novel HOPO-O_{10} chelator, along with preliminary metal coordination studies using non-radioactive La^{3+} and Tb^{3+} studied via ^{1}H NMR, MS, and UV-vis. ^{135}La, $^{155/161}$Tb, ^{225}Ac, and ^{227}Th radiolabeling studies of HOPO-O_{10} were conducted and compared to results obtained for HOPO-O_8; human serum stability of the most promising radiometal complexes was also assessed. The complex formation and stability of both structures are further compared by density functional theory (DFT) calculations, and the results of the radiolabeling and stability studies were rationalized by the computational studies to gain further insight into the coordination behaviour of HOPO-O_{10} and HOPO-O_8 with the series of radioactinides and lanthanides studied.

2.2. Results and discussion

2.2.1. Synthesis

The novel decadentate HOPO-O_{10} consists of a linear polyamine backbone with five amino groups and five 1,2-HOPO moieties. Unlike its octadentate analog HOPO-O_8, the backbone is not commercially available and thus the synthesis of HOPO-O_{10} requires the preparation of the backbone 1,16-diamino-4,8,13-triazahexadecane (referred to as pentaamine) followed by the coupling of five 1,2-HOPO groups (**Scheme 2.1**). The previously reported strategy to synthesize pentaamine is by prolonging spermine, the tetramine backbone used in the synthesis of HOPO-O_8.[262,263] The same strategy was adopted in this work; however, two procedures were explored to incorporate the fifth amine to spermine via reductive amination (route 1) or tosylation (route 2). Both routes started with the synthesis of compound **2.1** following a procedure described by König et al.[264]

Route 1 is the previously reported route involving the synthesis of aldehyde **2.2** and the coupling to compound **2.3** via reductive amination which is similar to the first 6 steps of the synthesis of the bifunctional HOPO-O_8.[261] The reductive amination of **2.2** and **2.3** proved to be challenging. The first issue encountered was the impossibility to track the imine formation since neither TLC nor MS would reliably show its formation which led to various amounts of double alkylated product. The second challenge was the isolation of compound **2.5** from the double alkylated byproduct which was difficult due to the inherent stickiness of aliphatic amines. Moreover, on larger scales purification required a second column chromatography to increase product recovery.

Route 2 was investigated after Bhupathiraju et al. reported an improved synthesis of the *p*-SCN-Bn-HOPO.[265] It is worth noting that at the time of publication, we had already developed the synthetic route for HOPO-O_{10} and we only evaluated the coupling of compound **2.4** to the Boc-protected compound **2.3** and didn't attempt the shorter route to couple compound **2.4** directly to spermine as reported. In our case, the formation of intermediate **2.5** via tosylate coupling of compounds **2.3** and **2.4** resulted in a much cleaner crude reaction. Purification of the crude by automated column chromatography resulted simpler using C18 cartridges instead of SiO_2 which eliminated the need for a second column in large scale reactions. Subsequent Cbz and Boc deprotection proceeded as previously described yielding pentaamine **2.7** in the form of a TFA salt. Overall, the synthesis of pentaamine involves two low-yielding steps, the formation of compounds **2.3** and **2.5**. Small improvements were made on the initially published route using the tosylate coupling instead of reductive amination. We believe that a higher synthetic cumulative yield would be achieved by directly coupling compound **2.4** to spermine avoiding the low-yielding 3-step one-pot reaction to prepare compound **2.3**.

The second part of the synthesis was straightforward following the procedure reported for the preparation of HOPO-O_8.[260] We modified their procedure to avoid the use of the acyl chloride derivative of 1,2-HOPO which has to be prepared and used immediately due to its instability. Instead, we activated the acid with an N-hydroxysuccinimide (NHS) group to form the ester **2.8** which can be purified by chromatographic column and stored in the freezer for later use.[266] An excess of compound

2.8 was used to achieve the complete addition of five 1,2-HOPO moieties to the backbone to yield compound **2.9**.

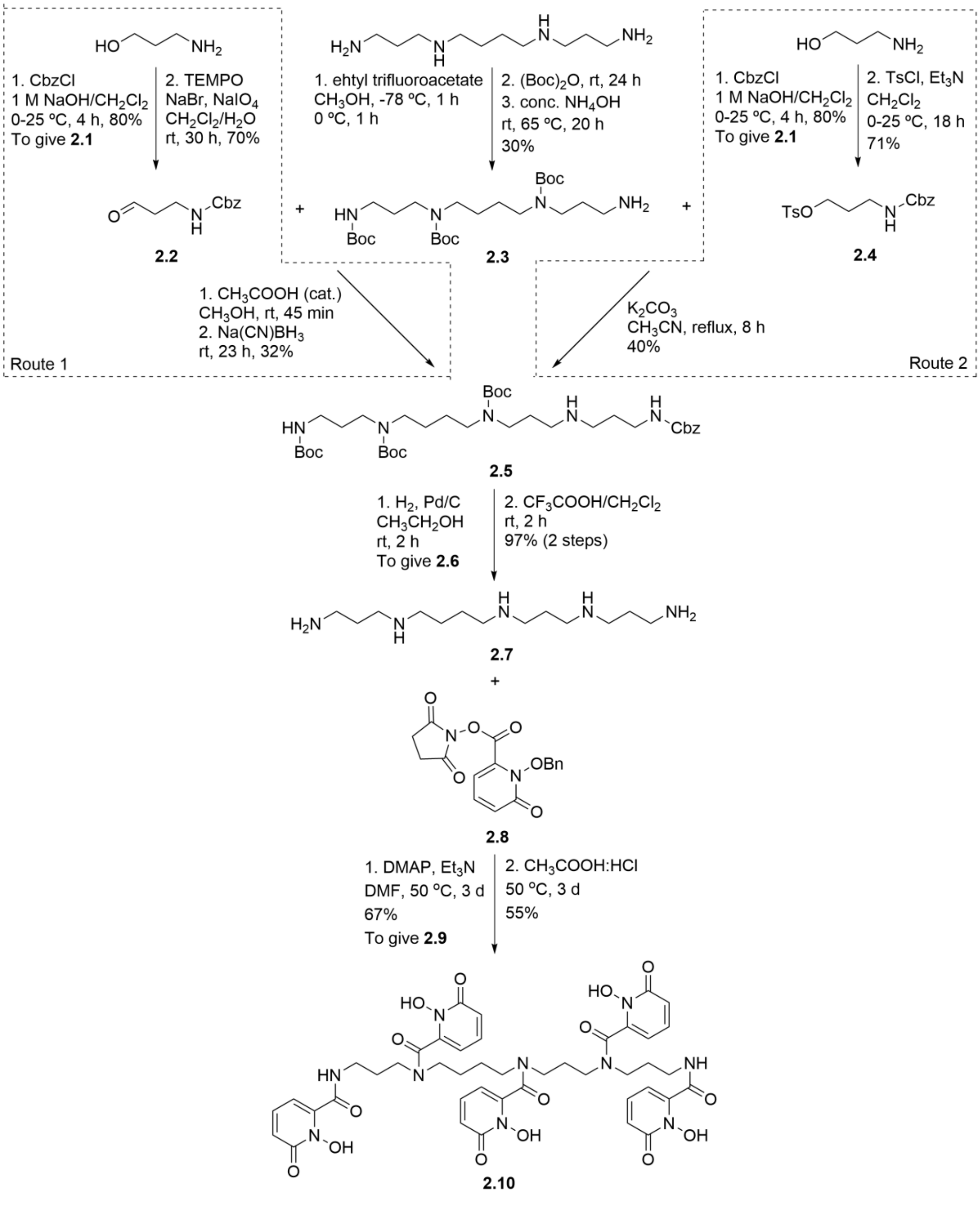

Scheme 2.1. Synthetic route developed for HOPO-O$_{10}$. Dashed boxes indicate the two routes investigated to prepare compound 2.5.

Lastly, HOPO-O_{10} (**2.10**) was obtained by deprotection of the benzyl groups under acidic conditions. The crude was purified by semi-preparative RP-HPLC and **2.10** was obtained as an off-white solid. Hydrogenation with Pd/C was not attempted because we wanted to investigate a route that could be used in the future when the ligand is bifunctionalized with a p-benzyl-SCN which would not be preserved under these reducing conditions.

2.2.2. Metal complexes

With one extra 1,2-HOPO moiety, HOPO-O_{10} offers two additional coordination sites for a total of ten oxygen donor atoms compared to the eight ones in HOPO-O_8. To understand the effect that this extra pendant arm has on the coordination chemistry of large lanthanides and actinides, we prepared non-radioactive complexes of both HOPO-O_{10} and HOPO-O_8 with the diamagnetic La^{3+} ion – Ac^{3+} closest surrogate metal – and the paramagnetic Tb^{3+} ion. The complexes were characterized by mass spectrometry, UV-vis spectroscopy, and NMR spectroscopy (La^{3+} only as Tb^{3+} is paramagnetic). Non-radioactive characterization of Th^{4+} was only possible via UV-vis spectroscopy due to the radioactive nature of the only naturally occurring Th isotope, ^{232}Th ($t_{1/2}$ = 1.4 x 10^{10} y) which limits its use in non-radioactive spaces.

The La^{3+} and Tb^{3+} metal complexes were prepared by dissolving equimolar amounts of HOPO-O_{10} or HOPO-O_8 and the corresponding metal salt in methanol. The resulting complexes were isolated by centrifugation and identified first by mass spectrometry. Strikingly, MS analysis of the La-HOPO-O_{10} complex revealed the formation of two species in solution corresponding to the 1:1 and 2:1 metal-to-ligand complexes. In contrast, only the 1:1 complex was observed for HOPO-O_8. To further investigate the formation of a bimetallic complex, ^1H NMR spectroscopy was employed to track the formation of the two metal species in solution by observing the changes in the spectra of the aromatic signals (**Figure 2.1** red triangle and green diamond). The results were compared to the single species formed with HOPO-O_8 (**Figures 2.2 and 2.3**). The ^1H NMR titration was performed by adding 0.5 eq of a concentrated $La(ClO_4)_3 \cdot 6\ H_2O$ to a solution of the chelate in DMSO-d_6 until no changes in the spectrum were observed. The gradual formation of the 1:1 and 2:1 species in the HOPO-O_{10} complex is observed by the merging of the aromatic protons indicated by a green diamond (**Figure 2.1**), which are the most affected by the coordination of La^{3+} due to their proximity to both coordinating oxygen atoms. The proton signals of the secondary amines (purple hexagon) decrease drastically after the addition of 0.5 metal equivalents upon metal coordination. The asymmetry of the peaks due to the multiple conformations of the ligand makes the interpretation of the various species and ratios between them not feasible by NMR. The final solution was analyzed by MS to confirm the formation of the monometallic and bimetallic complexes. In contrast, titration of HOPO-O_8 with La^{3+} indicated the formation only of a 1:1 complex since there were no spectral changes past 1.0 eq of the metal salt (**Figure 2.3**). The MS spectrum of the final NMR solution correlated with the formation of a monometallic species.

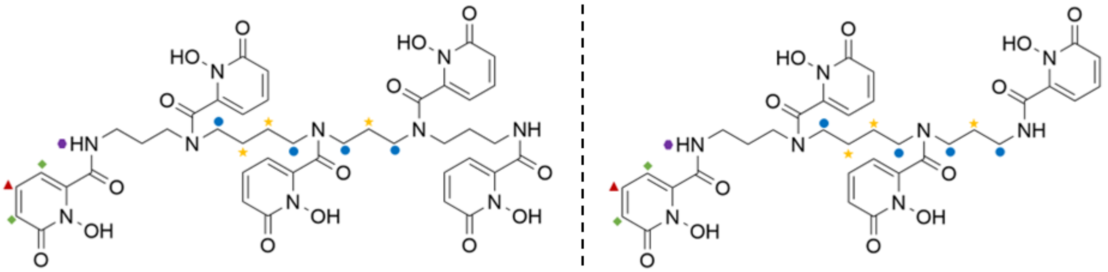

Figure 2.1. Chemical structures of HOPO-O_{10} (left) and HOPO-O_8 (right) with labels for NMR peak assignment.

Further characterization of the HOPO-O_{10} complexes with La^{3+}, $Tb^{3+,}$ and Th^{4+} was attempted using UV-vis spectroscopy to gain more insight into the formation of the 1:1 and 2:1 metal-to-ligand species. The absorption maximum (λ_{max}) at 324 nm of the free chelate – assigned to ligand $\pi \rightarrow \pi^*$ transitions – experienced a blue-shift in the formation of all complexes. However, the complexes did not show a consistent stopping point corresponding to a specific ratio of metal-to-ligand as observed by ^{1}H NMR (**Figure 2.4A and B** and Appendix, Figure A.1 for Tb^{3+} and Th^{4+}). This absence of a clear trend was also observed with HOPO-O_8 and La^{3+} as shown in **Figure 2.4C and D**. The inconsistency observed in the UV-vis spectroscopy studies has also been reported before by Deri et al. in the formation of the Zr^{4+} and HOPO-O_8 complex.[260] The divergence in the spectrometric titrations could be explained by the formation of stacked metal complexes that could incorporate an unpredictable number of ions between molecules of chelate and is highly dependent on various factors such as buffer, equilibration time, chelate folding structure, etc. Indirect spectrophotometric competition titrations between metal ions with similar thermodynamic affinities would be a better approach to investigating the complexation differences of HOPO-O_8 and HOPO-O_{10}.[267]

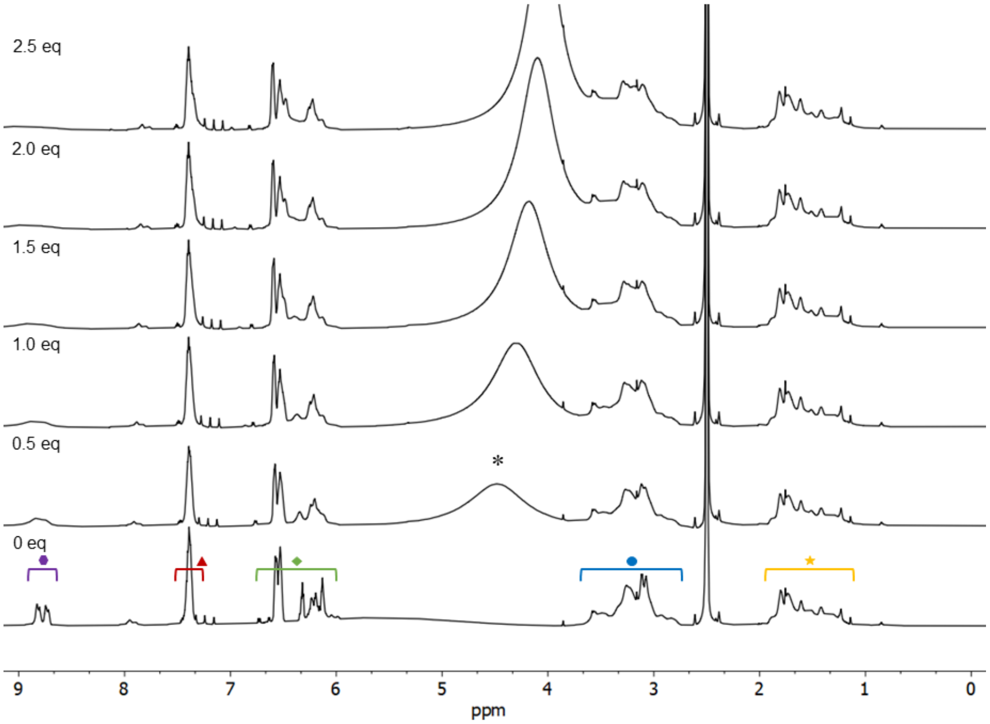

Figure 2.2. ^{1}H NMR (600 MHz, DMSO-d_6, 298 K) La^{3+}-HOPO-O_{10} titration at increasing equivalents of the metal salt (0-2.5 eq). Peak assignment in agreement with Figure 2. * indicates the H_2O peak corresponding to the three H_2O equivalents introduced in every 0.5 eq increment of La^{3+}.

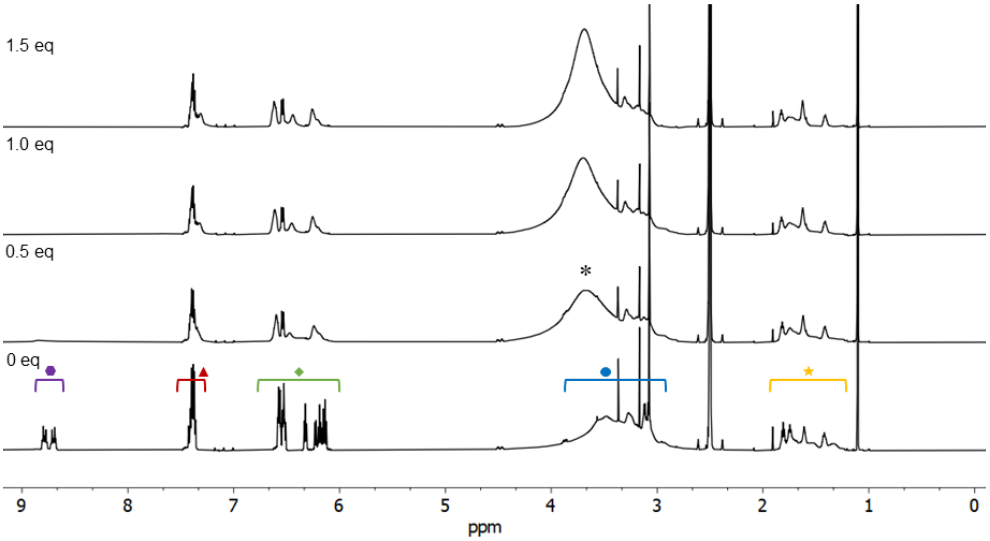

Figure 2.3. ^{1}H NMR (600 MHz, DMSO-d_6, 298 K) La^{3+}-HOPO-O_8 titration at increasing equivalents of the metal salt (0-1.5 eq). Peak assignment in agreement with Figure 2. * indicates the H_2O peak corresponding to the three H_2O equivalents introduced in every 0.5 eq increment of La^{3+}.

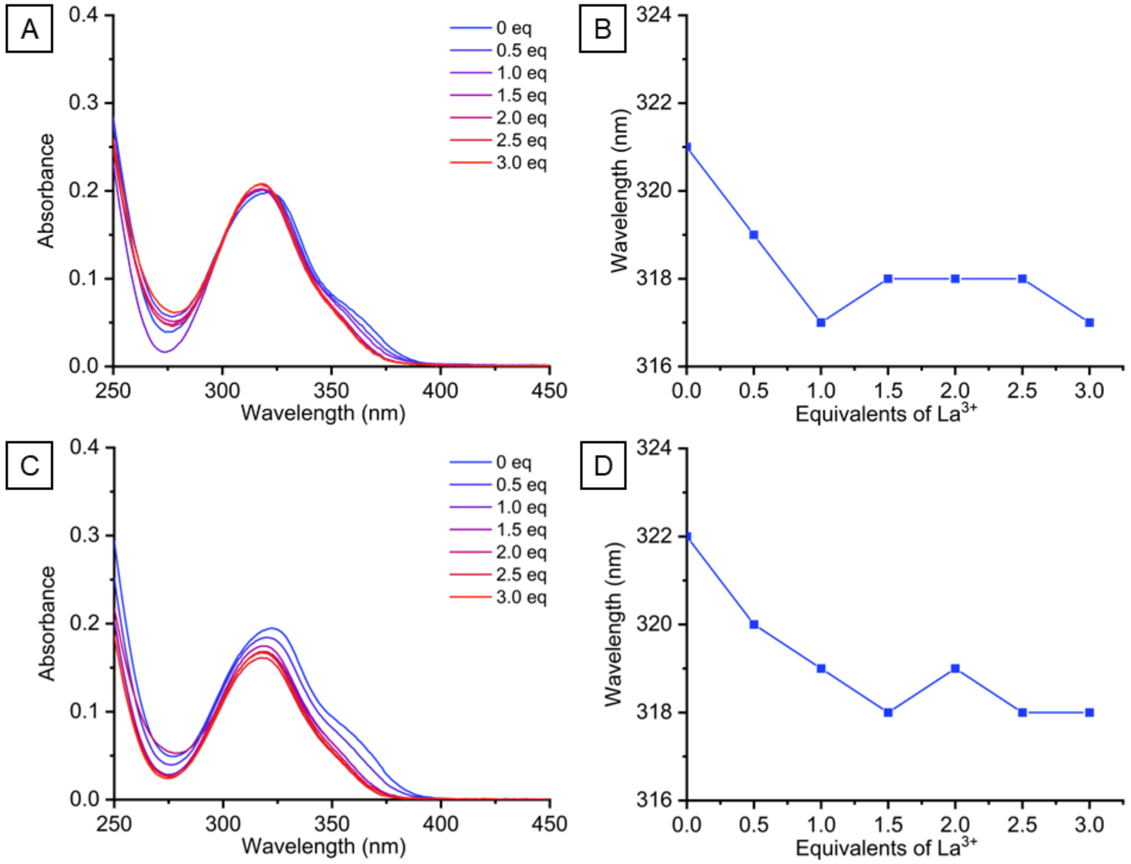

Figure 2.4. UV-vis spectroscopic titration of La^{3+} with HOPO-O_{10} (A) and HOPO-O_8 (C) and a profile of the peak wavelength as a function of the equivalents of La^{3+} added (B and D) (0.1 M HEPES pH 7.4, 10^{-5} M , room temperature).

2.2.3. Radiolabeling

The radiolabeling properties of the novel decadentate HOPO-O_{10} and its commercially available octadentate analog HOPO-O_8 were screened with the radiolanthanides ^{135}La and ^{155}Tb and the radioactinides ^{225}Ac and ^{227}Th. According to the previously reported solution thermodynamics of HOPO-O_8 across the lanthanide and actinide series, HOPO-O_8 should have the highest affinity for Th^{4+} with a pM of 40.1, followed by Tb^{3+} (pM = 21.8) and La^{3+} (17.2) with the lowest affinity. The pM of HOPO-O_8 and Ac^{3+} is not available due to the lack of stable isotopes of Ac^{3+}; based on the bond covalency and oxidation states study by Kelley et al., it is expected to be much lower than that of Th^{4+}.[268] However, it is worth noting that the correlation between the characterization studies such as solution thermodynamics or NMR and MS is not straightforward. The experimental conditions are significantly different, due to extremely low radiometal concentrations present in solution compared to the ligand (~ 10,000 higher chelate concentration) and the effect that trace non-radioactive metal impurities can have at such low concentrations.

Preliminary radiolabeling at higher concentrations (10^{-4} M) was performed for each radiometal-chelate pair under various conditions of buffer (0.5 M NH_4OAc, 0.5 M NaOAc, PBS), pH (5, 6, 7), temperature (room temperature and/or 80 °C), and time (15-60 min). It was found that 0.5 M NH_4OAc at pH 6 gave the highest radiochemical yields (RCYs) in all cases except for ^{227}Th labeling which was done at pH 5.

The octadentate HOPO-O_8 and the decadentate HOPO-O_{10} were incubated at different concentrations with ^{225}Ac (100 kBq) and quantitative (>99% radiometal incorporation) RCYs were only achieved for [^{225}Ac][Ac(HOPO-O_{10})] at 100 μM chelate concentration at room temperature in 15 min (**Figure 2.5A**). [^{225}Ac][Ac(HOPO-O_8)] was unable to chelate ^{225}Ac; further optimization of the labeling conditions at different pH or buffer did not achieve any improvements. At 10-fold lower concentrations, a M:L ratio of 1:2400, [^{225}Ac][Ac(HOPO-O_{10})] failed to complex at room temperature (**Figure 2.5A**) or 80 ^{o}C (Appendix, Figure A.2). These results indicate low radiolabeling compatibility of HOPO-O_8 and HOPO-O_{10} with ^{225}Ac, which clearly fall short of the most efficient ^{225}Ac chelates reported to date (e.g., macropa, H_4py4pa).[59,62]

The radiolabeling efficiency of HOPO-O_{10} and HOPO-O_8 with ^{135}La (600 kBq) exhibited a similar concentration-dependent profile as with ^{225}Ac. All ^{135}La was only complexed by either chelate at 10^{-4} M ligand concentration at room temperature in 15 min (**Figure 2.5B**). At 10 μM ligand concentrations, HOPO-O_8 and HOPO-O_{10} showed 0% RCYs even at 80 °C (Appendix, Figure A.2). Under similar radiolabeling conditions, macropa gave rise to complexes with almost equimolar amounts of metal and ligand (M:L ~ 1:4), clearly outperforming HOPO-O_{10} and HOPO-O_8 which can only successfully complex ^{135}La at 1:99000 ratios. These results are a clear example of the complexity of correlating the complexation thermodynamics and kinetics of the non-radioactive complexes (millimolar range) with the radiolabeling observations (picomolar concentrations of ^{135}La). The fast complex formation observed for $^{nat}La^{3+}$ by ^{1}H NMR spectroscopy is unfortunately not feasible under radiolabeling conditions.

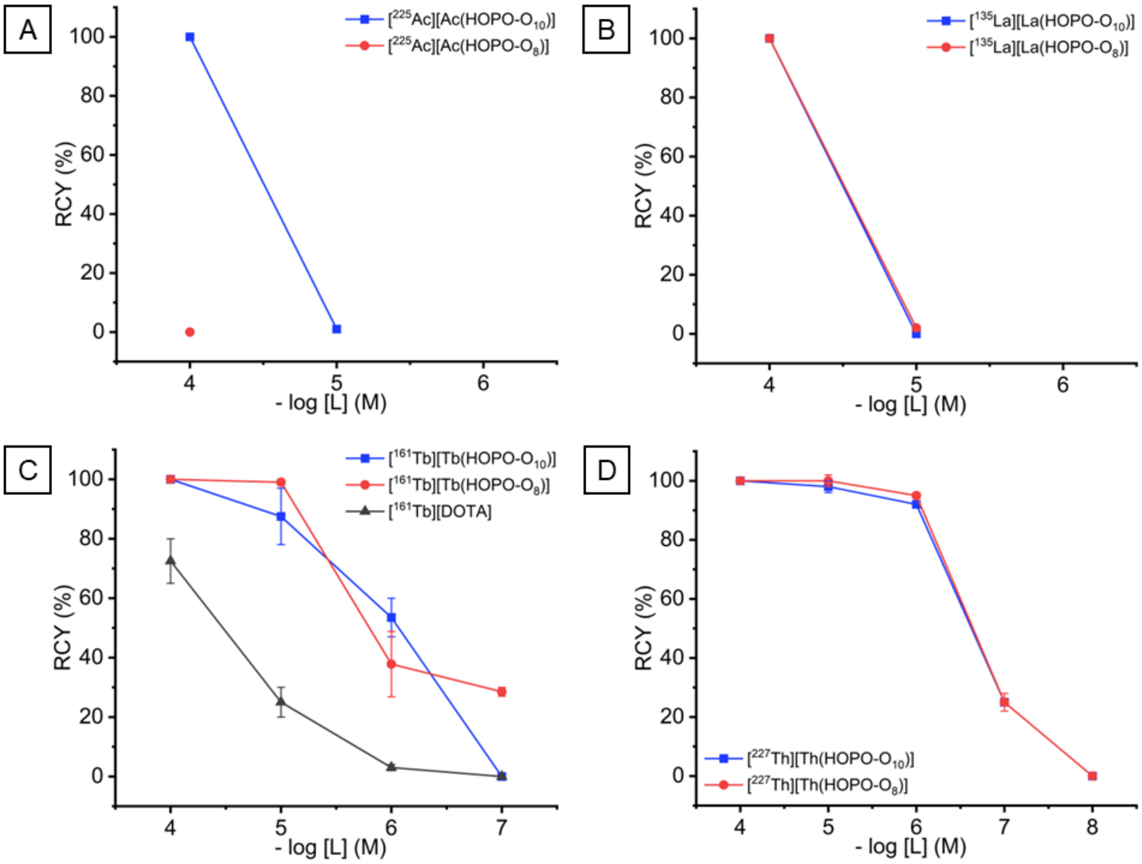

Figure 2.5. Concentration-dependant radiolabeling plots of HOPO-O_{10} (blue squares) and HOPO-O_8 (red dots) with ^{225}Ac (100 kBq) in 0.5 M NH_4OAc pH 6 at room temperature in 15 min (top left), ^{135}La (600 kBq) in 0.5 M NH_4OAc pH 6 at room temperature in 15 min (top right), ^{161}Tb (91 kBq) in 0.5 M NH_4OAc pH 6 at room temperature in 15 min including DOTA (bottom left), and ^{227}Th (1 kBq) in 0.5 M NH_4OAc pH 5 at room temperature in 15 min (bottom right). n = 3 for each data point, except for ^{227}Th where n = 2.

Radiolabeling studies of HOPO-O_{10} and HOPO-O_8 with ^{161}Tb were performed at a range of 10^{-4} to 10^{-7} M chelate concentrations (**Figure 2.5C**). DOTA, the $^{155/161}$Tb gold standard, was added to these experiments due to the lack of literature on the labeling efficiency of DOTA with Tb^{3+}, since all reported studies use bifunctional DOTA by itself or conjugated to targeting vectors.[40,269] HOPO-O_8 exhibits the highest radiolabeling efficiency achieving 99 ± 1 % RCYs under mild conditions in 15 min at 10 µM giving rise to complexes with a maximum apparent molar activity (max. A_m) of 81.5 MBq/nmol. Under the same conditions, HOPO-O_{10} reached 88 ± 10 % RCYs and a max. A_m of 85.4 MBq/nmol. In comparison to DOTA, which is known to have slow binding kinetics for large radiometals at room temperature, both the octadentate and the decadentate chelate show drastically improved binding affinity for ^{161}Tb.[59,219] These results demonstrate that DOTA is not ideal for the fast chelation of temperature-sensitive radiopharmaceuticals. Similar to the other radiometals, no significant differences were observed at 80 °C (Appendix, Figure A.2). HOPO-O_{10} and HOPO-O_8 together with the recently reported [$^{155/161}$Tb]Tb-crown represent the first chelates capable of effectively binding ^{161}Tb in 15 min at room temperature.

Concentration-dependant radiolabeling of the octadentate and decadentate chelate with ^{227}Th revealed excellent radiochemical affinity of both chelates for the radioactinide. Analogous to the other radiometals, HOPO-O_{10} and HOPO-O_8 had a very similar performance achieving RCYs >95% at 10^{-6} M ligand concentration in 15 min at room temperature (**Figure 2.5D**). Small improvements in RCYs were observed when increasing the reaction temperature to 80 °C; the RCYs incremented from 95 $\pm$ 1 to 100 $\pm$ 0% (HOPO-O_8) and 92 $\pm$ 0 to 100 $\pm$ 0% (HOPO-O_{10}) (Appendix, Figure A.2). These promising radiolabeling results could not be directly compared to the ^{227}Th gold standard, 3,2-Me-HOPO, which is not commercially available. Thus, it was deemed prudent to calculate the specific activity (A_s) and molar activity (A_m) of the octadentate and decadentate complex to have means of comparison with 3,2-Me-HOPO. The calculated max. A_m and A_s for HOPO-O_8 and HOPO-O_{10} are 13.2 MBq/μmol (17.77 MBq/mg) and 18.2 MBq/μmol (19.24 MBq/mg), respectively. The A_s of HOPO-O_{10} is comparable to that of 3,2-Me-HOPO which has a reported A_m of 18.4 MBq/μmol and A_s of 14.082 MBq/mg[120] while HOPO-O_8 has a lower capacity to incorporate the radionuclide. These findings indicate that the extra 1,2-HOPO moiety improves the binding affinity for Th^{4+} giving rise to higher radiolabeling efficiencies.

2.2.4. Human serum stability

The kinetic inertness of the four most promising complexes [^{155}Tb]Tb-HOPO-O_{10}, [^{161}Tb]Tb-HOPO-O_8, [^{227}Th]Th-HOPO-O_{10}, and [^{227}Th]HOPO-O_8 was evaluated in an in vitro human serum stability assay (**Figure 2.6**). ^{155}Tb was used for the serum stability of [^{155}Tb]Tb-HOPO-O_{10} due to isotope availability. This is a preliminary test to investigate if the metal-chelate complex can withstand transchelation and transmetallation to endogenous proteins (e.g., albumin or transferrin) in vivo. The corresponding ^{155}Tb and ^{227}Th complexes were incubated at 37 °C for approximately one half-life, 5 and 14 days, respectively, and the intact complex was monitored at multiple time points by TLC.

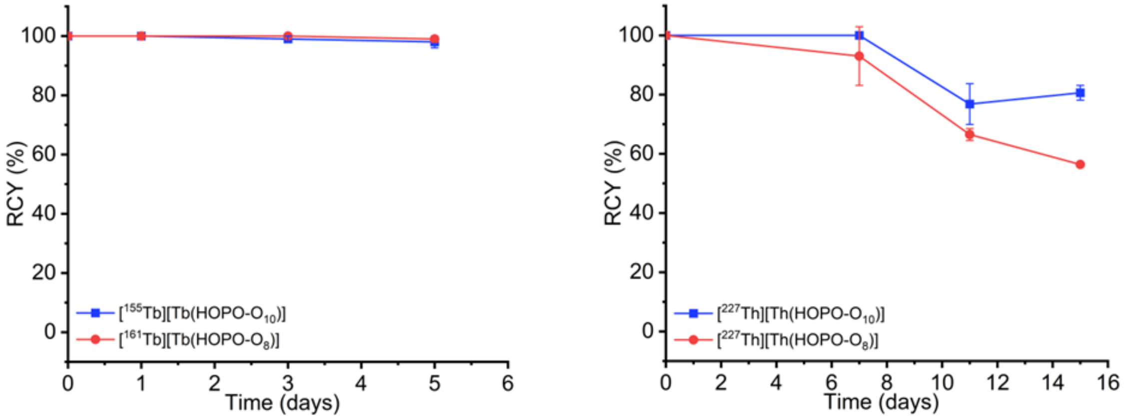

Figure 2.6. Human serum stability (37 °C) of [^{155}Tb]Tb-HOPO-O$_{10}$ and [^{161}Tb]Tb-HOPO-O$_8$ (left) and [^{227}Th]Th-HOPO-O$_{10}$, and [^{227}Th]HOPO-O$_8$ (right) complexes. n = 3 for each data point, except for ^{227}Th where n = 2.

[^{155}Tb]Tb-HOPO-O$_{10}$ and [^{161}Tb]Tb-HOPO-O$_8$ remained stable over 5 days retaining >98% of their radiochemical purity. These results indicate that both $^{155/161}$Tb complexes have exceptional stability in human serum and are promising candidates for nuclear medicine applications. Some differences were observed in the case of [^{227}Th]Th-HOPO-O$_{10}$ and [^{227}Th]HOPO-O$_8$. On day 7, [^{227}Th]HOPO-O$_{10}$ remained intact whereas [^{227}Th]HOPO-O$_8$ exhibited a 93 ± 10 % stability. Lastly, after 15 days [^{227}Th]HOPO-O$_{10}$ was 79 ± 7 % stable compared to 67 ± 2 % of [^{227}Th]Th-HOPO-O$_8$. The decrease in the stability observed for [^{227}Th]Th-HOPO-O$_{10}$ and [^{227}Th]HOPO-O$_8$ is similar to the values reported for [^{225}Ac]Ac-macropa and [^{225}Ac]Ac-crown which is attributed to the radiolysis of the radiometal caused by the potency of the α-particles emitted.[59,61] These results highlight the improvement of HOPO-O$_{10}$ over HOPO-O$_8$ due to its ability to form kinetically more inert complexes. Collectively, the radiolabeling and serum stability data demonstrate that HOPO-O$_{10}$ is a valuable candidate for ^{227}Th radiopharmaceutical development.

2.2.5. DFT calculations

Note: Eu^{3+} and Lu^{3+} were added to the DFT calculations for comparison across the lanthanide series. Unfortunately, ^{177}Lu radiolabeling could not be studied due to isotope availability.

3.5.1. Geometries

Structures of the ligands [3,4,3-LI(1,2-HOPO)]$^{4-}$ and [3,4,3,3-LI(1,2-HOPO)]$^{5-}$ as well as their complexes with Ac^{3+}, Th^{4+}, La^{3+}, Eu^{3+}, Tb^{3+} and Lu^{3+} were optimized using DFT. All metal ions maintain coordination numbers of 8 in their HOPO-O$_8$ complexes and form relatively symmetric structures (**Figure 2.7**). However, with an additional 1,2-HOPO unit, in the HOPO-O_{10} complexes, Ac^{3+}, Th^{4+}, Eu^{3+} and La^{3+} coordinate with all the available 10 oxygen atoms while Lu^{3+} and Tb^{3+} only coordinate with 9 oxygen atoms of the HOPO-O_{10} ligand, leaving one oxygen unbound to the metal ions with M-O distances of 3.476 Å and 3.221 Å respectively (**Figure 2.8**). This can be explained by their smaller ionic radii relative to Ac^{3+}, Th^{4+} and La^{3+}.[68] Due to the steric effects and constraints of the ring, there is less space for Lu^{3+} and Tb^{3+} to form a bond with the 10th oxygen atom. **Table 2.3** summarizes the average M-O distances in the optimized structures of HOPO-O_8 and HOPO-O_{10} complexes. It shows a consistent decreasing trend of average M-O distances along the series Ac^{3+}, Th^{4+}, La^{3+}, Eu^{3+}, Tb^{3+} and Lu^{3+}, which is also in line with the trend of their ionic radii.[68]

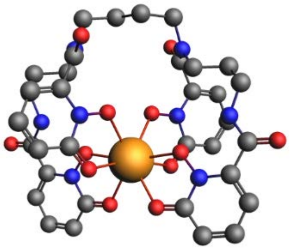

Figure 2.7. General geometry for optimized An/Ln-3,4,3-LI(1,2-HOPO) complexes (An = Ac^{3+} and Th^{4+}, Ln = La^{3+}, Eu^{3+}, Tb^{3+} and Lu^{3+}) at PBE-D3/TZ2P level of theory. Hydrogen atoms were hidden for clarity. (Yellow: metal ions; grey: carbon; blue: nitrogen; red: oxygen.) [La-3,4,3-LI(1,2-HOPO)]$^-$ is shown.

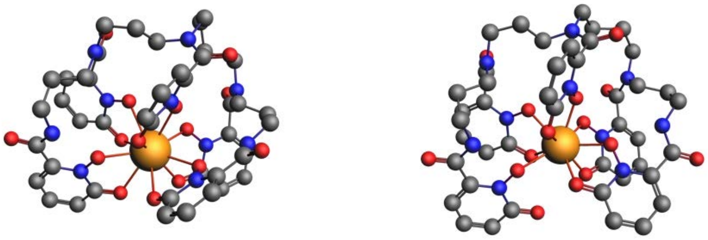

Figure 2.8. General geometry for optimized An/Ln-3,4,3,3-LI(1,2-HOPO) complexes (An = Ac^{3+} and Th^{4+}, Ln = La^{3+} and Eu^{3+}) (left) and general geometry for optimized structures of [Ln-3,4,3,3-LI(1,2-HOPO)]$^{2-}$ (right) (Ln = Lu^{3+} and Tb^{3+}) at PBE-D3/TZ2P level of theory. Hydrogen atoms were hidden for clarity. (Yellow: metal ions; grey: carbon; blue: nitrogen; red: oxygen.) [La-3,4,3,3-LI(1,2-HOPO)]$^{2-}$ and [Lu-3,4,3,3-LI(1,2-HOPO)]$^{2-}$ are shown.

Table 2.3. Average M-O distances (Å) in optimized structures of HOPO-O_8 and HOPO-O_{10} complexes with Ac^{3+}, Th^{4+}, La^{3+}, Eu^{3+}, Tb^{3+} and Lu^{3+}.

	La^{3+}	**Tb^{3+}**	**Eu^{3+}**	**Lu^{3+}**	**Ac^{3+}**	**Th^{4+}**
HOPO-O_8	2.520	2.393	2.441	2.334	2.601	2.432
HOPO-O_{10}	2.624	2.468*	2.582	2.407*	2.695	2.525

*Values were calculated excluding the distance between metal ions and an unbound oxygen atom.

3.5.2. Thermodynamics

Stabilities of the radionuclide-HOPO complexes (i.e., the affinities of both $[3,4,3\text{-LI}(1,2\text{-HOPO})]^{4-}$ and $[3,4,3,3\text{-LI}(1,2\text{-HOPO})]^{5-}$ for Ac^{3+}, La^{3+}, Eu^{3+}, Tb^{3+}, $Lu^{3+,}$ and Th^{4+}) were evaluated by the Gibbs free energies of the designed reactions shown below. The hydration number of the hydrated ions was assumed to be 9 under aqueous conditions based on the determination of the coordination number of hydrated Ac (III) ion.[270] Precise determination of hydration numbers of the hydrated An/Ln ions is not considered in the current work. The values for ΔG are the Gibbs free energies for complexation reactions (R1 – R3) of hydrated An/Ln ions with ligands, L_1 ($[3,4,3\text{-LI}(1,2\text{-HOPO})]^{4-}$) and L_2 ($[3,4,3,3\text{-LI}(1,2\text{-HOPO})]^{5-}$). To compare the affinities of L_1 and L_2 to the same An/Ln ions, ligand exchange reactions (R4) were designed. A negative ΔΔG value indicates that the complex with L_2 is more stable than that with L_1. Metal exchange reactions (R5) are designed for comparing the stabilities of complexes with Ac^{3+}, La^{3+}, Eu^{3+}, Tb^{3+}, $Lu^{3+,}$ and Th^{4+} with these two ligands, respectively.

<u>Ligand substitution reactions (complex formation reactions)</u>

$[M_1(H_2O)_9]^{n+}+L_1^{x-}\leftrightharpoons[M_1L_1]^{n-x}+9H_2O$ (R1)

$\Delta G_1 = G([M_1L_1]^{n-x}) + 9\times G(H_2O) - G([M_1(H_2O)_9]^{n+}) - G(L_1^{x-})$

$[M_1(H_2O)_9]^{n+}+L_2^{x-}\leftrightharpoons[M_1L_2]^{n-x}+9H_2O$ (R2)

$\Delta G_2 = G([M_1L_2]^{n-x}) + 9\times G(H_2O) - G([M_1(H_2O)_9]^{n+}) - G(L_2^{x-})$

$[M_2(H_2O)_9]^{n+}+L_1^{x-}\leftrightharpoons[M_2L_1]^{n-x}+9H_2O$ (R3)

$\Delta G_3 = G([M_2L_1]^{n-x}) + 9\times G(H_2O) - G([M_2(H_2O)_9]^{n+}) - G(L_1^{x-})$

<u>Ligand exchange reactions</u>

$[ML_1]^{n-x}+L_2^{y-}\leftrightharpoons[ML_2]^{y-n}+L_1^{x-}$ (R4)

$\Delta\Delta G_1 = \Delta G_2 - \Delta G_1$

Metal exchange reactions

$[M_1L]^{n-x}+[M_2(H_2O)_9]^{3+}\leftrightharpoons[M_1(H_2O)_9]^{3+}+[M_2L]^{n-}$ (R5)

$\Delta\Delta G_2 = \Delta G_3 - \Delta G_1$

In these equations, n is the charge carried by metal ions, and x is the number of (negative) charges carried by the ligands.

The free energies of complex formation reactions (R1–R3) of hydrated metal ions and ligands are listed in **Table 2.4**. Negative ΔG values indicate that stable complexes form in the modelled aqueous conditions. To compare the effect of the additional 1,2-HOPO unit on the stability of HOPO complexes, ΔΔG values of the designed ligand exchange reactions (R4) are straightforward (**Table 2.4**). For all evaluated metal ions except Th^{4+}, ΔΔG values are positive enough to indicate non-spontaneous reactions when the HOPO-O_{10} ligand (L_2) is used to substitute HOPO-O_8 (L_1) in the complexes. In contrast, with the additional 1,2-HOPO unit, HOPO-O_{10} (L_2) stabilizes Th^{4+} better than HOPO-O_8 (L_1) in the complex.

Table 2.4. Calculated ΔG (in kcal/mol) for complex formation reactions (R1-R3) and ΔΔG (in kcal/mol) for L_1-L_2 ligand exchange reactions (R4) in aqueous phase at the PBE-D3/TZ2P level of theory.

	ΔG (kcal/mol)		ΔΔG (kcal/mol)
	L_1 (HOPO-O_8)	L_2 (HOPO-O_{10})	L_1-L_2
Ac^{3+}	-92.34	-89.86	2.48
La^{3+}	-97.54	-90.85	6.69
Eu^{3+}	-109.08	-90.10	18.98
Tb^{3+}	-103.98	-87.99	15.99
Lu^{3+}	-106.79	-88.72	18.07
Th^{4+}	-151.47	-159.61	-8.14

The M_1-M_2 metal exchange reaction (R5) compares the affinities of the ligands to metal ions. Negative ΔΔG values show a higher affinity of the ligand to M_2 over M_1. Through these reactions, the stability of the HOPO-O_8 complexes is found to obey the following trend (**Figure 2.9**): $Th^{4+} > Eu^{3+} > Lu^{3+} > Tb^{3+} > La^{3+} > Ac^{3+}$, while that of the HOPO-O_{10} complexes is observed to be: $Th^{4+} > Eu^{3+} > La^{3+} > Ac^{3+} > Lu^{3+} > Tb^{3+}$. The abnormal order of Lu^{3+} and Tb^{3+} in HOPO-O_{10} complexes is consistent with their geometry results – the lack of one coordination site makes them less stable than the other, decadentate complexes.

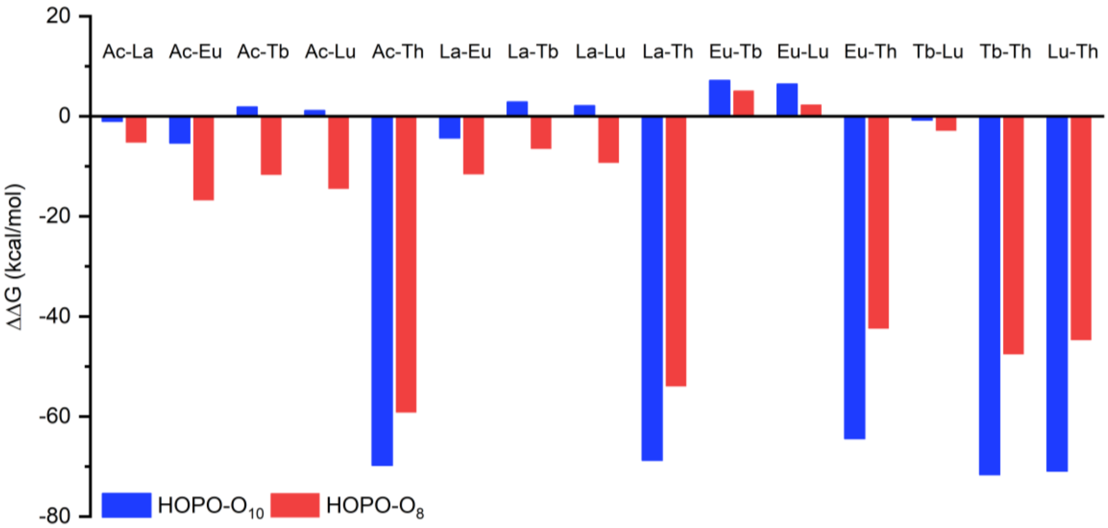

Figure 2.9. Calculated ΔΔG (in kcal/mol) for M_1-M_2 metal exchange reactions (R5 above) in aqueous phase at the PBE-D3/TZ2P level of theory.

The partial charges on the metal ions in each of the HOPO complexes were analyzed using the Hirshfeld and Voronoi charge analysis methods **Table 2.5.**[271] Generally, it is not the absolute values that are of interest, but the trends: Metal charges smaller than the formal +3/+4 charge indicate charge transfer from O atoms in the ligands to the metal ions. The absolute values do not show any obvious correlations with the stabilities and geometries of the complexes (i.e., average M-O distances in each complex). However, the trend of Voronoi Deformation density (VDD) charge transfer on metal ions excluding Th^{4+} exhibits a strong correlation with the intrinsic interaction energy ΔE_{int} which is defined below.

Table 2.5. Hirshfeld and Voronoi charge (in e) on metal ions in HOPO-O_8 and HOPO-O_{10} complexes in aqueous phase at the PBE-D3/TZ2P level of theory.

	HOPO-O_8		**HOPO-O_{10}**	
	Hirshfeld	**VDD**	**Hirshfeld**	**VDD**
Ac^{3+}	0.519	0.129	0.431	0.143
La^{3+}	0.421	0.121	0.363	0.151
Eu^{3+}	0.518	0.362	0.498	0.393
Tb^{3+}	0.582	0.464	0.584	0.507
Lu^{3+}	0.447	0.306	0.464	0.353
Th^{4+}	0.591	0.171	0.505	0.195

To get further insight into the bonding between metal ions and ligands, Energy Decomposition Analysis (EDA)[272] was performed for HOPO-O_8 and HOPO-O_{10} complexes, using metal cations and ligand anions as interacting fragments. The intrinsic interaction energy ΔE_{int} between metal ions and ligands in the complexes is decomposed into different terms: (1) the electrostatic interaction ΔE_{elstat} between the fragments; (2) the repulsive exchange (Pauli) interaction ΔE_{Pauli} between electrons of the two fragments of the same spin, (3) the orbital (covalent) interaction ΔE_{orb} which comes from the orbital relaxation and the orbital mixing between the fragments, and (4) dispersion correction energy ΔE_{disp}.[273] It can be written as:

$$\Delta E_{int} = \Delta E_{pauli} + \Delta E_{elstat} + \Delta E_{orb} + \Delta E_{disp}$$

Table 2.6. EDA results (in kcal/mol) for HOPO-O_8 and HOPO-O_{10} complexes in aqueous phase at the PBE-D3/TZ2P level of theory.

Fragments Energy terms	HOPO-O_8					
	Ac^{3+}	La^{3+}	Eu^{3+}	Tb^{3+}	Lu^{3+}	Th^{4+}
ΔE_{int}	-1342.30	-1397.81	-1631.41	-1652.71	-1519.93	-2108.17
ΔE_{Pauli}	196.15	199.37	188.94	200.00	187.44	317.00
ΔE_{elstat}	-1112.76 (72.33%)	-1127.53 (70.60%)	-1144.32 (62.86%)	-1158.66 (62.54%)	-1169.97 (68.52%)	-1542.52 (63.60%)
ΔE_{orb}	-422.81 (27.48%)	-466.06 (29.18%)	-672.37 (36.94%)	-688.89 (37.18%)	-534.39 (31.30%)	-878.26 (36.21%)
ΔE_{disp}	-2.88 (0.19%)	-3.59 (0.22%)	-3.66 (0.20%)	-5.16 (0.28%)	-3.01 (0.18%)	-4.39 (0.18%)

Fragments Energy terms	HOPO-O_{10}					
	Ac^{3+}	La^{3+}	Eu^{3+}	Tb^{3+}	Lu^{3+}	Th^{4+}
ΔE_{int}	-1527.27	-1579.80	-1804.85	-1822.42	-1684.62	-2363.76
ΔE_{Pauli}	170.45	165.79	149.65	163.46	155.07	270.41
ΔE_{elstat}	-1259.68 (74.20%)	-1268.71 (72.68%)	-1275.26 (65.25%)	-1287.24 (64.82%)	-1134.70 (61.68%)	-1728.26 (65.61%)
ΔE_{orb}	-434.81 (25.61%)	-472.74 (27.08%)	-674.77 (34.52%)	-691.93 (34.84%)	-546.10 (29.68%)	-900.80 (34.20%)
ΔE_{disp}	-3.24 (0.19%)	-4.14 (0.24%)	-4.46 (0.23%)	-6.71 (0.34%)	-3.82 (0.21%)	-5.10 (0.19%)

Values in percentage show the contribution of each attractive energy term to the total attractive energy term ($\Delta E_{elstat} + \Delta E_{orb} + \Delta E_{disp}$).

Through EDA (**Table 2.6**), it can be observed that, for all complexes, ΔE_{elstat} contributes most to the total bonding energy compared to ΔE_{orb}, ranging from 61% to 75%, indicating more electrostatic characteristics in bonding, especially for Ac^{3+} and La^{3+}. Besides, with a higher coordination number, the electrostatic character contributes more to bonding except for Lu^{3+}. The lack of one coordination site in Lu and Tb complexes with

HOPO-O_{10} accounts for a lower portion of electrostatic character in bonding. Interestingly, the higher portion of electrostatic character it has, the less stable the M-HOPO-O_8 complex is. However, this trend is not in line with that in M-HOPO-O_{10} complexes. The significantly larger absolute values of ΔE_{int} of Th-HOPO complexes compared to the others are a direct result of the charge difference. (i.e., Th is in the 4+ state while the other metals are in a 3+ state.)

2.3. Conclusions

Overall, the additional 1,2-HOPO moiety in the novel decadentate acyclic chelate HOPO-O_{10} has demonstrated a moderate improvement in the radiolabeling efficiency and a significant increase in the stability of the tetravalent radioisotope ^{227}Th compared to its octadentate analog HOPO-O_8. In this chapter, we have successfully synthesized HOPO-O_{10} and investigated two routes to prepare intermediate **2.5**; route 2 led to higher yield and easier purification. Non-radioactive La^{3+} and Tb^{3+} complexes of both chelates were prepared and characterized. ^{1}H NMR and MS suggested the formation of a bimetallic HOPO-O_{10} species compared to a monometallic HOPO-O_8 complex at a millimolar scale. These findings cannot be directly correlated with the radiolabeling studies due to the lower concentrations employed. HOPO-O_{10} was comparable or even superior to HOPO-O_8 in all concentration-dependent radiolabeling studies. The improved affinity and stability of HOPO-O_{10} were drastically shown in the radiolabeling of ^{227}Th. [^{227}Th]Th-HOPO-O_{10} exhibited higher maximum A_m - comparable to the standard (3,2-Me-HOPO) chelate – and excellent stability to transchelation in the in vitro human serum stability challenge with 93 ± 10% intact complex after 15 days compared to the 67 ± 2% of [^{227}Th]Th-HOPO-O_8. HOPO-O_{10} and HOPO-O_8 showed similar performance in the radiolabeling of ^{161}Tb and complex stability both outperforming the gold-standard DOTA at room temperature. Our DFT calculations have shown that among all the studied An/Ln, Th^{4+}-HOPO-O_{10} is the only complex with higher stability than its octadentate analog in agreement with the experimental results. The design of HOPO-O_{10} also contributes to gaining insight into the chelation of large radioactinides to inspire future ligand designs.

The excellent in vitro stability of [^{227}Th]Th-HOPO-O_{10} will have to be further demonstrated when conjugated to a targeting vector (i.e., antibody) before its preclinical application. As such, efforts towards the preparation of a bifunctional HOPO-O_{10} chelate, which can be prepared via intermediate 5 in the described synthetic route, is currently underway. Additionally, these encouraging results open the door to evaluating other tetravalent radioactinides with medically relevant properties such as ^{134}Ce, a highly promising PET imaging pair for ^{227}Th, or the α-emitter ^{230}U for personalized radiotheranostic applications.

2.4. Experimental section

2.4.1. General materials and methods

All chemicals, unless otherwise noted were purchased from commercial suppliers (Sigma-Aldrich, TCI America, Fisher Scientific) and used as received without further purification. All solvents noted as "dry" were obtained following storage over 3 Å molecular sieves. All instruments were calibrated and maintained following standard quality-control procedures. High-resolution mass spectrometry (HR-MS) was carried out through electrospray ionization (ESI) in an Agilent 6210 time-of-flight instrument (TOF). Low-resolution mass spectrometry was performed on an Advion ExpressionL CMS equipped with an ESI source. 1H and 13C nuclear magnetic resonance (NMR) spectra were recorded at 25 °C on Bruker AV400 or AV600 instruments; NMR spectra are expressed on the δ scale and referenced to residual solvent peaks. Reactions were monitored by thin-layer chromatography (TLC) performed on aluminum sheets pre-coated with silica gel 60 (HF254, E. Merck), and spots were visualized by UV and charring with permanganate or ninhydrin solutions. Flash column chromatography was carried out with silica gel 60 (40-63 μm, 230-400 mesh) using a stepwise solvent polarity gradient correlated with TLC mobility. Automated column chromatography was performed using a Teledyne ISCO Combiflash Rf or with an Isolera One Biotage. Semi-preparative high-performance liquid chromatography (HPLC) was carried out using an Agilent 1100 series consisting of a G1311A Quaternary Pump, G2260A autosampler, and G1315B variable wavelength absorbance detector. Semi-preparative purification was performed with a Kinetex semi-preparative C18 column, 5 μm, 100 Å, 150 x 10.0 mm at a flow rate of 3.0 mL/min unless otherwise noted. All HPLC methods employed an H_2O/acetonitrile biphasic solvent system buffered with 0.1% TFA. UV-vis spectra were recorded with a Cary100 UV-vis spectrometer at room temperature with 1 cm length cuvettes.

2.4.2. Synthesis

Compound **2.1** was synthesized and characterized as previously described by König et al.[47] Compound **2.8** was prepared following a 3-step synthetic route described by Deri et al. and Guérard et al.[261,266]

3-[(benzyloxycarbonyl)amino]propanal (**2.2**). The oxidation of **2.1** was performed according to a modified literature procedure.[274] Benzyl (3-hydroxypropyl)carbamate (1.00 g, 4.80 mmol) and TEMPO (0.150 g, 0.96 mmol) were dissolved in dichloromethane (40 mL) and added to a solution of NaBr (0.103 g, 0.96 mmol) and $NaIO_4$ (2.05 g, 9.6 mmol) in H_2O (40 mL). The reaction mixture was vigorously stirred for 30 h at RT. The organic phase was separated, and the aqueous phase was extracted with 40 ml of CH_2Cl_2 (x5). The combined organic phases were washed with $Na_2S_2O_3$, and brine and dried over $MgSO_4$. The solvents were removed under reduced pressure after filtration. The residue was purified by chromatographic column on silica gel with hexane/ethyl acetate (1:1). The solvents were evaporated under vacuum to obtain **2.2** as an off-white solid (0.693 g, 70 %). ^{1}H NMR (400 MHz, Chloroform-*d*) δ 9.80 (s, 1H), 7.40 – 7.28 (m, 5H), 5.15 (s, 1H), 5.08 (s, 2H), 3.49 (q, *J* = 6.1 Hz, 2H), 2.74 (t, *J* = 5.8 Hz, 2H). ^{13}C NMR (101 MHz, $CDCl_3$) δ 201.14, 156.44, 136.58, 128.67, 128.28, 128.21, 66.93, 44.26, 34.69. HR-ESI-MS (CH_3OH) *m/z* for $C_{11}H_{14}NO_3$ ($[M+H]^+$) calc. (found): 208.0968 (208.0989).

(N1,N4,N9-Tri-tert-butoxycarbonyl)-1,12-diamino-4,9-diazadodecan (**2.3**). Compound **2.3** was synthesized using a published procedure with minor modifications.[264] Spermine (2.00 g, 9.90 mmol) was dissolved in dry CH_3OH (140 mL) under argon at -78 ºC and ethyl trifluoroacetate (1.17 mL, 9.90 mmol) was added dropwise over 30 min. After 30 min, the reaction mixture was warmed to 0 ºC and stirred for another hour. Di-tert-butyl carbonate (8.64 g, 39.6 mmol) was dissolved in dry CH_3OH (10 mL), slowly added to the reaction mixture, and stirred at room temperature for 24 h. The pH of the solution was increased to 11 adding dropwise a concentrated solution of NH_4OH and the mixture was stirred at 65 ºC for 20 h. After evaporation in vacuo, the crude was purified by a chromatographic column on silica (0-10% CH_3OH in CH_2Cl_2 with 1% NH_3 in CH_3OH). The pure compound was obtained in the form of a yellow oil (2.01 g, 30%). ^{1}H NMR (600 MHz, Methanol-*d*$_4$) δ 3.37 – 3.32 (m, 2H), 3.22 (q, *J* = 6.5 Hz, 6H), 3.03 (t, *J* = 6.7 Hz, 2H), 2.92 (t, *J* = 7.2 Hz, 2H), 1.89 (p, *J* = 7.0 Hz, 2H), 1.74 – 1.63 (m, 2H), 1.57 – 1.50 (m, 4H), 1.50 – 1.39 (m, 27H). ^{13}C (151MHz, Methanol-d$_4$) δ 158.44, 157.88, 157.35, 81.21, 80.97, 79.94, 49.85, 47.89(*), 45.86(*), 44.72, 38.81, 30.25, 29.65, 28.76(*), 26.90(*). HR-ESI-MS (CH_3OH) *m/z* for $C_{25}H_{51}N_4O_6$ calc. ($[M+H]^+$) calc. (found): 503.3803 (503.3690). (*) indicates peak splitting due to the presence of different conformers in solution.

Phenylmethyl N-[3-[[(4-methylphenyl)sulfonyl]oxy]propyl]carbamate (**2.4**). Compound **2.4** was synthesized using a published procedure with minor modifications.[275] To a stirring solution of **2.1** (1.00 g, 4.9 mmol) in dry CH_2Cl_2 (10 mL) was added Et_3N (1.28 mL, 33.5 mmol), and a solution of 4-toluenesulfonyl chloride (1.02 g, 5.4 mmol) in dry CH_2Cl_2 (6 mL) at 0 °C under argon atmosphere. The reaction mixture was allowed to warm up to room temperature and stirred for 18 h. The solution was evaporated in vacuo, and the resulting solid was redissolved in ethyl acetate. The organic phase was washed with H_2O and brine and dried over $MgSO_4$. After concentration under reduced pressure, the crude was purified via automated silica gel chromatography (Isolera One, Sfar HC 10 g, gradient: A: hexanes, B: ethyl acetate; 0-10 CV: 30% B, 10-12 CV: 30-100% B) to yield **2.4** as a colourless oil (1.23 g, 71%). ^1H NMR (400 MHz, chloroform-d_3) δ 7.78 (d, J = 8.6 Hz, 2H), 7.40 – 7.28 (m, 7H), 5.07 (s, 2H), 4.09 (t, J = 6.0 Hz, 2H), 3.26 (q, J = 6.4 Hz, 2H), 2.43 (s, 3H), 1.93 – 1.83 (m, 2H). ^{13}C NMR (101 MHz, chloroform-d_3) δ 156.48, 145.13, 136.56, 133.01, 130.08, 128.69, 128.31, 128.24, 128.03, 67.93, 66.89, 37.43, 29.22, 21.77. HR-ESI-MS (CH_3OH) *m/z* for $C_{25}H_{64}N_5O_8$ ($[M+H]^+$) calc. (found): 694.4749 (694.4771).

N1,N5,N10-tri-tert-butoxycarbonyl-N18-benzyloxycarbonyl-1,5,10,14,18-pentaazaoctadecane (**2.5**). *Route 1* – This compound was synthesized using a published procedure with minor modifications.[264] To a solution of **2.3** (0.50 g, 1.0 mmol) dissolved in dry methanol (12 mL) were added **2.2** (0.207 g, 1.00 mmol), two drops of glacial acetic acid and molecular sieves (2000 mg). The mixture was stirred at room temperature for 45 min before the addition of $Na(CN)BH_3$ (0.127 g, 2.00 mmol), and the reduction reaction was continued for 23 h at room temperature. The molecular sieves were removed by filtration and the reaction was quenched with H_2O (10 mL) followed by extraction of the aqueous layer with CH_2Cl_2 (x3). The organic phases were combined, washed with brine, dried over $MgSO_4$, and filtered. The clear solution was concentrated under reduced pressure and the crude oil was purified using automated column chromatography (Teledyne ISCO, 40 g gold silica column, gradient: A: CH_2Cl_2 with 1% NH_3 in CH_3OH, B: 20% CH_3OH in CH_2Cl_2 with 1% NH_3 in CH_3OH; 0-20 CV: 0-100% B). The pure product fractions were combined, and the solvents were evaporated to give **2.5** as a pale-yellow oil (0.221 g, 32%). ^1H NMR (600 MHz, methanol-d_4) δ 7.43 – 7.26 (m, 5H), 5.07 (s, 2H), 3.29 – 3.13 (m, 10H), 3.03 (t, *J* = 6.7 Hz, 2H), 2.55 (dt, *J* = 29.6, 7.1 Hz, 4H), 1.70 (m, *J* = 14.0, 7.9 Hz, 6H), 1.59 – 1.38 (m, 31H). ^{13}C NMR (151 MHz, methanol-*d*$_4$) δ 158.91, 158.39, 157.46, 157.29, 138.47, 129.45, 128.94, 128.76, 80.91, 79.90, 67.30, 48.20, 48.00, 47.75 (d, J = 14.8 Hz), 47.50, 46.04, 45.57, 39.62, 38.86 (*), 30.66, 30.23, 29.55(*), 28.77, 27.09(*), 26.53(*). HR-ESI-MS (CH_3OH) *m/z* for $C_{25}H_{64}N_5O_8$ ($[M+H]^+$) calc. (found): 694.4749 (694.4771). (*) indicates peak splitting due to the presence of different conformers in solution.

Route 2 – Compound **2.4** (0.20 g, 0.55 mmol) and compound **2.3** (0.56 g, 1.1 mmol) were dissolved in CH_3CN (35 mL). K_2CO_3 (0.30 g, 2.2 mmol) was added and the mixture was heated to reflux for 8 h. After cooling down, the salts were filtered out and the solvent was evaporated resulting in a yellow oil. The crude was redissolved in the minimum amount of CH_3CN and purified by reverse-phase automated column chromatography (Isolera One, Sfar C18 12 g, gradient: A: H_2O, B: CH_3CN; 0-5 CV: 10% B, 5-30 CV: 10-50% B, 30-31 CV: 100% B). The product was obtained as a yellow oil (0.15 g, 40%).

21-amino-2,2-dimethyl-4-oxo-3-oxa-5,9,14,18-tetraazaheneicosane-9,14-acid bis(1,1dimethylethyl-) ester (**2.6**). Pd/C 10 wt. % loading (0.047 g) was added to a stirring solution of **2.5** (0.100 g, 0.15 mmol) in ethanol (15 mL). The flask was stoppered and sealed and first purged with argon followed by H_2 gas from a balloon. The reaction was stirred at room temperature for 4 h under H_2 atmosphere. The reaction mixture was filtered through a pad of Celite and washed with ethanol. The filtrate was concentrated *in vacuo* to obtain **2.6** as a yellow oil which was used without further purification (0.074 g, 89%). ESI-MS (CH_3OH) *m/z* for $C_{28}H_{58}N_5O_6$ ($[M+H]^+$) calc. (found) 560.6 (560.6).

1,16-diamino-4,8,13-triazagexadecane (**2.7**). Compound **2.6** (0.074 g, 0.13 mmol) was dissolved in a 1:1 mixture of trifluoroacetic acid (TFA) (1 mL) and CH_2Cl_2 (1 mL). After stirring for 2 h at RT, the solvents were evaporated under reduced pressure and the residual TFA was removed by the addition and evaporation of small amounts of CH_3OH (5 x 5 mL). The pale brown solid was dissolved in the minimum amount of H_2O and freeze-dried overnight to yield **2.7** as a TFA salt (0.105 g, 97%). ^{1}H NMR (600 MHz, Methanol-*d*$_4$) δ 3.19 – 3.03 (m, 16H), 2.18 – 2.04 (m, 5H), 1.85 – 1.75 (m, 4H). ^{13}C NMR (150 MHz, Methanol-*d*$_4$) δ 163.18 (TFA anion), 118.18 (TFA anion), 48.21 (*), 45.97 (*), 45.81 (*), 37.78 (*), 25.40 (*), 24.23, 24.17. HR-ESI-MS (CH_3OH) *m/z* for $C_{13}H_{34}N_5$ ($[M+H]^+$) calc.

(found): 260.2809 (260.2800). (*) indicates peak splitting due to the presence of different conformers in solution.

3,4,3,3-(LI-1,2-HOPO)Bn (**2.9**). To a stirring solution of **2.7** (0.208 g, 0.25 mmol) in dry dimethylformamide (mL) under N_2 was added compound **2.8** (0.60 g, 1.75 mmol), 4-(dimethylamino)pyridine (0.003 g, 0.025 mmol) and triethylamine (0.28 mL, 2 mmol). The solution was heated to 50 °C and stirred for 3 days. After cooling to room temperature H_2O was added and the aqueous phase was extracted with ethyl acetate (x2). The combined organic layers were washed with H_2O and brine, dried over anhydrous $MgSO_4$, and filtered. The solvent was then removed, and the crude was purified through a gravity column (0-5% CH_3OH in CH_2Cl_2) to obtain **2.9** as an orange oil (0.235 g, 67%). ^1H NMR (600 MHz, chloroform-d) δ 7.82 – 7.00 (m, 30H), 6.87 – 5.75 (m, 10H), 5.75 – 4.78 (m, 10H), 3.72 – 2.12 (m, 16H), 1.88 – 0.42 (m, 10H). ^{13}C NMR (151 MHz, chloroform-d) δ 158.64, 157.92, 143.38, 138.33, 137.86, 133.42, 130.71, 129.17, 128.78, 128.36, 125.43, 123.38, 122.77, 104.81, 102.74, 79.49, 47.24, 46.12, 42.63, 42.27, 36.85, 31.57, 30.35, 29.44, 27.14, 25.30, 20.78, 21.62.* HR-ESI-MS (CH_3OH) *m/z* for $C_{78}H_{79}O_{10}N_{15}$ ($[M+H]^+$) calc. (found): 1395.5721 (1395.5709). *signals were assigned to the best of our possibilities with ^1H-^{13}C HSQC and HMBC experiments due to low ^{13}C resolution.

3,4,3,3-(LI-1,2-HOPO)(**2.10**). Compound **2.9** (0.235 g, 0.17 mmol) was dissolved in a 1:1 mixture of concentrated HCl (3 mL) and CH_3COOH (3 mL). The solution was heated to 50 °C for 3 days and then the solvents were evaporated under reduced pressure. The crude was redissolved in H_2O and purified by semi-preparative HPLC (gradient: A: 0.1% TFA in H_2O, B: 0.1% TFA in CH_3CN; 0-0.5 min: 10% B, 0.5-1.5 min: 10-20% B, 1.5-7.5 min: 20% B, 7.5-8.5 min: 20-90% B, 8.5-10.5 min: 90% B, 10.5-11.5 min: 10% B, 11.5-16 min: 10% B, t_R = 4.57 min, flow rate: 3.5 mL/min). The product peaks were collected and the combined fractions were evaporated under reduced pressure and lyophilized to obtain **2.10** as an off-white solid (0.087 g, 55%). Elemental analysis for 3,4,3,3-(LI-1,2-HOPO)·1.6 CH_4O·5.4 HCl calc. (found): C, 44.9 (44.66); H, 5.05 (5.39); N, 11.74 (12.06). ^1H NMR (600 MHz, methanol-d_4) δ 7.62 (m, 5H), 6.93 – 6.30 (m, 10H), 3.93 – 2.91 (m, 16H), 2.22 – 1.19 (m, 10H). ^{13}C NMR (151 MHz, methanol-d_4) δ 163.29(*), 162.28(*), 160.20(*), 143.17(*), 142.25(*), 140.58(*), 140.09(*), 139.66(*), 120.26(*), 109.61(*), 49.85, 47.43(*), 43.52(*), 38.27(*), 38.07(*), 29.63, 29.03, 27.80, 26.27(*), 25.27(*). HR-ESI-MS (CH_3OH) *m/z* for $C_{78}H_{79}O_{10}N_{15}$ ($[M+H]^+$) calc. (found): 945.3373 (945.3344).(*) indicates peak splitting due to the presence of different conformers in solution.

2.4.3. Metal complexation

[La_n(3,4,3,3-(LI-1,2-HOPO))]$^{(3n-5)}$ (**2.11**). $La(ClO_4)_3 \cdot 6H_2O$ (0.007 g, 0.012 mmol) was dissolved in 0.2 mL of MeOH and the solution was added dropwise to a solution of **2.10** (0.012 g, 0.013 mmol) in 0.8 mL of MeOH. A precipitate formed immediately after each drop leaving a bright yellow suspension. The reaction was mixed thoroughly with a vortex mixer at 1000 rpm for 2 min. The precipitate was separated by centrifuge and the pellet was washed with Et_2O (x3) and then air-dried on filter paper to give **2.11** as a beige solid (0.016 g). ESI-MS (CH_3OH) *m/z* for $C_{43}H_{44}LaN_{10}O_{15}$ ([M-3H+La]$^-$) calc. (found): 1079.2 (1079.5); m/z for $C_{43}H_{43}La_2N_{10}O_{15}$ ([M-5H+2La]$^+$) calc. (found): 1217.1 (1217.5). M = compound **2.10**.

[Tb_n(3,4,3,3-(LI-1,2-HOPO))]$^{(3n-5)}$(**2.12**). $TbCl_3 \cdot 6H_2O$ (0.004 g, 0.011 mmol) was dissolved in 0.2 mL of CH_3OH and the solution was added dropwise to a solution of **2.10** (0.011 g, 0.012 mmol) in 0.8 mL of MeOH. A precipitate formed immediately after each drop leaving a bright yellow suspension. The reaction was mixed thoroughly with a vortex mixer at 1000 rpm for 2 min. The precipitate was separated by centrifuge and the pellet was washed with Et_2O (x3) and then air-dried on filter paper to give **2.12** as a beige solid (0.015 g). ESI-MS (CH_3OH) *m/z* for $C_{43}H_{44}TbN_{10}O_{15}$ ([M-3H+Tb]$^-$) calc. (found): 1099.2 (1079.6); m/z for $C_{43}H_{43}Tb_2N_{10}O_{15}$ ([M-5H+2Tb]$^+$) calc. (found): 1257.2 (1257.7). M = compound **2.10**.

2.4.4. UV-vis spectroscopy

Stock solutions at 10^{-3} M of ligand HOPO-O_{10} and HOPO-O_8 and the metal salts $La(ClO_4)_3 \cdot 6H_2O$, $TbCl_3 \cdot 6H_2O$ and $Th(NO_3)_4 \cdot 4H_2O$ were prepared in MilliQ H_2O. The molecular weight of HOPO-O_{10} was calculated according to the results of elemental analysis (1190.45 g/mol). The buffer solution was 0.1 M HEPES pH 7.4 and the ionic strength was adjusted with 0.1 M KCl. In situ complexation was studied by recording independent absorption spectra of increasing equivalents of the corresponding metal salt (0.5 – 3 eq, 15 – 90 µL) in a buffering solution containing 30 µL of HOPO-O_{10} or HOPO-O_8 stock solution (10^{-5} M final concentration) to a total final volume of 3000 µL. All experiments were performed at room temperature.

2.4.5. Isotope production and purification

Caution: ^{135}La, $^{155/161}$Tb, ^{225}Ac, ^{227}Th emit ionizing radiation and should only be handled in a facility designed in accordance with appropriate safety protocols.

2.4.5.1. General materials and methods

Natural barium (99.99% trace metals basis) dendritic pieces were purchased from Sigma Aldrich (St. Louis, MO, USA). Ultrapure nitric acid (Environmental grade) was purchased from VWR (Radnor, PA, USA) and Ultrapure HCl (TraceSE-LECT) was purchased from Fisher Scientific (Hampton, NH, USA). Branched DGA resin (50 – 100 μm) was purchased from Eichrom (Lisle, IL, USA). 4 mL polypropylene cartridges and 1/8″ polyethylene frits were purchased from United Chemical Technologies (Lewistown, PA, USA). Deionized water was produced on-site using a Millipore Direct-Q® 3UV water purification system. All radioactivity measurements for the purification of $^{132/135}$La from Ba targets were performed using gamma-ray spectroscopy on an N-type co-axial high purity germanium (HPGe) gamma spectrometer (Canberra Industries) calibrated with a 20 mL ^{152}Eu and ^{133}Ba source. Aliquots were removed and diluted to a 20 mL standard volume and measured at a distance of 15 cm from the detector until the uncertainty in the peak area was below 5%; for all measurements, the dead time was kept below 5%. Spectra were analyzed using the Genie 2000 software package (Version X, Canberra Industries) using the 464.55 and 567.14 keV gamma lines for ^{132}La measurement and 480.51, 587.83, and 874.51 keV gamma lines for ^{135}La measurement. The radioactive RP-HPLC system used to analyze the radiolabeling reactions consisted of a Phenomenex Luna C18(2) 100 ÅRP analytical column (5 μm,100 x 4.6 mm) using an Agilent S16HPLC equipped with a model 1200 quaternary pump, a model 1200 UV absorbance detector (set at 220nm) and a Raytest Gabi Star NaI(Tl) radiation detector. The thin layer chromatography (TLC) plates and instant TLC (iTLC) plates were measured on a BioScan 200 imaging scanner equipped with a BioScan Autochanger 1000 and WinScan software.

2.4.5.2. ^{135}La production and purification

Ba target manufacturing: Using a hydraulic press (Desktop pellet press, Across International, 4 MPa), 210-220 mg of natural barium was pressed into a pellet with a 10 mm diameter using a 10 mm die set and then pressed into an aluminum backing (4 MPa). The aluminum backing (6082 alloy) used to hold the barium was 1.6 mm thick and 28 mm in diameter with a centred 10 mm indent (0.55 mm depth). The thickness of the backing was chosen to completely stop the proton beam. Target manufacturing was performed rapidly due to the air-sensitive nature of metallic barium. To test the structural integrity of the target, it was dropped onto the floor from a height of 1.5 m and inspected for signs of damage before being vacuum sealed and immediately installed on TRIUMF's TR13 (13 MeV) cyclotron.

Ba target irradiation: The target was installed into a solid target holder[276] and during irradiation, the target was cooled with water at the back and with helium at the front. The 13 MeV protons were degraded to approximately 12.8 MeV using a 25 μm-thick aluminum foil to separate the target system from the vacuum of the cyclotron. Irradiation was performed at 10 μA for 2-4 h and after irradiation, the target was left in the holder for 1.5 hours to allow for the decay of short-lived ^{130}La ($t_{1/2}$ = 8.7 min), ^{134}La ($t_{1/2}$ = 6.5 min), ^{136}La ($t_{1/2}$ = 9.9 min), and ^{137m}Ba ($t_{1/2}$ = 2.6 min) to reduce radiation exposure. With a proton energy of 12.8 MeV, ^{135}La was produced via the ^{135}Ba(p,n)^{135}La and ^{136}Ba(p,2n)^{135}La reaction and ^{132}La was produced via the ^{132}Ba(p,n)^{132}La reaction.[113,277]

Separation of $^{132/135}$La: The method utilized to separate $^{132/135}$La from the Ba target was based on methods in literature,[278] with modification to the HCl concentration used to elute the $^{132/135}$La. The irradiated target was placed in a beaker and the barium dissolved using 5 mL of MilliQ water. After dissolution, the aluminum backing was removed and rinsed with an additional 5 mL of water. 10 mL of 6 M HNO_3 was added to aid in Ba dissolution to bring the final solution concentration of HNO_3 to 3 M. A 4 mL polypropylene cartridge was packed with 250 mg of branched DGA resin and immediately prior to use, the column was conditioned with 15 mL of MilliQ water and 15 mL of 3 M HNO_3. The target solution was loaded onto the column by gravity and then washed with 50 mL of 3 M HNO_3, followed by 5 mL of 0.5 M HNO_3, to remove residual Ba. The $^{132/135}$La was then eluted with 2 mL of 0.01 M HCl at 1 mL/min. The yield and radionuclide purity of $^{132/135}$La was assessed using gamma spectroscopy.

2.4.5.3. ^{155}Tb production and purification

^{155}Tb was collected at TRIUMF's ISAC (Isotope Separator and Accelerator) implantation station using the reported method.[278] Briefly, the 0.14 mol/cm^2 tantalum metal foil target was irradiated with a 480 MeV p^+ beam. The isotopes produced through spallation reactions are extracted as an ion beam and accelerated subsequently up to 30 keV. Mass over charge ratio 155, which mainly contains isobars of Er^+, Ho^+, Dy^+, and Tb^+, was separated and collected at the ISAC implantation station. A 5-day cool down period was required to let most precursor isotope decay into ^{155}Tb. The isotopes were implanted into an ammonium chloride salt layer, which was dissolved in water and used without purification.

2.4.5.4. ^{161}Tb production and purification

^{161}Tb was obtained pure in the form of [^{161}Tb]$TbCl_3$ from SCK CEN (Belgium) and used without further purification.[269]

2.4.5.5. ^{225}Ac production and purification

^{225}Ac was produced via the spallation of thorium on TRIUMF's 500 MeV cyclotron and isolated as previously described.[93]

2.4.5.6. ^{227}Th production and purification

^{227}Th was purified from ^{227}Ac after reaching secular equilibrium. ^{227}Ac was produced from thorium spallation and subsequent purification.[93] After ^{225}Ac was decayed, ^{227}Ac in 36 mL 4 M HNO_3 was loaded on a DGA column (100 mg) and eluted with 1.5 mL H_2O to reduce the volume. The eluent from DGA resin was mixed with 1.5 mL of 8 M HNO_3 and loaded on a UTEVA resin (400 mg). After washing with 1 mL of 4 M HNO_3, ^{227}Th was eluted with 0.05 M HCl and used as is.

2.4.6. Radiolabeling studies

Stock solutions of HOPO-O_8 and HOPO-O_{10} (10^{-3} M) were prepared in deionized H_2O and diluted to give serial dilutions (10^{-4}, 10^{-5}, and 10^{-6} M) suitable for radiolabeling. A 5 µL aliquot of each chelate stock solution was added to an Eppendorf tube containing buffer (0.5 M NH_4OAc, pH 6) such that the final volume was 50 µL after the addition of [$^{132/135}$La]$LaCl_3$ (500 kBq), [^{225}Ac]$Ac(NO_3)_3$ (100 kBq), [^{155}Tb]$TbCl_3$ (80 kBq) to give final ligand concentrations of 10^{-4} M to 10^{-7} M for each sample (n = 3). For [^{227}Th]$Th(NO_3)_2$ (1 kBq) radiolabeling experiments, the same procedure was followed with small modifications in the buffer solution (0.5 M NH_4OAc pH 5) and in the number of replicates due to the low isotope availability (n = 2). Each concentration-dependent study included a negative control containing only the corresponding radioisotope solution and the reaction buffer. The reactions were allowed to radiolabel at room temperature or 85 °C and monitored at

15 min (^{135}La, ^{225}Ac, $^{155/161}$Tb, and ^{227}Th) and 1 h ($^{155/161}$Tb and ^{227}Th) only for the highest concentration. The $^{155/161}$Tb reaction progress was monitored by spotting (1-10 µL) aliquots on silicic acid (SA) impregnated iTLC plates and developed using an EDTA solution (50 mM, pH 7). ^{227}Th reactions were monitored by spotting 10 µL aliquots on aluminum backing silica gel 60 (SG F_{254}) TLC plates and developed in citric acid (0.4 M, pH 4). The radiochemical yields (RCYs) of $^{155/161}$Tb experiments were analyzed using radio-TLC by integrating the peaks in the radio-chromatogram. Under these conditions, uncomplexed $^{155/161}$Tb travels up to the solvent front (R_f = 1) and the complexed $^{155/161}$Tb stays halfway up the plate (R_f = 0.5). In the case of ^{227}Th, the TLC plates were cut in half and counted individually on an HPGe γ-spectrometer using the 235.96 keV (12.9%), 256.23 keV (7.0%), and 329.85 keV (2.9%) γ lines to quantify ^{227}Th. Under these conditions, uncomplexed ^{227}Th travels up to the solvent front (R_f = 1) and the complexed ^{227}Th sticks to the bottom plate (R_f = 0.). The reaction progress of the ^{135}La and ^{225}Ac reactions was analyzed by analytical radio-RP-HPLC (gradient: A: 0.1% TFA in H_2O, B: 0.1% TFA in CH_3CN; 0-10 min: 5-70% B, 10-10.5 min: 70-95% B, 10.5-12 min: 95% B, 12-12.5 min: 95-5% B, 12.5-15 min: 5% B, flow rate: 1 mL/min). Under these conditions, the uncomplexed radioisotope elutes at the solvent front (<1 min) and the ^{135}La complexes elute at minute 3.68 and the ^{225}Ac complexes between minutes 3.76-4.97. The RCYs of the ^{135}La were calculated by integrating the peaks in the radio-chromatogram. To calculate the RCYs of the ^{225}Ac reactions, each radio-chromatogram peak was collected in a separate fraction and measured in a γ-spectrometer after 6 h to allow ^{225}Ac and ^{213}Bi to reach secular equilibrium. The ^{213}Bi and ^{221}Fr content were quantified using the 440.5 keV (25.9%) and 218.0 keV (11.4%) γ lines, respectively.

2.4.7. Human serum stability challenge

$^{155/161}$Tb complexes: Pre-formed [^{155}Tb]Tb-HOPO-O_8 and [^{155}Tb]Tb-HOPO-O_{10} complexes (100 kBq, RCY >99%) or unchelated $^{155/161}$Tb in the radiolabeling buffer solution as control were incubated in human serum in a 1:1 mixture at 37 °C over 5 days. The solutions were monitored on days 1, 3, and 5 using aluminum backing SiO_2 TLC plates. A 5 µL aliquot of the reaction mixture was diluted with 5 µL of citric acid (0.4 M, pH 4), spotted on SiO_2 TLC plates, and developed in citric acid (0.4 M, pH 4).

^{227}Th complexes: Pre-formed [^{227}Th]Th-HOPO-O_8 and [^{227}Th]Th-HOPO-O_{10} complexes (3 kBq, RCY >99%) or unchelated ^{227}Th in the radiolabeling buffer solution as control were incubated in human serum in a 1:1 mixture at 37 °C over 14 days. The solutions were monitored on days 1, 7, 11, and 14 by first quenching 5 µL of the reaction mixture with 5 µL of citric acid (0.4 M, pH 4), spotting the 10 µL on an aluminum backing SiO_2 TLC plate, and developing them in citric acid (0.4 M, pH 4).

All serum stability experiments were performed in triplicates. Percent in-tact radiometal complex was calculated by integrating the peaks in the radio-chromatogram as described in section 2.4.6.

2.4.8. Maximum apparent molar activity (A_m) and specific activity (A_s) measurements

<u>$^{155/161}$Tb complexes:</u> A 0.5-1 µL aliquot of a 10^{-4} M stock solution of HOPO-O_8 and HOPO-O_{10} was added to increasing amounts of ^{161}Tb to obtain 3.8-4.8 MBq/reaction and the total volume was adjusted with buffer (0.5 M NH_4OAc pH 5) to 5 µL. The reactions were kept at room temperature and monitored after 15 min as described in section 2.4.6.

<u>^{227}Th complexes:</u> A 5 µL aliquot of 10^{-4} M stock solutions of HOPO-O_8 and HOPO-O_{10} was added to increasing amounts of ^{227}Th to obtain 3, 5, 8, and 10 kBq per reaction. The reaction volume was adjusted to 50 µL with buffer solution (0.5 M NH_4OAc, pH 5) and the reactions were allowed to react at room temperature for 15 min. The reactions were monitored and analyzed as described in section 2.4.6.

2.4.9. DFT calculations

To search for the most stable structures for complexes and ligands, GFN-xTB,[279] a semi-empirical tight-binding quantum chemical method, was used for conformational searches using the Molclus program.[280] Molecular dynamic (MD) simulations were utilized to provide a sufficient number of initial conformations of molecules, which were then classified into clusters based on their energy and bond length differences. After ranking by the program according to their energies, the structures of the lowest 10 in the ranking list were then further optimized using density functional theory (DFT) with the PBE-D3 functional,[281,282] a scalar relativistic zeroth-order regular approximation (ZORA) Hamiltonian,[283–286] and triple-ζ plus two polarization functions (TZ2P) Slater-type basis sets with the frozen core approximation applied to the inner shells [1s2−4f14] for actinium and thorium, [1s2-4d10] for lanthanum, europium, terbium and lutetium, [1s2] for carbon, nitrogen and oxygen, and all electrons for hydrogen. Since all structures were computed under aqueous conditions, the implicit solvation model conductor-like screening solvation model (COSMO)[287,288] was applied. Frequency calculations were performed to determine the thermodynamic properties (Gibbs free energy) of each structure and to verify that true minima on the potential energy surface have been found. Geometry optimizations were performed without imposing any symmetric constraints. Since parameters in the GFN-xTB method are only available for elements with atomic number Z = 1-86,[279] conformational searches for Ac and Th complexes were not performed. Based on the fact that La possesses similar properties with Ac, initial structures for Ac^{3+} and Th^{4+} complexing with $[3,4,3,3\text{-LI}(1,2\text{-HOPO})]^{5-}$ that were input to DFT calculation were obtained by substituting La^{3+} with Ac^{3+} and Th^{4+} in the lowest energy structure of $[La\text{-}3,4,3,3\text{-LI}(1,2\text{-HOPO})]^{2-}$. As for the initial structures for Ac^{3+} and Th^{4+} complexing with $[3,4,3\text{-LI}(1,2\text{-HOPO})]^{4-}$, the optimized structures by Kelly et al.[268] at the PBE0/TZ2P level of theory were used. A pressure of 1354 atm, which simulates the experimental density of liquid water for the ideal water gas at 298 K, was used in free energy calculations of water for translational entropy correction.[289,290] To get further insight into the nature of bonding between the An/Ln ions and the coordinating O atoms in the complexes, the EDA[272,291] and charge transfer analysis VDD and Hirshfeld[292] charge analysis methods) were carried out. The calculations were performed using the Amsterdam Density Functional package (ADF 2017).[293]

Chapter 3.

1,2-HOPO and catechol-based tripodal acyclic chelates for ^{45}Ti, ^{47}Sc, and ^{68}Ga radiopharmaceuticals

3.1. Introduction

Radiopharmaceutical imaging plays a vital role in the clinical assessment and treatment monitoring of patients in oncology. Contrast-enhanced CT and MRI are standard imaging techniques used in clinical routing to identify and monitor cancer progression.[294] However, these morphological techniques only offer limited information and result in insufficiencies in answering diagnostic questions at a molecular level. In this context, SPECT and PET are essential nuclear imaging techniques for the management of patients with cancer to provide them with personalized treatments.[295–297]

SPECT imaging requires radionuclides that emit low energy gamma (γ)-rays (70-400 keV) compared to PET imaging which is based on isotopes that decay by emitting a positron (β+) that subsequently annihilates with an electron to produce two 511 keV photons at 180°. SPECT is currently a workhorse in clinical nuclear medicine due to its lower cost per scan despite being less flexible and having a lower sensitivity than PET.[2,298] Therefore, there is a growing interest in developing novel PET isotopes and radiopharmaceuticals to make them more readily available for clinical routine.

Nowadays, the halogen radioisotope ^{18}F ($t_{1/2}$ = 109.8 min, $E(\beta^+_{avg})$ = 250 keV, I = 97%) is the leading isotope for PET imaging with the radiotracer [^{18}F]-FDG, a glucose analogue, being the gold standard of PET radiopharmaceuticals. Other routine radioisotopes include the radiometal ^{68}Ga ($t_{1/2}$ = 67.7 min, $E(\beta^+_{avg})$ = 830 keV, I = 89%) in [^{68}Ga]Ga-DOTATATE or [^{68}Ga]Ga-DOTATOC or ^{64}Cu ($t_{1/2}$ = 12.7 h, $E(\beta^+_{avg})$ = 278 keV, I = 18%) in [^{64}Cu]Cu-DOTATATE for imaging of somatostatin receptor positive neuroendocrine tumours NETs.

Gallium exists in the 3+ oxidation state in aqueous solution and its preferred coordination number is six (0.62 Å).[68] Its close chemistry to Fe^{3+} requires chelates that are highly stable in vivo to prevent its demetallation and transchelation to iron-containing biomolecules such as transferrin.[299] Another challenge associated with the labeling of ^{68}Ga is the propensity to form hydroxide species at low pH demanding chelates with high kinetic inertness and thermodynamic stability from acidic to biologically relevant pH values. Clinically approved ^{68}Ga radiopharmaceuticals employ the widely used DOTA which requires harsh labeling conditions compatible only with peptide and small molecule drug constructs. A wide variety of alternative chelates have been developed to achieve high radiolabeling yields under mild conditions, some examples include NOTA and its derivatives,[300] AAZTA,[155] (see **Table 1.2**), H_2hox[301], DFO,[302,303] TREN-CAM [304] or HBED-CC (**Table 3.1**) which is probably the most clinically investigated acyclic chelate for ^{68}Ga.[305,306] An extensive review on the chelation of ^{68}Ga can be found elsewhere.[6]

Table 3.1. Chemical structures of the most relevant ^{68}Ga and ^{45}Ti chelates described in this chapter.

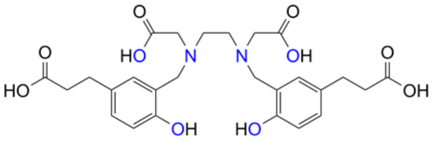 **HBED-CC** Ga^{3+}		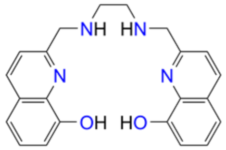 **H_2hox** Ga^{3+}
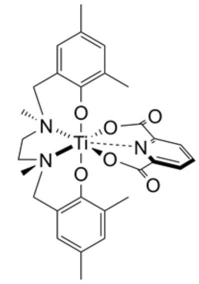 **[^{45}Ti](salan)Ti(dipic)** Ti^{4+}	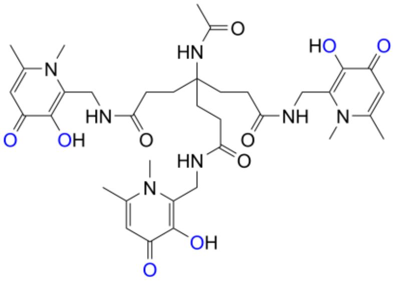 **THP^{Me}** Ti^{4+}	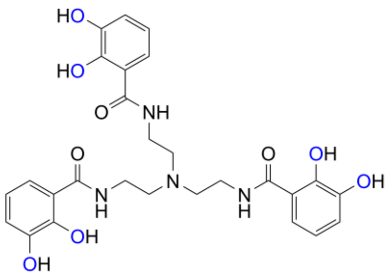 **TREN-CAM** Ga^{3+}, Ti^{4+}
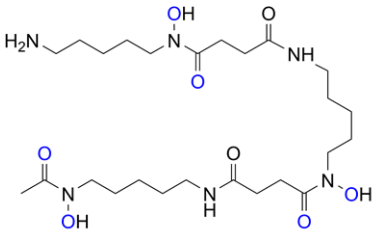 **DFO** Ga^{3+}, Ti^{4+}	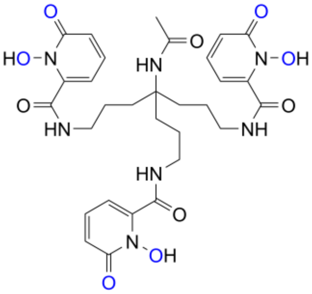 **HOPO-O$_6$-C4** This work	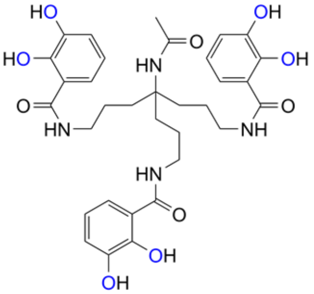 **CAM-O$_6$-C4** This work

Coordinating atoms labeled in blue.

Through the advancement in the production of medical radioisotopes, multiple novel radiometals are being investigated in preclinical and clinical studies to expand the properties of PET isotopes (e.g., longer half-lives, various mean β^+ ranges). Among the most promising radiometals are ^{45}Ti ($t_{1/2}$ = 3.08 h, E(β^+_{avg}) = 439 keV, I = 84%) and ^{44}Sc ($t_{1/2}$ = 3.97 h, E(β^+_{avg}) = 632 keV, I = 94%), see section 1.3.1 for the chemistry and chelates of interest for Sc^{3+}. The interest in ^{45}Ti lies on its slightly longer half-life than ^{68}Ga, a low mean β^+ energy, and a medical cyclotron production route using naturally monoisotopic scandium via proton bombardment through a ^{45}Sc(p,n)^{45}Ti reaction with high production yields.[307,308] The chemistry of Ti^{4+} (0.605 Å, CN = 6), like that of Ga^{3+}, resembles that of Fe^{3+} (0.645 Å, CN = 6) with similar ionic radii and preference to form hexacoordinate complexes.[68] Consequently, Ti^{4+} effectively binds to siderophores such as deferoxamine (DFO), transferrin or enterobactin.[309–312] However, the high charge density in Ti^{4+} results in H_2O instability due to extensive hydrolysis at a wide range of pH.[313]

In the medical field, Ti^{4+} complexes were first demonstrated three decades ago to exhibit antitumour activity against a variety of tumors and later on, ^{45}Ti radiolabeled complexes were used to attempt to elucidate the mechanism of action of the drugs.[314,315] In 2015, [^{45}Ti](salan)Ti(dipic) (**Table 3.1**) was used to study the biodistribution and pharmacokinetics of its antineoplastic non-radioactive analog. However, the radiopharmaceutical suffered from low in vivo stability with high liver, lung and spleen uptake and significant bone and blood uptake.[316] Recently, ^{45}Ti has been studied to radiolabel the highly promising prostate cancer targeting agent, PSMA.[317,318] Its feasibility was demonstrated using [^{45}Ti]Ti-DFO-DUPA which exhibited high tumor uptake and improved in vivo stability. However, lung (10%ID/g) and blood (~1%ID/g) uptake could still hint at possible decomplexation.[318] In 2022, Koller et al. performed an in-depth study of the thermodynamics of multiple bidentate ligands and identified catechol and deferiprone ligands to have the most favourable properties to bind Ti^{4+}.[313] TREN-CAM and THP^{Me} are two known hexadentate chelates that incorporate catechol amide (CAM) and deferiprone moieties, respectively, that have been evaluated for ^{68}Ga radiopharmaceuticals. Both chelates were selected for ^{45}Ti radiolabeling and the complexes were evaluated in vivo. Despite identical kinetic inertness in mouse serum (>96% intact after 6 hours), [^{45}Ti]Ti-TREN-CAM outperformed [^{45}Ti]Ti-THP^{Me} in vivo with no indication of $^{45}Ti^{4+}$ decomplexation after 1 hour. This work provides excellent insight into the thermodynamics of Ti^{4+}

complexes setting the bases for the future development of kinetically inert ^{45}Ti chelates for biomedical imaging applications.

Inspired by the enhanced stability of catechol moieties for the formation of $^{45}Ti^{4+}$ hexadentate chelates and the successful stable coordination of $^{44}Sc^{3+}$ with HOPO-O_8, we sought to investigate two tripodal hexadentate chelates bearing catechol or 1,2-HOPO pendant arms to expand the library of ^{45}Ti and $^{44/47}$Sc chelates for the development of radiotracers. In particular, we aim to design, synthesize, and characterize chelates that can meet the requirements of the ideal bifunctional chelate (section 1.1.1.1) with easy conjugation to a disease targeting vector. Despite the high radiolabeling affinity of TREN-CAM with ^{68}Ga and ^{45}Ti, its incorporation into radiopharmaceuticals remains challenging due to the synthetic complexity of bifunctionalizing the TREN backbone.[304,313] Keeping its structure in mind, we chose a tripodal backbone developed by Ji et al. as a tris-catecholate siderophore conjugated to ampicillin and amoxicillin to target antibiotic-resistant Gram-negative bacteria.[319] This backbone contains three aliphatic carbons instead of two and offers an easy conjugation site through a versatile amine functional group as in THP^{Me}. We hypothesized that the larger backbone size would accommodate larger metals such as Sc^{3+} but still maintain a high binding affinity for Ti^{4+} as it did with Fe^{3+}.

In this chapter, we present the synthesis and characterization of two novel tripodal chelates, HOPO-O_6-C4 and CAM-O_6-C4. The thermodynamic and kinetic properties of the Sc^{3+} and Ga^{3+} complexes of HOPO-O_6-C4 and CAM-O_6-C4 and their radiolabeling affinities with ^{45}Ti and ^{47}Sc will be explored to assess their potential for TRT. Structural optimization of the corresponding chelates and complexes by DFT is presented as well to complement the experimental data and gain more insight into the structure geometries.

3.2. Results and discussion

3.2.1. Chelate synthesis

The ligand synthesis of HOPO-O_6-C4 and CAM-O_6-C4 involves the synthesis of the tripodal backbone following a reported procedure and the installation of three 1,2-HOPO or CAM pendant arms with a total of 6 steps for each chelate (**Scheme 3.1**). The synthesis of the backbone starts from tris(2-cyanoethyl)nitromethane to obtain intermediate **3.1** following a 2-step procedure described in literature.[319] At this point, the literature procedure functionalizes the backbone with methyl succinyl chloride to later access a carboxylic acid for conjugation. However, for the scope of this work to screen the radiolabeling properties with different metals, we opted to cap the amine group with an acetamide which would readily be substituted with any bifunctional handle (e.g., *p*-benzyl-SCN or maleimide) and subsequently conjugated to a targeting vector. The capping was achieved using acetyl chloride and intermediate **3.2** was deprotected under mild acidic conditions to obtain the backbone **3.3** in the form of an HCl salt.

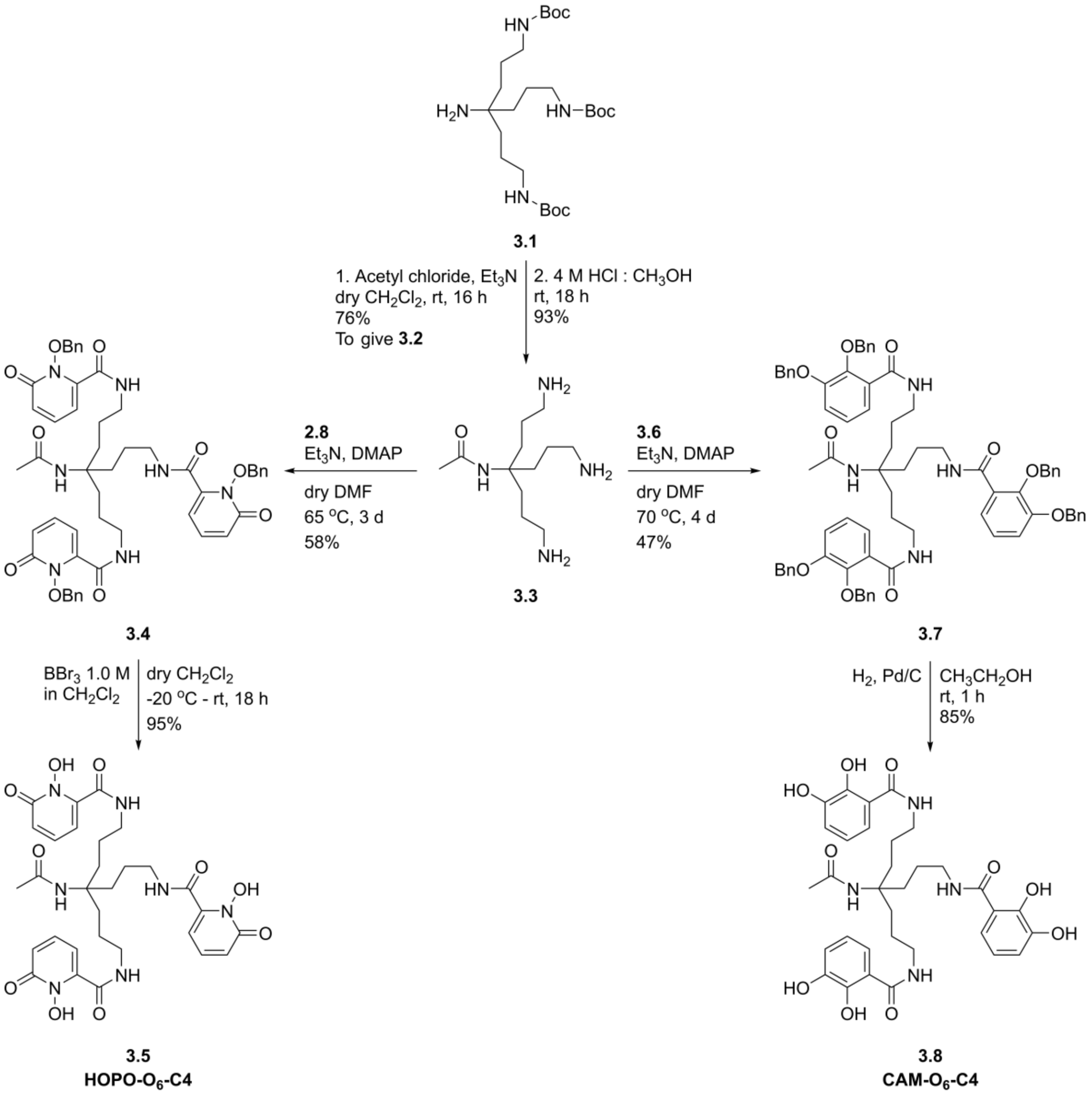

Scheme 3.1. Synthetic route developed for the synthesis of HOPO-O$_6$-C4 and CAM-O$_6$-C4.

The addition of the activated pendant arms proceeded under the same conditions for both chelates following the conditions previously reported in chapter 2 (section 2.2.1). The NHS-activated 1,2-HOPO **2.8** was conjugated to the three primary amines via amide coupling to give compound **3.4**. Obtaining the chelate precursor **3.4** highly pure is key to avoiding the HPLC purification of the final product after deprotection with the mild Lewis acid BBr_3. As the deprotection reaction proceeded, a precipitate was formed which was washed with acetone and diethyl ether to give the final ligand HOPO-O_6-C4 (**3.5**). Similarly, we opted to activate the acid of the benzyl-protected catechol intermediate with an NHS to form **3.6**. The coupling of this pendant arm to the backbone required longer reaction times than the 1,2-HOPO probably due to the bulkiness of two benzyl groups. After obtaining **3.7** in high purity, the compound was transformed into the final product CAM-O_6-C4 (**3.8**) via palladium-catalyzed hydrogenation in high yield (85%). CAM-O_6-C4 was obtained as a purple solid and stored at -20 °C to prevent catechol oxidation.

3.2.2. Proton equilibria of the chelates

The protonation constants of HOPO-O_6-C4 were studied in aqueous solution by ^{1}H NMR spectroscopy at 25 °C and ionic strength (*I*) equal to 0.1 M KCl. The spectra also reveal important information about the dynamics of the equilibrium and its structural properties. The ligand protonation constants are listed in **Table 3.2** and the ^{1}H NMR spectra and the ^{1}H chemical shift variation as a function of pH are shown in **Figure 3.1A**. The spectra at pH 2.02 and 10.11 are identical to pH 3.07 and 9.33, correspondingly, and were removed for clarity.

Table 3.2. Ligand protonation constants

Ligand	Ligand Protonations $\log\beta_{011}$, $\log\beta_{012}$
HOPO-O_6-C4	5.11 ± 0.05
CAM-O_6-C4	-
1,2-HOPO	5.75 ± 0.04[a]
Catechol	13, 22.44 ± 0.03[a]

[a]Ref[313]

The proton assignments are indicated by the letters a-i in **Figure 3.1B**. In HOPO-O_6-C4, the aromatic protons (a-b) at 7.65-6.60 ppm are the signals that experience a chemical shift with the pH variations as they are close to the protonation sites compared to the aliphatic protons (e-g) and the methyl from the acetamide (i) which shift only 0.02 ppm. The *ortho* and *meta* proton positions (b, c) experience minor chemical shifts since they are not involved in the hydrogen bond network formed by O_1, O_2, N_1 and N_2 (**Figure 3.2**). In contrast, the *para* hydrogen atom (a) resonates downfield as the pH increases with a significant shift of ~ 0.4 ppm as this position is the closest to O_2 which loses its contribution to the hydrogen network upon deprotonation. This behaviour has been reported before with the similar chelate 1,2-HOPO-TREN.[320] Another noticeable change in the spectra occurs between pH 3-5 with the disappearance of the 1,2-HOPO amide proton (d) signal at 9-9.3 ppm. Due to the high basicity of amide protons and the absence of shifting in proton (e), we hypothesize that the absence of the signal above pH 5 is a result of the faster exchange rate with the solvent as the concentration of hydroxide anions increases. This effect also results in a multiplicity change in the neighbouring proton (e) from a triplet of doublets to a triplet. This exchange is not quantifiable since the proton signal only integrates for two protons at pH 3 indicating some degree of exchange is already occurring.

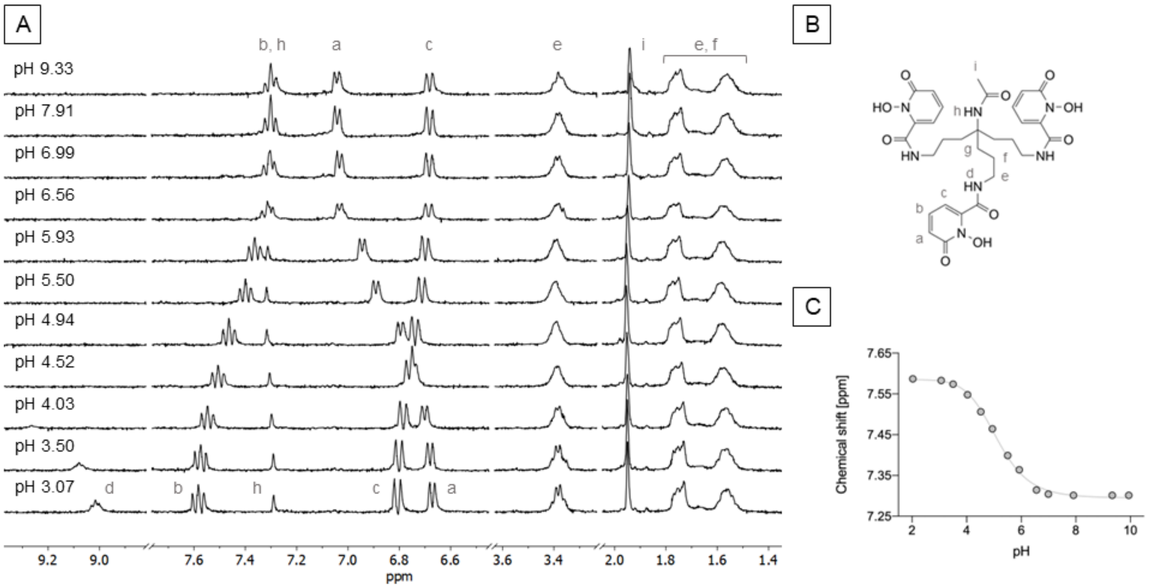

Figure 3.1. HOPO-O$_6$-C4 characterization. (A) Variable pH - ^{1}H NMR spectra (400 MHz, 90% H_2O + 10% D_2O, 298 K, 1 mM), (B) chemical structure with labels for NMR peak assignment, (C) Representative ^{1}H NMR titration curves and corresponding fitting lines.

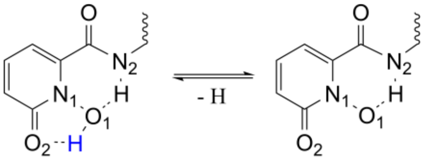

Figure 3.2. Changes associated with the hydrogen bond network with the deprotonation of HOPO-O_6-C4.

To calculate the pK_a from the experimental data, the triplet signal in the aromatic region was chosen and the chemical shift was plotted as a function of pH (**Figure 3.1C**). HOPO-O_6-C4 possesses seven ionizable protons, three N-hydroxy and four amide protons; however, only the former protons will ionize in a relevant pH range (2-10) for these studies and the latter would possess highly basic acidity constants. Due to the high degree of symmetry, only one pK_a was determined for HOPO-O_6-C4 to be 5.11 ± 0.05. These values are in agreement with those reported in literature for the corresponding bidentate ligands 1,2-HOPO and CAM determined by UV-vis spectroscopy and potentiometric titrations.[313]

Attempts to study the protonation constants of CAM-O_6-C4 by ^{1}H NMR spectroscopy following the same protocol as in HOPO-O_6-C4 proved unsuccessful. The chelate exhibits poor water solubility at 1 mM concentration at low and high pH values (<4 and >12). Additionally, adjusting the pH in the neutral region was complex with difficulties reaching stable pH values. Thus, ^{1}H NMR spectroscopy is not a suitable technique to study the pK_a values of CAM-O_6-C4. The unstable pH issues could be overcome by using potentiometry which conducts the measurements in a cell under inert conditions removing the CO_2 gas which can sometimes be the cause of pH drifting or by UV-vis spectroscopy with a 24 h sample equilibration period before measurement to ensure thermodynamic equilibrium is reached. Moreover, the two techniques work in the sub-millimolar concentration range.

3.2.3. Sc^{3+} and Ga^{3+} complex characterization

The complex formation of HOPO-O_6-C4 and CAM-O_6-C4 with Sc^{3+} was studied in aqueous solution at 25 °C by ^{1}H NMR spectroscopy similar to the protonation studies. The corresponding Ti^{4+} complexes were not studied in this chapter since Koller et al. recently characterized the thermodynamics of 1,2-HOPO and CAM with Ti^{4+}.[313] The former was identified to only coordinate Ti^{4+} at acidic pH ranges and thus not interesting for radiopharmaceutical applications which require radiolabeling to occur at pH 4-8. The latter was found to form highly stable Ti^{4+} complexes up to pH 9 and oxidize at higher pH values. TREN-CAM (**Table 3.1**) was studied as the CAM hexadentate analog with the formation of an unhydrolyzed 1:1 species at physiological pH and a pM (Ti^{4+}) = 10.01.

The ^{1}H NMR spectra of the aqueous solutions of Sc^{3+} and HOPO-O_6-C4 at equimolar concentrations were recorded at pH 2 and 5 to investigate the stability and speciation of the system. Higher pH values could not be recorded due to the low solubility of the complex above pH 6.5. As shown in **Figure 3.3**, significant spectral changes occur immediately at both pH values after the addition of Sc^{3+} observed by the broadening of both the aromatic and aliphatic regions indicating fast complexation kinetics. The samples were further measured over 72 h with no spectral changes suggesting the complex is highly stable since it formed at low pH and is stable over time. Additionally, in an attempt to gain more insight into the speciation, variable temperature (VT) ^{1}H NMR was performed between 25-46 °C. No significant shifts were observed as the temperature increased. Due to the complexity of the spectra, the determination of the speciation was not possible. We hypothesize the peak broadness could indicate the presence of multiple stable conformers that do not exchange with small temperature changes.

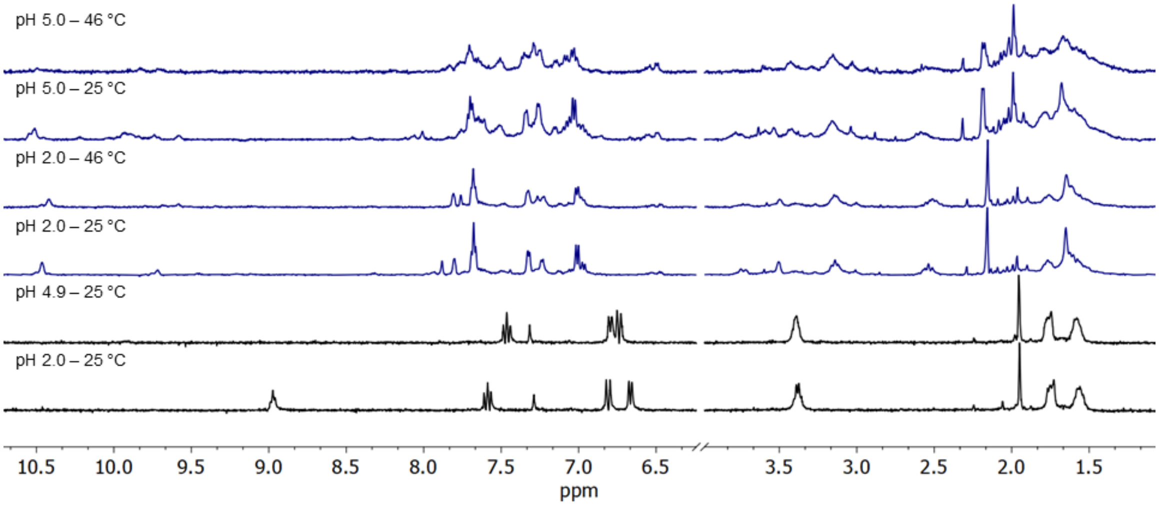

Figure 3.3. Variable pH and T - ^{1}H NMR spectra of Sc^{3+} and HOPO-O_6-C4 (blue) and HOPO-O_6-C4 (black) (400 MHz, 90% H_2O + 10% D_2O, 1 mM).

Similar complexation experiments were performed with Ga^{3+}. The variable ^{1}H NMR spectra at pH 2.0, 5.0 and 7.9 are reported in **Figure 3.4**. Comparison between the free ligand spectra and the Ga^{3+}-chelate undoubtedly demonstrated the complexation as significant changes in the chemical shift are recognizable. Interestingly, the proton amide peaks from 1,2-HOPO are still visible at pH 5 and the acetamide proton signal remains as in the ligand. The sharpness of the signals and the absence of multiple patterns in the complexation indicate the formation of a single Ga-HOPO-O_6-C4 species with fast reaction kinetics. However, at pH 7.9 a broad multiplet between 7.4-7.6 ppm could indicate the formation of a new species. The stability of the complexes was studied over 48 h with no spectral changes suggesting that the complex is thermodynamically stable in aqueous media in the range of pH 2-8.

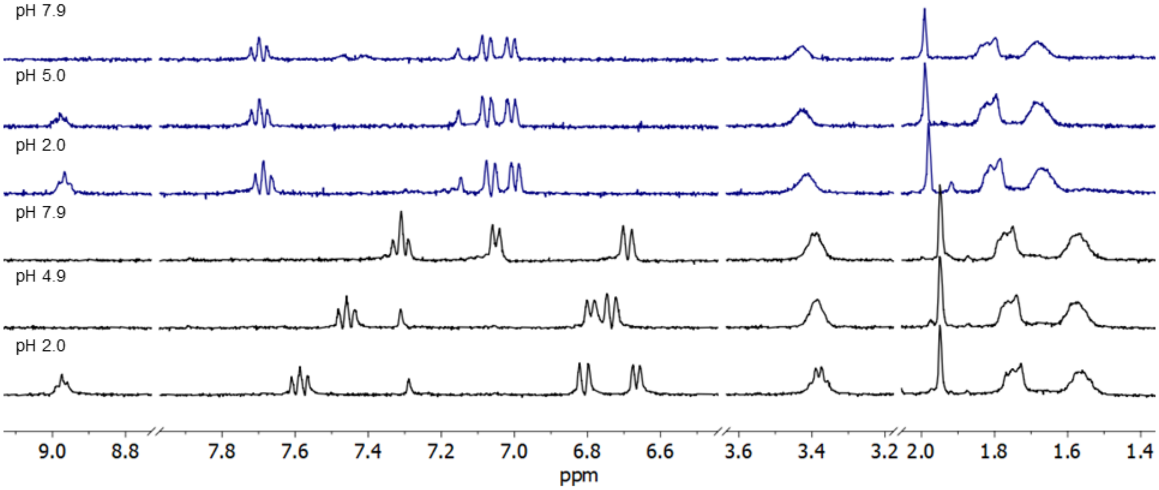

Figure 3.4. Variable pH - ^{1}H NMR spectra of Ga^{3+} and HOPO-O_6-C4 (blue) and HOPO-O_6-C4 (black) of (400 MHz, 90% H_2O + 10% D_2O, 298 K, 1 mM).

Based on the difficulties encountered in the pKa calculations, CAM-O_6-C4 stability studies in aqueous media were performed before investigating the complexation with Sc^{3+} and Ga^{3+}. ^{1}H NMR spectroscopy revealed low sample stability at room temperature observed in the disappearance of all compound peaks in the spectrum after 12 h (Appendix, Figure A.3). At this point, it is not clear whether the sample decomposes, or it oxidizes, as no precipitate was observed in the sample after 12 h. The aqueous instability suggests CAM-O_6-C4 is not ideal for radiopharmaceutical applications. However, we still attempted to investigate the complexation with Sc^{3+} and Ga^{3+}. Attempts to form the corresponding complexes by precipitation in aqueous media or in situ in DMSO-d_6 failed and no species was observed by ^{1}H NMR or MS. The free ligand could not be detected either. Further experiments are needed to understand the behaviour of CAM-O_6-C4.

Ti^{4+} complexation studies were not conducted due to the complexity of preparing $TiCl_4$ solutions with an exact concentration which requires quantification by inductively coupled plasma (ICP). Instead, we collaborated with the Boros group, who recently published a comprehensive study on the coordination of Ti^{4+} (see introduction), to evaluate only CAM-O_6-C4 since a mismatch of 1,2-HOPO for Ti^{4+} chelation under biologically relevant conditions was anticipated.[313] Similar ligand protonation constants were expected between CAM-O_6-C4 and TREN-CAM due to their almost analogous structures. This parallelism could not be applied to the thermodynamic stability constants because the larger backbone significantly affects the binding cavity of CAM-O_6-C4. Due to isotope availability, the Ti-CAM-O_6-C4 complex was only characterized by LC-MS before the radiolabeling studies. The complexation between equimolar amounts of CAM-O_6-C4 and Ti^{4+} in methanol occurred immediately and it was observed by a solution colour change to yellow. The LC trace of the solution indicated the formation of one major Ti-CAM-O_6-C4 species with the corresponding molecular weight confirming the fast kinetics of the complex formation (Appendix, Figure A.4).

3.2.4. Radiolabeling

Due to a cyclotron shutdown at TRIUMF, the ^{47}Sc and ^{45}Ti radiolabeling experiments were performed by our collaborators at the University of Alabama and the University of Madison-Wisconsin, respectively. $^{68}Ga^{3+}$ radiolabeling will be performed at TRIUMF when the $^{68}Ge/^{68}Ga$ generator becomes available.

Based on the characterization of the non-radioactive Sc^{3+} and Ti^{4+} complexes, the next step was to assess the radiolabeling properties of HOPO-O_6-C4 and CAM-O_6-C4 with the β^--emitter ^{47}Sc and the β^+-emitter ^{45}Ti, respectively, at low radiometal concentrations (picomolar range).

Concentration-dependant radiolabeling experiments with ^{47}Sc (~ 800 kBq) were performed in 0.25 M NH_4OAc pH 4 at 37 °C and monitored after 30 min. HOPO-O_6-C4 was able to quantitatively chelate ^{47}Sc at 37 °C at an apparent A_m of 1565 ± 17 MBq/μmol, clearly outperforming the widely used DOTA chelate which requires high temperatures to quantitatively radiolabel ^{47}Sc. HOPO-O_6-C4 also seems to have a higher affinity for ^{47}Sc compared to the octadentate HOPO-O_8 with an A_m of 236.8 MBq/μmol under the same conditions except for the pH which was adjusted to 8.[158]

^{45}Ti radiolabeling studies were conducted with 460 kBq of [^{45}Ti]Ti-citrate in 0.5 M HEPES buffer at 20 °C and monitored after 15-60 min based on the optimization results of TREN-CAM. RCY analysis by iTLC reveled the formation of multiple species streaking on the plate making the quantification complicated. Radio-HPLC was used to confirm the RCY. **Figure 3.5** shows an overlap of the radioactive trace (blue spectrum) and the corresponding UV trace (black spectra). The absence of a peak at the solvent front of the radioactive trace demonstrates that all ^{45}Ti has been complexed and the first two UV active peaks are suspected to be unchelated CAM-O_6-C4 and a Fe-CAM-O_6-C4 complex formed with residual Fe^{3+} in the system. However, the peaks associated with [^{45}Ti]Ti-CAM-O_6-C4 indicate the formation of one major species accompanied by multiple minor species, confirming the data observed by iTLC. In general, radioactive complexes form one discrete complex species at such low metal concentrations (pm-nm), as in the case of [^{45}Ti]Ti-TREN-CAM (Appendix, Figure A.5). The presence of more than one discrete species is problematic because the identification of the species in not possible with the available techniques and calculations of the A_m or stability would not be accurate. Moreover, this behaviour could also be an indication of a high degree of instability of some of the minor species in vivo prompting metal transchelation. Thus, CAM-O_6-C4 was found not suitable for radiopharmaceutical development.

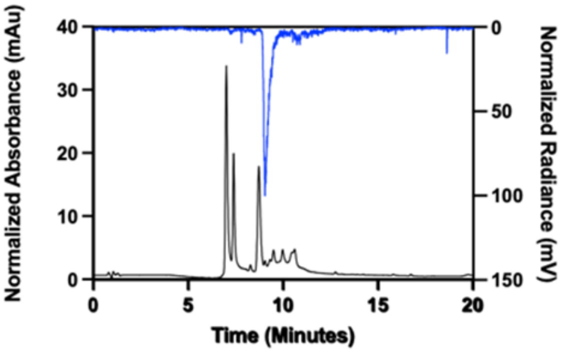

Figure 3.5. HPLC characterization of [^{45}Ti]Ti-CAM-O_6-C4. The black trace corresponds to the UV profile and the blue to the radioactive measurement.

3.2.5. Stability

Since kinetic inertness plays a crucial role in the development of radiopharmaceuticals, a variety of stability assays can be performed before the preclinical evaluation to predict the likelihood of demetallation in vivo. In this case, preformed

[^{47}Sc]Sc-HOPO-O_6-C4 complexes were incubated in an excess of four metal ions (Fe^{3+}, Cu^{2+}, Mg^{2+}, Zn^{2+}) that can compete in vivo and promote transmetallation as well as human and mouse serum to investigate the complex integrity against endogenous proteins (e.g., albumin) (**Figure 3.6**). As some degree of demetallation was expected to occur fast in the presence of metal excess, the stability of the complex was assessed in intervals of 15 min during the first hour and then analyzed every 24 h for a total of 7 days. **Figure 3.6** shows that [^{47}Sc]Sc-HOPO-O_6-C4 is highly unstable in the presence of Cu^{2+} with only 36% intact complex remaining after 1 h and moderately unstable against Fe^{3+} and Zn^{2+} with 62% and 72% intact complex, respectively. High stability over the first hour was observed against Mg^{2+} or human and mouse serum. However, over 1 day the radioactive complex was completely demetallated when incubated in human or mouse serum. All other metal ion challenge reactions resulted in a substantial decomplexation after 1 day as well with almost complete demetallation after 5 days. The highest stability was observed against Mg^{2+} with 65% intact complex after 7 days.

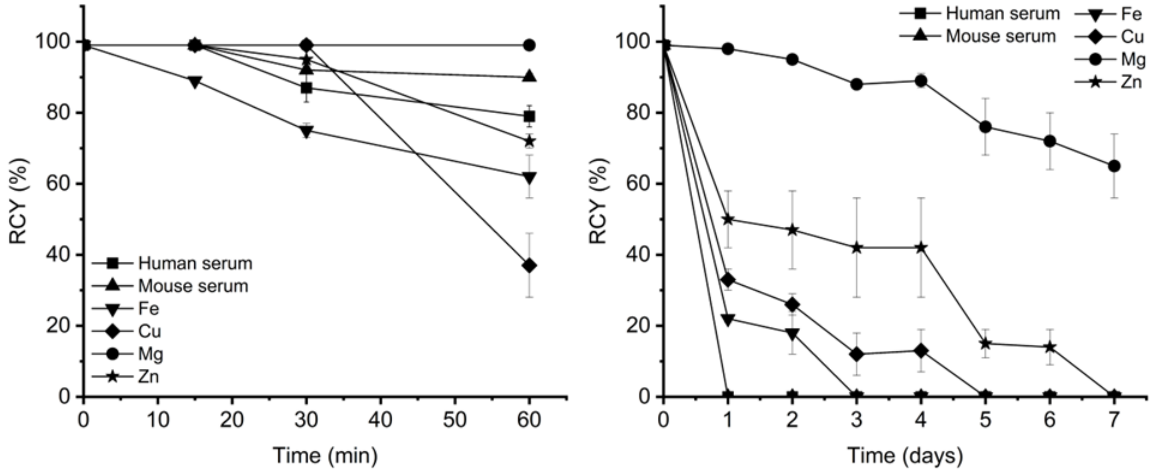

Figure 3.6. Stability studies of [^{47}Sc]Sc-HOPO-O_6-C4 in human serum (square), mouse serum (triangle), and 100 μM of Fe^{3+} (inverse triangle), Cu^{2+} (diamond), Mg^{2+} (circle), and Zn^{2+} (star) at various timepoints: 0-1 h (left) and 0-7 days (right) (n = 3).

An interesting comparison can be done with HOPO-O_8, one of the few chelates available for radioscandium (Appendix, Figure A.6).[158] [^{47}Sc]Sc-HOPO-O_6-C4 is remarkably more stable than [^{47}Sc]Sc-HOPO-O_8 in the metal ion challenge assay. [^{47}Sc]Sc-HOPO-O_8 failed to completely retain the radiometal against Fe^{2+} and Zn^{2+} and only 9.0 ± 7 % remained intact against Cu^{2+} after 1 day compared to [^{47}Sc]Sc-HOPO-O_6-C4 which showed 22.0 ± 0.8, 50.0 ± 7.8, and 33.0 ± 2.6 % RCY, respectively, after 1 day.

Similar complex stability against Mg^{2+} over 7 days was observed in both cases with 73.3 ± 21.5 and 65.0 ± 8.6 % of intact [^{47}Sc]Sc-HOPO-O_8 and [^{47}Sc]Sc-HOPO-O_6-C4, respectively. It is important to note that these stability challenge assays against excess metal ions occur under extreme conditions and do not represent the metal concentrations in biologically relevant media. Thus, despite the low kinetic inertness even in human serum, we decided to evaluate the stability of this compound in vivo in a biodistribution assay to probe its feasibility in a preclinical setup.

3.2.6. Biodistribution

Ex-vivo biodistribution analysis of [^{47}Sc]Sc-HOPO-O_6-C4 was conducted on healthy mice at 10, 30, 1 h and 24 h p.i. (n = 4) together with [^{47}Sc]$ScCl_3$ used as a negative control to understand where transchelated ^{47}Sc accumulates and how it is excreted from the body. **Figure 3.7** shows the biodistribution profile of [^{47}Sc]Sc-HOPO-O_6-C4 at four timepoints. The biodistribution analysis of [^{47}Sc]$ScCl_3$ can be found in the Appendix, Figure A.7.

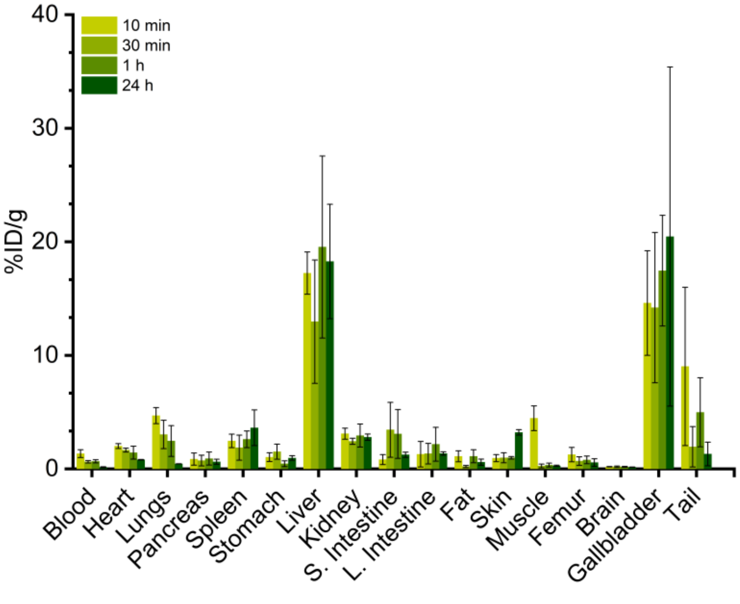

Figure 3.7. Ex vivo biodistribution studies of ~ 162 kBq of [^{47}Sc]Sc-HOPO-O_6-C4 in healthy mice at 10 min, 30 min, 1 h (n = 4), and 24 h (n = 3).

[^{47}Sc]Sc-HOPO-O_6-C4 exhibited a different distribution pattern than that of unchelated ^{47}Sc at 1 h with major accumulation in the liver (19.5 ± 8.0 %ID/g) and the gallbladder (17.4 ± 4.9 %ID/g) compared to the unchelated radiometal which has the highest activity concentration in the blood (8.8 ± 1.1 %ID/g), lungs (5.0 ± 1.3 %ID/g), and kidneys (4.7 ± 0.5 %ID/g) indicating early excretion via the renal system. The blood, heart and liver uptakes were compared in a t-test analysis revealing statistically significant values between the tracer and the unchelated radiometal (Appendix, Figure A.8). At 24 h, the tracer activity in the liver and kidneys remains constant although an increased activity is observed (20.5 ± 14.9 % ID/g). The ^{47}Sc activity is concentrated in the intestines and liver indicating uptake and excretion via the gastrointestinal system compared to the tracer which is excreted through the hepatobiliary system. Although the gallbladder information of the negative control mice could not be collected at this time, these data suggest that [^{47}Sc]Sc-HOPO-O_6-C4 is stable in vivo with significant differences in the organ uptake and excretion pathways compared to unchelated ^{47}Sc. The gallbladder %ID/g will be determined shortly to confirm the data.

3.2.7. DFT

Density functional theory (DFT) was utilized to probe the coordination geometry of HOPO-O_6-C4 and CAM-O_6-C4 with Sc^{3+} and Ga^{3+}. Firstly, the structures of the chelators, HOPO-O_6-C4 and CAM-O_6-C4, were modelled at the molecular mechanics (MM) level using manually-constructed geometries to best represent an appropriate initial geometry optimization structure in the Gaussian16 software program. Following this, the ligands were optimized at the B3LYP-D3/cc-pVDZ/SMD(H_2O) level of theory and the lowest energy conformers are outlined in **Figure 3.8**. This combination of functional and basis sets, including Grimme's dispersion correction, has previously shown good agreement with experimental findings in similar geometry optimizations of ligands and their resulting complexes.[313] Minimal structural distortions are present in both optimized structures, and both were found to be true minima of the respective potential energy surfaces by frequency calculations.

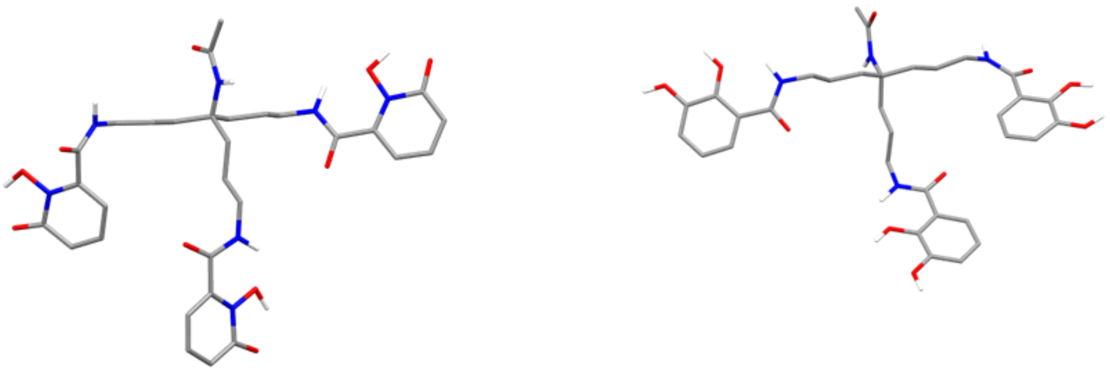

Figure 3.8. Optimized geometries of HOPO-O_6-C4 (left) and CAM-O_6-C4 (right) at the B3LYP-D3/cc-pVDZ/SMD level of theory. Colour code: gray – carbon; blue – nitrogen; red – oxygen; white – hydrogen. Carbon-bonded hydrogen atoms have been omitted for clarity.

In both cases, there is a stabilization effect imparted by a hydrogen-bonding interaction of one arm (benzyl or alkyl proton) and the adjacent amide carbonyl. The ligands were then screened for their ability to complex Sc^{3+} and Ga^{3+} at the same level of theory. The resulting DFT-optimized geometries of the Sc^{3+} complex of HOPO-O_6-C4, namely [Sc(HOPO-O_6-C4)], and the Ga^{3+} complex, namely [Ga(HOPO-O_6-C4)], are outlined in **Figure 3.9**. In both complexes, the coordination spheres of the metal ions are fully encapsulated by the tripodal pendant arms, with no interaction at the amide. This is promising when considering further functionalization through derivatization of the amide with biorthogonal functional groups.

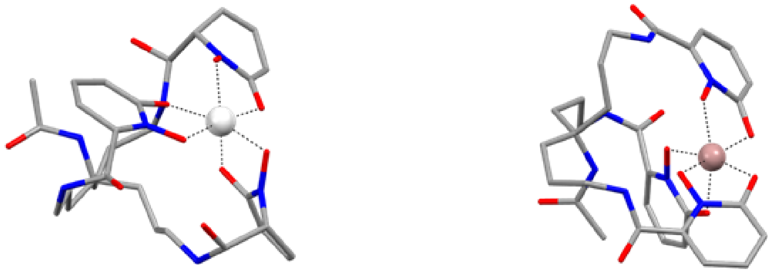

Figure 3.9. Optimized geometry of [Sc(HOPO-O_6-C4)] and [Ga(HOPO-O_6-C4)] at the B3LYP-D3/cc-pVDZ/SMD(H_2O) level of theory. Colour code: gray: carbon; blue: nitrogen; red: oxygen; white: scandium, pink: gallium. Hydrogen atoms have been omitted for clarity.

The Sc^{3+} ion is six-coordinate, bonding through the three carbonyl and three deprotonated *N*-hydroxy donor atoms of the HOPO pendant arms to form six five-membered chelate rings. The average Sc-O bond length is 2.059 Å (**Table 3.3**) and the average O-Sc-O *trans* angle is 157.58° (**Table 3.4**).

Table 3.3. Calculated metal-donor atom bond lengths (Å) for [Ga(HOPO-O_6-C4)], [Sc(HOPO-O_6-C4)], [Ga(CAM-O_6-C4)]$^{3-}$, and [Sc(CAM-O_6-C4)]$^{3-}$ at the B3LYP-D3/cc-pVDZ/SMD(H_2O) level of theory.

	Complex bond lengths (Å)			
Bond	**[Ga(HOPO-O_6-C4]**	**[Sc(HOPO-O_6-C4]**	**[Ga(CAM-O_6-C4]$^{3-}$**	**[Sc(CAM-O_6-C4]$^{3-}$**
M-O1	1.984[a]	2.074[a]	2.048	2.172
M-O2	2.009[b]	2.055[b]	2.007	2.119
M-O3	1.975[a]	2.022[a]	1.977	2.115
M-O4	2.033[b]	2.110[b]	2.014	2.153
M-O5	2.027[a]	2.017[a]	1.974	2.123
M-O6	2.008[b]	2.076b	2.011	2.145
M-O_{av}	2.006	2.059	2.005	2.138

[a]M-O=C bond; [b]M-O-N bond

Similarly, the Ga^{3+} ion is also six-coordinate, bonding through the same donor atoms. The average Ga-O bond length is shorter than the respective Sc-O bond length (2.006 Å, **Table 3.4**), most likely attributed to the higher oxophylic nature of the Ga^{3+} compared to Sc^{3+}.[321] However, the root-mean-square difference (RMSD) in total bond lengths between the two complexes (0.013 Å) highlights the close structural similarities between [Ga(HOPO-O_6-C4)] and [Sc(HOPO-O_6-C4)]. The average O-Ga-O *trans* angle (164.70°) is significantly larger than the Sc^{3+} complex, indicating a less distorted octahedral coordination sphere.

Table 3.4. Calculated donor atom-metal-donor atom bond angles (°) for [Ga(HOPO-O_6-C4)], [Sc(HOPO-O_6-C4)], [Ga(CAM-O_6-C4)]$^{3-}$, and [Sc(CAM-O_6-C4)]$^{3-}$ at the B3LYP-D3/cc-pVDZ/SMD(H_2O) level of theory.

	Complex bond lengths (Å)			
Bond	**[Ga(HOPO-O_6-C4]**	**[Sc(HOPO-O_6-C4]**	**[Ga(CAM-O_6-C4]$^{3-}$**	**[Sc(CAM-O_6-C4]$^{3-}$**
O1-M-O4[c]	166.45	174.07	165.73	159.31
O2-M-O5[c]	160.40	163.95	171.38	165.31
O3-M-O[c]	167.24	134.72	173.60	155.41
O-M-O_{av} (trans)	164.70	157.58	170.24	160.01
O1-M-O2[d]	79.73	75.13	82.30	75.52
O3-M-O4[d]	78.99	83.96	89.18	75.28
O5-M-O6[d]	78.99	80.80	82.01	75.16

[c]Trans angles; [d]donor atoms belonging to the same five-membered chelate ring around the M^{3+} ion.

The DFT-optimized geometries of the Sc^{3+} complex of CAM-O_6-C4, namely $[Sc(CAM-O_6-C4)]^{3-}$, and the Ga^{3+} complex, namely $[Ga(CAM-O_6-C4)]^{3-}$, are outlined in **Figure 3.10**. As seen in the HOPO-O_6-C4 complexes, the metal ion coordination spheres are comprised solely of the donor atoms of the pendant CAM groups with no interaction at the amide. The Sc^{3+} ion is coordinated by six deprotonated hydroxyl donor atoms, forming a 3^- complex ($[Sc(CAM-O_6-C4)]^{3-}$). The average Sc-O bond length is longer (2.138 Å) than the respective HOPO-O_6-C4 complex (2.059 Å) but shows a similar average O-Sc-O *trans* angle (160.01° vs 157.58° for [Sc(HOPO-O_6-C4)]).

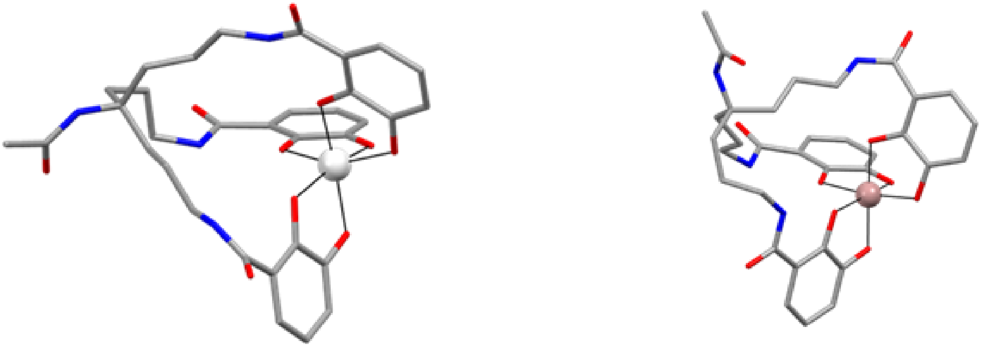

Figure 3.10. Optimized geometry of $[Sc(CAM-O_6-C4)]^{3-}$ and $[Ga(CAM-O_6-C4)]^{3-}$ at the B3LYP-D3/cc-pVDZ/SMD(H_2O) level of theory. Colour code: gray – carbon; blue – nitrogen; red – oxygen; white – scandium. Hydrogen atoms have been omitted for clarity.

The Ga^{3+} ion is also six-coordinate, bonding through the same six donor atoms, forming an octahedral complex. The average Ga-O bond length is again shorter than the respective Sc-O bond length (2.005 Å, **Table 3.3**). However, RMSD in total bond lengths between the two complexes (0.016 Å) highlights the close structural similarities between [Ga(CAM-O_6-C4)] and [Sc(CAM-O_6-C4)]. The average O-Ga-O *trans* angle (170.24°) is significantly larger than the Sc^{3+} complex, indicating a less distorted octahedral coordination sphere. There seems to be more overall structural distortion between the respective Ga^{3+} complexes (total difference in bond lengths between $[Ga(CAM-O_6-C4)]^{3-}$ and [Ga(HOPO-O_6-C4)], RMSD = 0.291 Å), and between the Sc^{3+} complexes (total difference in bond lengths between $[Sc(CAM-O_6-C4)]^{3-}$ and [Sc(HOPO-O_6-C4)], RMSD = 0.291 Å). However, the difference in the donor atom-to-metal bond lengths is far less pronounced for both sets of complexes. The RMSD for the difference in donor atom-to-metal bond lengths for the Ga^{3+} complexes was found to be 0.035 Å, whilst the RMSD for the Sc^{3+} complexes was found to be longer at 0.082 Å. This suggests that whilst both sets of ligands (CAM and HOPO) are able to accommodate both metal ions successfully, the degree to which this effect is observed around the metal ion is highly metal-dependent. This may have ramifications for the respective experimental stabilities of the complexes.

3.3. Conclusions

This chapter presents the design and synthesis of two novel chelates, HOPO-O_6-C4 and CAM-O_6-C4, and their evaluation as potential Ti^{4+}, Sc^{3+}, and Ga^{3+} chelates. HOPO-O_6-C4 showed fast complexation kinetics with Sc^{3+} and Ga^{3+} with high stability in aqueous media. CAM-O_6-C4 was found to be unstable under similar conditions and the formation of Sc^{3+} or Ga^{3+} was not observed. Preliminary complexation studies of Ti^{4+} with CAM-O_6-C4 revealed the fast formation of Ti-CAM-O_6-C4 while HOPO-O_6-C4 was not evaluated because coordination with the metal ion only occurs at low pH. Radiolabeling experiments of HOPO-O_6-C4 with ^{47}Sc at 37 °C yielded remarkably high apparent A_m of 1565 ± 17 MBq/µmol surpassing its linear octadentate analog HOPO-O_8. Despite low in vitro stability in human serum and the presence of an excess of biologically relevant metal ions, [^{47}Sc]Sc-HOPO-O_6-C4 exhibited very promising stability in vivo as seen in the analysis of the ex vivo biodistribution over 24 h. On the other hand, ^{45}Ti radiolabeling at room temperature with CAM-O_6-C4 produced multiple radioactive species which deemed this complex not suitable for further in vitro or in vivo stability studies. Preliminary DFT calculations showed the formation of hexadentate species for both chelates with Sc^{3+} and Ga^{3+}. Structural optimization with Ti^{4+} and thermodynamic calculations are currently underway.

This work will continue with additional [^{47}Sc]$ScCl_3$ biodistribution studies to calculate the activity concentration in the gallbladder to confirm the difference in uptake with [^{47}Sc]Sc-HOPO-O_6-C4 and with the evaluation of its imaging pair ^{43}Sc as proof of the potential of HOPO-O_6-C4 for the theranostic pair $^{43/47}$Sc. Radiolabeling studies with ^{68}Ga are planned for the near future along with the synthesis of the bifunctional chelate which can be readily prepared from the primary amine in the backbone and conjugated to a biomolecule for targeted theranostic applications. Lastly, it is important to note that there is currently only one macrocyclic bioconjugate, [^{47}Sc]Sc(picaga)-DUPA, reported in literature for radioscandium chelation. Thus, HOPO-O_6-C4 holds great promise to expand the toolbox of $^{43/47}$Sc chelates for preclinical evaluation.

3.4. Experimental

3.4.1. General materials and methods

The general materials and methods for this chapter followed closely those reported in chapter 2. LC-MS analysis was performed on an Agilent 1260 Infinity II and Agilent InfinityLab LC/MSD with a binary gradient pump, UV–vis detector, and auto-injector on a Phenomenex Luna C18 column (150 mm x 3 mm, 100 Å, AXIA packed).

3.4.2. Chelate synthesis

Compound **3.1** was synthesized using the commercially available 1,1,1-Tris(2-cyanoethyl)nitromethane starting material following a reported 3-step procedure.[319]

di-tert-butyl(4-acetamido-4-(3-((tert-butoxycarbonyl)amino)propyl)heptane-1,7-diyl)-dicarbamate (**3.2**). To a stirring solution of compound **3.1** (100 mg, 0.20 mmol) in dry CH_2Cl_2 (3.5 mL) was added triethylamine (56 μL, 0.40 mmol) and acetyl chloride (29 μL, 0.40 mmol) dropwise and stirred under N_2 at room temperature for 16 h. The reaction mixture was washed with 1 M HCl and brine. The organic layer was dried over $MgSO_4$ and evaporated. The residue was redissolved in CH_2Cl_2 and purified via automated flash chromatography on silica gel (solvent A: CH_2Cl_2, solvent B: ethyl acetate, gradient: 30% B, 4 CV; 30-100% B, 4 CV; 100% B, 10 CV) to obtain **3.2** as a colourless oil (81.6 mg, 76%). ^1H NMR (400 MHz, chloroform-d) δ 4.65 (s, 3H), 3.15 – 3.01 (m, 6H), 1.92 (s, 3H), 1.70 – 1.61 (m, 6H), 1.49 – 1.34 (m, 33H). ^{13}C NMR (151 MHz, chloroform-d) δ 169.69, 156.21, 79.29, 58.33, 40.75, 32.28, 28.55, 24.50, 23.90.HR-ESI-MS (CH_3OH) m/z for $C_{27}H_{52}N_4O_7$ ($[M+H]^+$) calc. (found): 545.3909 (545.3890).

N-(1,7-diamino-4-(3-aminopropyl)heptan-4-yl)acetamide (**3.3**). Compound **3.2** (81.6 mg, mmol) was dissolved in a 2:1 mixture of 4 M HCl and CH_3OH (1 mL) and stirred at room temperature for 18 h. The solvents were evaporated under reduced pressure and the residue was washed with diethyl ether (x3) to obtain the final product as a colourless oil (49.5 mg, 93%). ^1H NMR (600 MHz, deuterium oxide-d_2) δ 2.94 (t, J = 7.5 Hz, 6H), 1.91 (s, 3H), 1.78 – 1.48 (m, 12H). ^{13}C NMR (151 MHz, deuterium oxide-d_2) δ 173.59, 57.95, 39.41, 30.65, 22.76, 20.71. HR-ESI-MS (CH_3OH) m/z for $C_{12}H_{28}N_4O$ ($[M+H]^+$) calc. (found): 245.2336 (245.2327).

N,N'-(4-acetamido-4-(3-(1-(benzyloxy)-6-oxo-1,6-dihydropyridine-3-carboxamido)propyl)-heptane-1,7-diyl)bis(1-(benzyloxy)-6-oxo-1,6-dihydropyridine-2-carboxamide) (**3.4**). The synthesis of this intermediate was adapted from a literature procedure to prepare a similar compound.[322] To a suspension of compound **3.3** (40.0 mg, 0.11 mmol), triethylamine (90 µL, 0.66 mmol) and DMAP (1.4 mg, 0.011 mmol) in dry dimethylformamide (6 mL) was added a solution of compound **2.8** (193.5 mg, 0.55 mmol) in dimethylformamide (1 mL). The reaction mixture was stirred at 65 °C for 3 days and allowed to cool down to room temperature before the addition of H_2O (70 mL). The organic phase was extracted with ethyl acetate (70 mL x 5) and washed with H_2O and brine. The organic layer was dried over $MgSO_4$ and evaporated to dryness. The crude product was redissolved in CH_2Cl_2 and purified using automated flash chromatography on a silica gel column (solvent A: CH_2Cl_2, solvent B: 20% CH_3OH in CH_2Cl_2; gradient: 0% B, 4 CV; 0-25% B, 1 CV; 25% B, 8 CV; 25-50% B, 1 CV; 50% B, 5 CV; 50-100% B, 1 CV; 100% B 2 CV). Compound **3.4** was obtained as a pale yellow oil with a purity higher than 95% (60.7 mg, 58%). ^{1}H NMR (600 MHz, chloroform-d) δ 7.54 – 7.48 (m, 6H), 7.41 – 7.31 (m, 12H), 6.74 – 6.60 (m, 6H), 6.29 (dd, *J* = 6.8, 1.7 Hz, 3H), 5.26 (s, 6H), 3.08 – 2.95 (m, 6H), 1.34 – 1.07 (m, 12H). ^{13}C NMR (151 MHz, chloroform-d) δ 169.87, 160.73, 158.56, 142.82, 138.46, 133.64, 130.86, 129.68, 128.81, 124.17, 105.31, 79.41, 57.95, 39.77, 31.78, 24.44, 22.91. HR-ESI-MS (CH_3OH) m/z for $C_{51}H_{55}N_7O_{10}$ ($[M+H]^+$) calc. (found): 926.4083 (926.4077).

N,N'-(4-acetamido-4-(3-(1-(benzyloxy)-6-oxo-1,6-dihydropyridine-3-carboxamido)propyl)-heptane-1,7-diyl)bis(1-(benzyloxy)-6-oxo-1,6-dihydropyridine-2-carboxamide (**3.5**). Compound **3.5** was synthesized following a literature procedure for the O-benzyl deprotection of a similar compound.[265] Compound **3.4** (60.7 mg, 0.066 mmol) was dissolved in dry CH_2Cl_2 (25 mL) under N_2 and cooled down to -20 °C. A solution of 1 M BBr_3 in CH_2Cl_2 (6.6 mL, 6.6 mmol) was added dropwise and the reaction mixture was warmed up to room temperature. After 18 h, the solvent was blown down with an air stream to about half the volume (~ 15 mL) and the remaining suspension was spined down in a centrifuge (8000 rpm, 5 min). The precipitate was washed with acetone (x4) until the supernatant was colourless and washed with diethyl ether. Compound **3.5** was obtained pure as a pale brown solid (40.9 mg, 95%). ^{1}H NMR (601 MHz, dimethylsulfoxide-d_6 + 10% deuterium oxide-d_2) δ 7.40 (dd, *J* = 9.1, 6.9 Hz, 3H), 6.57 (dd, *J* = 9.1, 1.7 Hz, 3H), 6.31 (dd, *J* = 7.0, 1.7 Hz, 3H), 3.18 – 3.12 (m, 6H), 1.78 (s, 3H), 1.63 – 1.57 (m, 6H), 1.43 – 1.35 (m, 6H). ^{13}C NMR (151 MHz, dimethylsulfoxide-d_6 + 10% deuterium oxide-d_2) δ

169.63, 160.45, 157.96, 142.48, 137.94, 119.73, 104.35, 57.57, 48.80, 31.95, 23.77, 22.91. HR-ESI-MS (CH_3OH) m/z for $C_{51}H_{55}N_7O_{10}$ ($[M+H]^+$) calc. (found): 656.2675 (656.2705).

2,3-dibenzyloxybenzoic acid N-hydroxysuccinimide ester (**3.6**). This intermediate was prepared from 2,3-dihydroxybenzoic acid following a 2-step literature procedure with minor modifications on the 2 steps.[323] O,O'-dibenzyl-2,3-dihydroxybenzoic acid (1000.0 mg, 3.0 mmol), N-hydroxysuccinimide (414.3 mg, 3.6 mmol), and EDC·HCl (690.1 mg, 3.6 mmol) were dissolved in dry CH_2Cl_2 (60 mL) and stirred at room temperature for 17 h. The reaction mixture was washed with H_2O and brine and dried over $MgSO_4$. After evaporation of the solvents, the crude was redissolved in CH_2Cl_2 and purified on silica gel using automated flash chromatography (solvent A: hexanes, solvent B: ethyl acetate; gradient: 20% B, 3 CV; 20-40% B, 1 CV; 40% B, 8 CV; 40-100% B, 2 CV) to obtain compound **3.6** as a light brown solid (519.1 mg, 40%). Characterization was according to literature.[324]

N,N'-(4-acetamido-4-(3-(2,3-bis(benzyloxy)benzamido)propyl)heptane-1,7-diyl)bis(2,3-bis(benzyloxy)benzamide) (**3.7**). The synthesis of this molecule was adapted from a literature procedure to prepare a similar compound.[322] To a suspension of compound **3.3** (40.0 mg, 0.11 mmol), triethylamine (90 µL, 0.66 mmol) and DMAP (1.4 mg, 0.011 mmol) in dry dimethylformamide (7 mL) was added a solution of compound **3.6** (273.3 mg, 0.55 mmol) in dimethylformamide (1 mL). The reaction mixture was stirred at 70 °C for 4 days and allowed to cool down to room temperature before the addition of H_2O (80 mL). The organic phase was extracted with ethyl acetate (80 mL x 5) and washed with H_2O and brine. The organic layer was dried over $MgSO_4$ and evaporated to dryness. The crude product was redissolved in CH_2Cl_2 and purified using a chromatography column on a silica gel (solvent A: hexanes, solvent B: ethyl acetate, solvent C: CH_3OH; gradient: 1:1:0, 0:1:0, 0:9.5:0.5, 0:9:1). Compound **3.7** was obtained as a colourless oil (62.1 mg, 47%). ^1H NMR (601 MHz, $CDCl_3$) δ 7.91 (t, *J* = 5.7 Hz, 3H), 7.69 (dd, *J* = 6.6, 3.0 Hz, 3H), 7.47 – 7.41 (m, 6H), 7.41 – 7.27 (m, 24H), 7.15 – 7.06 (m, 6H), 5.11 (s, 6H), 5.05 (s, 6H), 3.20 – 3.13 (m, 6H), 1.82 (s, 3H), 1.47 – 1.41 (m, 6H), 1.20 – 1.12 (m, 6H). ^{13}C NMR (151 MHz, $CDCl_3$) δ 169.44, 165.24, 151.85, 146.90, 136.60, 136.59, 128.82, 128.80, 128.79, 128.36, 127.76, 127.57, 124.53, 123.37, 76.40, 71.37, 58.10, 39.97, 32.33, 23.39. ESI-MS (CH_3OH) m/z for $C_{51}H_{55}N_7O_{10}$ ($[M+H]^+$) calc. (found): 1193.5 (1193.5).

N-[4-acetamido-7-[(2,3-dihydroxybenzoyl)amino]-4-[3-[(2,3-dihydroxybenzoyl)amino]-propyl]heptyl]-2,3-dihydroxybenzamide (**3.8**). Pd/C 10 % wt loading (3.3 mg) was added to a solution of compound **3.7** (12.7 mg, 0.011 mmol) in ethanol (1.1 mL) containing formic acid (1µL). The flask was capped with a rubber stopper, sealed, and purged with argon, followed by H_2 gas from a balloon. The reaction was stirred at room temperature for 1.5 h under the H_2 atmosphere. After purging with argon, the reaction mixture was filtered over a pad of Celite and washed with ethanol. The resulting purple filtrate was concentrated in vacuo. The crude was redissolved in H_2O and lyophilized to yield compound **3.8** as a purple solid (8.3 mg, 85%). Residual formic acid could not be removed by lyophilization and was quantified by ^1H NMR to be equal to 5 molecules of product and included in the yield calculation. ^1H NMR (601 MHz, deuterium oxide-d$_2$) δ 7.29 (dd, *J* = 8.1, 1.7 Hz, 3H), 6.87 (dd, *J* = 7.5, 1.8 Hz, 3H), 6.48 (t, *J* = 7.8 Hz, 3H), 3.34 (t, *J* = 6.8 Hz, 6H), 1.92 (d, *J* = 1.3 Hz, 3H), 1.85 – 1.73 (m, 6H), 1.62 – 1.52 (m, 6H). ^{13}C NMR (151 MHz, deuterium oxide-d$_2$) δ 173.15, 170.32, 156.68, 148.22, 119.71, 116.95, 114.75, 112.93, 53.77, 39.18, 31.40, 22.75, 22.57. HR-ESI-MS (CH_3OH) m/z for $C_{51}H_{55}N_7O_{10}$ ($[M+H]^+$) calc. (found): 653.2817 (653.2815).

3.4.3. Non-radioactive metal complexes

3.4.3.1. Variable pH-^1H NMR titrations

^1H NMR spectra were collected at 25 °C using an AV00 Bruker spectrometer. 3-(trimethylsilyl) propionic acid (TSP) sodium salt was used as the internal reference. The water signal was suppressed using an excitation sculpting suppression pulse scheme. The pH measurements were carried out with a LE422 micro pH electrode (Mettler Toledo).

pKa determination: 1 mM ligand solutions were prepared in 90% ultrapure H_2O + 10% D_2O with KCl to adjust *I* = 0.1 M. The pH of the solutions was adjusted by the addition of small aliquots of 1-0.005 M HCl or KOH.

Sc^{3+} and Ga^{3+} complexation: ligand solutions at the selected pH were prepared according to the above procedure. Stock solutions of 40 mM $ScCl_3$ x 6 H_2O or $Ga(NO_3)_3$ x $6H_2O$ were prepared in ultrapure H_2O. A small aliquot corresponding to 1 equivalent of the metal salt was added to the ligand solution and the pH was adjusted again with 1-0.005 M HCl or KOH.

3.4.3.1. Data treatment

All data were processed using MestReNova 14.1.2-25024. The acidity constants of each ligand are referred to the equilibrium $H_hL^{n+} \rightleftharpoons H_{h-1}L^{(n-1)+} + H^+$ and were refined using the least-squares fitting program PITMAP. The water ionization constant (pK_w, $2H_2O \rightleftharpoons H_3O^+ + OH^-$) was calculated by the same program at T = 25°C and *I* = $NaNO_3$ 0.15 M, and it resulted equal to 13.54 on average. The errors quoted are the standard deviations calculated by the PITMAP program.

3.4.3.2. LC-MS characterization

Compound **3.8** (2 mg, 0.003 mmol) was dissolved in 0.2 mL of CH_3OH. Titanium isopropoxide (0.89 µL, 0.003 mmol) was added to the solution. The solution immediately turned a light yellow colour. The solution was then analyzed via LC-MS (A: 0.1 % FA in H_2O, B: 0.1 % FA in CH_3CN; gradient: 0-3 min: 5% B, 3-10 min: 5-95%, 10-13 min: 95% B, 13-13.5 min: 95-5% B, 13.5-16 min: 5% B, t_R = 6.1 min, flow rate: 0.8 mL/min). LR-MS (CH_3OH) m/z for $C_{33}H_{34}N_4O_{10}Ti$ ($[M+3H+Ti]^+$) calc. (found): 697.17 (697.2).

3.4.4. Isotope production and purification

Caution! ^{45}Ti and ^{47}Sc emit ionizing radiation and should only be handled in a facility designed according to appropriate safety protocols.

3.4.4.1. General materials and methods

All chemicals were purchased from Fisher or Sigma-Aldrich and used without purification. All water was ultrapure (>18.2 MΩ). Instruments were calibrated and maintained according to standard quality control procedures. Natural vanadium foils were obtained from the ESPI metals. Proton irradiations were performed on TR-24 cyclotron (Advanced Cyclotron Systems (ACSI, INC)). Activity measurements were performed on a Canberra S5000 HPGe and analyzed with the Canberra Genie 2000 software. The energy and efficiency calibration for the HPGe was performed using a mixed nuclide sealed source from Eckert and Ziegler Analytics.

Radio-TLC was performed on plastic-backed iTLC-SG purchased from Agilent Technologies (Santa Clara, CA, USA) and measured on an Eckert & Ziegler AR-2000 and processed using Winscan Radio-TLC software (Eckert and Zeigler, AR2000, Winscan software, Berlin, Germany). The HPLC system used for ^{47}Sc work was an Agilent

Technologies 1260 Infinity HPLC with UV and radioactivity detectors and an Xterra MS packed C18 4.6 × 150 mm column from Waters. A purity of >95% was confirmed using quantitative HPLC analysis for nonradioactive compounds and radio-TLC for radioactive compounds. Tissue weight and radioactivity were measured via an automated gamma counter (Hidex AMG, Turku, Finland).

Radio HPLC was carried out using Agilent 1220 Infinity II LC system equipped with a binary gradient pump, UV–vis detector, manual injector, and radio detector on a Phenomenex Luna 5 µm C18(2) column (150 mm × 3 mm).

3.4.4.2. ^{47}Sc production and purification

Natural vanadium foils were irradiated at 24 MeV protons, at 80 µA for 4 hours. AG MP-50 resin was packed into a solid phase extraction fritted column, 1.5 g, and conditioned before the addition of the dissolved vanadium foil in 8 M HCl. Washes of 8 M HCl, 4 M HCl and water were added before ^{47}Sc was collected in 1 M Ammonium acetate pH 4. The ^{47}Sc was immediately concentrated using CM weak cation exchange column into 1 mL 0.1 M HCl. The ^{47}Sc was brought down to dryness and reconstituted in 50 µL of 0.1 M HCl. Activity measurements were performed using HPGe and Capintec Dose Calibrator set at calibration number 30.

3.4.4.3. ^{45}Ti production and purification

^{45}Ti was obtained following previously published methods.[308]

3.4.5. Radiolabeling experiments

A stock solution of either DOTA or HOPO-O$_6$-C4 was prepared in a 5 mg/mL stock solution dissolved in chelex-treated MQ water H_2O. Stock solutions of CAM-O$_6$-C4 were prepared in ethanol at 10-0.01 mM concentrations. All samples were prepared using low-retention Eppendorf tubes and pipette tips to minimize tracer loss.

3.4.5.1. ^{47}Sc radiolabeling

All ^{47}Sc was obtained in 0.1 M HCl. All trace metal ammonium acetate buffer (0.25 M, pH 4) was prepared from chelex-treated water and prepared on the day of labeling. The =aApparent molar activity was calculated by a series of radiolabeling of ^{47}Sc with either HOPO-O$_6$-C4 or DOTA. A serial dilution of either DOTA or HOPO-O$_6$-C4 was performed under the same mass conditions. Appendix Table A.9 contains the mass of each chelator per vial and molar mass. The final volume was maintained at 52.76 µL and the average activity per vial was 817.7 ± 44.4 kBq. The apparent molar activity was performed in triplicate. Vials containing HOPO-O_6-C4 were incubated at 37° C, 800 rpm for 30 minutes while DOTA was incubated at 95° C, 800 rpm for 30 minutes. After 30 minutes, the ethanol was added to each solution, where the ethanol volume was 10% of the total volume.

3.4.1.2. ^{45}Ti radiolabeling

10 µL of the corresponding CAM-O_6-C4 stock solution was dissolved in 0.1 mL of chelex-treated 0.5 M HEPES buffer at pH 8 followed by the addition of 8 µL of ^{45}Ti in 1.0 M citric acid (460 kBq). The final pH of the reaction was confirmed to be 7-7.5. Samples were thoroughly mixed and incubated at 20 °C for 15, 30, and 60 min prior to spotting on an aluminum-backed SiO_2 TLC plate. The plates were developed in CH_3OH as the mobile phase. Under these conditions, chelated ^{45}Ti runs to the solvent front (R_f = 0.9-0.95) and unchelated ^{45}Ti remains at the baseline (R_f = 0). Radio-HPLC analysis was performed to confirm the RCY. (A: 0.1% TFA in H_2O, B: CH_3CN; gradient: 0–3 min: 95% A, 3-17 min: 5–95% B, 17-20 min: 95-5% B).

3.4.6. Complex stability assay

3.4.6.1. Serum challenge assay

[^{47}Sc]Sc-HOPO-O_6-C4 were prepared according to the radiolabeling protocol described above for a final concentration of 2.278 MBq/µg (0.149 MBq/nmol). This stock solution was used for all serum, metal challenge and in vivo biodistribution studies. These stock solutions diluted in reaction buffer up to a 100 µL for an average of 370 kBq and 400 µL of either human or mouse serum were added following incubation at 37 °C over 7 days (n = 3). At 15 and 30 minutes, 1 h, and everyday day up to day 7, 6 µL of the reaction mixture was spotted on iTLC (SG paper plates, 1 M citrate buffer pH 4.5). The stability of the complexes was measured as the percentage of intact complex (Rf = 0). Under these conditions, free ^{47}Sc moves with the solvent front and [^{47}Sc]Sc-HOPO-O_6-C4 remains at the origin.

3.4.6.1. Metal challenge assay

Each vial contained 100 μL of the stock solution of [^{47}Sc]Sc-HOPO-O_6-C4 for an average of 370 kBq, prepared from the same stock as the serum stability studies. 50 μL of either $MgCl_2$, $CuCl_2$, $FeCl_3$ or $ZnCl_2$ were added to the solution and then diluted to 500 μL with chelex-purified H_2O to a final metal ion concentration of 100 μM. The metal challenge study was also incubated at 37° C and assessed identically as the serum assay above.

3.4.7. Ex-vivo biodistribution

The [^{47}Sc]Sc-HOPO-O_6-C4 or [^{47}Sc]$ScCl_3$ was diluted with saline to yield 100 μL doses of 185 kBq per dose of the complex and 296 kBq per dose of unchelated scandium. There was no filtering performed on the final dose. Mice doses were administered via tail-vein injection. Four time points were analyzed 10 minutes (Balb/c male mice, n = 4), 30 minutes (Athymic nude male, n = 4), 1 h (Balb/c, n = 4) and 24 h (Athymic nude male, n = 3). These time points are based on the average time of injection. The mice were euthanized and the organs were harvested followed by the collection of organ weights and activity measurements on a gamma counter.

3.4.8. DFT calculations

DFT calculations were performed using the Gaussian 16 (Revision B.01) program package with the Becke, 3-parameter, Lee-Yang-Par (B3LYP) functional.[325–327] Empirical dispersion was employed using Grimme's dispersion correction with Becke-Johnson damping (D3-BJ).[282,328] Geometry optimizations were performed using the double- ζ cc-pVDZ basis set for all atoms, which has shown good agreement with experimental observations previously.[313,329] Geometry optimizations were performed without imposing any symmetry constraints. All ligands and complexes were fully optimized in aqueous solution (dielectric constant $\varepsilon = 78.36$) using the SMD model.[330] Frequency calculations indicated no imaginary frequencies at the optimized molecular geometries, which indicate that they are real minima of the respective potential energy surfaces. Single-point energy calculations were performed at the same level of theory previously described. Unless specified, all calculations were performed at 298.15 K and 1 atm. Initial input geometries were constructed manually and optimized at the molecular mechanics (MM) level prior to optimization using DFT. Calculation results were visualized and interpreted using GaussView version 5.0.9 and VMD version 1.9.4a53.[331,332] Root-mean-square deviations were calculated according to the following equation:

$$RMSD = \sqrt{\frac{1}{N}\sum_{i=1}^{n}\delta_i^2}$$

where δ is the difference in bond lengths (Å) of the respective systems.[333]

Chapter 4.

Exploring click chemistry for radiopharmaceutical development: a novel tetrazine (Tz) containing HOPO-O_8 chelate for ^{89}Zr and ^{161}Tb theranostic agents

4.1. Introduction

In nuclear medicine, radiolabeled antibodies (radioimmunoconjugates) have long demonstrated excellent potential for imaging and therapy of cancer, as such, numerous antibody-based radiopharmaceuticals have resulted in successful clinical applications (e.g., [^{131}I]I-metuximab, [^{90}Y]Y-Ibritumomab tiuxetan (Zevalin)) and many more are being evaluated in clinical studies.[334–336] Monoclonal antibodies (mAbs) are powerful tools for the selective delivery of radiation to tumour sites sparing healthy tissue due to their ability to recognize cell antigens with high affinity and specificity. Traditionally, radioimmunoconjugates are radiolabeled with long-lived radioisotopes (^{131}I, $t_{1/2}$ = 8.0 d; ^{177}Lu, $t_{1/2}$ = 6.6 d) to match the pharmacokinetics of the immunoglobulins which can take several days to achieve optimal biodistribution in the body. The slow blood circulation results in the long circulation of the radiopharmaceutical in the body inevitably irradiating healthy tissue.[337] This high radiation dose received by healthy organs and tissue contradicts the general purpose and use of mAbs with high specificity and hampers the widespread use in clinics. Several alternative strategies have been proposed to circumvent this issue including the use of small antibody fragments such as Fab (~10-100 kDa) which can accelerate the blood circulation time. Although, one of the most attractive and fascinating approaches is the in vivo pretargeting method.[338,339]

In vivo pretargeting relies on the decoupling of the radioimmunoconjugate to exploit the high selectivity of mAbs avoiding the unnecessary radiation dose associated with the slow pharmacokinetics of the drug complex. This approach essentially divides the radiopharmaceutical into two parts: a small molecule radiolabeled with the isotope of interest and an antibody – preferably not internalized after binding the cell receptor. Each component is designed to incorporate a recognition moiety so that they can selectively combine at the tumour site. In practical terms, the antibody unit will be injected first to accumulate in the tumour and after several days, the radioactive moiety will be injected and, due to its smaller size, it will quickly circulate the bloodstream and either ligate with the antibody or clear from the body.[337,340] In this way, in vivo pretargeting diminishes the time the radioactive isotopes circulate in the body and allows the use of shorter-lived isotopes (^{18}F, $t_{1/2}$ = 109.8 min; ^{68}Ga, $t_{1/2}$ = 67.7 min) which are incompatible with the traditional methodology.[341] Moreover, in vivo pretargeting can easily be combined with radiotheranostics by the sequential injection of two radiolabeled chelate molecules: the first one radiolabeled with an imaging radionuclide and the second with its therapeutic pair.

Various molecular pairs have been evaluated for nuclear medicine applications in the past two decades with some ligation reactions such as the streptavidin-biotin couple making their way into clinical trials. Unfortunately, the patient outcome was not favourable.[342,343] Recently, the click chemistry approach consisting of the fast (k~ 1×10^{6} $M^{-1} \cdot s^{-1}$) and bio-orthogonal Inverse Electron Demand [4+2] Diels-Alder (IEDDA) cycloaddition reaction between a trans-cyclooctene (TCO) and a Tz has shown remarkable progress (**Figure 4.1**).[337,344] This strategy has been explored using a variety of radioisotopes for imaging or therapy individually or integrating both concepts for radiotheranostics such as the ^{64}Cu/^{67}Cu pair.[345–347]

Figure 4.1. Schematic representation of the click reaction between a tetrazine (Tz)-bearing radiolabeled chelate and a trans-cyclooctene (TCO) conjugated to an antibody.

Encouraged by the promising preclinical results of in vivo IEDDA pretargeting strategies, we sought to apply this chemistry using HOPO-O_8 to the two most promising isotopes investigated in chapter 2, ^{227}Th ($t_{1/2}$ = 18.7 d, E(α) = 6.0 MeV) and the theranostic isotope ^{161}Tb ($t_{1/2}$ = 6.9 d, $E(\beta^{-}_{avg})$ = 154 keV, I = 101 %, E(γ) = 48.9 and 74.5 keV, I= 17 and 10%) (section 1.2.4 and 1.3.3). Despite the higher kinetic inertness of [^{227}Th]Th-HOPO-O_{10} over [^{227}Th]Th-HOPO-O_8, I chose to synthesize a Tz-based bifunctional version of the octadentate chelate due to the easier synthetic pathway. ^{134}Ce (^{134}Ce, $t_{1/2}$ = 3.16 d, EC (100%) has been proposed as a better imaging pair to ^{227}Th than ^{89}Zr (^{89}Zr, $t_{1/2}$ = 78.4 h, $E(\beta^{+}_{avg})$ = 396 keV, I = 23%).[112] However, this isotope is currently accessible to very few research centers and we are collaborating with Dr. R. Flavell at the University of California San Francisco (UCSF) who will be performing in vivo pretargeting preclinical studies with ^{134}Ce/^{227}Th. For this preliminary work, ^{89}Zr was used as an imaging surrogate for ^{134}Ce.

Herein, we present the synthetic route and the ^{89}Zr, ^{161}Tb and ^{227}Th radiolabeling evaluation of a novel HOPO-O_8 bifunctional chelate containing a methyl-tetrazine handle (HOPO-O_8-Me-Tz) for in vivo pretargeting applications. The click chemistry reaction between HOPO-O_8-Me-Tz and the TCO-modified trastuzumab – targeting HER2-positive breast cancer – was validated in vitro and the resulting radioimmunoconjugate was evaluated in a proof-of-concept in vivo study with the imaging isotopes ^{89}Zr and ^{161}Tb.

4.2. Results and discussion

4.2.1. Synthesis

The synthesis of HOPO-O_8-Me-Tz (**Scheme 4.1**) was designed following the improved synthetic route of its p-SCN-Bn-HOPO analog reported by Bhupathiraju et al.[265]. This route was partially explored in the synthesis of HOPO-O_{10} demonstrating significant improvements in the purification of intermediate **2.5** formed via tosylate coupling compared to the reductive amination product (section 2.2.1).

Initial attempts explored the possibility of coupling tosyl functionalized Tz directly to the backbone spermine followed by the addition of four 1,2-HOPO units (**2.8**) and deprotecting the O-benzyl protecting group as the last step – a 3-step synthesis. As expected, the Tz molecule decomposed quickly under the tosyl coupling reaction at 60 °C in acetonitrile. To overcome the instability of the tetrazine, the synthesis was redesigned to couple the Tz to the chelate towards the end of the synthetic route. This path required the addition of a terminal Boc-protected amine to spermine since the direct coupling of the activated 1,2-HOPO (**2.8**) to spermine would result in four amide bonds unreactive to the alkylation of the tetrazine under mild conditions. To keep it simple, spermine was extended by a short Boc-protected ethylamine activated with a tosyl group (**4.1**) which can be readily prepared from commercially available N-Boc ethanolamine.[348] Half an equivalent of intermediate **4.1** was reacted with spermine under reflux and monitored by TLC (100% CH_2Cl_2) until no more compound **4.1** was observed. Due to the lack of UV absorbance of spermine or the products, the only possibility to isolate the desired product (**4.2**) was by preparative HPLC coupled to mass selective detection (MSD) monitoring the 346.0 m/z product peak. The single ion monitoring spectrum showed two peaks which were isolated and characterized by ^{1}H NMR. The first peak corresponded to a mixture of **4.2** and spermine alkylated on a secondary amine and the second one contained the pure product in the form of a TFA salt. A total ion count spectrum revealed the formation of small quantities of double alkylated spermine as well. The yield could not be calculated due to the presence of residual p-toluene sulfonic acid that coeluted with the product though it was estimated to be around 15-20%. A direct comparison to the formation of compound **2.5** is not possible due to the different lengths of the alkylated chain although we can say that the direct alkylation is faster – one step versus four steps – and overall higher yielding.

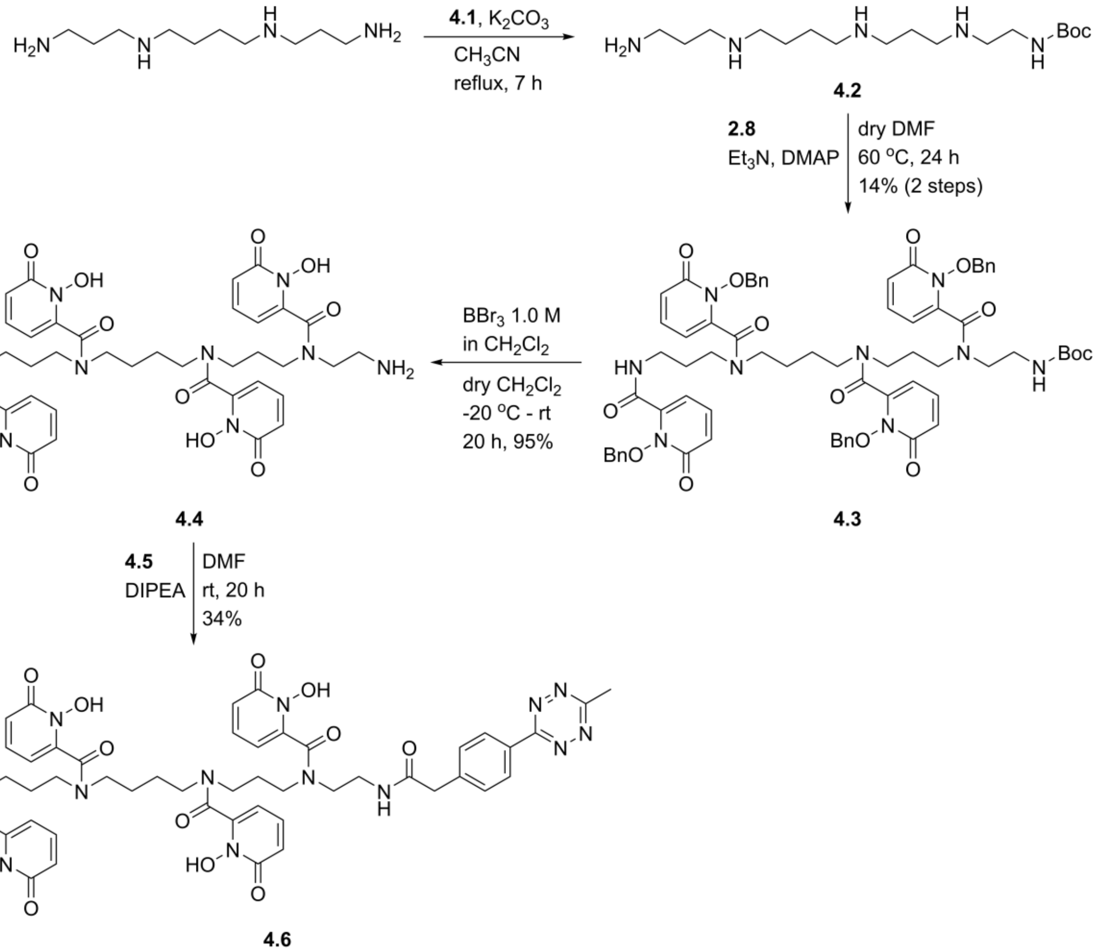

Scheme 4.1. Synthetic route towards HOPO-O$_8$-Me-Tz

Intermediate **4.2** was then reacted with an excess of activated 1,2-HOPO-OBn (**2.8**) following our previously reported conditions (section 2.4.2, compound **2.9**) to obtain the fully protected compound **4.3**. Two pathways were investigated at this point. *Route 1* consisted of the selective deprotection of the Boc group under acidic conditions (10% TFA in CH_2Cl_2) to subsequently alkylate the primary amine with an NHS-activated Tz and lastly hydrogenate the O-benzyl groups to obtain the final product. Our group has previously demonstrated that tetrazines are reduced under hydrogenation conditions yet they are spontaneously oxidized when exposed to air.[349] *Route 2* consisted of the complete deprotection of **4.3** by the mild Lewis acid BBr_3, in CH_2Cl_2, followed by the alkylation of an NHS-activated Tz. The uncertainty of this route was the reactivity of the oxygen atoms of the N-OH groups. Attempts to deprotect the O-benzyl groups with H_2 on Pd/C in ethanol resulted unsuccessful even at high pressure (100 PSI) or under acidic conditions (10% acetic acid). These synthetic challenges deemed *route 1* to be unfeasible and the efforts were focused on *route 2*. The one-step deprotection was successful using 1.0 M $BrBr_3$ in CH_2Cl_2 yielding **4.4.** in quantitative yield. NHS ester Tz was first used to alkylate compound **4.4** with DIPEA in DMF. Unfortunately, the desired molecule was very unstable and despite observing the formation by MS, the bifunctional chelate would decompose quickly after isolation. The stability of the final product was improved by using the methyl-substituted analog, methyltetrazine NHS ester (**4.5**), which was successfully alkylated under the same conditions. Purification of **4.6** was achieved by washing the reaction crude with CH_2Cl_2 to remove the excess base and **4.5** to yield the bifunctional chelate (**4.6**) as a pink solid.

4.2.2. Bifunctional chelate-antibody conjugation.

The evaluation of the in vitro efficiency of the IEDDA reaction requires first the conjugation of TCO units to the antibody tzmb. TCO moieties can easily be conjugate to the amine side chains of lysine residues present in trastuzumab. Previous work in our group showed that TCO-NHS ester has only a 20% conjugation yield. To improve the efficiency, a 4-chain polyethylene glycol (PEG4) linker was incorporated in the form of TCO-PEG4-NHS ester. Additionally, the use of short PEG linkers has been demonstrated to contribute to the fast clearance of the bioconjugate in the blood compared to its non-PEGylated analog.[350] The coupling of TCO-PEG4-NHS ester and trastuzumab proceeded rapidly at room temperature yielding Tzmb-PEG4-TCO.[337] The number of TCO molecules per trastuzumab was determined to be 6.2 by MALDI-ToF MS/MS, indicating a conjugation efficiency of 77% – calculated from the 10 equivalents of TCO added – a drastically improved coupling efficiency compared to the non-PEGylated analog.

The efficiency of the click reaction was then investigated in vitro. Methyltetrazines are known to have slower reaction kinetics compared to their hydrogen-substituted counterparts; however, their kinetic rates are still extremely fast for radiopharmaceutical applications. Typically, an antibody conjugation reaction can take 1-24 h.[265,350] In our case, 20 equivalents of HOPO-O_8-Me-Tz were used and the reaction was allowed to proceed for 2 h at 25 °C. After purification and analysis, the number of HOPO-O_8 units per modified antibody was found to be 5.2 by MALDI-ToF MS/MS. The number of TCO and chelate units incorporated into the antibody were not expected to significantly alter the immunoreactivity of the bioconjugate based on a recent systematic study with DFO-pSCN-Bn-trastuzumab.[351]

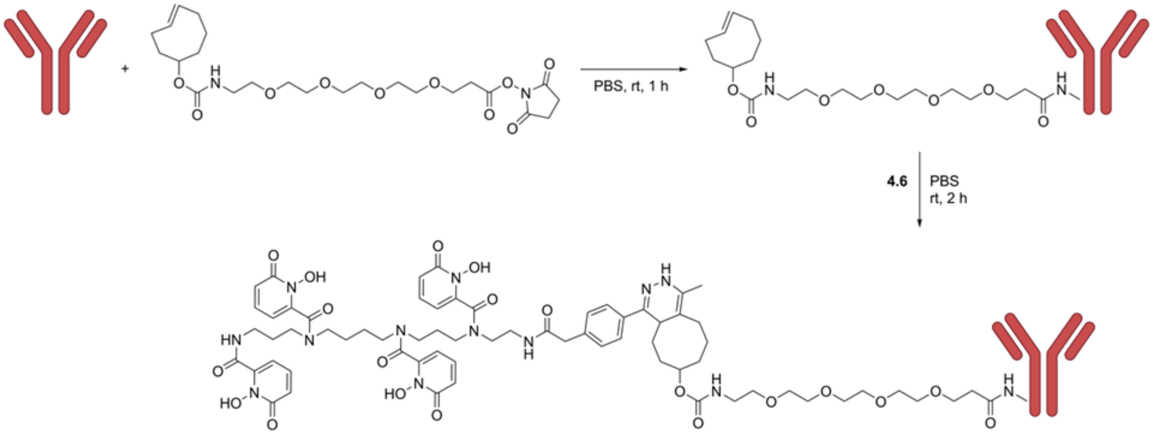

Figure 4.2 Coupling of TCO to the antibody and subsequent IEDDA click reaction with HOPO-O_8-Me-Tz to prepare Tzmb-HOPO-O_8.

4.2.3. Radiolabeling

The BFC and the immunoconjugate compounds were radiolabeled with the imaging isotope ^{89}Zr under mild conditions at room temperature or 37 °C, respectively, compatible with the stability of antibodies. ^{227}Th radiolabeling was only screened with the BFC since the activity eluted from the ^{227}Ac/^{227}Th generator was insufficient to reproduce the amounts required for an in vivo preclinical mouse study.

The optimal conditions for radiolabeling HOPO-O_8-Me-Tz with $^{89}Zr^{4+}$ were found to be 0.5 M NH_4OAc pH 6. PBS, commonly used for DFO radiolabeling, gave significantly lower RCYs under the same conditions. Quantitative radiolabeling (>96%) of 10 μM of HOPO-O_8-Me-Tz with 1.2 MBq of ^{89}Zr was achieved at 25 °C after 30 min, a metal-to-ligand ratio of 1:613. The radiolabeling efficiency decreased to 77.3% ± 4.1 at 1 μM of chelate under the same conditions after 1 h. Interestingly, at 30 min the radio TLC analysis showed the formation of multiple ^{89}Zr complex species with one main sharp peak with a broad shoulder and an extra small bump. However, after 1 h of reaction, only the main sharp peak was observed at the origin. This effect was first reported in the formation of the [^{89}Zr]Zr-HOPO-O_8 complex and it has also been observed in a similar Tz-HOPO structure. The appearance of multiple peaks indicates the formation of a small percentage of a kinetic product (shoulder and bump peaks) that converts to the thermodynamic product (main peak) over time.[260,352]

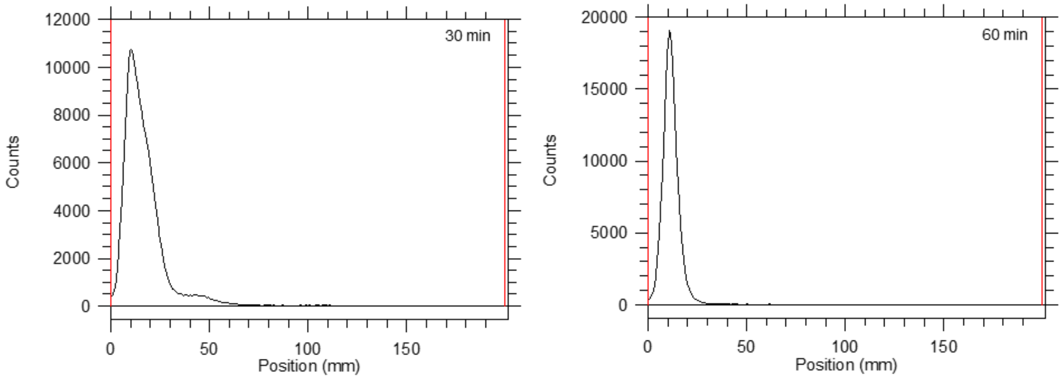

Figure 4.3. iTLC chromatograms of [^{89}Zr]Zr-HOPO-O_8-Me-Tz radiolabeling reaction at 30 min (left) and 60 min (right).

The radiolabeling of HOPO-O_8-Me-Tz with $^{161}Tb^{3+}$ was studied according to the previously reported conditions, 0.5 M NH4OAc pH 6 at 25 °C except that this time the buffer was prepared in chelex-treated H_2O (see section 2.4.6). The BFC exhibited comparable or even superior radiolabeling properties to HOPO-O_8 achieving 91.7 ± 0.5 RCYs at 1 μM chelate concentration and 100 kBq of ^{161}Tb in 30 min (1:34 metal-to-ligand ratio). These results reveal that the Tz handle does not interfere with the metal binding affinity.

$^{227}Th^{4+}$ radiolabeling was performed following the previously optimized conditions, 0.5 M NH_4OAc pH 5 at 25 °C with chelex-treated H_2O. At 10 μM of HOPO-O_8-Me-Tz with 20 kBq of ^{227}Th, a metal-to-ligand ratio of only 1:13, RCYs reached 95.2 ± 0.5 after 20 min. These results reveal that the BFC still exhibits excellent radiolabeling kinetics at room temperature comparable to those of HOPO-O_8 (section 2.2.3) and similar to ^{161}Tb, the Tz moiety does not affect the radiolabeling affinity.

Following the successful radiochemistry of the BFC, the ^{89}Zr and ^{161}Tb radiolabeling of the pre-clicked immunoconjugate (HOPO-O_8-Tzmb) was evaluated. The reactions were performed in 0.5 M NH_4OAc pH 7 by incubating 100 μg of Tzmb-HOPO-O_8 with 150 MBq of neutralized ^{89}Zr or 100 MBq ^{161}Tb at 37 °C. RCYs >99% were obtained after 30 min reaching a high A_s of ~ 2 and 1 GBq/mg, respectively. The radioimmunoconjugates were then purified by size-exclusion chromatography (SEC) and the purified radiotracer was collected in PBS pH 7.4 in five fractions (200-450 μL each fraction). Fractions 2 and 3 contained the highest concentration of labeled tracer and were used for the corresponding in vivo studies.

4.2.4. Human serum stability.

The stability of the ^{89}Zr, ^{227}Th, and ^{161}Tb BFC complexes and the ^{161}Tb radioimmunoconjugates was evaluated in human serum at 37 °C. All BFC complexes displayed excellent stability in a biologically relevant environment with over 99% of intact [^{89}Zr]Zr-HOPO-O_8-Me-Tz and [^{161}Tb]Tb-HOPO-O_8-Me-Tz over 7 days and 97.4 ± 3.6% intact of [^{227}Th]Th-HOPO-O_8-Me-Tz over 6 days. The stability of the radioimmunoconjugates was studied with the purified complexes incubated with human serum under the same conditions as the BFC. The [^{161}Tb]Tb-HOPO-O_8-Tzmb bioconjugate showed the same stability profile as the BFC with >99% of the intact complex after 7 days. Due to isotope availability, the stability of [^{89}Zr]Zr-HOPO-O_8-Tzmb could not be measured at the time of writing and will be performed shortly.

4.2.5. In vivo imaging studies.

Given the high radiochemical yields and complex stability in human serum, we sought to evaluate the in vivo biodistribution and pharmacokinetics of the bioconjugates in a preliminary targeted (non-pretargeting) study. Female NRG mice (n = 2 for each group) with subcutaneous SKOV3 xenografts were injected with either [^{161}Tb]Tb-HOPO-O_8-Tzmb or [^{89}Zr]Tb-HOPO-O_8-Tzmb and imaged over 6 days along with [^{161}Tb]$TbCl_3$ or [^{89}Zr]Zr-oxalate as control of unchelated radiometal. Due to an issue with the cell line, the tumors did not grow even after 10 weeks post-inoculation. Among all the animals, only one mouse presented a very small bump on the left shoulder (the size of a grain of sand) that could potentially be a microscopic tumor. However, the status of the tumoral cells could not be assessed. Despite this, we decided to proceed with the study as valuable biodistribution and pharmacokinetics could still be obtained. The activity concentration quantitative analysis of the SPECT/CT images was done in regions of interest (ROI).

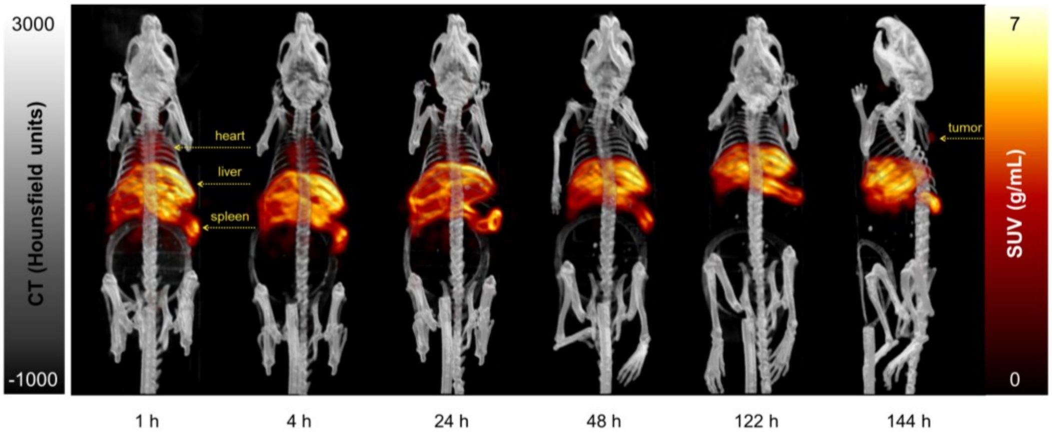

Figure 4.4. SPECT/CT images of [^{161}Tb]Tb-HOPO-O$_8$-Tzmb (6.06-6.2 MBq) in female Nu/J mice bearing SKOV3 tumor xenografts (n = 4) on the left shoulder over 144 h.

All images were filtered with the same threshold except for the 144 h image which had a higher filter to show the tumor activity.

The [^{161}Tb]Tb-HOPO-O$_8$-Tzmb SPECT/CT results are presented in **Figure 4.4** and include the mice with a potential tumor. The standardized uptake value (SUV) of the most relevant organs can be found in Appendix, Table A.11. The tracer showed a long circulation time in the bloodstream with low uptake after 48 h – expected for a large radioimmunoconjugate (~ 150 kDa) – and slow decrease over time as seen in the time activity curves (**Figure 4.5**). A similar trend was also shown in the lungs and bladder. High liver uptake was observed at earlier than expected timepoints with an SUV of 7.11 ± 0.14 g/mL after 1 h. Its decrease over time correlates well with the increased and exceptionally large spleen uptake. An explanation for the notable activity concentration is the formation of molecular aggregates which are known to accumulate in the reticuloendothelial system (RES) (e.g., liver, spleen). These could be resolved by analyzing the tracer using size-exclusion HPLC. At later timepoints, the SPECT/CT images revealed increasing uptake in the small intestines indicating a tracer excretion pathway through the RES. Low uptake in the joints started at 1 h with an SUV of 0.79 ± 0.11 g/mL reaching a plateau after 24 h at ~ 1.5 g/mL, still too low to be appreciated in **Figure 4.4**. These concentration values indicate a small degree of demetallation in vivo as unchelated [^{161}Tb]Tb^{3+} accumulated in the joints and extensively in the spine (Appendix, Table A.12). The SUV of the tracer in the joints represents 17% of the [^{161}Tb]TbCl$_3$ in the same ROI.

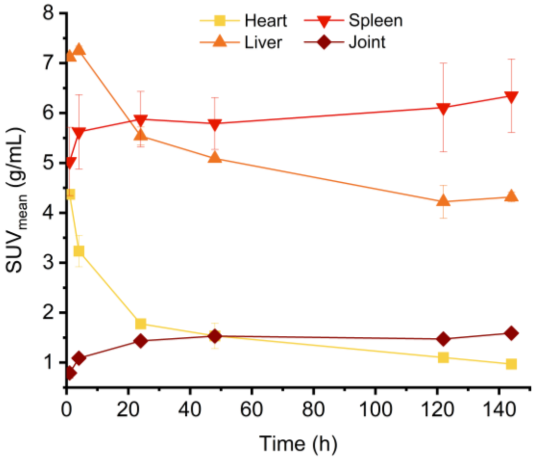

Figure 4.5. Representative time-activity concentration curves for [^{161}Tb]Tb-HOPO-O$_8$-Tzmb in female NUD mice bearing SKOV3 xenografts.

In vivo imaging of the [^{89}Zr]Tb-HOPO-O$_8$-Tzmb tracer was interrupted during the study by an equipment failure and only the 4 h and 24 h time points could be acquired. These frame files contained multiple errors making imaging reconstruction extremely complex. Thus, the data is not presented here and the study will be repeated shortly with mice bearing optimal tumor size.

4.2.6. Ex vivo biodistribution studies

Post-mortem biodistribution studies were carried out on day 6 for [^{161}Tb]Tb-HOPO-O$_8$-Tzmb or [^{89}Zr]Tb-HOPO-O$_8$-Tzmb and at 24 h for [^{161}Tb]TbCl$_3$ (n = 4 or 2 for tracers or unchelated activity, respectively). The [^{161}Tb]Tb-HOPO-O$_8$-Tzmb results shown in **Figure 4.6** align well with the observations made in the SPECT/PET images. The biodistribution data of [^{161}Tb]Tb-HOPO-O$_8$-Tzmb reveals exceptionally large spleen uptake (113.4 ± 36.2 %ID/g) and high liver uptake (14.4 ± 1.5 %ID/g) (**Table 4.1**). The presence of activity in the suspected tumor region confirms the observations made with the SPECT/CT images although the calculated 13.5 ± 1.5 %ID/g is not a quantitative value since extra tissue was harvested with the tumors due to their microscopic size. Comparing the bone uptake between the unchelated radiometal and the tracer confirms a very low degree of demetallation in vivo with 14.7 ± 1.3 %ID/g versus 3.0 ± 0.5 %ID/g (Appendix, Table A.13). Unfortunately, the joints of the negative control mice were not harvested this time but they will be harvested in the future for comparison.

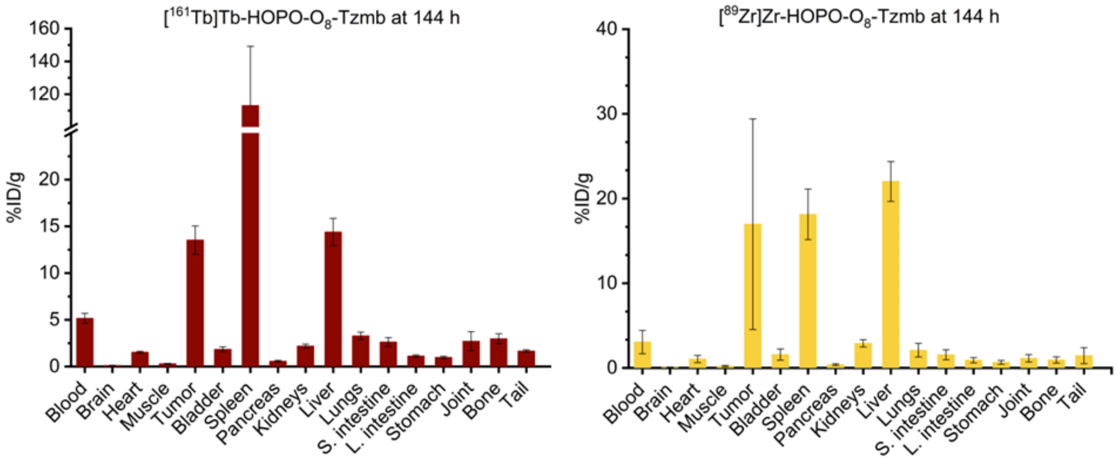

Figure 4.6. Ex vivo biodistribution analysis of [^{161}Tb]Tb-HOPO-O$_8$-Tzmb (3.9-6.2 MBq) (left) at 144 h and [^{89}Zr]Zr-HOPO-O$_8$-Tzmb (right) (2.3-6.6 MBq) at 120 h in female Nu/J mice with SKOV3 xenografts (n = 4).

Limited information can be obtained from the [^{89}Zr]Zr-HOPO-O$_8$-Tzmb animal study with only the biodistribution data (**Figure 4.6**). The tracer clearing pattern is equal to that of the [^{161}Tb]Tb-HOPO-O$_8$-Tzmb with high liver uptake at 120 h (22.0 ± 2.4 %ID/g) indicative of excretion through the RES system. However, in this case, the spleen uptake was almost one order of magnitude lower (18.1 ± 3.0 ID/g) compared to the ^{161}Tb tracer and is reasonable for healthy mice (**Table 4.1**). Since none of the mice in this study group had any visible or palpable tumors even when the organs were harvested, the animals could be considered healthy. The absence of tumors is seen by the large standard deviation in the tissue harvested in an attempt to find the tumors. The data is not representative of tumor uptake. The analysis reveals key information about the tracer stability with minimal bone or joint uptake after 120 h indicating no demetallation in vivo.

Table 4.1. Comparison of the activity concentrations in ROIs measured via quantitative SPECT/CT versus ex vivo biodistribution analysis at 144 h for [^{161}Tb]Tb-HOPO-O$_8$-Tzmb and at 120 h for [^{89}Zr]Zr-HOPO-O$_8$-Tzmb.

	[^{161}Tb]Tb-HOPO-O$_8$-Tzmb		[^{89}Zr]Tb-HOPO-O$_8$-Tzmb
	SPECT	BioD	BioD
Organ	SUV	%ID/g	%ID/g
Heart	0.97 ± 0.02	1.5 ± 0.1	1.1 ± 0.4
Liver	4.32 ± 0.03	14.4 ± 1.5	22.0 ± 2.4
Spleen	6.35 ± 0.01	113.1 ± 36.1	18.1 ± 3.0
Joint	1.59 ± 0.01	2.7 ± 1.0	1.1 ± 0.4
Tumor	5.41[a]	13.5 ± 1.5	17.0 ± 12.4

[a]Based on one data point.

4.3. Conclusions

With the excellent results obtained in chapter 2 for HOPO-O_{10} and HOPO-O_8, the next logical step was the development of a bifunctional chelate. This chapter focuses on the development of the novel BFC. To simplify the synthesis, HOPO-O_8 was chosen for preliminary studies. A novel bifunctional chelate bearing a Tz moiety, HOPO-O_8-Me-Tz, was synthesized and characterized for its application in pretargeting strategies. HOPO-O_8-Me-Tz was demonstrated to retain its ability to quantitatively label $^{89}Zr^+$, ^{161}Tb, and ^{227}Th in under 30 min at room temperature with excellent in vitro stability with >95% intact complex in human serum over 7 days. The BFC was then evaluated for conventional conjugation to trastuzumab, a mAb targeting the HER2 receptor overexpressed in many breast and ovarian cancers. The biodistribution and pharmacokinetics of [^{89}Zr]Zr-HOPO-O_8-Tzmb and [^{161}Tb]Tb-HOPO-O_8-Tzmb were evaluated in vivo. Due to difficulties with tumor growth, quantification of tumor uptake of the radioimmunoconjugates was not possible at this time. [^{89}Zr]Zr-HOPO-O_8-Tzmb exhibited excellent in vivo stability with minimal uptake in the bones compared to [^{161}Tb]Tb-HOPO-O_8-Tzmb which showed a small degree of demetallation which will have to be further investigated with mice bearing tumors. Both radiotracers exhibited long circulation times and excretion through the RES.

In the near future, the in vivo studies will be repeated with mice bearing optimal image size tumors to evaluate the tumor uptake and compare tumor:bone ratios. However, at this point of the study, we can suggest that [^{89}Zr]Zr-HOPO-O_8-Me-Tz and [^{161}Tb]Tb-HOPO-O_8-Tzmb could be promising radioimmunoconjugates. Additionally, at the time of writing, our collaborators at UCSF are starting to plan the evaluation of the HOPO-O_8-Me-Tz chelate for pretargeting strategies with the PET agent ^{134}Ce and its therapeutic pair ^{227}Th.

4.4. Experimental

4.4.1. General materials and methods

The general materials and methods follow closely those reported in chapter 2 (section 2.4.1). Methyltetrazine NHS ester (**4.5**) and TCO-PEG4-NHS ester were purchased from Click Chemistry Tools and used as received. Trastuzumab was purchased as Herceptin from Genentech and purified using a SEC column (PD-10, Sephadex G-25 resin, Cytiva) followed by spin filtration using a 50,000 molecular weight cut-off filter (Amicon Ultra-4 centrifugal units, Ultracel 50: regenerated cellulose, Millipore). The antibody solution in PBS (pH 7.4) was stored at -20 °C for 6 months. Preparative HPLC was performed on an Agilent 1290 Infinity II Preparative LC/MSD system consisting of a G7110B isocratic pump and a G7161B preparative binary pump, a G7165A variable wavelength absorbance detector, a G7158B automatic liquid sampler and open-bed fraction collector, and a G6125B LC/MSD unit. Preparative purification was carried out using an Agilent 10 Prep-C18 column (10 µm, 100 Å, 150 x 50.0 mm) at a low rate of 25 mL/min.

The average number of TCO or moieties per antibody was determined by MALDI-ToF MS/MS on a Bruker autoflex speed at the Alberta Proteomics and Mass Spectrometry Facility (University of Alberta, Canada) following previously reported procedures.[337] The $[M+2H]^{2+}$ mass signals were used to determine the average mass and calculate the antibody-to-TCO and antibody-to-chelate ratios. UV-vis measurements to determine the concentration of the antibody solutions were performed on a Thermo Scientific NanoDrop™ 1000 using the antibody (~150 kDa) extinction coefficient of 210,000 $M^{-1} \cdot cm^{-1}$.

4.4.2. Bifunctional chelate synthesis

Compound **2.8** was synthesized following a 3-step procedure described in section 2.4.2.

2-(tert-butoxycarbonylamino)ethyl-4-methylbenzenesulfonate (**4.1**). Compound **4.1** was synthesized following a published procedure with small modifications.[348] Tert-Butyl (2-hydroxyethyl)carbamate (1.0 g, 6.20 mmol) and triethylamine (12.4 mmol, 1.73 mL) were dissolved in dry CH_2Cl_2 (15 mL) under N_2 and cooled in an ice bath. A solution of p-toluenesulfonyl chloride (1181.4 g, 6.2 mmol) was added dropwise and the reaction was allowed to warm up to room temperature and stir for 48 h. The reaction mixture was washed with 1 M HCl and brine and dried over $MgSO_4$. After evaporating the solvents under vacuum, the crude was purified via automated silica gel chromatography (Isolera One, Sfar 25 g, A: CH_2Cl_2, B: 20% CH_3OH in CH_2Cl_2, gradient: 0-4 CV: 0% B, 4-5 CV: 0-20% B, 4-14 CV: 20% B, 14-15CV: 20-50% B, 15-16 CV: 50% B). The fractions containing the product were combined and the solvents were removed in vacuo to give compound 2 as a white solid (1.37 g, 70%). ^{1}H NMR (400 MHz, chloroform-d_3) δ 7.78 (d, 2H), 7.34 (d, 2H), 4.06 (t, *J* = 5.1 Hz, 2H), 3.37 (dd, *J* = 5.5 Hz, 2H), 2.44 (s, 3H), 1.40 (s, 9H). ^{13}C NMR (101 MHz, chloroform-d_3) δ 155.74, 145.16, 130.09, 128.07, 79.94, 69.59, 39.90, 28.42, 21.77. ESI-MS (CH_3OH) m/z for $C_{14}H_{21}NnaO_5S$ ($[M+Na]^+$) calc. (found): 338.1 (338.0)

tert-butyl (1-(1-(benzyloxy)-6-oxo-1,6-dihydropyridin-2-yl)-6,11,15-tris(1-(benzyloxy)-6-oxo-1,6-dihydropyridine-2-carbonyl)-1-oxo-2,6,11,15-tetraazaheptadecan-17-yl)carbamate (**4.3**) The synthesis of compound **4.2** was adapted from a published procedure to prepare a similar structure.[265] To a cooled (ice bath) stirring solution of spermine (508 mg, 2.5 mmol) and potassium carbonate (691, 5.0 mmol) in CH_3CN (75 mL) was added dropwise a solution of compound **4.1** (395 mg, 1.3 mmol) in CH_3CN (75 mL) using an addition funnel. The reaction mixture was refluxed for 7 h until no compound **4.1** was observed (monitored via TLC in 100% CH_2Cl_2). The potassium carbonate was filtered through a small plug of Celite® 545 and the solvent was evaporated in vacuo. The reaction crude was redissolved in H_2O (0.1% TFA) and purified by preparative LC-MSD (A: 0.1% TFA in H_2O, B: 0.1% TFA in CH_3CN; gradient: 0-3 min: 10% B, 3-29 min: 10-30% B, 29-31 min: 30-100% B, 31-35 min: 100% B, 336 min: 100-10% B, 37-45 min: 10% B, collection m/z: 346.0, flow rate: 25 mL/min). The single ion monitoring spectrum at m/z 346.0 showed two peaks; the fractions for each peak were combined, lyophilized, and analyzed by ^{1}H NMR. The first peak (t_R= 18.8 min) corresponded to a mixture of alkylation on the primary amine (desired product) and alkylation on the secondary amine (byproduct). The second peak (t_R= 20.66 min) corresponded to the pure product (>90%) with residual p-toluenesulfonic acid. Due to the presence of this impurity, the yield of this step could not be quantified.

Note: do not evaporate the solvents in a rotary evaporator at 40 °C, the Boc protecting group will fall off.

To the purified intermediate **4.2** (93 mg), DMAP (1.5 mg, 0.012 mmol), triethylamine (0.13 mL, 0.96 mmol) in dry dimethylformamide (6 mL) under N_2 was added a solution of compound **2.8** (226 mg, 0.66 mmol) in dry dimethylformamide (1 mL). The mixture was heated to 55 °C and stirred for 2 days. After cooling to room temperature, H_2O (60 mL) was added and the product was extracted with dichloromethane (80 mL x 4). The combined organic layers were washed with H_2O and brine and dried over $MgSO_4$. The pale orange crude was purified by column chromatography in silica (0-5% methanol in dichloromethane) to obtain **4.3** as a light brown solid (131 mg, 14 % over two steps). ^{1}H NMR (600 MHz, chloroform-d_3) δ 8.10 – 4.63 (m, 40H), 3.87 – 2.27 (m, 16H), 1.87 – 0.45 (m, 17H). ^{13}C NMR (151 MHz, chloroform-d_3) δ 162.02, 161.30, 158.30, 142.80, 138.42, 138.02, 133.53, 130.80, 130.46, 129.68, 129.60, 128.74, 128.66, 128.36, 125.43, 123.09, 104.75, 103.17, 102.93, 79.70, 79.58, 79.50, 47.21, 45.45, 40.52, 38.44, 37.03, 28.57, 28.50, 21.61.* HR-ESI-MS (CH_3OH) m/z for $C_{69}H_{75}N_9O_{14}$ ($[M+H]^+$) calc. (found): 1254.5506 (1254.5511). ^{13}C peak assignment was challenging due to the presence of rotamers in solution. The peaks were assigned to the best of our possibilities with ^{1}H and ^{13}C HSQC and HMBC.

N-(2-aminoethyl)-1-hydroxy-N-(3-(1-hydroxy-N-(4-(1-hydroxy-N-(3-(1-hydroxy-6-oxo-1,6-dihydropyridine-2-carboxamido)propyl)-6-oxo-1,6-dihydropyridine-2-carboxamido)butyl)-6-oxo-1,6-dihydropyridine-2-carboxamido)propyl)-6-oxo-1,6-dihydropyridine-2-carboxamide (**4.4**). The synthesis of compound 4.4 was adapted from literature to prepare a similar structure.[265] Compound **4.3** (50 mg, 0.040 mmol) was dissolved in dry CH_2Cl_2 (15 mL) and cooled down to -20 °C under N_2. A solution of 1.0 M BBr_3 in CH_2Cl_2 (4.0 mL, 4 mmol) was added dropwise and the solution was warmed up to room temperature and stirred for 20 h. The brown suspension was centrifuged down (6000 rpm, 5 min) and the precipitate was washed and centrifuged with acetone (x4). The light brown precipitate was then washed with diethyl ether to yield the fully deprotected compound **4.4** (30.3 mg, 95%). ^{1}H NMR (600 MHz, methanol-d_3) δ 8.32 – 6.12 (m, 12H), 4.18 – 2.82 (m, 16H), 2.30 – 1.23 (m, 8H). ^{13}C NMR (151 MHz, methanol-d_3) δ 163.59, 160.32, 142.86, 140.03, 120.91, 120.57, 120.46, 105.95, 48.00, 47.91, 47.01, 46.60, 45.12, 44.81, 44.01, 43.92, 43.47, 43.20, 38.89, 38.67, 38.32, 38.07, 29.03, 27.86, 27.81, 26.27, 26.20, 25.30, 25.13. HR-ESI-MS (CH_3OH) m/z for $C_{69}H_{75}N_9O_{14}$ ($[M+H]^+$) calc. (found): 794.3104 (794.3136).

1-hydroxy-N-(3-(1-hydroxy-6-oxo-1,6-dihydropyridine-2-carboxamido)propyl)-N-(4-(1-hydroxy-N-(3-(1-hydroxy-N-(2-(2-(4-(6-methyl-1,2,4,5-tetrazin-3-yl)phenyl)acetamido)-ethyl)-6-oxo-1,6-dihydropyridine-2-carboxamido)propyl)-6-oxo-1,6-dihydropyridine-2-carboxamido)butyl)-6-oxo-1,6-dihydropyridine-2-carboxamide (**4.6**). To a stirring suspension of compound **4.4** (16.5 mL, 0.021 mmol) and DIPEA (0.014 mL, 0.084 mmol) in dry dimethylformamide (1.6 mL) was added dropwise a solution of methyltetrazine NHS ester (**4.5**) in dry dimethylformamide (0.65 mL). The pink reaction mixture was covered in aluminum foil to avoid decomposition of the tetrazine and stirred at room temperature for

16 h. The solvents were evaporated to dryness under a stream of air. CH_2Cl_2 (~ 3 mL) was added to the flask and the sticky solid was triturated with a plastic spatula. The suspension was then centrifuged (8000 rpm, 5 min) and the pink precipitate was washed with CH_2Cl_2 (x4). Lastly, the solid was washed with diethyl ether and centrifuged to isolate pure compound **4.6** as a pink solid (7.2 mg, 34%). ^{1}H NMR (601 MHz, dimethylsulfoxide-d_6 + 5% deuterium oxide-d_2) δ 8.36 (d, *J* = 7.9 Hz, 2H), 7.58 – 7.23 (m, 6H), 6.60 – 5.93 (m, 8H), 3.49 (s, 21H), 1.87 – 1.13 (m, 8H). ^{13}C NMR (151 MHz, dimethylsulfoxide-d_6 + 5% deuterium oxide d_2) δ 173.07, 167.29, 163.42, 161.38, 157.69, 142.14, 141.06, 138.02, 130.43, 130.37, 130.35, 127.55, 119.70, 119.32, 104.09, 102.14, 47.66, 45.76, 42.29, 36.71, 27.78, 25.00, 20.99. HR-ESI-MS (CH_3OH) m/z for $C_{69}H_{75}N_9O_{14}$ ([M+H]+) calc. (found): 1006.3802 (1006.3836).

Note: 5% deuterium oxide was added to exchange all exchangeable protons (N-H, O-H).

4.4.3. Bioconjugate synthesis

Trastuzumab-TCO modification. The conjugation reaction closely followed previously reported procedures.[337] The pH of a solution of purified trastuzumab (120 µL, 23.0 mg/mL) in PBS (pH 7.4) was adjusted to 8.8-9 by the addition of small aliquots of a solution of 0.1 M Na_2CO_3 (10-15 µL). TCO-PEG4-NHS ester (9.5 µL, 40 mg/mL) in dimethylformamide was added slowly with agitation to the antibody solution. The reaction was incubated at 25 °C in a thermoshaker at 500 rpm for 1 h. The resulting solution was purified by SEC (PD-10, Sephadex G-25 resin, Cytiva) and the purified Trastuzumab-PEG4-TCO was collected in PBS (pH 7.4, 3.5 mL). The sample was concentrated by spin filtration (Amicon ultra-4, 50k) at 3,500g for 15 min and the solution was transferred to a 1.5 mL Eppendorf tube. The filter was washed with 0.2 mL of PBS (pH 7.4) and combined with the modified antibody solution (106 µL, 20.6 mg/mL). The number of TCO units per antibody was found to be 6.2 by MALDI-ToF MS/MS.

HOPO-O_8-Tzmb in vitro click reaction. To a solution of modified antibody (61 µL, 35 mg/mL) diluted with 439 µL of PBS (pH 7.4) was added slowly (2 µL/s) a solution of HOPO-O_8-Me-Tz in DMF (60 µL, 10^{-2} M). The resulting solution was sonicated for 1 min and incubated at 25 °C in a thermoshaker at 500 rpm for 2 h. Purification to remove unclicked chelate was carried out by SEC (PD10, Sephadex G-25 resin, Cytiva) and the HOPO-O_8-Tzmb bioconjugate was collected in PBS (pH 7.4, 3.5 mL) and concentrated down by spin filtration (Amicon ultra-4) at 4,000g for 20 min. The filter was washed with 0.2 mL of PBS (pH 7.4) and combined with the clicked antibody solution (420 μL, 4.01 mg/mL). The ratio of molecules of chelates per modified antibody was 5.2 by MALDI-ToF MS/MS.

4.4.4. Isotope production and purification

Caution! ^{89}Zr, ^{161}Tb, and ^{227}Th emit ionizing radiation and they should only be handled in a facility designed in accordance with appropriate safety protocols.

4.4.4.1. General materials and methods

The general materials and methods followed closely those reported in section 2.4.5.1. Radioactivity measurements were carried out using a HPGe as specified in section 2.4.5.1 for ^{227}Th or analyzed using a Capintec CRC-15R dose calibrator (Capintec) for ^{161}Tb and ^{89}Zr.

4.4.4.2. ^{89}Zr production and purification

^{89}Zr in 1 M oxalic acid was purchased from Sylvia Fedoruk Canadian Center for Nuclear Innovation Inc., (SK, Canada) and used without further purification.

4.4.4.3. ^{161}Tb production and purification

^{161}Tb was obtained pure in the form of [^{161}Tb]$TbCl_3$ from SCK CEN (Belgium) and used without further purification.

4.4.4.4. ^{227}Th production and purification

^{227}Th was obtained from a ^{227}Ac/^{227}Th generator following the previously reported procedure (section 2.4.5.6).[322]

4.4.5. Radiolabeling studies

All radiolabeling chemistry was performed with ultrapure MilliQ water (>18.5 MΩ cm^{-1} at 25 °C, Milli-Q) treated with Chelex-100 resin (BioRad Laboratories) following a previously reported protocol.[351] A stock solution of HOPO-O_8-Me-Tz (10^{-3} M) was prepared in a 1:1 mixture of chelex-treated H_2O and DMSO and diluted in the same solvent mixture to give serial dilutions (10^{-4} - 10^{-7} M) suitable for radiolabeling. All bioconjugates were prepared using low-retention Eppendorf tubes and pipette tips to minimize tracer loss.

4.4.4.1. ^{89}Zr radiolabeling

Aliquots of [^{89}Zr]Zr-oxalate (1 M) were neutralized to pH 7.0-7.5 using 1 M Na_2CO_3 prior to each set of radiolabeling experiments.

[^{89}Zr]Zr-HOPO-O_8-Me-Tz radiolabeling. A 5 µL aliquot of the corresponding chelate stock solution (10^{-4} – 10^{-6} M) was further diluted with various buffers (0.5 M NH_4OAc pH 6 or 7 and PBS pH 7.4) so that the total reaction volume was 50 µL after the addition of a neutralized solution of ^{89}Zr (0.5 – 1.2 MBq) (n = 3). The reactions were incubated at 25 °C at 350 rpm over 1 h. The RCY was analyzed at 30 min and 1 h by radio-TLC (SG paper plates, 50 mM EDTA pH 5). With this system, uncomplexed ^{89}Zr travels up to the solvent front (R_f = 1) and complexed ^{89}Zr remains at the baseline (R_f = 0). Each set of experiments included a negative control containing only ^{89}Zr and the reaction buffer.

[^{89}Zr]Zr-HOPO-O_8-Tzmb. Aliquots of neutralized ^{89}Zr (140 MBq) were mixed with 25 µL of a solution of HOPO-O_8-Tzmb in PBS (100 µg) diluted in 0.5 M NH_4OAc pH 7 (650 µL). The reaction was incubated at 37 °C for 1 h and monitored at 30 and 60 min by iTLC (SG paper plates, 50mM EDTA pH 5). After reaction completion, ^{89}Zr radioimmunoconjugate was purified by small SEC columns (PD miniTrap G-25, Cytiva) and eluted in PBS (pH 7.4, 1.5 mL) collected in five small fractions (250-450 µL). The highest labeled tracer concentration was found in fractions 2 (250 µL) and 3 (260 µL) with 10.6 MBq and 24.2 µg and 12.6 MBq and 25.0 µg, respectively.

4.4.4.2. ^{161}Tb radiolabeling

[^{161}Tb]Tb-HOPO-O_8-Me-Tz radiolabeling. A 5 µL aliquot of a stock solution of HOPO-O_8-Me-Tz (10^{-4} - 10^{-7} M) was added to 43.8 µL of 0.5 M NH4OAc pH 6 and 1.2 µL of [^{161}Tb]Tb^{3+} (100 kBq) (n = 3). The reaction was incubated at 25 °C at 350 rpm over 1 h and monitored at 30 and 60 min by radio-TLC (silicic acid (SA) paper plates, 50 mM EDTA pH 5). Under these conditions, uncomplexed ^{161}Tb travels to the solvent front (R_f = 1) and the complexed ^{161}Tb remains at the baseline (R_f = 0). A negative control including only ^{161}Tb and buffer was performed at the same time.

[^{161}Tb]Tb-HOPO-O$_8$-Tzmb radiolabeling. To a solution of 25 µL of HOPO-O$_8$-Tzmb in PBS (100 µg) and 450 µL of 0.5 M NH$_4$OAc pH 7 was added 31 µL of ^{161}Tb (85 MBq) and the reaction was incubated at 37 °C for 30 min. After confirming reaction completion by iTLC (SA plates, 0.4 M citric acid pH 4), the [^{161}Tb]Tb-HOPO-O$_8$-Tzmb was purified by small SEC columns (PD miniTrap G-25, Cytiva) and eluted in PBS (pH 7.4, 1.5 mL) collected in five small fractions (250-450 µL). The labeled tracer was eluted in fractions 2 (225 µL) and 3 (280 µL) containing 15.3 MBq and 24.3 µg of modified mAb and 20.5 MBq and 34.5 µg, respectively.

4.4.4.3. ^{227}Th radiolabeling

HOPO-O$_8$-Me-Tz radiolabeling. A 5 or 10 µL aliquot of the corresponding stock solution (10^{-4} - 10^{-6} M) was added to a buffer solution (0.5M NH$_4$OAc pH 5) such as the final volume was 50 or 100 µL after the addition of ^{227}Th (5-20 kBq) (n = 2). The reactions were incubated at 25 °C at 350 rpm over 1 h. The RCY was monitored at 20 min and 1 h by γ spectroscopy following the procedure reported in section 2.4.6. Each set of experiments included a negative control containing only ^{227}Th and the reaction buffer.

4.4.6. Human serum stability assay

4.4.5.1. [^{89}Zr]Zr-HOPO-O$_8$-Me-Tz and [^{89}Zr]Zr-HOPO-O$_8$-Tzmb

[^{89}Zr]Zr-HOPO-O$_8$-Me-Tz (800 kBq) and [^{89}Zr]Zr-HOPO-O$_8$-Tzmb complexes were prepared according to the radiolabeling protocol described above. The ^{89}Zr complexes or unchelated ^{89}Zr in the reaction buffer were incubated with human serum in a 1:1 (v/v) mixture at 37 °C over 7 days (n = 3). At days 1,3, 5, and 7 5 µL of the reaction mixture were quenched with 5 µL of 50 mM EDTA pH 5 and spotted on iTLC (SG paper plates, 50 mM EDTA pH 5). The stability of the complexes was measured as the percentage of intact complex (R_f = 0).

4.4.5.2. [^{161}Tb]Tb-HOPO-O$_8$-Me-Tz and [^{161}Tb]Tb-HOPO-O$_8$-Tzmb

[^{161}Tb]Tb-HOPO-O$_8$-Me-Tz (100 kBq) and [^{161}Tb]Tb-HOPO-O$_8$-Tzmb (2 MBq) were prepared according to the radiolabeling protocol described above. The ^{161}Tb complexes stability protocol followed closely that of the ^{89}Zr complexes with minor differences, the reaction mixture was quenched with 0.4 M citric acid pH 4 and the iTLC strip (SA paper plates) was developed in 0.4 M citric acid pH 4.

4.4.5.3. *[^{227}Th]Th-HOPO-O_8-Me-Tz*

[^{227}Th]Th- HOPO-O_8-Me-Tz (10 kBq) was prepared according to the radiolabeling protocol described above. The ^{227}Th complexes stability protocol followed closely that of the ^{161}Tb complexes with minor differences, the reactions were monitored on days 1,3, and 6 and analyzed by gamma spectroscopy following the radiolabeling protocol.

4.4.7. In vivo imaging

The study was conducted in compliance with the guidelines set by the Canadian Council on Animal Care (CCAC) and approved by the Animal Care Committee (ACC) at the University of British Columbia (A20-0132). A total of six male Nu/J mice weighing approximately 21 g were used in the study. The mice were divided into two groups: group 1 (n = 4) receiving [^{161}Tb]Tb-HOPO-O_8-Tzmb, and group 2 (n = 2) receiving free [^{161}Tb]$TbCl_3$. Within each group, half of the animals were assigned for imaging purposes, while the remaining mice were designated for biodistribution analysis.

The mice assigned for imaging purposes were anesthetized using isoflurane via a precision vaporizer. For induction, 5% isoflurane in oxygen was used, and for maintenance, isoflurane between 1.5% and 2.5% in oxygen was administered. To ensure hydration before each imaging scan, the mice received a subcutaneous injection of 0.5 mL Lactated Ringer's solution. Following the induction of anesthesia, an injection containing 150 µL of [^{161}Tb]Tb-HOPO-O_8-Tzmb or [^{161}Tb]$TbCl_3$ in PBS was administered via the tail vein. The average injected activity for group 1 was 6.13 MBq, and similar amounts were administered to the animals in group 2.

After the injection, a VECTor/CT multimodal preclinical scanner (MILabs, The Netherlands) equipped with a XUHS mouse pinhole collimator was used to obtain whole-body images. For group 1, the first scans were obtained with a dynamic scan lasting 60 min (5 frames x 12 min), followed by static scans at 4, 24, 48, 122, and 144 h p.i..

Throughout the scanning process, the mice were maintained under isoflurane anesthesia and kept warm with a heating pad to ensure constant body temperature. Following each SPECT acquisition, a whole-body CT scan was performed to obtain anatomical information, and the two images were registered. The ^{161}Tb photopeak window was centred at 47 keV with a 50% energy window width. SPECT image reconstructions were carried out using a pixel-ordered subset expectation maximization (POSEM) algorithm with 16 subsets, 6 iterations, and an isotropic 0.4 mm voxel grid to enable quantitative analysis. The images were decay corrected, and after CT registration, attenuation correction was applied. For a visual representation, the reconstructed volumes of the SPECT scans were post-filtered with a 3D Gaussian filter.

CT scans were conducted using a tube setting of 55 kV and 615 µA, and 2 frames of 180 projections over 360 degrees were captured in step and shoot rotation mode. The acquired projection data were reconstructed using SkyScan NRecon software to generate a 3D CT image with a voxel size of 0.169 mm^3. ROIs, including the heart, lungs, liver, spleen, bladder, joint, bone, and tumor were manually defined using AMIDE software (v.1.0.5) to determine the time activity curves per target organ. The average organ activity per volume was obtained from the SPECT images, and the SUVs were extracted from each organ. To relate the scanner units (counts/pixel) to radioactivity concentration (MBq/mL), a calibration factor was determined by scanning a source with a known concentration of ^{161}Tb.

4.4.8. Ex vivo biodistribution

The lateral tail vein was used to administer [^{161}Tb]Tb-HOPO-O_8-Tzmb (3.90 MBq, 120 µL), [^{161}Tb]$TbCl_3$ (1.00 MBq, 120 µL) or [^{89}Zr]Zr-HOPO-O8-Tzmb (2.64, 2.38, 5.71, 6.63 MBq, 120-150 µL) (n = 4) intravenously using a Tailveiner restrainer. Subsequently, the mice were allowed unrestricted movement within their cages. Biodistribution studies were conducted 144 hours after administering [^{161}Tb]Tb-HOPO-O_8-Tzmb, 24 hours for [^{161}Tb]$TbCl_3$, and 120 h for [^{89}Zr]Zr-HOPO-O8-Tzmb. To euthanize the mice, CO_2 asphyxiation was employed under 2% isoflurane anesthesia. Activity within the blood pool was retrieved via cardiac puncture. The organs of interest were completely extracted, weighed, and subjected to activity measurement usig a gamma counter (Packard Cobra II, Perkin Elmer, Waltham, MA, USA). The results are reported as the percentage of %ID/g.

Chapter 5. Conclusions and future work

5.1. Thesis conclusions and future work

The projects presented in this thesis have been primarily focused on exploring acyclic chelates that incorporate the 1,2-HOPO ligand into metal-based radiopharmaceuticals. The main interest at the beginning of my Ph.D. research program was the stable chelation of radiolanthanides and actinides such as ^{225}Ac or ^{227}Th which are explored in chapters 2 and 4. However, as the Ramogida group was growing, we also became interested in first-row transition metals such as ^{44}Sc or ^{45}Ti, which can be produced with the TR-13 (13 MeV) at TRIUMF. For the chelation of these smaller radiometals, I designed and evaluated a hexadentate 1,2-HOPO chelate, HOPO-O_6-C4, along with a catechol analog, CAM-O6-C_4. Through lengthy and complex synthetic routes, I have synthesized a total of three novel chelates and one bifunctional chelate which was conjugated to trastuzumab, to treat HER2+ tumors. Coordination chemistry, DFT, radiolabeling, stability, in vitro, and in vivo studies were performed to evaluate the novel chelates as candidates for incorporation into radiopharmaceuticals.

Chapter 2 investigated the effect of incorporating an extra 1,2-HOPO ligand into the highly promising ^{89}Zr octadentate chelate, HOPO-O_8, for the chelation of the larger radiolanthanides and actinides. We hypothesized that the decadentate analog of HOPO-O_8, named HOPO-O_{10}, would be able to incorporate larger metal ions such as ^{225}Ac or ^{227}Th. This hypothesis was supported by the thermodynamic constants calculated by the Abergel group with HOPO-O_8. The coordination chemistry studies with La^{3+}, Tb^{3+} and Th^{4+} did not reveal enough information about the complex structures thus we complemented the study with geometry optimization and thermodynamic calculations through DFT. The radiolabeling studies revealed an excellent binding affinity of both HOPO-O_8 and HOPO-O_{10} for the β^--emitter ^{161}Tb and the α-emitter ^{227}Th. The in vitro human serum assay revealed the enhanced stability of the [^{227}Th]Th-HOPO-O_{10} complex over the [^{227}Th]Th-HOPO-O_8 demonstrating the benefit of the extra 1,2-HOPO unit in forming stable radioactive complexes.

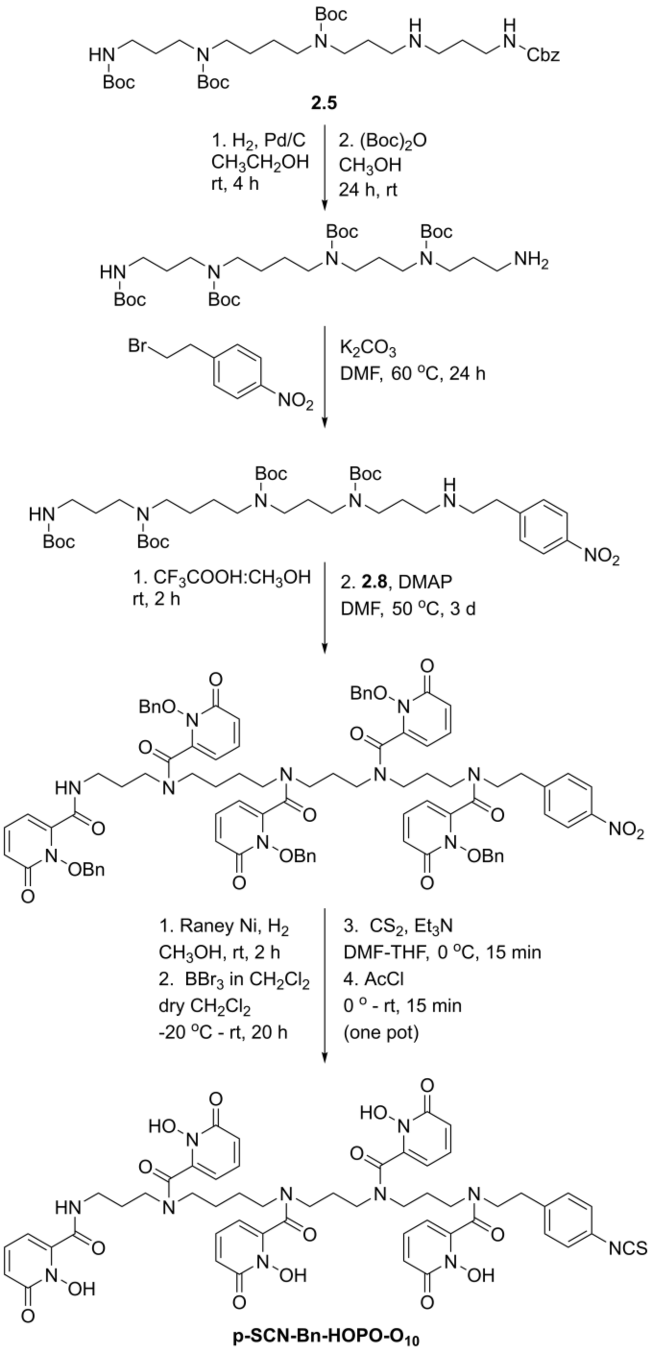

Figure 5.1. Proposed synthetic route towards p-SCN-Bn-HOPO-O$_{10}$.

The logical continuation of this project would be to evaluate the stability of the ^{161}Tb and ^{227}Th complexes of HOPO-O$_{10}$ and HOPO-O$_8$ in healthy mice as the ultimate proof of the benefits of the extra 1,2-HOPO arm in the complex stability. Only if the stability of HOPO-O$_{10}$ is largely superior, I would suggest making HOPO-O$_{10}$ bifunctional due to its complexity. Although the current route was designed to include intermediate **2.5** for functionalization, the addition of a p-SCN-Bn involves 6 extra steps with a large molecule (>1000 MW) which may result in difficult purification of the intermediates. Despite this, we propose a synthetic route to prepare p-SCN-Bn-HOPO-O_{10} (**Figure 5.1**). This pathway is designed based on the similar chemistry employed to prepare p-SCN-Bn-HOPO-O_8 with additional knowledge from the cryptand work developed by our postdoc Dr. Anthony McDonagh.[261,349] It is worth mentioning that each step could require some optimization or even a change of conditions since the chemistry of such a large molecule is not always predictable. To prepare intermediate **2.5** efficiently, the direct addition of the Cbz-protected amine via tosylate coupling to spermine following LC/MSD purification would be the best option.

In chapter 3, we sought to explore the potential of branched hexadentate backbones containing three 1,2-HOPO or CAM ligands for the chelation of ^{47}Sc, ^{45}Ti and ^{68}Ga. The chelate structures were based on a tripodal backbone reported for iron transport-mediated drug delivery. Though not discussed in chapter 3, initially, the backbone was conjugated to three picolinic acids, and three carboxylic acids. These potentially nonadentate and dodecadentate chelators, respectively, were successfully synthesized and characterized. However, these chelators exhibited a high degree of steric hindrance and failed to complex La^{3+} or Tb^{3+}. Additionally, they did not exhibit significant radiometal incorporation when radiolabeled with ^{135}La, ^{225}Ac, or ^{89}Zr. Based on the recent progress made with catechol ligands for the stable coordination of ^{45}Ti, we maintained the tripodal backbone structure and changed the pendant arms to 1,2-HOPO and CAM, to form HOPO-O_6-C4 and CAM-O_6-C4, respectively. HOPO-O_6-C4 exhibited fast and stable coordination with Sc^{3+} and Ga^{3+} and highly promising radiolabeling properties with ^{47}Sc. Despite low in vitro stability, the complex exhibited a significantly different uptake profile compared to the unchelated radiometal suggesting high stability in vivo. However, these results will have to be confirmed after the biodistribution of $^{47}ScCl_3$ is repeated and the gallbladder is collected. On the other hand, CAM-O_6-C4 proved to be unstable in aqueous media after 12 h and thermodynamic and kinetic studies with Sc^{3+} and Ga^{3+} via ^{1}H NMR spectroscopy failed. Characterization of the Ti^{4+} and ^{45}Ti was performed by our collaborators in the Boros group (University of Wisconsin-Madison); HOPO-O_6-C4 was not included due to the complex formation only at low pH values. Multiple complexation species were identified with the non-radioactive and radioactive experiments which can be an indication of complex instability. Overall, CAM-O_6-C4 is not a suitable chelate for radiopharmaceutical development. The CAM-O_6-C_4 work is part of a manuscript in preparation for ^{45}Ti PSMA-based tracers. Lastly, ^{68}Ga radiolabeling will be performed at TRIUMF once the ^{68}Ge/^{68}Ga generators become available.

With the encouraging results of [^{47}Sc]Sc-HOPO-O_6-C4, the future of this project should look into making the chelate bifunctional and conjugation to a disease-targeting vector. A peptide or small molecule such as FAPI – which is attracting interest for fibroblast-associated cancer – would be best suited to match the shorter half-life of the ^{47}Sc imaging pair ^{43}Sc. Similar to HOPO-O_{10}, we propose a synthetic route based on our previously investigated chemistry to prepare a bifunctional version of HOPO-O_6-C4 through the free NH_2 group on the backbone (intermediate **3.1**) (**Figure 5.2**).[349]

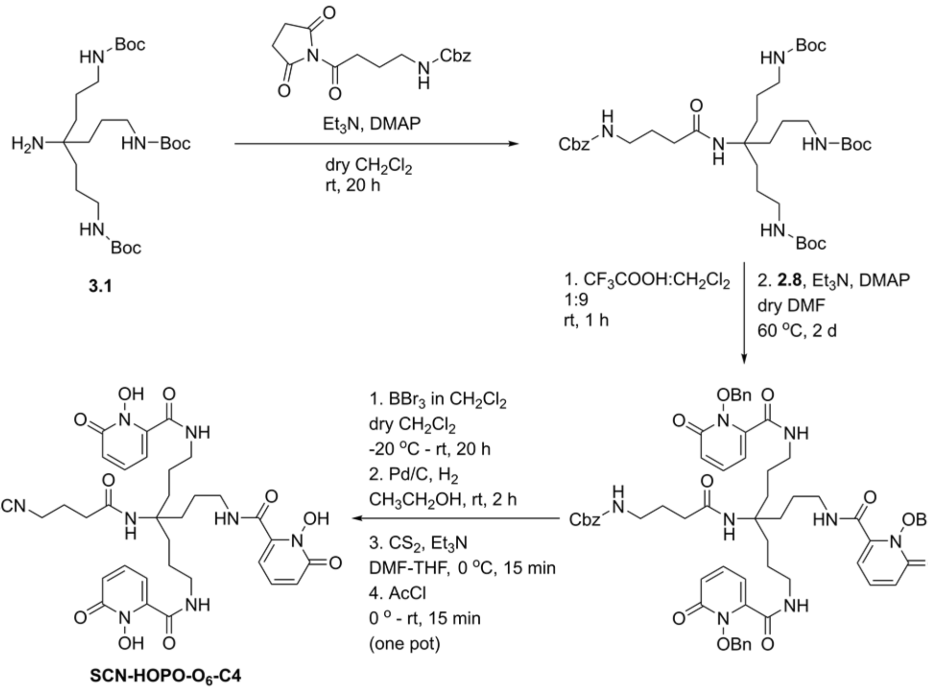

Figure 5.2. Proposed synthetic route to prepare bifunctional SCN-HOPO-O_6-C4.

In literature, the authors used methyl succinyl chloride to ultimately obtain a free carboxylic acid to conjugate with the targeting vector. However, for the conjugation to FAPI, an SCN group was chosen due to its higher reactivity because the NH group is located in a hexagon ring and our group has observed lower reactivity in these configurations (**Figure 5.3**). Both the synthesis of SCN-HOPO-O_6-C4 and the conjugation to FAPI are rather straightforward and even though some optimization may be required, obtaining the bioconjugate is expected to be easily accessible. The radiolabeling and preclinical evaluation of FAPI-O_6-C4 with ^{44}Sc could potentially be carried out at TRIUMF by an incoming graduate student in our group who is interested in the isotope production since ^{44}Sc has been previously produced and purified in-house.

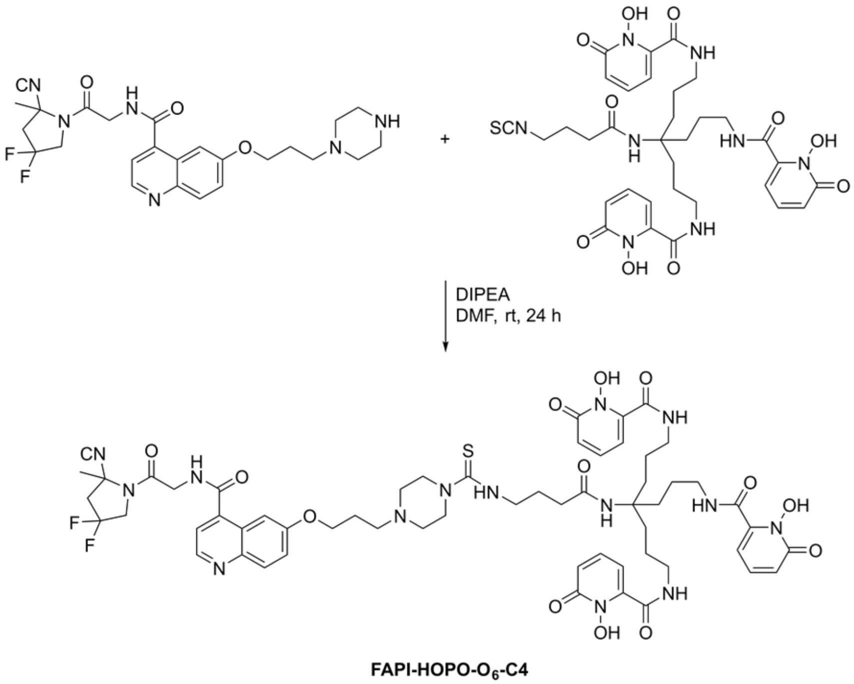

Figure 5.3. Preparation of the bioconjugate FAPI-HOPO-O_6-C4 via the NCS coupling of SCN-HOPO-O_6-C4 to FAPI.

Chapter 4 presented the synthesis of a novel bifunctional HOPO-O_8 derivative (HOPO-O_8-Me-Tz) based on the excellent radiolabeling results obtained in chapter 2. The BFC incorporates a Tz moiety for pretargeting strategies. This approach uses click chemistry to conjugate in vivo the mAb and the radiolabeled BFC via a click chemistry reaction, in this case, a Tz and a TCO. Doing so, the circulation time of the radioisotope is reduced from 3-7 days to 1-2 days reducing drastically the radiation deposition to off-target tissue. HOPO-O_8-Me-Tz was demonstrated to retain the ^{89}Zr, ^{161}Tb, and ^{227}Th radiolabeling efficiency compared to HOPO-O_8 and showed high in vitro stability. Due to the complexity of performing pretargeting studies, we opted to follow the conventional strategy by conjugating the BFC and mAb in vitro in a proof-of-concept study. The pre-clicked tracer was radiolabeled with ^{89}Zr and ^{161}Tb and evaluated in vivo. Issues with the tumor growth resulted in microscopic or absent SKOV3 tumor xenografts impeding the observation of tumor uptake. The pharmacokinetics and uptake analysis of [^{161}Tb]Tb-

HOPO-O_8-Tzmb revealed long circulation times, excretion via the RES and an exceptionally high spleen uptake which will have to be further investigated to confirm if it was caused by the presence of tracer aggregates. In vivo PET/CT was not possible at the time of the [^{89}Zr]Zr-HOPO-O_8-Tzmb study; however, excellent in vivo stability was observed by the absence of joint or bone uptake in the ex vivo biodistribution analysis at 144 h.

The near future of the HOPO-O_8-Me-Tz project involves repeating both animal studies with optimal tumor sizes to reevaluate the biodistribution and tumor uptake as well as the BFC [^{89}Zr]Zr-HOPO-O_8-Me-Tz in healthy mice to ensure in vivo stability for pretargeting studies. The long-term goal of this project will be the in vivo evaluation of the theranostic pair ^{134}Ce and ^{227}Th in a pretargeting study. These studies will be carried out at the University of California San Francisco by the Flavell group with whom we have been collaborating for the past 8 months. At the time of writing, the radiolabeling efficiency of HOPO-O_8-Me-Tz with ^{134}Ce has already been evaluated revealing high molar activities (~ 1:1 metal-to-chelate ratio) and an efficient click reaction with their mAb YS5. The next steps for this project would be the following:

1. Radiolabeling of the HOPO-O_8-Me-Tz with ^{227}Th.
2. In vivo evaluation of both [^{134}Ce]Ce-HOPO-O_8-Me-Tz and [^{227}Th]Th-HOPO-O_8-Me-Tz to confirm their stability.
3. Comparing the ex vivo biodistribution of the radiopharmaceutical prepared via the conventional way (preclicked tracer) or in vivo pretargeting to demonstrate the benefits of pretargeting strategies in the tumor and healthy tissue uptake.
4. Optimize the interval time between injection of YS5 and the radiolabeled BFC.
5. Evaluate the theranostic pretargeting strategy by first injecting [^{134}Ce]Ce-HOPO-O_8-Me-Tz to obtain a PET/CT image of the mice followed by therapeutic studies with multiple treatment cycles of [^{227}Th]Th-HOPO-O_8-Me-Tz.

The success of this project could represent the first pretargeting approach using two exotic radiometals.

5.2. Thesis outlook and future directions

The future of nuclear medicine for theranostics is very promising due to its capacity to simultaneously image and treat cancer, differing from the majority of other cancer therapies. A variety of novel isotopes (e.g., ^{225}Ac or ^{161}Tb) have been recently introduced in the preclinical research portfolio and are being assessed in multiple clinical trials even though global availability still remains a challenge. Finding suitable chelates for these exotic radiometals is key to their success along with the discovery of more specific tumor targets.

In the Ramogida group, we have an excellent team dynamic between the synthetic and the production team to pursue research according to our discoveries and needs. For example, the students in the production of novel isotopes work closely with the students focused on finding chelates suitable for such isotopes and vice versa, chelates that were unsuccessful with the expected isotopes can be tested with other radiometals available in-house. This team effort is leading to highly promising results, some of them presented in this work. In my opinion, once a suitable radiometal-chelate pair is found, the research should continue toward its preclinical application. With the new cell lab at TRIUMF and the collaborations with CCM for imaging and therapy studies, our group has an excellent network to complete the process of developing and evaluating a novel radiopharmaceutical.

Two of the projects with more research and novelty potential are the ^{44}Sc and ^{227}Th radiopharmaceuticals. Both radiometals have low availability worldwide and TRIUMF is one of the exclusive research centers with access to them. In the case of ^{227}Th, there is extremely limited preclinical and clinical data. Based on this, my fellow MSc student Lucas London started a project a few months ago to explore the potential of ^{227}Th peptide-based radiopharmaceuticals, coupling the peptide α-MSH to the previously reported p-SCN-Bn-HOPO-O_8 BFC, opening a new unexplored area (**Figure 5.4**). A very interesting in vitro and in vivo comparison could be performed with the radioimmunoconjugate HOPO-O_8-Tzmb and his peptide-based tracer. The preclinical evaluation would be of high interest to understand the potential of such a powerful α emitter with both types of drug complexes. Besides this project, investigations on novel second-generation chelates for ^{227}Th would be worth pursing.

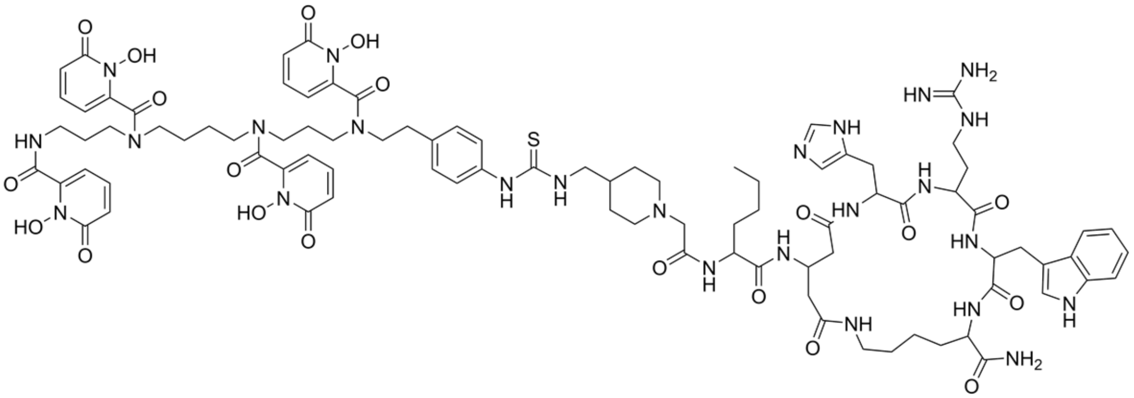

Figure 5.4. Chemical structure of the peptide bioconjugate α-MSH-HOPO-O_8 for ^{227}Th chelation.

On the other hand, investigations on ^{44}Sc are of interest due to the longer half-life compared to the widely used imaging isotope ^{68}Ga allowing for imaging at later time points. The development of ^{44}Sc radiopharmaceuticals in our group is at an earlier stage. We presented here some efforts toward the stable chelation of these labile radiometals setting the base for further bifunctional chelate development. After the preclinical evaluation of FAPI-HOPO-O_6-C4, a second generation of chelates could be designed to tune the pharmacological properties of the drug to improve the radiopharmaceutical performance. These modifications could include modifying the length of the backbone or changing the bifunctional handle and linker to change its lipophilicity and charge.

Overall, nuclear medicine is rapidly evolving and in the coming years, I would expect to see an increasing number of radiopharmaceuticals become available for routine treatment. I believe the Ramogida group will positively contribute to its success.

References

(1) Sgouros, G.; Bodei, L.; McDevitt, M. R.; Nedrow, J. R. Radiopharmaceutical Therapy in Cancer: Clinical Advances and Challenges. *Nature Reviews Drug Discovery* **2020**, *19* (9), 589–608. https://doi.org/10.1038/s41573-020-0073-9.

(2) Madsen, M. T. Recent Advances in SPECT Imaging. *Journal of Nuclear Medicine* **2007**, *48* (4), 661–673. https://doi.org/10.2967/jnumed.106.032680.

(3) Slomka, P. J.; Pan, T.; Germano, G. Recent Advances and Future Progress in PET Instrumentation. *Seminars in Nuclear Medicine* **2016**, *46* (1), 5–19. https://doi.org/10.1053/j.semnuclmed.2015.09.006.

(4) Cutler, C. S.; Hennkens, H. M.; Sisay, N.; Huclier-Markai, S.; Jurisson, S. S. Radiometals for Combined Imaging and Therapy. *Chemical Reviews* **2013**, *113* (2), 858–883. https://doi.org/10.1021/cr3003104.

(5) Ramogida, C. F.; Orvig, C. Tumour Targeting with Radiometals for Diagnosis and Therapy. *Chemical Communications* **2013**, *49* (42), 4720. https://doi.org/10.1039/c3cc41554f.

(6) Kostelnik, T. I.; Orvig, C. Radioactive Main Group and Rare Earth Metals for Imaging and Therapy. *Chemical Reviews* **2019**, *119* (2), 902–956. https://doi.org/10.1021/acs.chemrev.8b00294.

(7) Brechbiel, M. W. Bifunctional Chelates for Metal Nuclides. *The quarterly journal of nuclear medicine and molecular imaging* **2008**, *52* (2), 166–173.

(8) Price, E. W.; Orvig, C. Matching Chelators to Radiometals for Radiopharmaceuticals. *Chemical Society Reviews* **2014**, *43* (1), 260–290. https://doi.org/10.1039/c3cs60304k.

(9) Parker, C.; Nilsson, S.; Heinrich, D.; Helle, S. I.; O'Sullivan, J. M.; Fosså, S. D.; Chodacki, A.; Wiechno, P.; Logue, J.; Seke, M.; Widmark, A.; Johannessen, D. C.; Hoskin, P.; Bottomley, D.; James, N. D.; Solberg, A.; Syndikus, I.; Kliment, J.; Wedel, S.; Boehmer, S.; Dall'Oglio, M.; Franzén, L.; Coleman, R.; Vogelzang, N. J.; O'Bryan-Tear, C. G.; Staudacher, K.; Garcia-Vargas, J.; Shan, M.; Bruland, Ø. S.; Sartor, O. Alpha Emitter Radium-223 and Survival in Metastatic Prostate Cancer. *New England Journal of Medicine* **2013**, *369* (3), 213–223. https://doi.org/10.1056/NEJMoa1213755.

(10) Van Der Gucht, A.; Jreige, M.; Denys, A.; Blanc-durand, P.; Boubaker, A.; Pomoni, A.; Mitsakis, P.; Silva-monteiro, M.; Gnesin, S.; Lalonde, M. N.; Duran, R.; Prior, J. O.; Schaefer, N. Resin Versus Glass Microspheres for 90Y Transarterial Radioembolization: Comparing Survival in Unresectable Model Dosimetry. *Journal of Nuclear Medicine* **2017**, *58* (8), 1334–1341. https://doi.org/10.2967/jnumed.116.184713.

(11) Ognjanović, M.; Radović, M.; Mirković, M.; Prijović, Ž.; Puerto Morales, M. D.; Čeh, M.; Vranješ-Durić, S.; Antić, B. 99mTc-, 90Y-, and 177Lu-Labeled Iron Oxide Nanoflowers Designed for Potential Use in Dual Magnetic Hyperthermia/Radionuclide Cancer Therapy and Diagnosis. *ACS Applied Materials and Interfaces* **2019**, *11* (44), 41109–41117. https://doi.org/10.1021/acsami.9b16428.

(12) Peltek, O. O.; Muslimov, A. R.; Zyuzin, M. V.; Timin, A. S. Current Outlook on Radionuclide Delivery Systems: From Design Consideration to Translation into Clinics. *Journal of Nanobiotechnology* **2019**, *17*, 90. https://doi.org/10.1186/s12951-019-0524-9.

(13) Jadvar, H.; Chen, X.; Cai, W.; Mahmood, U. Radiotheranostics in Cancer. *Radiology* **2018**, *286* (2), 388–400. https://doi.org/10.1148/radiol.2017170346.

(14) Notni, J.; Wester, H.-J. Re-thinking the Role of Radiometal Isotopes: Towards a Future Concept for Theranostic Radiopharmaceuticals. *Journal of Laballed Compounds and Radiopharmaceuticals* **2018**, *61*, 141–153. https://doi.org/10.1002/jlcr.3582.

(15) Miller, C.; Rousseau, J.; Ramogida, C. F.; Celler, A.; Rahmim, A.; Uribe, C. F. Implications of Physics, Chemistry and Biology for Dosimetry Calculations Using Theranostic Pairs. *Theranostics* **2022**, *27* (1), 232–259. https://doi.org/10.7150/THNO.62851.

(16) Nagarajah, J.; Janssen, M.; Hetkamp, P.; Jentzen, W. Iodine Symporter Targeting with 124I/131I Theranostics. *Journal of Nuclear Medicine* **2017**, *58* (9), 34–39. https://doi.org/10.2967/jnumed.116.186866.

(17) Rösch, F.; Herzog, H.; Qaim, S. M. The Beginning and Development of the Theranostic Approach in Nuclear Medicine, as Exemplified by the Radionuclide Pair 86Y and 90Y. *Pharmaceuticals* **2017**, *10* (56). https://doi.org/10.3390/ph10020056.

(18) Ballinger, J. R. Theranostic Radiopharmaceuticals: Established Agents in Current Use. *The British Journal of Radiology* **2018**, *91* (1091), 20170969. https://doi.org/10.1259/bjr.20170969.

(19) Lau, J.; Kwon, D.; Rousseau, E.; Zhang, Z.; Zeisler, J.; Uribe, C. F.; Kuo, H.-T.; Zhang, C.; Lin, K.-S.; Bénard, F. [68Ga]Ga/[177Lu]Lu-BL01, a Novel Theranostic Pair for Targeting C-X-C Chemokine Receptor 4. *Molecular Pharmaceutics* **2019**, *16* (11), 4688–4695. https://doi.org/10.1021/acs.molpharmaceut.9b00808.

(20) Weineisen, M.; Schottelius, M.; Simecek, J.; Baum, R. P.; Yildiz, A.; Beykan, S.; Kulkarni, H. R.; Lassmann, M.; Klette, I.; Eiber, M.; Schwaiger, M.; Wester, H.-J. 68Ga- and 177 Lu-Labeled PSMA I&T: Optimization of a PSMA-Targeted Theranostic Concept and First Proof-of-Concept Human Studies. *Journal of Nuclear Medicine* **2015**, *56* (8), 1169–1177. https://doi.org/10.2967/jnumed.115.158550.

(21) Basu, S.; Abhyankar, A. The Use of 99mTc-HYNIC-TOC and 18F-FDG PET/CT in the Evaluation of Duodenal Neuroendocrine Tumor with Atypical and Extensive Metastasis Responding. *Journal of Nuclear Medicine Technology* **2014**, *42* (4), 296–299. https://doi.org/10.2967/jnmt.114.139238.

(22) Pouget, J. P.; Navarro-Teulon, I.; Bardiès, M.; Chouin, N.; Cartron, G.; Pèlegrin, A.; Azria, D. Clinical Radioimmunotherapy-the Role of Radiobiology. *Nature Reviews Clinical Oncology* **2011**, *8* (12), 720–734. https://doi.org/10.1038/nrclinonc.2011.160.

(23) Pouget, J.-P.; Lozza, C.; Deshayes, E.; Boudousq, V.; Navarro-Teulon, I. Introduction to Radiobiology of Targeted Radionuclide Therapy. *Frontiers in Medicine* **2015**, *2* (12). https://doi.org/10.3389/fmed.2015.00012.

(24) Kassis, A. I. Therapeutic Radionuclides: Biophysical and Radiobiologic Principles. *Seminars in Nuclear Medicine* **2008**, *38* (5), 358–366. https://doi.org/10.1053/j.semnuclmed.2008.05.002.

(25) Dekempeneer, Y.; Keyaerts, M.; Krasniqi, A.; Puttemans, J.; Muyldermans, S.; Lahoutte, T.; D'huyvetter, M.; Devoogdt, N. Targeted Alpha Therapy Using Short-Lived Alpha-Particles and the Promise of Nanobodies as Targeting Vehicle. *Expert Opinion on Biological Therapy* **2016**, *16* (8), 1035–1047. https://doi.org/10.1080/14712598.2016.1185412.

(26) Mothersill, C.; Rusin, A.; Fernandez-Palomo, C.; Seymour, C. History of Bystander Effects Research 1905-Present; What Is in a Name? *International Journal of Radiation Biology* **2018**, *94* (8), 696–707. https://doi.org/10.1080/09553002.2017.1398436.

(27) Hope, T. A.; Abbott, A.; Colucci, K.; Bushnell, D. L.; Gardner, L.; Graham, W. S.; Lindsay, S.; Metz, D. C.; Pryma, D. A.; Stabin, M. G.; Strosberg, J. R. NANETS/SNMMI Procedure Standard for Somatostatin Receptor – Based Peptide Receptor Radionuclide Therapy with 177Lu-DOTATATE. *Journal of Nuclear Medicine* **2019**, *60* (7), 937–944. https://doi.org/10.2967/jnumed.118.230607.

(28) Robertson, A. K. H.; Ramogida, C. F.; Schaffer, P.; Radchenko, V. Development of 225Ac Radiopharmaceuticals: TRIUMF Perspectives and Experiences. *Current Radiopharmaceuticals* **2018**, *11* (3), 156–172. https://doi.org/10.2174/1874471011666180416161908.

(29) Scheinberg, D. A.; McDevit, M. R. Actinium-225 in Targeted Alpha-Particle Therapeutic Applications. *Current Radiopharmaceuticals* **2011**, *4* (4), 306–320.

(30) Sgouros, G.; Roeske, J. C.; McDevitt, M. R.; Palm, S.; Allen, B. J.; Fisher, D. R.; Brill, A. B.; Song, H.; Howell, R. W.; Akabani, G. MIRD Pamphlet No. 22 (Abridged): Radiobiology and Dosimetry of α-Particle Emitters for Targeted Radionuclide Therapy. *Journal of Nuclear Medicine* **2010**, *51* (2), 311–328. https://doi.org/10.2967/jnumed.108.058651.

(31) Bäck, T.; Jacobsson, L. The α-Camera: A Quantitative Digital Autoradiography Technique Using a Charge-Coupled Device for Ex Vivo High-Resolution Bioimaging of α-Particles. *Journal of Nuclear Medicine* **2010**, *51* (10), 1616–1623. https://doi.org/10.2967/jnumed.110.077578.

(32) FDA Approves Pluvicto/Locametz for Metastatic Castration-Resistant Prostate Cancer. *Journal of Nuclear Medicine* **2022**, *63* (5), 13N.

(33) Kratochwil, C.; Bruchertseifer, F.; Giesel, F. L.; Weis, M.; Verburg, F. A.; Mottaghy, F.; Kopka, K.; Apostolidis, C.; Haberkorn, U.; Morgenstern, A. 225Ac-PSMA-617 for PSMA-Targeted -Radiation Therapy of Metastatic Castration-Resistant Prostate Cancer. *Journal of Nuclear Medicine* **2016**, *57* (12), 1941–1944. https://doi.org/10.2967/jnumed.116.178673.

(34) Kratochwil, C.; Giesel, F. L.; Bruchertseifer, F.; Mier, W.; Apostolidis, C.; Boll, R.; Murphy, K.; Haberkorn, U.; Morgenstern, A. 213Bi-DOTATOC Receptor-Targeted Alpha-Radionuclide Therapy Induces Remission in Neuroendocrine Tumours Refractory to Beta Radiation: A First-in-Human Experience. *European Journal of Nuclear Medicine and Molecular Imaging* **2014**, *41* (11), 2106–2119. https://doi.org/10.1007/s00259-014-2857-9.

(35) Marcu, L.; Bezak, E.; Allen, B. J. Global Comparison of Targeted Alpha vs Targeted Beta Therapy for Cancer: In Vitro, in Vivo and Clinical Trials. *Critical Reviews in Oncology/Hematology* **2018**, *123*, 7–20. https://doi.org/10.1016/j.critrevonc.2018.01.001.

(36) Orozco, J. J.; Bäck, T.; Kenoyer, A.; Balkin, E. R.; Hamlin, D. K.; Wilbur, D. S.; Fisher, D. R.; Frayo, S. L.; Hylarides, M. D.; Green, D. J.; Gopal, A. K.; Press, O. W.; Pagel, J. M. Anti-CD45 Radioimmunotherapy Using 211At with Bone Marrow Transplantation Prolongs Survival in a Disseminated Murine Leukemia Model. *Blood* **2013**, *121* (18), 3759–3767. https://doi.org/10.1182/blood-2012-11-467035.

(37) Beyer, G.-J.; Miederer, M.; Vranješ-Đurić, S.; Čomor, J. J.; Künzi, G.; Hartley, O.; Senekowitsch-Schmidtke, R.; Soloviev, D.; Buchegger, F. Targeted Alpha Therapy in Vivo: Direct Evidence for Single Cancer Cell Kill Using 149Tb-Rituximab. *European Journal of Nuclear Medicine and Molecular Imaging* **2004**, *31* (4), 547–554. https://doi.org/10.1007/s00259-003-1413-9.

(38) Umbricht, C. A.; Köster, U.; Bernhardt, P.; Gracheva, N.; Johnston, K.; Schibli, R.; van der Meulen, N. P.; Müller, C. Alpha-PET for Prostate Cancer: Preclinical Investigation Using 149Tb-PSMA-617. *Scientific Reports* **2019**, *9* (1), 17800. https://doi.org/10.1038/s41598-019-54150-w.

(39) Müller, C.; Reber, J.; Haller, S.; Dorrer, H.; Köster, U.; Johnston, K.; Zhernosekov, K.; Türler, A.; Schibli, R. Folate Receptor Targeted Alpha-Therapy Using Terbium-149. *Pharmaceuticals* **2014**, *7* (3), 353–365. https://doi.org/10.3390/ph7030353.

(40) Müller, C.; Zhernosekov, K.; Köster, U.; Johnston, K.; Dorrer, H.; Hohn, A.; van der Walt, N. T.; Türler, A.; Schibli, R. A Unique Matched Quadruplet of Terbium Radioisotopes for PET and SPECT and for α- and β- Radionuclide Therapy: An in Vivo Proof-of-Concept Study with a New Receptor-Targeted Folate Derivative. *Journal of Nuclear Medicine* **2012**, *53* (12), 1951–1959. https://doi.org/10.2967/jnumed.112.107540.

(41) Baum, R. P.; Singh, A.; Benešová, M.; Vermeulen, C.; Gnesin, S.; Köster, U.; Johnston, K.; Müller, D.; Senftleben, S.; Kulkarni, H. R.; Türler, A.; Schibli, R.; Prior, J. O.; van der Meulen, N. P.; Müller, C. Clinical Evaluation of the Radiolanthanide Terbium-152: First-in-Human PET/CT with 152Tb-DOTATOC. *Dalton Transactions* **2017**, *46* (42), 14638–14646. https://doi.org/10.1039/C7DT01936J.

(42) Müller, C.; Singh, A.; Umbricht, C. A.; Kulkarni, H. R.; Johnston, K.; Benešová, M.; Senftleben, S.; Müller, D.; Vermeulen, C.; Schibli, R.; Köster, U.; van der Meulen, N. P.; Baum, R. P. Preclinical Investigations and First-in-Human Application of 152Tb-PSMA-617 for PET/CT Imaging of Prostate Cancer. *European Journal of Nuclear Medicine and Molecular Imaging Research* **2019**, *9* (1), 68. https://doi.org/10.1186/s13550-019-0538-1.

(43) Müller, C.; Fischer, E.; Behe, M.; Köster, U.; Dorrer, H.; Reber, J.; Haller, S.; Cohrs, S.; Blanc, A.; Grünberg, J.; Bunka, M.; Zhernosekov, K.; van der Meulen, N.; Johnston, K.; Türler, A.; Schibli, R. Future Prospects for SPECT Imaging Using the Radiolanthanide Terbium-155 — Production and Preclinical Evaluation in Tumor-Bearing Mice. *Nuclear Medicine and Biology* **2014**, *41*, e58–e65. https://doi.org/10.1016/j.nucmedbio.2013.11.002.

(44) Zhang, X.; Gallazzi, F.; Deutscher, S.; Quinn, T. Pb-212-Labeled α-MSH Analogue Modified with a Nuclear Localization Sequence for Melanoma Targeting. *Nuclear Medicine and Biology* **2010**, *37* (6), 693–694. https://doi.org/10.1016/j.nucmedbio.2010.04.064.

(45) Stallons, T. A. R.; Saidi, A.; Tworowska, I.; Delpassand, E. S.; Torgue, J. J. Preclinical Investigation of 212Pb-DOTAMTATE for Peptide Receptor Radionuclide Therapy in a Neuroendocrine Tumor Model. *Molecular Cancer Therapeutics* **2019**, *18* (5), 1012–1021. https://doi.org/10.1158/1535-7163.MCT-18-1103.

(46) Banerjee, S. R.; Minn, I.; Kumar, V.; Josefsson, A.; Lisok, A.; Brummet, M.; Chen, J.; Kiess, A. P.; Baidoo, K.; Brayton, C.; Mease, R. C.; Brechbiel, M.; Sgouros, G.; Hobbs, R. F.; Pomper, M. G. Preclinical Evaluation of 203/212Pb-Labeled Low-Molecular-Weight Compounds for Targeted Radiopharmaceutical Therapy of Prostate Cancer. *Journal of Nuclear Medicine* **2020**, *61* (1), 80–89. https://doi.org/10.2967/jnumed.119.229393.

(47) dos Santos, J. C.; Schäfer, M.; Bauder-Würst, U.; Lehnert, W.; Leotta, K.; Morgenstern, A.; Kopka, K.; Haberkorn, U.; Mier, W.; Kratochwil, C. Development and Dosimetry of Pb-203/Pb-212 Labeled PSMA Ligands – Bringing “the Lead” into PSMA-Targeting Alpha Therapy? *European Journal of Nuclear Medicine and Molecular Imaging* **2019**, *46*, 1081–1091. https://doi.org/10.1055/s-0039-1683594.

(48) Meredith, R. F.; Torgue, J. J.; Rozgaja, T. A.; Banaga, E. P.; Bunch, P. W.; Alvarez, R. D.; Straughn, J. M. J.; Dobelbower, M. C.; Lowy, A. M. Safety and Outcome Measures of First-in-Human Intraperitoneal α Radioimmunotherapy With 212Pb-TCMC-Trastuzumab. *American Journal of Clinical Oncology* **2018**, *41* (7), 716–712.

(49) Meredith, R. F.; Torgue, J.; Azure, M. T.; Shen, S.; Saddekni, S.; Banaga, E.; Carlise, R.; Bunch, P.; Yoder, D.; Alvarez, R. Pharmacokinetics and Imaging of 212-

Pb-TCMC-Trastuzumab After Intraperitoneal Administration in Ovarian Cancer Patients. *Cancer Biotherapy and Radiopharmaceuticals* **2014**, *29* (1), 12–17. https://doi.org/10.1089/cbr.2013.1531.

(50) Stenberg, V. Y.; Juzeniene, A.; Chen, Q.; Yang, X.; Bruland, Ø. S.; Larsen, R. H. Preparation of the Alpha-Emitting Prostate-Specific Membrane Antigen Targeted Radioligand [212Pb]Pb-NG001 for Prostate Cancer. *Journal of Labelled Compounds and Radiopharmaceuticals* **2020**, *63*, 129–143. https://doi.org/10.1002/jlcr.3825.

(51) McDonagh, A. W.; McNeil, B. L.; Patrick, B. O.; Ramogida, C. F. Synthesis and Evaluation of Bifunctional [2.2.2]-Cryptands for Nuclear Medicine Applications. *Inorganic Chemistry* **2021**, *60* (13), 10030–10037. https://doi.org/10.1021/acs.inorgchem.1c01274.

(52) McNeil, B. L.; Kadassery, K. J.; McDonagh, A. W.; Zhou, W.; Schaffer, P.; Wilson, J. J.; Ramogida, C. F. Evaluation of the Effect of Macrocyclic Ring Size on [203Pb]Pb(II) Complex Stability in Pyridyl-Containing Chelators. *Inorganic Chemistry* **2022**, *61* (25), 9638–9649. https://doi.org/10.1021/acs.inorgchem.2c01114.

(53) Jurcic, J. G.; Levy, M. Y.; Park, J. H.; Ravandi, F.; Perl, A. E.; Pagel, J. M.; Smith, B. D.; Estey, E. H.; Kantarjian, H.; Cicic, D.; Scheinberg, D. A. Phase I Trial of Targeted Alpha-Particle Therapy with Actinium-225 (225Ac)-Lintuzumab and Low-Dose Cytarabine (LDAC) in Patients Age 60 or Older with Untreated Acute Myeloid Leukemia (AML). *Blood* **2016**, *128* (22), 4050–4050. https://doi.org/10.1182/blood.V128.22.4050.4050.

(54) Krolicki, L.; Bruchertseifer, F.; Kunikowska, J.; Koziara, H.; Krolicki, B.; Pawlak, D.; Apostolidis, C.; Rola, R.; Merlo, A.; Morgenstern, A. Targeted Alpha Therapy of Glioblastoma Multiforme: Clinical Experience with 213Bi- and 225Ac-Substance P. In *Proceedings of the 10th International Symposium on Target Alpha Therapy*; Kanazawa, Japan, 2017.

(55) Zhang, J.; Kulkarni, H. R.; Baum, R. P. Peptide Receptor Radionuclide Therapy Using 225Ac-DOTATOC Achieves Partial Remission in a Patient With Progressive Neuroendocrine Liver Metastases After Repeated β-Emitter Peptide Receptor Radionuclide Therapy. *Clinical Nuclear Medicine* **2020**, *45* (3), 241–243. https://doi.org/10.1097/RLU.0000000000002915.

(56) Norenberg, J.; Daniels, T.; Kevin, J.; Heloisa, S.; Kusewitt, D.; Hesterman, J.; Orcutt, K.; Nysus, M.; Goff, C.; Jacquez, Q.; Rixe, O.; Fair, J. Pre-Clinical Evaluation of 225Ac-DOTATOC Pharmacokinetics, Dosimetry, and Histopathology to Enable Phase-1 Clinical Trial in Patients with Neuroendocrine Tumors. *Journal of Medical Imaging and Radiation Sciences* **2019**, *50* (1), S33–S34. https://doi.org/10.1016/j.jmir.2019.03.103.

(57) Sathekge, M.; Bruchertseifer, F.; Knoesen, O.; Reyneke, F.; Lawal, I.; Lengana, T.; Davis, C.; Mahapane, J.; Corbett, C.; Vorster, M.; Morgenstern, A. 225Ac-PSMA-617 in Chemotherapy-Naive Patients with Advanced Prostate Cancer: A Pilot Study. *European Journal of Nuclear Medicine and Molecular Imaging* **2019**, *46* (1), 129–138. https://doi.org/10.1007/s00259-018-4167-0.

(58) Kelly, V. J.; Wu, S.; Gottumukkala, V.; Coelho, R.; Palmer, K.; Nair, S.; Erick, T.; Puri, R.; Ilovich, O.; Mukherjee, P. Preclinical Evaluation of an 111In/225Ac Theranostic Targeting Transformed MUC1 for Triple Negative Breast Cancer. *Theranostics* **2020**, *10* (15), 6946–6958. https://doi.org/10.7150/thno.38236.

(59) Thiele, N. A.; Brown, V.; Kelly, J. M.; Amor-Coarasa, A.; Jermilova, U.; MacMillan, S. N.; Nikolopoulou, A.; Ponnala, S.; Ramogida, C. F.; Robertson, A. K. H.; Rodríguez-Rodríguez, C.; Schaffer, P.; Williams, C.; Babich, J. W.; Radchenko, V.;

Wilson, J. J. An Eighteen-Membered Macrocyclic Ligand for Actinium-225 Targeted Alpha Therapy. *Angewandte Chemie International Edition* **2017**, *56* (46), 14712–14717. https://doi.org/10.1002/anie.201709532.

(60) Comba, P.; Jermilova, U.; Orvig, C.; Patrick, B. O.; Ramogida, C. F.; Rück, K.; Schneider, C.; Starke, M. Octadentate Picolinic Acid-Based Bispidine Ligand for Radiometal Ions. *Chemistry European Journal* **2017**, *23* (63), 15945–15956. https://doi.org/10.1002/chem.201702284.

(61) Yang, H.; Zhang, C.; Yuan, Z.; Rodriguez-Rodriguez, C.; Robertson, A.; Radchenko, V.; Perron, R.; Gendron, D.; Causey, P.; Gao, F.; Bénard, F.; Schaffer, P. Synthesis and Evaluation of a Macrocyclic Actinium-225 Chelator, Quality Control and In Vivo Evaluation of 225Ac-crown-αMSH Peptide. *Chemistry – A European Journal* **2020**, *26* (50), 11435–11440. https://doi.org/10.1002/chem.202002999.

(62) Li, L.; Rousseau, J.; Jaraquemada-Peláez, M. de G.; Wang, X.; Robertson, A.; Radchenko, V.; Schaffer, P.; Lin, K.-S.; Bénard, F.; Orvig, C. 225Ac-H4py4pa for Targeted Alpha Therapy. *Bioconjugate Chemistry* **2021**, *32* (7), 1348–1363. https://doi.org/10.1021/acs.bioconjchem.0c00171.

(63) Abbas, N.; Heyerdahl, H.; Bruland, O.; Brevik, E.; Dahle, J. Comparing High LET 227Th- and Low LET 177Lu-Trastuzumab in Mice with HER-2 Positive SKBR-3 Xenografts. *Current Radiopharmaceuticals* **2013**, *6* (2), 78–86. https://doi.org/10.2174/18744710113069990017.

(64) Hagemann, U. B.; Ellingsen, C.; Schuhmacher, J.; Kristian, A.; Mobergslien, A.; Cruciani, V.; Wickstroem, K.; Schatz, C. A.; Kneip, C.; Golfier, S.; Smeets, R.; Uran, S.; Hennekes, H.; Karlsson, J.; Bjerke, R. M.; Ryan, O. B.; Mumberg, D.; Ziegelbauer, K.; Cuthbertson, A. S. Mesothelin-Targeted Thorium-227 Conjugate (MSLN-TTC): Preclinical Evaluation of a New Targeted Alpha Therapy for Mesothelin-Positive Cancers. *Clinical Cancer Research* **2019**, *25* (15), 4723–4734. https://doi.org/10.1158/1078-0432.CCR-18-3476.

(65) Hammer, S.; Hagemann, U. B.; Zitzmann-Kolbe, S.; Larsen, A.; Ellingsen, C.; Geraudie, S.; Grant, D.; Indrevoll, B.; Smeets, R.; von Ahsen, O.; Kristian, A.; Lejeune, P.; Hennekes, H.; Karlsson, J.; Bjerke, R. M.; Ryan, O. B.; Cuthbertson, A. S.; Mumberg, D. Preclinical Efficacy of a PSMA-Targeted Thorium-227 Conjugate (PSMA-TTC), a Targeted Alpha Therapy for Prostate Cancer. *Clinical Cancer Research* **2020**, *26* (8), 1985–1996. https://doi.org/10.1158/1078-0432.CCR-19-2268.

(66) Beyer, G. J.; Čomor, J. J.; Daković, M.; Soloviev, D.; Tamburella, C.; Hagebø, E.; Allan, B.; Dmitriev, S. N.; Zaitseva, N. G.; Starodub, G. Y.; Molokanova, L. G.; Vranješ, S.; Miederer, M. Production Routes of the Alpha Emitting 149Tb for Medical Application. *Radiochimica Acta* **2002**, *90* (5), 247–252. https://doi.org/10.1524/ract.2002.90.5_2002.247.

(67) Steyn, G. F.; Vermeulen, C.; Szelecsényi, F.; Kovács, Z.; Hohn, A.; Meulen, N. P. V. D.; Schibli, R.; Walt, T. N. V. D. Cross Sections of Proton-Induced Reactions on 152Gd , 155Gd and with Emphasis on the Production of Selected Tb Radionuclides Tb. *Nuclear Instruments and Methods in Physics Research B: Beam Interactions with Materials and Atoms* **2014**, *319*, 128–140. https://doi.org/10.1016/j.nimb.2013.11.013.

(68) Shannon, R. D. Revised Effective Ionic Radii and Systematic Studies of Interatomic Distances in Halides and Chalcogenides. *Acta Crystallographica Section A* **1976**, *32* (5), 751–767. https://doi.org/10.1107/S0567739476001551.

(69) Müller, C.; Umbricht, C. A.; Gracheva, N.; Tschan, V. J.; Pellegrini, G.; Bernhardt, P.; Zeevaart, J. R.; Köster, U.; Schibli, R.; van der Meulen, N. P. Terbium-161 for

PSMA-Targeted Radionuclide Therapy of Prostate Cancer. *European Journal of Nuclear Medicine and Molecular Imaging* **2019**, *46* (9), 1919–1930. https://doi.org/10.1007/s00259-019-04345-0.

(70) Müller, C.; Vermeulen, C.; Köster, U.; Johnston, K.; Türler, A.; Schibli, R.; van der Meulen, N. P. Alpha-PET with Terbium-149: Evidence and Perspectives for Radiotheragnostics. *European Journal of Nuclear Medicine and Molecular Imaging Radiopharmacy and Chemistry* **2017**, *1* (1), 5. https://doi.org/10.1186/s41181-016-0008-2.

(71) Baidoo, K. E.; Milenic, D. E.; Brechbiel, M. W. Methodology for Labeling Proteins and Peptides with Lead-212 (212Pb). *Nuclear Medicine and Biology* **2013**, *40* (5), 592–599. https://doi.org/10.1016/j.nucmedbio.2013.01.010.

(72) Westrøm, S.; Generalov, R.; Bønsdorff, T. B.; Larsen, R. H. Preparation of 212Pb-Labeled Monoclonal Antibody Using a Novel 224Ra-Based Generator Solution. *Nuclear Medicine and Biology* **2017**, *51*, 1–9. https://doi.org/10.1016/j.nucmedbio.2017.04.005.

(73) Bharara, M. S.; Atwood, D. A. Lead: Inorganic Chemistry Based in Part on the Article Lead: Inorganic Chemistry by Philip G. Harrison Which Appeared in the Encyclopedia of Inorganic Chemistry, First Edition. In *Encyclopedia of Inorganic and Bioinorganic Chemistry*; John Wiley & Sons, Ltd, 2011. https://doi.org/10.1002/9781119951438.eibc0111.

(74) Chappell, L. L.; Dadachova, E.; Milenic, D. E.; Garmestani, K.; Wu, C.; Brechbiel, M. W. Synthesis, Characterization, and Evaluation of a Novel Bifunctional Chelating Agent for the Lead Isotopes 203Pb and 212Pb. *Nuclear Medicine and Biology* **2000**, *27* (99), 93–100.

(75) Mirzadeh, S.; Kumar, K.; Gansow, O. A. The Chemical Fate of 212Bi-DOTA Formed by B- Decay of 212Pb(DOTA)2-. *Radiochimica Acta* **1993**, *60*, 1–10. https://doi.org/10.1524/ract.1993.60.1.1.

(76) Horak, E.; Hartmann, F.; Garmestani, K.; Wu, C.; Brechbiel, M.; Gansow, O. A.; Landolfi, N. F.; Waldmann, T. A. Radioimmunotherapy Targeting of HER2/Neu Oncoprotein on Ovarian Tumor Using Lead-212-DOTA-AE1. *Journal of Nuclear Medicine* **1997**, *38* (12), 893–895.

(77) Ruble, G.; Chuanchu, W.; Squire, R. A.; Gansow, O. A.; Strand, M. The Use of 212PB-Labeled Monoclonal Antibody in the Treatment of Murine Erythroleukemia. *International Journal of Radiation Oncology Biology Physics* **1996**, *34* (3), 609–616. https://doi.org/10.1016/0360-3016(95)02119-1.

(78) Yong, K.; Brechbiel, M. Application of 212Pb for Targeted α-Particle Therapy (TAT): Pre-Clinical and Mechanistic Understanding through to Clinical Translation. *AIMS Medical Science* **2015**, *2* (3), 228–245. https://doi.org/10.3934/medsci.2015.3.228.

(79) Yong, K. J.; Milenic, D. E.; Baidoo, K. E.; Brechbiel, M. W. Pb-Radioimmunotherapy Induces G2 Cell-Cycle Arrest and Delays DNA Damage Repair in Tumor Xenografts in a Model for Disseminated Intraperitoneal Disease. *Molecular Cancer Therapeutics* **2012**, *11* (3), 639–649. https://doi.org/10.1158/1535-7163.MCT-11-0671.

(80) Meredith, R.; Torgue, J.; Shen, S.; Fisher, D. R.; Banaga, E.; Bunch, P.; Morgan, D.; Fan, J.; Straughn, Jr, J. M. Dose Escalation and Dosimetry of First-in-Human Radioimmunotherapy with 212Pb-TCMC-Trastuzumab. *Journal of Nuclear Medicine* **2014**, *55* (10), 1636–1642. https://doi.org/10.2967/jnumed.114.143842.

(81) Yong, K. J.; Milenic, D. E.; Baidoo, K. E.; Brechbiel, M. W. Sensitization of Tumor to 212Pb-Radioimmunotherapy by Gemcitabine Involves Initial Abrogation of G2 Arrest and Blocked DNA Damage Repair by Interface with Rad51. *International*

Journal of Radiation Oncology Biology Physics **2013**, *85* (4), 1119–1126. https://doi.org/10.1038/jid.2014.371.

(82) Kurth, J.; Krause, B. J.; Schwarzenböck, S. M.; Stegger, L.; Schäfers, M.; Rahbar, K. External Radiation Exposure, Excretion, and Effective Half-Life in 177Lu-PSMA-Targeted Therapies. *European Journal of Nuclear Medicine and Molecular Imaging Research* **2018**, *8* (1), 32. https://doi.org/10.1186/s13550-018-0386-4.

(83) Miao, Y.; Hylarides, M.; Fisher, D. R.; Shelton, T.; Moore, H.; Wester, D. W.; Fritzberg, A. R.; Winkelmann, C. T.; Hoffman, T.; Quinn, T. P. Melanoma Therapy via Peptide-Targeted A-Radiation. *Clinical Cancer Research* **2005**, *11* (15), 5616–5622.

(84) Zhang, C.; Lin, K.-S.; Bénard, F. Molecular Imaging and Radionuclide Therapy of Melanoma Targeting the Melanocortin 1 Receptor. *Molecular Imaging* **2017**, *16*, 1–15. https://doi.org/10.1177/1536012117737919.

(85) Garmestani, K.; Milenic, D. E.; Brady, E. D.; Plascjak, P. S.; Brechbiel, M. W. Purification of Cyclotron-Produced 203Pb for Labeling Herceptin. *Nuclear Medicine and Biology* **2005**, *32* (3), 301–305. https://doi.org/10.1016/j.nucmedbio.2004.11.004.

(86) Li, M.; Zhang, X.; Quinn, T. P.; Lee, D.; Liu, D.; Kunkel, F.; Zimmerman, B. E.; McAlister, D.; Olewein, K.; Menda, Y.; Mirzadeh, S.; Copping, R.; Johnson, F. L.; Schultz, M. K. Automated Cassette-Based Production of High Specific Activity [203/212Pb] Peptide-Based Theranostic Radiopharmaceuticals for Image-Guided Radionuclide Therapy for Cancer. *Applied Radiation and Isotopes* **2017**, *127*, 52–60. https://doi.org/10.1016/j.apradiso.2017.05.006.

(87) Zielinska, B.; Apostolidis, C.; Bruchertseifer, F.; Morgenstern, A. An Improved Method for the Production of Ac-225/Bi-213 from Th-229 for Targeted Alpha Therapy. *Solvent Extraction and Ion Exchange* **2007**, *25* (3), 339–349. https://doi.org/10.1080/07366290701285108.

(88) Boll, R. A.; Malkemus, D.; Mirzadeh, S. Production of Actinium-225 for Alpha Particle Mediated Radioimmunotherapy. *Applied Radiation and Isotopes* **2005**, *62* (5), 667–679. https://doi.org/10.1016/j.apradiso.2004.12.003.

(89) Apostolidis, C.; Molinet, R.; Rasmussen, G.; Morgenstern, A. Production of Ac-225 from Th-229 for Targeted α Therapy. *Analytical Chemistry* **2005**, *77* (19), 6288–6291. https://doi.org/10.1021/ac0580114.

(90) Morgenstern, A.; Apostolidis, C.; Bruchertseifer, F. Supply and Clinical Application of Actinium-225 and Bismuth-213. *Seminars in Nuclear Medicine* **2020**, *50* (2), 119–123. https://doi.org/10.1053/j.semnuclmed.2020.02.003.

(91) Melville, G.; J Allen, B. Cyclotron and Linac Production of Ac-225. *Applied Radiation and Isotopes* **2009**, *67* (4), 549–555. https://doi.org/10.1016/j.apradiso.2008.11.012.

(92) Melville, G.; Melville, P. A Theoretical Model for the Production of Ac-225 for Cancer Therapy by Neutron Capture Transmutation of Ra-226. *Applied Radiation and Isotopes* **2013**, *72*, 152–157. https://doi.org/10.1016/j.apradiso.2012.09.019.

(93) Robertson, A. K. H.; McNeil, B. L.; Yang, H.; Gendron, D.; Perron, R.; Radchenko, V.; Zeisler, S.; Causey, P.; Schaffer, P. 232Th-Spallation-Produced 225Ac with Reduced 227Ac Content. *Inorganic Chemistry* **2020**, *59* (17), 12156–12165. https://doi.org/10.1021/acs.inorgchem.0c01081.

(94) Thiele, N. A.; Wilson, J. J. Actinium-225 for Targeted α Therapy: Coordination Chemistry and Current Chelation Approaches. *Cancer Biotherapy and Radiopharmaceuticals* **2018**, *33* (8), 336–348. https://doi.org/10.1089/cbr.2018.2494.

(95) Keogh, D. W. Actinides: Inorganic & Coordination Chemistry Based in Part on the Article Actinides: Inorganic & Coordination Chemistry by Grigorii L. Soloveichik Which Appeared in the Encyclopedia of Inorganic Chemistry, First Edition. In *Encyclopedia of Inorganic and Bioinorganic Chemistry*; John Wiley & Sons, Ltd, 2011. https://doi.org/10.1002/9781119951438.eibc0001.

(96) Ferrier, M. G.; Stein, B. W.; Batista, E. R.; Berg, J. M.; Birnbaum, E. R.; Engle, J. W.; John, K. D.; Kozimor, S. A.; Lezama Pacheco, J. S.; Redman, L. N. Synthesis and Characterization of the Actinium Aquo Ion. *ACS Central Science* **2017**, *3* (3), 176–185. https://doi.org/10.1021/acscentsci.6b00356.

(97) Aldrich, K. E.; Lam, M. N.; Eiroa-Lledo, C.; Kozimor, S. A.; Lilley, L. M.; Mocko, V.; Stein, B. W. Preparation of an Actinium-228 Generator. *Inorganic Chemistry* **2020**, *59* (5), 3200–3206. https://doi.org/10.1021/acs.inorgchem.9b03563.

(98) McDevitt, M. R.; Ma, D.; Simon, J.; Frank, R. K.; Scheinberg, D. A. Design and Synthesis of 225Ac Radioimmunopharmaceuticals. *Applied Radiation and Isotopes* **2002**, *57* (6), 841–847. https://doi.org/10.1016/S0969-8043(02)00167-7.

(99) Chappell, L. L.; Deal, K. A.; Dadachova, E.; Brechbiel, M. W. Synthesis, Conjugation, and Radiolabeling of a Novel Bifunctional Chelating Agent for 225Ac Radioimmunotherapy Applications. *Bioconjugate Chemistry* **2000**, *11* (4), 510–519. https://doi.org/10.1021/bc990153f.

(100) McDevitt, M. R.; Ma, D.; Lai, L. T.; Simon, J.; Borchardt, P.; Frank, R. K.; Wu, K.; Pellegrini, V.; Curcio, M. J.; Miederer, M.; Bander, N. H.; Scheinberg, D. A. Tumor Therapy with Targeted Atomic Nanogenerators. *Science* **2001**, *294* (5546), 1537–1540. https://doi.org/10.1126/science.1064126.

(101) Maguire, W. F.; McDevitt, M. R.; Smith-Jones, P. M.; Scheinberg, D. A. Efficient 1-Step Radiolabeling of Monoclonal Antibodies to High Specific Activity with 225Ac for Alpha-Particle Radioimmunotherapy of Cancer. *Journal of Nuclear Medicine* **2014**, *55* (9), 1492–1498. https://doi.org/10.2967/jnumed.114.138347.

(102) Deal, K. A.; Davis, I. A.; Mirzadeh, S.; Kennel, S. J.; Brechbiel, M. W. Improved in Vivo Stability of Actinium-225 Macrocyclic Complexes. *Journal of Medicinal Chemistry* **1999**, *42* (15), 2988–2992. https://doi.org/10.1021/jm990141f.

(103) Ramogida, C. F.; Robertson, A. K. H.; Jermilova, U.; Zhang, C.; Yang, H.; Kunz, P.; Lassen, J.; Bratanovic, I.; Brown, V.; Southcott, L.; Rodríguez-Rodríguez, C.; Radchenko, V.; Bénard, F.; Orvig, C.; Schaffer, P. Evaluation of Polydentate Picolinic Acid Chelating Ligands and an α-Melanocyte-Stimulating Hormone Derivative for Targeted Alpha Therapy Using ISOL-Produced 225Ac. *European Journal of Nuclear Medicine and Molecular Imaging Radiopharmacy and Chemistry* **2019**, *4* (1), 21. https://doi.org/10.1186/s41181-019-0072-5.

(104) Kratochwil, C.; Bruchertseifer, F.; Rathke, H.; Hohenfellner, M.; Giesel, F. L.; Haberkorn, U.; Morgenstern, A. Targeted α-Therapy of Metastatic Castration-Resistant Prostate Cancer with 225Ac-PSMA-617: Swimmer-Plot Analysis Suggests Efficacy Regarding Duration of Tumor Control. *Journal of Nuclear Medicine* **2018**, *59* (5), 795–802. https://doi.org/10.2967/jnumed.117.203539.

(105) Escorcia, F. E.; Henke, E.; McDevitt, M. R.; Villa, C. H.; Smith-Jones, P.; Blasberg, R. G.; Benezra, R.; Scheinberg, D. A. Selective Killing of Tumor Neovasculature Paradoxically Improves Chemotherapy Delivery to Tumors. *Cancer Research* **2010**, *70* (22), 9277–9286. https://doi.org/10.1158/0008-5472.CAN-10-2029.

(106) Miederer, M.; McDevitt, M. R.; Borchardt, P.; Bergman, I.; Kramer, K.; Cheung, N.-K. V.; Scheinberg, D. A. Treatment of Neuroblastoma Meningeal Carcinomatosis with Intrathecal Application of Alpha-Emitting Atomic Nanogenerators Targeting Disialo-Ganglioside GD2. *Clinical Cancer Research* **2004**, *10* (20), 6985–6992. https://doi.org/10.1158/1078-0432.CCR-04-0859.

(107) Jurcic, J. G. Targeted Alpha-Particle Therapy for Hematologic Malignancies. *Journal of Medical Imaging and Radiation Sciences* **2019**, *50* (4), S53–S57. https://doi.org/10.1016/j.jmir.2019.05.008.

(108) Song, H. A.; Kang, C. S.; Baidoo, K. E.; Milenic, D. E.; Chen, Y.; Dai, A.; Brechbiel, M. W.; Chong, H. Efficient Bifunctional Decadentate Ligand 3p-C-DEPA for Targeted α-Radioimmunotherapy Applications. *Bioconjugate Chemistry* **2011**, *22* (6), 1128–1135. https://doi.org/10.1021/bc100586y.

(109) Kratochwil, C.; Bruchertseifer, F.; Rathke, H.; Bronzel, M.; Apostolidis, C.; Weichert, W.; Haberkorn, U.; Giesel, F. L.; Morgenstern, A. Targeted A-Therapy of Metastatic Castration-Resistant Prostate Cancer with 225Ac-PSMA-617: Dosimetry Estimate and Empiric Dose Finding. *Journal of Nuclear Medicine* **2017**, *58* (10), 1624–1631. https://doi.org/10.2967/jnumed.117.191395.

(110) Robertson, A. K. H.; Ramogida, C. F.; Rodríguez-Rodríguez, C.; Blinder, S.; Kunz, P.; Sossi, V.; Schaffer, P. Multi-Isotope SPECT Imaging of the 225Ac Decay Chain: Feasibility Studies. *Physics in Medicine and Biology* **2017**, *62* (11), 4406–4420. https://doi.org/10.1088/1361-6560/aa6a99.

(111) Pandya, D. N.; Hantgan, R.; Budzevich, M. M.; Kock, N. D.; Morse, D. L.; Batista, I.; Mintz, A.; Li, K. C.; Wadas, T. J. Preliminary Therapy Evaluation of 225Ac-DOTA-c(RGDyK) Demonstrates That Cerenkov Radiation Derived from 225Ac Daughter Decay Can Be Detected by Optical Imaging for In Vivo Tumor Visualization. *Theranostics* **2016**, *6* (5), 698–709. https://doi.org/10.7150/thno.14338.

(112) Bailey, T. A.; Mocko, V.; Shield, K. M.; An, D. D.; Akin, A. C.; Birnbaum, E. R.; Brugh, M.; Cooley, J. C.; Engle, J. W.; Fassbender, M. E.; Gauny, S. S.; Lakes, A. L.; Nortier, F. M.; O'Brien, E. M.; Thiemann, S. L.; White, F. D.; Vermeulen, C.; Kozimor, S. A.; Abergel, R. J. Developing the 134Ce and 134La Pair as Companion Positron Emission Tomography Diagnostic Isotopes for 225Ac and 227Th Radiotherapeutics. *Nature Chemistry* **2020**, *13*, 284–289. https://doi.org/10.1038/s41557-020-00598-7.

(113) Nelson, B. J. B.; Wilson, J.; Andersson, J. D.; Wuest, F. High Yield Cyclotron Production of a Novel 133/135La Theranostic Pair for Nuclear Medicine. *Scientific Reports* **2020**, *10*, 22203. https://doi.org/10.1038/s41598-020-79198-x.

(114) Aluicio-Sarduy, E.; Hernandez, R.; Olson, A. P.; Barnhart, T. E.; Cai, W.; Ellison, P. A.; Engle, J. W. Production and in Vivo PET/CT Imaging of the Theranostic Pair 132/135La. *Scientific Reports* **2019**, *9* (1), 10658. https://doi.org/10.1038/s41598-019-47137-0.

(115) Guseva, L. I. Radioisotope Generators of Short-Lived α-Emitting Radionuclides Promising for Use in Nuclear Medicine. *Radiochemistry* **2014**, *56* (5), 451–467. https://doi.org/10.1134/S1066362214050014.

(116) Henriksen, G.; Hoff, P.; Alstad, J.; Larsen, R. H. 223Ra for Endoradiotherapeutic Applications Prepared from an Immobilized 227Ac/227Th Source. *Radiochimica Acta* **2001**, *89* (10), 661–666. https://doi.org/10.1524/ract.2001.89.10.661.

(117) Kuznetsov, R. A.; Butkalyuk, P. S.; Tarasov, V. A.; Baranov, A. Yu.; Butkalyuk, I. L.; Romanov, E. G.; Kupriyanov, V. N.; Kazakova, E. V. Yields of Activation Products in 226Ra Irradiation in the High-Flux SM Reactor. *Radiochemistry* **2012**, *54* (4), 383–387. https://doi.org/10.1134/S1066362212040121.

(118) Kukleva, E.; Kozempel, J.; Vlk, M.; Mičolová, P.; Vopálka, D. Preparation of 227Ac/223Ra by Neutron Irradiation of 226Ra. *Journal of Radioanalytical and Nuclear Chemistry* **2015**, *304* (1), 263–266. https://doi.org/10.1007/s10967-014-3432-3.

(119) Tutson, C. D.; Gorden, A. E. V. Thorium Coordination: A Comprehensive Review Based on Coordination Number. *Coordination Chemistry Reviews* **2017**, *333*, 27–43. https://doi.org/10.1016/j.ccr.2016.11.006.

(120) Ramdahl, T.; Bonge-Hansen, H. T.; Ryan, O. B.; Larsen, Å.; Herstad, G.; Sandberg, M.; Bjerke, R. M.; Grant, D.; Brevik, E. M.; Cuthbertson, A. S. An Efficient Chelator for Complexation of Thorium-227. *Bioorganic & Medicinal Chemistry Letters* **2016**, *26* (17), 4318–4321. https://doi.org/10.1016/j.bmcl.2016.07.034.

(121) Deblonde, G. J. P.; Lohrey, T. D.; Booth, C. H.; Carter, K. P.; Parker, B. F.; Larsen, Å.; Smeets, R.; Ryan, O. B.; Cuthbertson, A. S.; Abergel, R. J. Solution Thermodynamics and Kinetics of Metal Complexation with a Hydroxypyridinone Chelator Designed for Thorium-227 Targeted Alpha Therapy. *Inorganic Chemistry* **2018**, *57* (22), 14337–14346. https://doi.org/10.1021/acs.inorgchem.8b02430.

(122) Heyerdahl, H.; Abbas, N.; Sponheim, K.; Mollatt, C.; Bruland, O.; Dahle, J. Targeted Alpha Therapy with 227Th-Trastuzumab of Intraperitoneal Ovarian Cancer in Nude Mice. *Current Radiopharmaceuticals* **2013**, *6* (2), 106–116. https://doi.org/10.2174/18744710113069990018.

(123) Hagemann, U. B.; Wickstroem, K.; Wang, E.; Shea, A. O.; Sponheim, K.; Karlsson, J.; Bjerke, R. M.; Ryan, O. B.; Cuthbertson, A. S. In Vitro and In Vivo Efficacy of a Novel CD33-Targeted Thorium-227 Conjugate for the Treatment of Acute Myeloid Leukemia. *Molecular Cancer Therapeutics* **2016**, *15* (10), 2422–2431. https://doi.org/10.1158/1535-7163.MCT-16-0251.

(124) Dahle, J.; Borrebæk, J.; Jonasdottir, T. J.; Hjelmerud, A. K.; Melhus, K. B.; Bruland, Ø. S.; Press, O. W.; Larsen, R. H. Targeted Cancer Therapy with a Novel Low-Dose Rate α-Emitting Radioimmunoconjugate. *Blood* **2007**, *110* (6), 2049–2056. https://doi.org/10.1182/blood-2007-01-066803.

(125) Heyerdahl, H.; Abbas, N.; Brevik, E. M.; Mollatt, C.; Dahle, J. Fractionated Therapy of HER2-Expressing Breast and Ovarian Cancer Xenografts in Mice with Targeted Alpha Emitting 227Th-DOTA-p-Benzyl-Trastuzumab. *PLOS ONE* **2012**, *7* (8), e42345. https://doi.org/10.1371/journal.pone.0042345.

(126) Abbas, N.; Bruland, Ø. S.; Brevik, E. M.; Dahle, J. Preclinical Evaluation of 227Th-Labeled and 177Lu-Labeled Trastuzumab in Mice with HER-2-Positive Ovarian Cancer Xenografts. *Nuclear Medicine Communications* **2012**, *33* (8), 838–847. https://doi.org/10.1097/MNM.0b013e328354df7c.

(127) Hagemann, U. B.; Mihaylova, D.; Uran, S. R.; Borrebaek, J.; Grant, D.; Bjerke, R. M.; Karlsson, J.; Cuthbertson, A. S. Targeted Alpha Therapy Using a Novel CD70 Targeted Thorium-227 Conjugate in in Vitro and in Vivo Models of Renal Cell Carcinoma. *Oncotarget* **2017**, *8* (34), 56311–56326. https://doi.org/10.18632/oncotarget.16910.

(128) Frantellizzi, V.; Cosma, L.; Brunotti, G.; Pani, A.; Spanu, A.; Nuvoli, S.; De Cristofaro, F.; Civitelli, L.; De Vincentis, G. Targeted Alpha Therapy with Thorium-227. *Cancer Biotherapy and Radiopharmaceuticals* **2020**, *35* (6), 437–445. https://doi.org/10.1089/cbr.2019.3105.

(129) Severin, G. W.; Fonslet, J.; Kristensen, L. K.; Nielsen, C. H.; Jensen, A. I.; Kjær, A.; Mazar, A. P.; Johnston, K.; Köster, U. PET in Vivo Generators 134Ce and 140Nd on an Internalizing Monoclonal Antibody Probe. *Scientific Reports* **2022**, *12* (1). https://doi.org/10.1038/s41598-022-07147-x.

(130) Strosberg, J.; El-Haddad, G.; Wolin, E.; Hendifar, A.; Yao, J.; Chasen, B.; Mittra, E.; Kunz, P. L.; Kulke, M. H.; Jacene, H.; Bushnell, D.; O'Dorisio, T. M.; Baum, R. P.; Kulkarni, H. R.; Caplin, M.; Lebtahi, R.; Hobday, T.; Delpassand, E.; Van Cutsem, E.; Benson, A.; Srirajaskanthan, R.; Pavel, M.; Mora, J.; Berlin, J.; Grande, E.; Reed, N.; Seregni, E.; Öberg, K.; Lopera Sierra, M.; Santoro, P.; Thevenet, T.;

Erion, J. L.; Ruszniewski, P.; Kwekkeboom, D.; Krenning, E. Phase 3 Trial of 177Lu-Dotatate for Midgut Neuroendocrine Tumors. *New England Journal of Medicine* **2017**, *376* (2), 125–135. https://doi.org/10.1056/NEJMoa1607427.

(131) Pryma, D. A.; Chin, B. B.; Noto, R. B.; Dillon, J. S.; Perkins, S.; Solnes, L.; Kostakoglu, L.; Serafini, A. N.; Pampaloni, M. H.; Jensen, J.; Armor, T.; Lin, T.; White, T.; Stambler, N.; Apfel, S.; DiPippo, V. A.; Mahmood, S.; Wong, V.; Jimenez, C. Efficacy and Safety of High-Specific-Activity 131 I-MIBG Therapy in Patients with Advanced Pheochromocytoma or Paraganglioma. *Journal of Nuclear Medicine* **2019**, *60* (5), 623–630. https://doi.org/10.2967/jnumed.118.217463.

(132) Krolicki, L.; Bruchertseifer, F.; Kunikowska, J.; Koziara, H.; Królicki, B.; Jakuciński, M.; Pawlak, D.; Apostolidis, C.; Mirzadeh, S.; Rola, R.; Merlo, A.; Morgenstern, A. Prolonged Survival in Secondary Glioblastoma Following Local Injection of Targeted Alpha Therapy with 213Bi-Substance P Analogue. *European Journal of Nuclear Medicine and Molecular Imaging* **2018**, *45* (9), 1636–1644. https://doi.org/10.1007/s00259-018-4015-2.

(133) Müller, C.; Bunka, M.; Haller, S.; Köster, U.; Groehn, V.; Bernhardt, P.; van der Meulen, N.; Türler, A.; Schibli, R. Promising Prospects for 44Sc-/47Sc-Based Theragnostics: Application of 47Sc for Radionuclide Tumor Therapy in Mice. *Journal of Nuclear Medicine* **2014**, *55* (10), 1658–1664. https://doi.org/10.2967/jnumed.114.141614.

(134) Połosak, M.; Piotrowska, A.; Krajewski, S.; Bilewicz, A. Stability of 47Sc-Complexes with Acyclic Polyamino-Polycarboxylate Ligands. *Journal of Radioanalytical and Nuclear Chemistry* **2013**, *295* (3), 1867–1872. https://doi.org/10.1007/s10967-012-2188-x.

(135) Nagy, G.; Szikra, D.; Trencsényi, G.; Fekete, A.; Garai, I.; Giani, A. M.; Negri, R.; Masciocchi, N.; Maiocchi, A.; Uggeri, F.; Tóth, I.; Aime, S.; Giovenzana, G. B.; Baranyai, Z. AAZTA: An Ideal Chelating Agent for the Development of 44Sc PET Imaging Agents. *Angewandte Chemie International Edition* **2017**, *56* (8), 2118–2122. https://doi.org/10.1002/anie.201611207.

(136) Fujiki, K.; Yano, S.; Ito, T.; Kumagai, Y.; Murakami, Y.; Kamigaito, O.; Haba, H.; Tanaka, K. A One-Pot Three-Component Double-Click Method for Synthesis of [67Cu]-Labeled Biomolecular Radiotherapeutics. *Scientific Reports* **2017**, *7*, 1912. https://doi.org/10.1038/s41598-017-02123-2.

(137) Kelly, J. M.; Ponnala, S.; Amor-Coarasa, A.; Zia, N. A.; Nikolopoulou, A.; Williams, C.; Schlyer, D. J.; DiMagno, S. G.; Donnelly, P. S.; Babich, J. W. Preclinical Evaluation of a High-Affinity Sarcophagine-Containing PSMA Ligand for 64Cu/67 Cu-Based Theranostics in Prostate Cancer. *Molecular Pharmaceutics* **2020**, *17* (6), 1954–1962. https://doi.org/10.1021/acs.molpharmaceut.0c00060.

(138) Jin, Z.; Furukawa, T.; Ohya, T.; Degardin, M.; Sugyo, A.; Tsuji, A. B.; Fujibayashi, Y.; Zhang, M.-R.; Higashi, T.; Boturyn, D.; Dumy, P.; Saga, T. 67Cu-Radiolabeling of a Multimeric RGD Peptide for αVβ3 Integrin-Targeted Radionuclide Therapy. *Nuclear Medicine Communications* **2017**, *38* (4), 347–355. https://doi.org/10.1097/MNM.0000000000000646.

(139) Mastren, T.; Pen, A.; Loveless, S.; Marquez, B. V.; Bollinger, E.; Marois, B.; Hubley, N.; Brown, K.; Morrissey, D. J.; Peaslee, G. F.; Lapi, S. E. Harvesting 67Cu from the Collection of a Secondary Beam Cocktail at the National Superconducting Cyclotron Laboratory. *Analytical Chemistry* **2015**, *87* (20), 10323–10329. https://doi.org/10.1021/acs.analchem.5b02322.

(140) Moreau, M.; Poty, S.; Vrigneaud, J.-M.; Walker, P.; Guillemin, M.; Raguin, O.; Oudot, A.; Bernhard, C.; Goze, C.; Boschetti, F.; Collin, B.; Brunotte, F.; Denat, F. MANOTA: A Promising Bifunctional Chelating Agent for Copper-64 immunoPET.

Dalton Transactions **2017**, *46* (42), 14659–14668. https://doi.org/10.1039/C7DT01772C.
(141) Cullinane, C.; Jeffery, C. M.; Roselt, P. D.; van Dam, E. M.; Jackson, S.; Kuan, K.; Jackson, P.; Binns, D.; van Zuylekom, J.; Harris, M. J.; Hicks, R. J.; Donnelly, P. S. Peptide Receptor Radionuclide Therapy with 67 Cu-CuSarTATE Is Highly Efficacious Against a Somatostatin Positive Neuroendocrine Tumor Model. *Journal of Nuclear Medicine* **2020**, jnumed.120.243543. https://doi.org/10.2967/jnumed.120.243543.
(142) Müller, C.; Reber, J.; Haller, S.; Dorrer, H.; Bernhardt, P.; Zhernosekov, K.; Türler, A.; Schibli, R. Direct in Vitro and in Vivo Comparison of 161Tb and 177Lu Using a Tumour-Targeting Folate Conjugate. *European Journal of Nuclear Medicine and Molecular Imaging* **2014**, *41* (3), 476–485. https://doi.org/10.1007/s00259-013-2563-z.
(143) Rane, S.; Harris, J. T.; Starovoitova, V. N. 47Ca Production for 47Ca/47Sc Generator System Using Electron Linacs. *Applied Radiation and Isotopes* **2015**, *97*, 188–192. https://doi.org/10.1016/j.apradiso.2014.12.020.
(144) Mamtimin, M.; Harmon, F.; Starovoitova, V. N. Sc-47 Production from Titanium Targets Using Electron Linacs. *Applied Radiation and Isotopes* **2015**, *102*, 1–4. https://doi.org/10.1016/j.apradiso.2015.04.012.
(145) Minegishi, K.; Nagatsu, K.; Fukada, M.; Suzuki, H.; Ohya, T.; Zhang, M.-R. Production of Scandium-43 and -47 from a Powdery Calcium Oxide Target via the Nat/44Ca(α,x)-Channel. *Applied Radiation and Isotopes* **2016**, *116*, 8–12. https://doi.org/10.1016/j.apradiso.2016.07.017.
(146) Jafari, A.; Aboudzadeh, M. R.; Sharifian, M.; Sadeghi, M.; Rahiminezhad, A.; Alirezapour, B.; Rajabifar, S. Cyclotron-Based Production of the Theranostic Radionuclide Scandium-47 from Titanium Target. *Nuclear Instruments and Methods in Physics Research Section A: Accelerators, Spectrometers, Detectors and Associated Equipment* **2020**, *961*. https://doi.org/10.1016/j.nima.2020.163643.
(147) Jafari, A.; Aboudzadeh, M. R.; Azizakram, H.; Sadeghi, M.; Alirezapour, B.; Rajabifar, S.; Yousefi, K. Investigations of Proton and Deuteron Induced Nuclear Reactions on Natural and Enriched Titanium, Calcium and Vanadium Targets, with Special Reference to the Production of 47Sc. *Applied Radiation and Isotopes* **2019**, *152* (June), 145–155. https://doi.org/10.1016/j.apradiso.2019.07.007.
(148) Hosseini, S. F.; Sadeghi, M.; Aboudzadeh, M. R. Theoretical Assessment and Targeted Modeling of TiO2 in Reactor towards the Scandium Radioisotopes Estimation. *Applied Radiation and Isotopes* **2017**, *127*, 116–121. https://doi.org/10.1016/j.apradiso.2017.05.016.
(149) Misiak, R.; Walczak, R.; Wąs, B.; Bartyzel, M.; Mietelski, J. W.; Bilewicz, A. 47Sc Production Development by Cyclotron Irradiation of 48Ca. *Journal of Radioanalytical and Nuclear Chemistry* **2017**, *313* (2), 429–434. https://doi.org/10.1007/s10967-017-5321-z.
(150) Cotton, S. A. Scandium, Yttrium & the Lanthanides: Inorganic & Coordination Chemistry. In *Encyclopedia of Inorganic Chemistry*; John Wiley & Sons, Ltd: Chichester, UK, 2006; pp 1–40. https://doi.org/10.1002/0470862106.ia211.
(151) Byegård, J.; Skarnemark, G.; Skålberg, M. The Stability of Some Metal EDTA, DTPA and DOTA Complexes: Application as Tracers in Groundwater Studies. *Journal of Radioanalytical and Nuclear Chemistry* **1999**, *241* (2), 281–290. https://doi.org/10.1007/BF02347463.
(152) Huclier-Markai, S.; Sabatie, A.; Ribet, S.; Kubícek, V.; Paris, M.; Vidaud, C.; Hermann, P.; Cutler, C. S. Chemical and Biological Evaluation of Scandium(III)-

Polyaminopolycarboxylate Complexes as Potential PET Agents and Radiopharmaceuticals. *Radiochimica Acta* **2011**, *99* (10), 653–662. https://doi.org/10.1524/ract.2011.1869.

(153) Pniok, M.; Kubíček, V.; Havlíčková, J.; Kotek, J.; Sabatie-Gogová, A.; Plutnar, J.; Huclier-Markai, S.; Hermann, P. Thermodynamic and Kinetic Study of Scandium(III) Complexes of DTPA and DOTA: A Step Toward Scandium Radiopharmaceuticals. *Chemistry European Journal* **2014**, *20* (26), 7944–7955. https://doi.org/10.1002/chem.201402041.

(154) Majkowska-Pilip, A.; Bilewicz, A. Macrocyclic Complexes of Scandium Radionuclides as Precursors for Diagnostic and Therapeutic Radiopharmaceuticals. *Journal of Inorganic Biochemistry* **2011**, *105* (2), 313–320. https://doi.org/10.1016/j.jinorgbio.2010.11.003.

(155) Waldron, B. P.; Parker, D.; Burchardt, C.; Yufit, D. S.; Zimny, M.; Roesch, F. Structure and Stability of Hexadentate Complexes of Ligands Based on AAZTA for Efficient PET Labelling with Gallium-68. *Chemical Communications* **2013**, *49* (6), 579–581. https://doi.org/10.1039/c2cc37544c.

(156) Aime, S.; Calabi, L.; Cavallotti, C.; Gianolio, E.; Giovenzana, G. B.; Losi, P.; Maiocchi, A.; Palmisano, G.; Sisti, M. [Gd-AAZTA]-: A New Structural Entry for an Improved Generation of MRI Contrast Agents. *Inorganic Chemistry* **2004**, *43* (24), 7588–7590. https://doi.org/10.1021/ic0489692.

(157) Vaughn, B. A.; Ahn, S. H.; Aluicio-Sarduy, E.; Devaraj, J.; Olson, A. P.; Engle, J.; Boros, E. Chelation with a Twist: A Bifunctional Chelator to Enable Room Temperature Radiolabeling and Targeted PET Imaging with Scandium-44. *Chemical Science* **2020**, *11* (2), 333–342. https://doi.org/10.1039/c9sc04655k.

(158) Phipps, M. D.; Cingoranelli, S.; Bhupathiraju, N. V. S. D. K.; Younes, A.; Cao, M.; Sanders, V. A.; Neary, M. C.; Devany, M. H.; Cutler, C. S.; Lopez, G. E.; Saini, S.; Parker, C. C.; Fernandez, S. R.; Lewis, J. S.; Lapi, S. E.; Francesconi, L. C.; Deri, M. A. Sc-HOPO: A Potential Construct for Use in Radioscandium-Based Radiopharmaceuticals. *Inorganic Chemistry* **2023**. https://doi.org/10.1021/acs.inorgchem.2c03931.

(159) Marceau, N.; Kruck, T. P. A.; McConnell, D. B.; Aspin, N. The Production of Copper 67 from Natural Zinc Using a Linear Accelerator. *The International Journal of Applied Radiation and Isotopes* **1970**, *21* (11), 667–669. https://doi.org/10.1016/0020-708X(70)90121-3.

(160) Mausner, L. F.; Kolsky, K. L.; Joshi, V.; Srivastava, S. C. Radionuclide Development at BNL for Nuclear Medicine Therapy. *Applied Radiation and Isotopes* **1998**, *49* (4), 285–294. https://doi.org/10.1016/S0969-8043(97)00040-7.

(161) Kawabata, M.; Hashimoto, K.; Saeki, H.; Sato, N.; Motoishi, S.; Takakura, K.; Konno, C.; Nagai, Y. Production and Separation of 64Cu and 67Cu Using 14 MeV Neutrons. *Journal of Radioanalytical and Nuclear Chemistry* **2015**, *303* (2), 1205–1209. https://doi.org/10.1007/s10967-014-3488-0.

(162) Medvedev, D. G.; Mausner, L. F.; Meinken, G. E.; Kurczak, S. O.; Schnakenberg, H.; Dodge, C. J.; Korach, E. M.; Srivastava, S. C. Development of a Large Scale Production of 67Cu from 68Zn at the High Energy Proton Accelerator: Closing the 68Zn Cycle. *Applied Radiation and Isotopes* **2012**, *70* (3), 423–429. https://doi.org/10.1016/j.apradiso.2011.10.007.

(163) Novak-Hofer, I.; Schubiger, A. P. Copper-67 as a Therapeutic Nuclide for Radioimmunotherapy. *European Journal of Nuclear Medicine and Molecular Imaging* **2002**, *29* (6), 821–830. https://doi.org/10.1007/s00259-001-0724-y.

(164) Hosseini, S. F.; Aboudzadeh, M.; Sadeghi, M.; Ahmadi Teymourlouy, A.; Rostampour, M. Assessment and Estimation of 67Cu Production Yield via Deuteron

Induced Reactions on natZn and 70Zn. *Applied Radiation and Isotopes* **2017**, *127*, 137–141. https://doi.org/10.1016/j.apradiso.2017.05.024.

(165) Kozempel, J.; Abbas, K.; Simonelli, F.; Bulgheroni, A.; Holzwarth, U.; Gibson, N. Preparation of 67Cu via Deuteron Irradiation of 70Zn. *Radiochimica Acta* **2012**, *100* (7), 419–424. https://doi.org/10.1524/ract.2012.1939.

(166) Skakun, Y.; Qaim, S. M. Excitation Function of the 64Ni(α,p)67Cu Reaction for Production of 67Cu. *Applied Radiation and Isotopes* **2004**, *60* (1), 33–39. https://doi.org/10.1016/j.apradiso.2003.09.003.

(167) Pupillo, G.; Sounalet, T.; Michel, N.; Mou, L.; Esposito, J.; Haddad, F. New Production Cross Sections for the Theranostic Radionuclide 67Cu. *Nuclear Instruments and Methods in Physics Research B: Beam Interactions with Materials and Atoms* **2018**, *415*, 41–47. https://doi.org/10.1016/j.nimb.2017.10.022.

(168) Smith, N. A.; Bowers, D. L.; Ehst, D. A. The Production, Separation, and Use of 67Cu for Radioimmunotherapy: A Review. *Applied Radiation and Isotopes* **2012**, *70* (10), 2377–2383. https://doi.org/10.1016/j.apradiso.2012.07.009.

(169) Pupillo, G.; Mou, L.; Martini, P.; Pasquali, M.; Boschi, A.; Cicoria, G.; Duatti, A.; Haddad, F.; Esposito, J. Production of 67Cu by Enriched 70Zn Targets: First Measurements of Formation Cross Sections of 67Cu, 64Cu, 67Ga, 66Ga, 69mZn and 65Zn in Interactions of 70Zn with Protons above 45 MeV. *Radiochimica Acta* **2020**, *108* (8), 593–602. https://doi.org/10.1515/ract-2019-3199.

(170) Solomon, E. I.; Heppner, D. E.; Johnston, E. M.; Ginsbach, J. W.; Cirera, J.; Qayyum, M.; Kieber-Emmons, M. T.; Kjaergaard, C. H.; Hadt, R. G.; Tian, L. Copper Active Sites in Biology. *Chemical Reviews* **2014**, *114* (7), 3659–3853. https://doi.org/10.1021/cr400327t.

(171) Linder, M. C. *Biochemistry of Copper*; Springer US: Boston, MA, 1991. https://doi.org/10.1007/978-1-4757-9432-8.

(172) Conry, R. R. Copper: Inorganic & Coordination Chemistry Based in Part on the Article Copper: Inorganic & Coordination Chemistry by Rebecca R. Conry & Kenneth D. Karlin Which Appeared in the Encyclopedia of Inorganic Chemistry, First Edition. In *Encyclopedia of Inorganic and Bioinorganic Chemistry*; John Wiley & Sons, Ltd, 2011. https://doi.org/10.1002/9781119951438.eibc0050.

(173) Bass, L. A.; Wang, M.; Welch, M. J.; Anderson, C. J. In Vivo Transchelation of Copper-64 from TETA-Octreotide to Superoxide Dismutase in Rat Liver. *Bioconjugate Chemistry* **2000**, *11* (4), 527–532. https://doi.org/10.1021/bc990167l.

(174) Mirick, G. R.; O'Donnell, R. T.; DeNardo, S. J.; Shen, S.; Meares, C. F.; DeNardo, G. L. Transfer of Copper from a Chelated 67Cu-Antibody Conjugate to Ceruloplasmin in Lymphoma Patients. *Nuclear Medicine and Biology* **1999**, *26* (7), 841–845. https://doi.org/10.1016/S0969-8051(99)00049-9.

(175) Green, M. A.; Klippenstein, D. L.; Tennison, J. R. Copper(II) Bis(Thiosemicarbazone) Complexes as Potential Tracers for Evaluation of Cerebral and Myocardial Blood Flow with PET. *Journal of Nuclear Medicine* **1988**, *29* (9), 1549–1557.

(176) Fujibayashi, Y.; Taniuchi, H.; Yonekura, Y.; Ohtani, H.; Konishi, J.; Yokoyama, A. Copper-62-ATSM: A New Hypoxia Imaging Agent with High Membrane Permeability and Low Redox Potential. *Journal of Nuclear Medicine* **1997**, *38* (7), 1155–1160.

(177) Paterson, B. M.; Donnelly, P. S. Copper Complexes of Bis(Thiosemicarbazones): From Chemotherapeutics to Diagnostic and Therapeutic Radiopharmaceuticals. *Chemical Society Reviews* **2011**, *40* (5), 3005. https://doi.org/10.1039/c0cs00215a.

(178) Wadas, T. J.; Wong, E. H.; Weisman, G. R.; Anderson, C. J. Coordinating Radiometals of Copper, Gallium, Indium, Yttrium, and Zirconium for PET and

SPECT Imaging of Disease. *Chemical Reviews* **2010**, *110* (5), 2858–2902. https://doi.org/10.1021/cr900325h.

(179) Donnelly, P. S. The Role of Coordination Chemistry in the Development of Copper and Rhenium Radiopharmaceuticals. *Dalton Transactions* **2011**, *40* (5), 999. https://doi.org/10.1039/c0dt01075h.

(180) Boschi, A.; Martini, P.; Janevik-Ivanovska, E.; Duatti, A. The Emerging Role of Copper-64 Radiopharmaceuticals as Cancer Theranostics. *Drug Discovery Today* **2018**, *23* (8), 1489–1501. https://doi.org/10.1016/j.drudis.2018.04.002.

(181) Clarke, E. T.; Martell, A. E. Stabilities of the Alkaline Earth and Divalent Transition Metal Complexes of the Tetraazamacrocyclic Tetraacetic Acid Ligands. *Inorganica Chimica Acta* **1991**, *190* (1), 27–36. https://doi.org/10.1016/S0020-1693(00)80228-5.

(182) Ramogida, C. F.; Boros, E.; Patrick, B. O.; Zeisler, S. K.; Kumlin, J.; Adam, M. J.; Schaffer, P.; Orvig, C. Evaluation of H2CHXdedpa, H2dedpa- and H2CHXdedpa-N,N′-Propyl-2-NI Ligands for 64Cu(II) Radiopharmaceuticals. *Dalton Transactions* **2016**, *45* (33), 13082–13090. https://doi.org/10.1039/C6DT00932H.

(183) Roux, A.; Nonat, A. M.; Brandel, J.; Hubscher-Bruder, V.; Charbonnière, L. J. Kinetically Inert Bispidol-Based Cu(II) Chelate for Potential Application to 64/67Cu Nuclear Medicine and Diagnosis. *Inorganic Chemistry* **2015**, *54* (9), 4431–4444. https://doi.org/10.1021/acs.inorgchem.5b00207.

(184) Juran, S.; Walther, M.; Stephan, H.; Bergmann, R.; Steinbach, J.; Kraus, W.; Emmerling, F.; Comba, P. Hexadentate Bispidine Derivatives as Versatile Bifunctional Chelate Agents for Copper(II) Radioisotopes. *Bioconjugate Chemistry* **2009**, *20* (2), 347–359. https://doi.org/10.1021/bc800461e.

(185) Ferdani, R.; Stigers, D. J.; Fiamengo, A. L.; Wei, L.; Li, B. T. Y.; Golen, J. A.; Rheingold, A. L.; Weisman, G. R.; Wong, E. H.; Anderson, C. J. Synthesis, Cu(II) Complexation, 64Cu-Labeling and Biological Evaluation of Cross-Bridged Cyclam Chelators with Phosphonate Pendant Arms. *Dalton Trans.* **2012**, *41* (7), 1938–1950. https://doi.org/10.1039/C1DT11743B.

(186) Hicks, R. J.; Jackson, P.; Kong, G.; Ware, R. E.; Hofman, M. S.; Pattison, D. A.; Akhurst, T. A.; Drummond, E.; Roselt, P.; Callahan, J.; Price, R.; Jeffery, C. M.; Hong, E.; Noonan, W.; Herschtal, A.; Hicks, L. J.; Hedt, A.; Harris, M.; Paterson, B. M.; Donnelly, P. S. 64Cu-SARTATE PET Imaging of Patients with Neuroendocrine Tumors Demonstrates High Tumor Uptake and Retention, Potentially Allowing Prospective Dosimetry for Peptide Receptor Radionuclide Therapy. *Journal of Nuclear Medicine* **2019**, *60* (6), 777–785. https://doi.org/10.2967/jnumed.118.217745.

(187) Liu, F.; Guo, X.; Liu, T.; Xu, X.; Li, N.; Xiong, C.; Li, C.; Zhu, H.; Yang, Z. Evaluation of Pan-SSTRs Targeted Radioligand [64Cu]NOTA-PA1 Using Micro-PET Imaging in Xenografted Mice. *ACS Medicinal Chemistry Letters* **2020**, *11* (4), 445–450. https://doi.org/10.1021/acsmedchemlett.9b00544.

(188) Cooper, M. S.; Ma, M. T.; Sunassee, K.; Shaw, K. P.; Williams, J. D.; Paul, R. L.; Donnelly, P. S.; Blower, P. J. Comparison of 64 Cu-Complexing Bifunctional Chelators for Radioimmunoconjugation: Labeling Efficiency, Specific Activity, and in Vitro / in Vivo Stability. *Bioconjugate Chemistry* **2012**, *23* (5), 1029–1039. https://doi.org/10.1021/bc300037w.

(189) Cai, H.; Fissekis, J.; Conti, P. S. Synthesis of a Novel Bifunctional Chelator AmBaSar Based on Sarcophagine for Peptide Conjugation and 64Cu Radiolabelling. *Dalton Transactions* **2009**, 5395–5400. https://doi.org/10.1039/b902210d.

(190) Paterson, B. M.; Roselt, P.; Denoyer, D.; Cullinane, C.; Binns, D.; Noonan, W.; Jeffery, C. M.; Price, R. I.; White, J. M.; Hicks, R. J.; Donnelly, P. S. PET Imaging of Tumours with a 64Cu Labeled Macrobicyclic Cage Amine Ligand Tethered to Tyr3-Octreotate. *Dalton Transactions* **2014**, *43* (3), 1386–1396. https://doi.org/10.1039/C3DT52647J.

(191) Maheshwari, V.; Dearling, J. L. J.; Treves, S. T.; Packard, A. B. Measurement of the Rate of Copper(II) Exchange for 64Cu Complexes of Bifunctional Chelators. *Inorganica Chimica Acta* **2012**, *393*, 318–323. https://doi.org/10.1016/j.ica.2012.07.012.

(192) Loft, M.; Carlsen, E. A.; Johnbeck, C. B.; Johannesen, H. H.; Binderup, T.; Pfeifer, A.; Mortensen, J.; Oturai, P.; Loft, A.; Berthelsen, A. K.; Langer, S. W.; Knigge, U.; Kjaer, A. 64Cu-DOTATATE PET in Patients with Neuroendocrine Neoplasms: Prospective, Head-to-Head Comparison of Imaging at 1 Hour and 3 Hours Post-Injection. *Journal of Nuclear Medicine* **2020**, *62* (1), 73–80. https://doi.org/10.2967/jnumed.120.244509.

(193) Hughes, O. D. M.; Bishop, M. C.; Perkins, A. C.; Wastie, M. L.; Denton, G.; Price, M. R.; Frier, M.; Denley, H.; Rutherford, R.; Schubiger, P. A. Targeting Superficial Bladder Cancer by the Intravesical Administration of Copper-67–Labeled Anti-MUC1 Mucin Monoclonal Antibody C595. *Journal of Clinical Oncology* **2000**, *18* (2), 363–363. https://doi.org/10.1200/JCO.2000.18.2.363.

(194) DeNardo, G. L.; Kukis, D. L.; Shen, S.; DeNardo, D. A.; Meares, C. F.; DeNardo, S. J. 67Cu-versus 131I-Labeled Lym-1 Antibody: Comparative Pharmacokinetics and Dosimetry in Patients with Non-Hodgkin's Lymphoma. *Clinical Cancer Research* **1999**, *5* (3), 533–541.

(195) O'Donnell, R. T.; DeNardo, G. L.; Kukis, D. L.; Lamborn, K. R.; Shen, S.; Yuan, A.; Goldstein, D. S.; Carr, C. E.; Mirick, G. R.; DeNardo, S. J. A Clinical Trial of Radioimmunotherapy with 67Cu-2IT-BAT-Lym-1 for Non-Hodgkin's Lymphoma. *Journal of Nuclear Medicine* **1999**, *40* (12), 2014–2020.

(196) Cullinane, C.; Jeffery, C. M.; Roselt, P. D.; Dam, E. M. van; Jackson, S.; Kuan, K.; Jackson, P.; Binns, D.; Zuylekom, J. van; Harris, M. J.; Hicks, R. J.; Donnelly, P. S. Peptide Receptor Radionuclide Therapy with 67Cu-CuSarTATE Is Highly Efficacious Against a Somatostatin-Positive Neuroendocrine Tumor Model. *Journal of Nuclear Medicine* **2020**, *61* (12), 1800–1805. https://doi.org/10.2967/jnumed.120.243543.

(197) Anderson, C. J.; Ferdani, R. Copper-64 Radiopharmaceuticals for PET Imaging of Cancer: Advances in Preclinical and Clinical Research. *Cancer Biotherapy and Radiopharmaceuticals* **2009**, *24* (4), 379–393. https://doi.org/10.1089/cbr.2009.0674.

(198) International Atomic Energy Agency. *Cyclotron Produced Radionuclides: Emerging Positron Emitters for Medical Applications: 64Cu and 124I*; Radioisotopes and Radiopharmaceuticals Reports; IAEA: Vienna, 2016.

(199) Ku, A.; Facca, V. J.; Cai, Z.; Reilly, R. M. Auger Electrons for Cancer Therapy – a Review. *European Journal of Nuclear Medicine and Molecular Imaging Radiopharmacy and Chemistry* **2019**, *4* (1), 27. https://doi.org/10.1186/s41181-019-0075-2.

(200) Lehenberger, S.; Barkhausen, C.; Cohrs, S.; Fischer, E.; Grünberg, J.; Hohn, A.; Köster, U.; Schibli, R.; Türler, A.; Zhernosekov, K. The Low-Energy Β− and Electron Emitter 161Tb as an Alternative to 177Lu for Targeted Radionuclide Therapy. *Nuclear Medicine and Biology* **2011**, *38* (6), 917–924. https://doi.org/10.1016/j.nucmedbio.2011.02.007.

(201) de Jong, M.; Breeman, W. A. P.; Bernard, B. F.; Rolleman, E. J.; Hoflande, L. J.; Visser, T. J.; Setyono-Han, B.; Bakker, W. H.; van der Pluijm, M. E.; Krenning, E. P. Evaluation in Vitro and in Rats of 161Tb-DTPA-Octreotide, a Somatostatin Analogue with Potential for Intraoperative Scanning and Radiotherapy. *European Journal of Nuclear Medicine* **1995**, *22* (7), 608–616. https://doi.org/10.1007/BF01254561.

(202) Uusijärvi, H.; Bernhardt, P.; Rösch, F.; Maecke, H. R.; Forssell-Aronsson, E. Electron- and Positron-Emitting Radiolanthanides for Therapy: Aspects of Dosimetry and Production. *Journal of Nuclear Medicine* **2006**, *47* (5), 807–814.

(203) Baum, R. P.; Singh, A.; Kulkarni, H. R.; Bernhardt, P.; Rydén, T.; Schuchardt, C.; Gracheva, N.; Grundler, P. V.; Köster, U.; Müller, D.; Pröhl, M.; Zeevaart, J. R.; Schibli, R.; Van Der Meulen, N. P.; Müller, C. First-in-Humans Application of ^{161} Tb: A Feasibility Study Using ^{161} Tb-DOTATOC. *J Nucl Med* **2021**, *62* (10), 1391–1397. https://doi.org/10.2967/jnumed.120.258376.

(204) Haller, S.; Pellegrini, G.; Vermeulen, C.; van der Meulen, N. P.; Köster, U.; Bernhardt, P.; Schibli, R.; Müller, C. Contribution of Auger/Conversion Electrons to Renal Side Effects after Radionuclide Therapy: Preclinical Comparison of 161Tb-Folate and 177Lu-Folate. *European Journal of Nuclear Medicine and Molecular Imaging Research* **2016**, *6* (1), 13. https://doi.org/10.1186/s13550-016-0171-1.

(205) Hindie, E.; Zanotti-Fregonara, P.; Quinto, M. A.; Morgat, C.; Champion, C. Dose Deposits from 90Y, 177Lu, 111In, and 161Tb in Micrometastases of Various Sizes: Implications for Radiopharmaceutical Therapy. *Journal of Nuclear Medicine* **2016**, *57* (5), 759–764. https://doi.org/10.2967/jnumed.115.170423.

(206) Champion, C.; Quinto, M. A.; Morgat, C.; Zanotti-Fregonara, P.; Hindié, E. Comparison between Three Promising SS-Emitting Radionuclides, 67Cu, 47Sc and 161Tb, with Emphasis on Doses Delivered to Minimal Residual Disease. *Theranostics* **2016**, *6* (10), 1611–1618. https://doi.org/10.7150/thno.15132.

(207) Reilly, R. M.; Kassis, A. Targeted Auger Electron Radiotherapy of Malignancies. In *Monoclonal Antibody and Peptide-Targeted Radiotherapy of Cancer*; 2010; pp 289–348. https://doi.org/10.1002/9780470613214.ch9.

(208) Paillas, S.; Ladjohounlou, R.; Lozza, C.; Pichard, A.; Boudousq, V.; Jarlier, M.; Sevestre, S.; Le Blay, M.; Deshayes, E.; Sosabowski, J.; Chardès, T.; Navarro-Teulon, I.; Mairs, R. J.; Pouget, J.-P. Localized Irradiation of Cell Membrane by Auger Electrons Is Cytotoxic Through Oxidative Stress-Mediated Nontargeted Effects. *Antioxidants & Redox Signaling* **2016**, *25* (8), 467–484. https://doi.org/10.1089/ars.2015.6309.

(209) O'Donoghue, J. A.; Wheldon, T. E. Targeted Radiotherapy Using Auger Electron Emitters. *Physics in Medicine and Biology* **1996**, *41* (10), 1973–1992. https://doi.org/10.1088/0031-9155/41/10/009.

(210) Roeske, J. C.; Aydogan, B.; Bardies, M.; Humm, J. L. Small-Scale Dosimetry: Challenges and Future Directions. *Seminars in Nuclear Medicine* **2008**, *38* (5), 367–383. https://doi.org/10.1053/j.semnuclmed.2008.05.003.

(211) Hsiao, Y.-Y.; Hung, T.-H.; Tu, S.-J.; Tung, C.-J. Fast Monte Carlo Simulation of DNA Damage Induction by Auger-Electron Emission. *International Journal of Radiation Biology* **2014**, *90* (5), 392–400. https://doi.org/10.3109/09553002.2014.892649.

(212) Fasih, A.; Fonge, H.; Cai, Z.; Leyton, J. V.; Tikhomirov, I.; Done, S. J.; Reilly, R. M. 111In-Bn-DTPA-Nimotuzumab with/without Modification with Nuclear Translocation Sequence (NLS) Peptides: An Auger Electron-Emitting Radioimmunotherapeutic Agent for EGFR-Positive and Trastuzumab (Herceptin)-Resistant Breast Cancer. *Breast Cancer Research and Treatment* **2012**, *135* (1), 189–200. https://doi.org/10.1007/s10549-012-2137-y.

(213) Costantini, D. L.; McLarty, K.; Lee, H.; Done, S. J.; Vallis, K. A.; Reilly, R. M. Antitumor Effects and Normal-Tissue Toxicity of 111In-Nuclear Localization Sequence-Trastuzumab in Athymic Mice Bearing HER-Positive Human Breast Cancer Xenografts. *Journal of Nuclear Medicine* **2010**, *51* (7), 1084–1091. https://doi.org/10.2967/jnumed.109.072389.

(214) Imstepf, S.; Pierroz, V.; Raposinho, P.; Bauwens, M.; Felber, M.; Fox, T.; Shapiro, A. B.; Freudenberg, R.; Fernandes, C.; Gama, S.; Gasser, G.; Motthagy, F.; Santos, I. R.; Alberto, R. Nuclear Targeting with an Auger Electron Emitter Potentiates the Action of a Widely Used Antineoplastic Drug. *Bioconjugate Chemistry* **2015**, *26* (12), 2397–2407. https://doi.org/10.1021/acs.bioconjchem.5b00466.

(215) Li, L.; Quang, T. S.; Gracely, E. J.; Kim, J. H.; Emrich, J. G.; Yaeger, T. E.; Jenrette, J. M.; Cohen, S. C.; Black, P.; Brady, L. W. A Phase II Study of Anti–Epidermal Growth Factor Receptor Radioimmunotherapy in the Treatment of Glioblastoma Multiforme. *Journal of Neurosurgery* **2010**, *113* (2), 192–198. https://doi.org/10.3171/2010.2.JNS091211.

(216) Vallis, K. A.; Reilly, R. M.; Scollard, D.; Merante, P.; Brade, A.; Velauthapillai, S.; Caldwell, C.; Chan, I.; Freeman, M.; Lockwood, G.; Miller, N. A.; Cornelissen, B.; Petronis, J.; Sabate, K. Phase I Trial to Evaluate the Tumor and Normal Tissue Uptake, Radiation Dosimetry and Safety of (111)In-DTPA-Human Epidermal Growth Factor in Patients with Metastatic EGFR-Positive Breast Cancer. *American Journal of Nuclear Medicine and Molecular Imaging* **2014**, *4* (2), 181–192.

(217) Cornelissen, B.; A Vallis, K. Targeting the Nucleus: An Overview of Auger-Electron Radionuclide Therapy. *Current Drug Discovery Technologies* **2010**, *7* (4), 263–279. https://doi.org/10.2174/157016310793360657.

(218) Kassis, A. I. Cancer Therapy with Auger Electrons: Are We Almost There? *Journal of Nuclear Medicine* **2003**, *44* (9), 1479–1481.

(219) Aluicio-Sarduy, E.; Thiele, N. A.; Martin, K. E.; Vaughn, B. A.; Devaraj, J.; Olson, A. P.; Barnhart, T. E.; Wilson, J. J.; Boros, E.; Engle, J. W. Establishing Radiolanthanum Chemistry for Targeted Nuclear Medicine Applications. *Chemistry – A European Journal* **2020**, *26* (6), 1238–1242. https://doi.org/10.1002/chem.201905202.

(220) Randhawa, P.; Gower-Fry, K. L.; Stienstra, C. M. K.; Tosato, M.; Chen, S.; Gao, Y.; McDonagh, A. W.; Di Marco, V.; Radchenko, V.; Schreckenbach, G.; Ramogida, C. F. Selective Chelation of the Exotic Meitner-Auger Emitter Mercury-197m/g with Sulfur-Rich Macrocyclic Ligands: Towards the Future of Theranostic Radiopharmaceuticals. *Chemistry – A European Journal* *29*, e202203815. https://doi.org/10.1002/chem.202203815.

(221) Blower, P. J.; Smith, R. J.; Jolley, C. Thiamacrocyclic Bifunctional Chelators for Labelling with Chemically “Soft” Radiometals. *Nuclear Medicine Communications* **1992**, *13* (4), 231.

(222) Emfietzoglou, D.; Nikjoo, H. Accurate Electron Inelastic Cross Sections and Stopping Powers for Liquid Water over the 0.1-10 keV Range Based on an Improved Dielectric Description of the Bethe Surface. *Radiation Research* **2007**, *167* (1), 110–120. https://doi.org/10.1667/RR0551.1.

(223) Fonslet, J.; Lee, B. Q.; Tran, T. A.; Siragusa, M.; Jensen, M.; Kibédi, T.; Stuchbery, A. E.; Severin, G. W. 135 La as an Auger-Electron Emitter for Targeted Internal Radiotherapy. *Physics in Medicine & Biology* **2017**, *63* (1), 015026. https://doi.org/10.1088/1361-6560/aa9b44.

(224) Bünzli, J.-C. G. Benefiting from the Unique Properties of Lanthanide Ions. *Accounts of Chemical Research* **2006**, *39* (1), 53–61. https://doi.org/10.1021/ar0400894.

(225) Roca-Sabio, A.; Mato-Iglesias, M.; Esteban-Gómez, D.; Tóth, É.; Blas, A. de; Platas-Iglesias, C.; Rodríguez-Blas, T. Macrocyclic Receptor Exhibiting Unprecedented Selectivity for Light Lanthanides. *Journal of the American Chemical Society* **2009**, *131* (9), 3331–3341. https://doi.org/10.1021/ja808534w.

(226) Greif, R. L.; Sullivan, W. J.; Jacobs, G. S.; Pitts, R. F. Distribution of Radiomercury Administered as Labelled Chlormerodrin (Neohydrin®) in the Kidneys of Rats and Dogs. *Journal of Clinical Investigation* **1956**, *35* (1), 38–43. https://doi.org/10.1172/JCI103250.

(227) Overton, M. C.; Haynie, T. P.; Snodgrass, S. R. Brain Scans in Nonneoplastic Intracranial Lesions. *Journal of the American Medical Association* **1965**, *191* (6), 431–436. https://doi.org/10.1001/jama.1965.03080060005001.

(228) Walther, M.; Preusche, S.; Bartel, S.; Wunderlich, G.; Freudenberg, R.; Steinbach, J.; Pietzsch, H. J. Theranostic Mercury: 197(m)Hg with High Specific Activity for Imaging and Therapy. *Applied Radiation and Isotopes* **2015**, *97*, 177–181. https://doi.org/10.1016/j.apradiso.2015.01.001.

(229) Lebeda, O.; Červenák, J. Revised Cross-Sections for Formation of Theranostic 197m,g-Hg in Proton- and Deuteron-Induced Reactions on 197Au. *Nuclear Instruments and Methods in Physics Research Section B: Beam Interactions with Materials and Atoms* **2020**, *478* (April), 85–91. https://doi.org/10.1016/j.nimb.2020.05.014.

(230) Despotopulos, J. D.; Kmak, K. N.; Shaughnessy, D. A. Production and Isolation of 197m,g-Hg. *Journal of Radioanalytical and Nuclear Chemistry* **2018**, *317* (2), 985–989. https://doi.org/10.1007/s10967-018-5927-9.

(231) Gloris, M.; Michel, R.; Sudbrock, F.; Herpers, U.; Malmborg, P.; Holmqvist, B. Proton-Induced Production of Residual Radionuclides in Lead at Intermediate Energies. *Nuclear Instruments and Methods in Physics Research Section A: Accelerators, Spectrometers, Detectors and Associated Equipment* **2001**, *463* (3), 593–633. https://doi.org/10.1016/S0168-9002(01)00174-7.

(232) Nayak, D.; Lahiri, S. Production of Tracer Packet of Heavy and Toxic Elements. *Journal of Radioanalytical and Nuclear Chemistry* **2002**, *254* (3), 619–623. https://doi.org/doi.org/10.1023/A:1021670928426.

(233) Samczyński, Z. Ion Exchange Behavior of Selected Elements on Chelex 100 Resin. *Solvent Extraction and Ion Exchange* **2006**, *24* (5), 781–794. https://doi.org/10.1080/07366290600846174.

(234) Gupta, C. B.; Tandon, S. N. Ion-Exchange Behavior of Mercury(II) in Mixed Solvents: Separation from Zinc(II), Cadmium(II), Gold(III), and Thallium(III). *Separation Science* **1972**, *7* (5), 513–525. https://doi.org/10.1080/00372367208056051.

(235) Randhawa, P.; Olson, A. P.; Chen, S.; Gower-Fry, K. L.; Hoehr, C.; Engle, J. W.; Ramogida, C. F.; Radchenko, V. Meitner-Auger Electron Emitters for Targeted Radionuclide Therapy: Mercury-197m/g and Antimony-119. *Current Radiopharmaceuticals* **2021**, *14* (4), 394–419. https://doi.org/10.2174/1874471014999210111201630.

(236) Walther, M.; Lebeda, O.; Preusche, S.; Pietzsch, H.-J.; Steinbach, J. Theranostic Mercury Part 1: A New Hg/Au Separation by a Resin Based Method. In *AIP Conference Proceedings*; American Institute of Physics, 2017; Vol. 1845, p 020023. https://doi.org/10.1063/1.4983554.

(237) Bebout, D. C. Mercury: Inorganic & Coordination Chemistry Based in Part on the Article Mercury: Inorganic & Coordination Chemistry by Gregory J. Grant Which Appeared in the Encyclopedia of Inorganic Chemistry, First Edition. In *Encyclopedia*

of Inorganic and Bioinorganic Chemistry; John Wiley & Sons, Ltd, 2011. https://doi.org/10.1002/9781119951438.eibc0124.

(238) Leiva-Presa, À.; Capdevila, M.; Gonzàlez-Duarte, P. Mercury(II) Binding to Metallothioneins: Variables Governing the Formation and Structural Features of the Mammalian Hg-MT Species. *European Journal of Biochemistry* **2004**, *271*, 4872–4880. https://doi.org/10.1111/j.1432-1033.2004.04456.x.

(239) Schurz, F.; Sabater-vilar, M.; Fink-gremmels, J. Mutagenicity of Mercury Chloride and Mechanisms of Cellular Defence : The Role of Metal-Binding Proteins. *Mutagenesis* **2000**, *15* (6), 525–530.

(240) Oram, P. D.; Fang, X.; Fernando, Q.; Letkeman, P.; Letkeman, D. The Formation Constants of Mercury(II)−Glutathione Complexes. *Chemical Research in Toxicology* **1996**, *9* (4), 709–712. https://doi.org/10.1021/tx9501896.

(241) Broussard, L. A.; Hammett-Stabler, C. A.; Winecker, R. E.; Ropero-Miller, J. D. The Toxicology of Mercury. *Laboratory Medicine* **2002**, *33* (8), 614–625. https://doi.org/10.1309/5HY1-V3NE-2LFL-P9MT.

(242) Fleischer, H.; Dienes, Y.; Mathiasch, B.; Schmitt, V.; Schollmeyer, D. Cysteamine and Its Homoleptic Complexes with Group 12 Metal Ions. Differences in the Coordination Chemistry of Zn(II) , Cd(II) , and Hg(II) with a Small N,S-Donor Ligand. *Inorganic Chemistry* **2005**, *44* (22), 8087–8096. https://doi.org/10.1021/ic050814m.

(243) Ocak, Ü.; Alp, H.; Gökçe, P.; Ocak, M. The Synthesis of New N 2 S 2 -Macrocyclic Schiff Base Ligands and Investigation of Their Ion Extraction Capability from Aqueous Media. *Separation Science and Technology* **2006**, *41* (2), 391–401. https://doi.org/10.1080/01496390500496942.

(244) Amani, V.; Alizadeh, R.; Alavije, H. S.; Heydari, S. F.; Abafat, M. Mononuclear Mercury(II) Complexes Containing Bipyridine Derivatives and Thiocyanate Ligands: Synthesis, Characterization, Crystal Structure Determination, and Luminescent Properties. *Journal of Molecular Structure* **2017**, *1142*, 92–101. https://doi.org/10.1016/j.molstruc.2017.04.034.

(245) Lebeda, O.; Kondev, F. G.; Červenák, J. Branching Ratio and γ-Ray Emission Probabilities in the Decay of the Jπ=13/2+ Isomer in 197Hg. *Nuclear Instruments and Methods in Physics Research Section A: Accelerators, Spectrometers, Detectors and Associated Equipment* **2020**, *959*, 163481. https://doi.org/10.1016/j.nima.2020.163481.

(246) Freudenberg, R.; Apolle, R.; Walther, M.; Hartmann, H.; Kotzerke, J. Molecular Imaging Using the Theranostic Agent 197(m)Hg: Phantom Measurements and Monte Carlo Simulations. *European Journal of Nuclear Medicine and Molecular Imaging Physics* **2018**, *5* (1), 15. https://doi.org/10.1186/s40658-018-0216-9.

(247) Kelly, V. J.; Wu, S.; Gottumukkala, V.; Coelho, R.; Palmer, K.; Nair, S.; Erick, T.; Puri, R.; Ilovich, O.; Mukherjee, P. Preclinical Evaluation of an 111In/225Ac Theranostic Targeting Transformed MUC1 for Triple Negative Breast Cancer. *Theranostics* **2020**, *10* (15), 6946–6958. https://doi.org/10.7150/thno.38236.

(248) Tóth, É.; Brücher, E.; Lázár, I.; Tóth, I. Kinetics of Formation and Dissociation of Lanthanide(III)-DOTA Complexes. *Inorganic Chemistry* **1994**, *33* (18), 4070–4076. https://doi.org/10.1021/ic00096a036.

(249) Cacheris, W. P.; Nickle, S. K.; Sherry, A. D. Thermodynamic Study of Lanthanide Complexes of 1,4,7-Triazacyclononane-N,N',N"-Triacetic Acid and 1,4,7,10-Tetraazacyclododecane-N,N',N",N"-Tetraacetic Acid. *Inorganic Chemistry* **1987**, *26* (6), 958–960. https://doi.org/10.1021/ic00253a038.

(250) Aime, S.; Botta, M.; Fasano, M.; Marques, M. P. M.; Geraldes, C. F. G. C.; Pubanz, D.; Merbach, A. E. Conformational and Coordination Equilibria on DOTA Complexes of Lanthanide Metal Ions in Aqueous Solution Studied by 1H-NMR

Spectroscopy. *Inorganic Chemistry* **1997**, *36* (10), 2059–2068. https://doi.org/10.1021/ic961364o.

(251) Wharton, L.; Kurakina, E.; Radchenko, V.; Schaffer, P.; Orvig, C. Chemical Promiscuity of Non-Macrocyclic Multidentate Chelating Ligands for Radiometal Ions: H4neunpa-NH2 vs H4noneunpa. *Inorganic Chemistry* **2021**, *60* (6), 4076–4092. https://doi.org/10.1021/acs.inorgchem.1c00152.

(252) Hu, A.; Aluicio-Sarduy, E.; Brown, V.; MacMillan, S. N.; Becker, K. V.; Barnhart, T. E.; Radchenko, V.; Ramogida, C. F.; Engle, J. W.; Wilson, J. J. Py-Macrodipa: A Janus Chelator Capable of Binding Medicinally Relevant Rare-Earth Radiometals of Disparate Sizes. *Journal of the American Chemical Society* **2021**, *143* (27), 10429–10440. https://doi.org/10.1021/jacs.1c05339.

(253) Kadassery, K. J.; King, A. P.; Fayn, S.; Baidoo, K. E.; MacMillan, S. N.; Escorcia, F. E.; Wilson, J. J. H2BZmacropa-NCS: A Bifunctional Chelator for Actinium-225 Targeted Alpha Therapy. *Bioconjugate Chemistry* **2022**, *33* (6), 1222–1231. https://doi.org/10.1021/acs.bioconjchem.2c00190.

(254) Wharton, L.; McNeil, S. W.; Merkens, H.; Yuan, Z.; Van de Voorde, M.; Engudar, G.; Ingham, A.; Koniar, H.; Rodríguez-Rodríguez, C.; Radchenko, V.; Ooms, M.; Kunz, P.; Bénard, F.; Schaffer, P.; Yang, H. Preclinical Evaluation of [155/161Tb]Tb-Crown-TATE—A Novel SPECT Imaging Theranostic Agent Targeting Neuroendocrine Tumours. *Molecules* **2023**, *28* (7), 3155. https://doi.org/10.3390/molecules28073155.

(255) Xu, J.; Durbin, P. W.; Kullgren, B.; Ebbe, S. N.; Uhlir, L. C.; Raymond, K. N. Synthesis and Initial Evaluation for in Vivo Chelation of Pu(IV) of a Mixed Octadentate Spermine-Based Ligand Containing 4-Carbamoyl-3-Hydroxy-1-Methyl-2(1H)-Pyridinone and 6-Carbamoyl-1-Hydroxy-2(1H)-Pyridinone. *Journal of Medicinal Chemistry* **2002**, *45* (18), 3963–3971. https://doi.org/10.1021/jm010564t.

(256) Ma, Y.; Zhou, T.; Kong, X.; C. Hider, R. Chelating Agents for the Treatment of Systemic Iron Overload. *Current Medicinal Chemistry* **2012**, *19* (17), 2816–2827. https://doi.org/10.2174/092986712800609724.

(257) Cilibrizzi, A.; Abbate, V.; Chen, Y.; Ma, Y.; Zhou, T.; Hider, R. C. Hydroxypyridinone Journey into Metal Chelation. *Chemical Reviews* **2018**, *118* (16), 7657–7701. https://doi.org/10.1021/acs.chemrev.8b00254.

(258) Deblonde, G. J.; Sturzbecher-Hoehne, M.; Abergel, R. J. Solution Thermodynamic Stability of Complexes Formed with the Octadentate Hydroxypyridinonate Ligand 3,4,3-LI(1,2-HOPO): A Critical Feature for Efficient Chelation of Lanthanide(IV) and Actinide(IV) Ions. *Inorganic Chemistry* **2013**, *52* (15), 8805–8811. https://doi.org/10.1021/ic4010246.

(259) Gorden, A. E. V.; Xu, J.; Raymond, K. N.; Durbin, P. Rational Design of Sequestering Agents for Plutonium and Other Actinides. *Chemical Reviews* **2003**, *103* (11), 4207–4282. https://doi.org/10.1021/CR990114X.

(260) Deri, M. A.; Ponnala, S.; Zeglis, B. M.; Pohl, G.; Dannenberg, J. J.; Lewis, J. S.; Francesconi, L. C. Alternative Chelator for 89Zr Radiopharmaceuticals: Radiolabeling and Evaluation of 3,4,3-(LI-1,2-HOPO). *Journal of Medicinal Chemistry* **2014**, *57* (11), 4849–4860. https://doi.org/10.1021/jm500389b.

(261) Deri, M. A.; Ponnala, S.; Kozlowski, P.; Burton-Pye, B. P.; Cicek, H. T.; Hu, C.; Lewis, J. S.; Francesconi, L. C. P-SCN-Bn-HOPO: A Superior Bifunctional Chelator for 89Zr ImmunoPET. *Bioconjugate Chemistry* **2015**, *26* (12), 2579–2591. https://doi.org/10.1021/acs.bioconjchem.5b00572.

(262) Winkler, J.; Saadat, K.; Díaz-Gavilán, M.; Urban, E.; Noe, C. R. Oligonucleotide–Polyamine Conjugates: Influence of Length and Position of 2′-Attached Polyamines

on Duplex Stability and Antisense Effect. *European Journal of Medicinal Chemistry* **2009**, *44* (2), 670–677. https://doi.org/10.1016/j.ejmech.2008.05.012.

(263) Geall, A. J.; Blagbrough, I. S. Homologation of Polyamines in the Rapid Synthesis of Lipospermine Conjugates and Related Lipoplexes. *Tetrahedron* **1998**, *39* (5–6), 443–446. https://doi.org/10.1016/S0040-4020(99)01082-0.

(264) König, S. G.; Öz, S.; Krämer, R. A Polyamine-Modified near-Infrared Fluorescent Probe for Selective Staining of Live Cancer Cells. *Chemical Communications* **2015**, *51* (34), 7360–7363. https://doi.org/10.1039/c5cc01637a.

(265) Bhupathiraju, N. V. S. D. K.; Younes, A.; Cao, M.; Ali, J.; Cicek, H. T.; Tully, K. M.; Ponnala, S.; Babich, J. W.; Deri, M. A.; Lewis, J. S.; Francesconi, L. C.; Drain, C. M. Improved Synthesis of the Bifunctional Chelator P-SCN-Bn-HOPO. *Organic and Biomolecular Chemistry* **2019**, *17* (28), 6866–6871. https://doi.org/10.1039/c9ob01068h.

(266) Guérard, F.; Beyler, M.; Lee, Y.-S.; Tripier, R.; Gestin, J.-F.; Brechbiel, M. W. Investigation of the Complexation of natZr(IV) and 89Zr(IV) by Hydroxypyridinones for the Development of Chelators for PET Imaging Applications. *Dalton Transactions* **2017**, *46* (14), 4749–4758. https://doi.org/10.1039/C6DT04625H.

(267) Sturzbecher-Hoehne, M.; Choi, T. A.; Abergel, R. J. Hydroxypyridinonate Complex Stability of Group (IV) Metals and Tetravalent f-Block Elements: The Key to the next Generation of Chelating Agents for Radiopharmaceuticals. *Inorganic Chemistry* **2015**, *54* (7), 3462–3468. https://doi.org/10.1021/acs.inorgchem.5b00033.

(268) Kelley, M. P.; Deblonde, G. J.-P.; Su, J.; Booth, C. H.; Abergel, R. J.; Batista, E. R.; Yang, P. Bond Covalency and Oxidation State of Actinide Ions Complexed with Therapeutic Chelating Agent 3,4,3-LI(1,2-HOPO). *Inorganic Chemistry* **2018**, *57* (9), 5352–5363. https://doi.org/10.1021/acs.inorgchem.8b00345.

(269) Cassells, I.; Ahenkorah, S.; Burgoyne, A. R.; Van de Voorde, M.; Deroose, C. M.; Cardinaels, T.; Bormans, G.; Ooms, M.; Cleeren, F. Radiolabeling of Human Serum Albumin With Terbium-161 Using Mild Conditions and Evaluation of in Vivo Stability. *Frontiers in Medicine* **2021**, *8*, 1359. https://doi.org/10.3389/fmed.2021.675122.

(270) Gao, Y.; Grover, P.; Schreckenbach, G. Stabilization of Hydrated Ac(III) Cation: The Role of Superatom States in Actinium-Water Bonding. *Chemical Science* **2021**, *12* (7), 2655–2666. https://doi.org/10.1039/D0SC02342F.

(271) Fonseca Guerra, C.; Handgraaf, J. W.; Baerends, E. J.; Bickelhaupt, F. M. Voronoi Deformation Density (VDD) Charges: Assessment of the Mulliken, Bader, Hirshfeld, Weinhold, and VDD Methods for Charge Analysis. *Journal of Computational Chemistry* **2004**, *25* (2), 189–210. https://doi.org/10.1002/JCC.10351.

(272) Ziegler, T.; Rauk, A. On the Calculation of Bonding Energies by the Hartree Fock Slater Method I. The Transition State Method. *Theoretica Chimica Acta* **1977**, *46*, 1–10.

(273) Zhao, L.; von Hopffgarten, M.; Andrada, D. M.; Frenking, G. Energy Decomposition Analysis. *Wiley Interdisciplinary Reviews: Computational Molecular Science* **2018**, *8* (3). https://doi.org/10.1002/WCMS.1345.

(274) Pinto Gomes, C.; Metz, A.; Bats, J. W.; Gohlke, H.; Göbel, M. W. Modular Solid-Phase Synthesis of Teroxazoles as a Class of α-Helix Mimetics. *European Journal of Organic Chemistry* **2012**, *2012* (17), 3270–3277. https://doi.org/10.1002/ejoc.201200339.

(275) Larionov, V. A.; Cruchter, T.; Mietke, T.; Meggers, E. Polymer-Supported Chiral-at-Metal Lewis Acid Catalysts. *Organometallics* **2017**, *36* (8), 1457–1460. https://doi.org/10.1021/acs.organomet.7b00016.

(276) Zeisler, S.; Clarke, B.; Kumlin, J.; Hook, B.; Varah, S.; Hoehr, C. A Compact Quick-Release Solid Target System for the TRIUMF TR13 Cyclotron. *Instruments* **2019**, *3* (16). https://doi.org/10.3390/instruments3010016.

(277) Koning, A. J.; Rochman, D.; Sublet, J. C.; Dzysiuk, N.; Fleming, M.; van der Marck, S. TENDL: Complete Nuclear Data Library for Innovative Nuclear Science and Technology. *Nuclear Data Sheets* **2019**, *155*, 1–55. https://doi.org/10.1016/J.NDS.2019.01.002.

(278) Fiaccabrino, D. E.; Kunz, P.; Radchenko, V. Potential for Production of Medical Radionuclides with On-Line Isotope Separation at the ISAC Facility at TRIUMF and Particular Discussion of the Examples of 165Er and 155Tb. *Nuclear Medicine and Biology* **2021**, *94–95*, 81–91. https://doi.org/10.1016/J.NUCMEDBIO.2021.01.003.

(279) Grimme, S.; Bannwarth, C.; Shushkov, P. A Robust and Accurate Tight-Binding Quantum Chemical Method for Structures, Vibrational Frequencies, and Noncovalent Interactions of Large Molecular Systems Parametrized for All Spd-Block Elements (Z = 1–86). *Journal of Chemical Theory and Computation* **2017**, *13* (5), 1989–2009. https://doi.org/10.1021/acs.jctc.7b00118.

(280) Lu, T. *molclus program*. Version 1.9.9.4. http://www.keinsci.com/research/molclus.html (accessed 2022-09-09).

(281) Perdew, J. P.; Burke, K.; Ernzerhof, M. Generalized Gradient Approximation Made Simple. *Physical Review Letters* **1996**, *77* (18), 3865–3868. https://doi.org/10.1103/PhysRevLett.77.3865.

(282) Grimme, S.; Antony, J.; Ehrlich, S.; Krieg, H. A Consistent and Accurate Ab Initio Parametrization of Density Functional Dispersion Correction (DFT-D) for the 94 Elements H-Pu. *The Journal of Chemical Physics* **2010**, *132* (15), 154104. https://doi.org/10.1063/1.3382344.

(283) van Lenthe, E.; Ehlers, A.; Baerends, E.-J. Geometry Optimizations in the Zero Order Regular Approximation for Relativistic Effects. *The Journal of Chemical Physics* **1999**, *110* (18), 8943–8953. https://doi.org/10.1063/1.478813.

(284) Lenthe, E. van; Baerends, E. J.; Snijders, J. G. Relativistic Regular Two-component Hamiltonians. *The Journal of Chemical Physics* **1993**, *99* (6), 4597–4610. https://doi.org/10.1063/1.466059.

(285) van Lenthe, E.; Snijders, J. G.; Baerends, E. J. The Zero-order Regular Approximation for Relativistic Effects: The Effect of Spin–Orbit Coupling in Closed Shell Molecules. *The Journal of Chemical Physics* **1996**, *105* (15), 6505–6516. https://doi.org/10.1063/1.472460.

(286) van Lenthe, E.; Baerends, E. J.; Snijders, J. G. Relativistic Total Energy Using Regular Approximations. *The Journal of Chemical Physics* **1994**, *101* (11), 9783–9792. https://doi.org/10.1063/1.467943.

(287) Pye, C. C.; Ziegler, T. An Implementation of the Conductor-like Screening Model of Solvation within the Amsterdam Density Functional Package. *Theoretical Chemistry Accounts* **1999**, *101*, 396–408. https://doi.org/10.1007/s00214990m184.

(288) Klamt, A.; Schüürmann, G. COSMO: A New Approach to Dielectric Screening in Solvents with Explicit Expressions for the Screening Energy and Its Gradient. *Journal of the Chemical Society, Perkin Transactions 2* **1993**, No. 2, 799–805. https://doi.org/10.1039/P29930000799.

(289) Shamov, G. A.; Schreckenbach, G. Density Functional Studies of Actinyl Aquo Complexes Studied Using Small-Core Effective Core Potentials and a Scalar Four-Component Relativistic Method. *The Journal of Physical Chemistry A* **2006**, *110* (43), 12072–12072. https://doi.org/10.1021/jp0662855.

(290) Martin, R. L.; Hay, P. J.; Pratt, L. R. Hydrolysis of Ferric Ion in Water and Conformational Equilibrium. *The Journal of Physical Chemistry A* **1998**, *102* (20), 3565–3573. https://doi.org/10.1021/jp980229p.

(291) Morokuma, K. Molecular Orbital Studies of Hydrogen Bonds. III. C=O···H–O Hydrogen Bond in H2CO···H2O and H2CO···2H2O. *The Journal of Chemical Physics* **2003**, *55* (3), 1236–1244. https://doi.org/10.1063/1.1676210.

(292) Hirshfeld, F. L. Bonded-Atom Fragments for Describing Molecular Charge Densities. *Theoretica Chimica Acta* **1977**, *44*, 129–138.

(293) te Velde, G.; Bickelhaupt, F. M.; Baerends, E. J.; Fonseca Guerra, C.; van Gisbergen, S. J. A.; Snijders, J. G.; Ziegler, T. Chemistry with ADF. *Journal of Computational Chemistry* **2001**, *22* (9), 931–967. https://doi.org/10.1002/JCC.1056.

(294) Yousaf, T.; Dervenoulas, G.; Politis, M. Chapter Two - Advances in MRI Methodology. In *International Review of Neurobiology*; Politis, M., Ed.; Academic Press, 2018; Vol. 141, pp 31–76. https://doi.org/10.1016/bs.irn.2018.08.008.

(295) Bailey, D. L.; Willowson, K. P. An Evidence-Based Review of Quantitative SPECT Imaging and Potential Clinical Applications. *Journal of Nuclear Medicine* **2013**, *54* (1), 83–89. https://doi.org/10.2967/jnumed.112.111476.

(296) Khalil, M. M.; Tremoleda, J. L.; Bayomy, T. B.; Gsell, W. Molecular SPECT Imaging: An Overview. *International Journal of Molecular Imaging* **2011**, *2011*, 1–15. https://doi.org/10.1155/2011/796025.

(297) Vaz, S. C.; Oliveira, F.; Herrmann, K.; Veit-Haibach, P. Nuclear Medicine and Molecular Imaging Advances in the 21st Century. *The British Journal of Radiology* *9* (1110), 20200095. https://doi.org/10.1259/bjr.20200095.

(298) Townsend, D. Physical Principles and Technology of Clinical PET Imaging. *Annals Academy of Medicine Singapore* **2004**, *33* (2), 133–145.

(299) Harris, W. R.; Chen, Y.; Wein, K. Equilibrium Constants for the Binding of Indium(III) to Human Serum Transferrin. *Inorganic Chemistry* **1994**, *33* (22), 4991–4998. https://doi.org/10.1021/ic00100a024.

(300) Gai, Y.; Sun, L.; Lan, X.; Zeng, D.; Xiang, G.; Ma, X. Synthesis and Evaluation of New Bifunctional Chelators with Phosphonic Acid Arms for Gallium-68 Based PET Imaging in Melanoma. *Bioconjugate Chemistry* **2018**, *29* (10), 3483–3494. https://doi.org/10.1021/acs.bioconjchem.8b00642.

(301) Wang, X.; Jaraquemada-Peláez, M. D. G.; Cao, Y.; Pan, J.; Lin, K.-S.; Patrick, B. O.; Orvig, C. H2hox: Dual-Channel Oxine-Derived Acyclic Chelating Ligand for 68Ga Radiopharmaceuticals. *Inorganic Chemistry* **2019**, *58* (4), 2275–2285. https://doi.org/10.1021/acs.inorgchem.8b01208.

(302) Kaeppeli, S. A. M.; Schibli, R.; Mindt, T. L.; Behe, M. Comparison of Desferrioxamine and NODAGA for the Gallium-68 Labeling of Exendin-4. *EJNMMI Radiopharmacy and Chemistry* **2019**, *4* (1), 9. https://doi.org/10.1186/s41181-019-0060-9.

(303) Smith-Jones, P. M.; Stolz, B.; Bruns, C.; Albert, R.; Reist, H. W.; Fridrich, R.; Mäcke, H. R. Gallium-67/Gallium-68-[DFO]-Octreotide—A Potential Radiopharmaceutical for PET Imaging of Somatostatin Receptor-Positive Tumors: Synthesis and Radiolabeling In Vitro and Preliminary In Vivo Studies. *Journal of Nuclear Medicine* **1994**, *35* (2), 317–325.

(304) Joaqui-Joaqui, M. A.; Pandey, M. K.; Bansal, A.; Raju, M. V. R.; Armstrong-Pavlik, F.; Dundar, A.; Wong, H. L.; DeGrado, T. R.; Pierre, V. C. Catechol-Based Functionalizable Ligands for Gallium-68 Positron Emission Tomography Imaging. *Inorganic Chemistry* **2020**, *59* (17), 12025–12038. https://doi.org/10.1021/acs.inorgchem.0c00975.

(305) Eder, M.; Neels, O.; Müller, M.; Bauder-Wüst, U.; Remde, Y.; Schäfer, M.; Hennrich, U.; Eisenhut, M.; Afshar-Oromieh, A.; Haberkorn, U.; Kopka, K. Novel Preclinical and Radiopharmaceutical Aspects of [68Ga]Ga-PSMA-HBED-CC: A New PET Tracer for Imaging of Prostate Cancer. *Pharmaceuticals* **2014**, *7* (7), 779–796. https://doi.org/10.3390/ph7070779.

(306) Satpati, D.; Sharma, R.; Kumar, C.; Sarma, H. D.; Dash, A. ^{68} Ga-Chelation and Comparative Evaluation of N,N′-Bis-[2-Hydroxy-5-(Carboxyethyl)Benzyl]Ethylenediamine-N,N′-Diacetic Acid (HBED-CC) Conjugated NGR and RGD Peptides as Tumor Targeted Molecular Imaging Probes. *Medicinal Chemistry Communications* **2017**, *8* (3), 673–679. https://doi.org/10.1039/C7MD00006E.

(307) Costa, P.; Metello, L. F.; Alves, F.; Duarte Naia, M. Cyclotron Production of Unconventional Radionuclides for PET Imaging: The Example of Titanium-45 and Its Applications. *Instruments* **2018**, *2* (2), 8. https://doi.org/10.3390/instruments2020008.

(308) Chaple, I. F.; Thiele, K.; Thaggard, G.; Fernandez, S.; Boros, E.; Lapi, S. E. Optimized Methods for Production and Purification of Titanium-45. *Applied Radiation and Isotopes* **2020**, *166*, 109398. https://doi.org/10.1016/j.apradiso.2020.109398.

(309) Tinoco, A. D.; Saxena, M.; Sharma, S.; Noinaj, N.; Delgado, Y.; Quiñones González, E. P.; Conklin, S. E.; Zambrana, N.; Loza-Rosas, S. A.; Parks, T. B. Unusual Synergism of Transferrin and Citrate in the Regulation of Ti(IV) Speciation, Transport, and Toxicity. *Journal of the American Chemical Society* **2016**, *138* (17), 5659–5665. https://doi.org/10.1021/jacs.6b01966.

(310) Jones, K. E.; Batchler, K. L.; Zalouk, C.; Valentine, A. M. Ti(IV) and the Siderophore Desferrioxamine B: A Tight Complex Has Biological and Environmental Implications. *Inorganic Chemistry* **2017**, *56* (3), 1264–1272. https://doi.org/10.1021/acs.inorgchem.6b02399.

(311) Saxena, M.; Loza-Rosas, S. A.; Gaur, K.; Sharma, S.; Perez Otero, S. C.; Tinoco, A. D. Exploring Titanium(IV) Chemical Proximity to Iron(III) to Elucidate a Function for Ti(IV) in the Human Body | Elsevier Enhanced Reader. *Coordination Chemistry Reviews* **2018**, *363*, 109–125. https://doi.org/10.1016/j.ccr.2018.03.006.

(312) Baramov, T.; Keijzer, K.; Irran, E.; Mösker, E.; Baik, M.-H.; Süssmuth, R. Synthesis and Structural Characterization of Hexacoordinate Silicon, Germanium, and Titanium Complexes of the *E. Coli* Siderophore Enterobactin. *Chemistry - A European Journal* **2013**, *19* (32), 10536–10542. https://doi.org/10.1002/chem.201301825.

(313) Koller, A. J.; Saini, S.; Chaple, I. F.; Joaqui-Joaqui, M. A.; Paterson, B. M.; Ma, M. T.; Blower, P. J.; Pierre, V. C.; Robinson, J. R.; Lapi, S. E.; Boros, E. A General Design Strategy Enabling the Synthesis of Hydrolysis-Resistant, Water-Stable Titanium(IV) Complexes. *Angewandte Chemie International Edition* **2022**, *61* (22). https://doi.org/10.1002/anie.202201211.

(314) Köpf-Maier, P.; Köpf, H. Organometallic Titanium, Vanadium, Niobium, Molybdenum and Rhenium Complexes — Early Transition Metal Antitumour Drugs. In *Metal Compounds in Cancer Therapy*; Fricker, S. P., Ed.; Springer Netherlands: Dordrecht, 1994; pp 109–146. https://doi.org/10.1007/978-94-011-1252-9_6.

(315) Vavere, A. L.; Welch, M. J. Preparation, Biodistribution, and Small Animal PET of 45Ti-Transferrin. *Journal of Nuclear Medicine 46* (4), 683–690.

(316) Severin, G. W.; Nielsen, C. H.; Jensen, A. I.; Fonslet, J.; Kjær, A.; Zhuravlev, F. Bringing Radiotracing to Titanium-Based Antineoplastics: Solid Phase Radiosynthesis, PET and Ex Vivo Evaluation of Antitumor Agent

[45Ti](Salan)Ti(Dipic). *Journal of Medicinal Chemistry* **2015**, *58* (18), 7591–7595. https://doi.org/10.1021/acs.jmedchem.5b01167.

(317) Pedersen, K. S.; Baun, C.; Nielsen, K. M.; Thisgaard, H.; Jensen, A. I.; Zhuravlev, F. Design, Synthesis, Computational, and Preclinical Evaluation of NatTi/45Ti-Labeled Urea-Based Glutamate PSMA Ligand. *Molecules* **2020**, *25* (5). https://doi.org/10.3390/molecules25051104.

(318) Chaple, I. F.; Houson, H. A.; Koller, A.; Pandey, A.; Boros, E.; Lapi, S. E. 45Ti Targeted Tracers for PET Imaging of PSMA. *Nuclear Medicine and Biology* **2022**, *108–109*, 16–23. https://doi.org/10.1016/j.nucmedbio.2022.01.005.

(319) Ji, C.; Miller, P. A.; Miller, M. J. Iron Transport-Mediated Drug Delivery: Practical Syntheses and In Vitro Antibacterial Studies of Tris-Catecholate Siderophore–Aminopenicillin Conjugates Reveals Selectively Potent Antipseudomonal Activity. *Journal of the American Chemical Society* **2012**, *134* (24), 9898–9901. https://doi.org/10.1021/ja303446w.

(320) Jocher, C. J.; Moore, E. G.; Xu, J.; Avedano, S.; Botta, M.; Aime, S.; Raymond, K. N. 1,2-Hydroxypyridonates as Contrast Agents for Magnetic Resonance Imaging: TREN-1,2-HOPO. *Inorganic Chemistry* **2007**, *46* (22), 9182–9191. https://doi.org/10.1021/ic700985j.

(321) Blower, J. E.; Cooper, M. S.; Imberti, C.; Ma, M. T.; Marshall, C.; Young, J. D.; Blower, P. J. The Radiopharmaceutical Chemistry of the Radionuclides of Gallium and Indium. In *Radiopharmaceutical Chemistry*; Lewis, J. S., Windhorst, A. D., Zeglis, B. M., Eds.; Springer International Publishing: Cham, 2019; pp 255–271. https://doi.org/10.1007/978-3-319-98947-1_14.

(322) Carbo-Bague, I.; Li, C.; McNeil, B. L.; Gao, Y.; McDonagh, A. W.; Van de Voorde, M.; Ooms, M.; Kunz, P.; Yang, H.; Radchenko, V.; Schreckenbach, G.; Ramogida, C. F. Comparative Study of a Decadentate Acyclic Chelate, HOPO-O10, and Its Octadentate Analogue, HOPO-O8, for Radiopharmaceutical Applications. *Inorganic Chemistry* **2023**. https://doi.org/10.1021/acs.inorgchem.2c03671.

(323) Degen, G. D.; Stow, P. R.; Lewis, R. B.; Andresen Eguiluz, R. C.; Valois, E.; Kristiansen, K.; Butler, A.; Israelachvili, J. N. Impact of Molecular Architecture and Adsorption Density on Adhesion of Mussel-Inspired Surface Primers with Catechol-Cation Synergy. *Journal of the American Chemical Society* **2019**, *141* (47), 18673–18681. https://doi.org/10.1021/jacs.9b04337.

(324) Raines, D. J.; Moroz, O. V.; Wilson, K. S.; Duhme-Klair, A.-K. Interactions of a Periplasmic Binding Protein with a Tetradentate Siderophore Mimic. *Angewandte Chemie International Edition* **2013**, *52* (17), 4595–4598. https://doi.org/10.1002/anie.201300751.

(325) Becke, A. D. Density-Functional Exchange-Energy Approximation with Correct Asymptotic Behavior. *Phys. Rev. A* **2009**, *38* (6), 3098–3100. https://doi.org/10.1103/PhysRevA.38.3098.

(326) Frisch, M. J.; Trucks, G. W.; Schlegel, H. B.; Scuseria, G. E.; Robb, M. A.; Cheeseman, J. R.; Scalmani, G.; Barone, V.; Petersson, G. A.; Nakatsuji, H.; Li, X.; Caricato, M.; Marenich, A. V.; Bloino, J.; Janesko, B. G.; Gomperts, R.; Mennucci, B.; Hratchian, H. P.; Ortiz, J. V.; Izmaylov, A. F.; Sonnenberg, J. L.; Williams; Ding, F.; Lipparini, F.; Egidi, F.; Goings, J.; Peng, B.; Petrone, A.; Henderson, T.; Ranasinghe, D.; Zakrzewski, V. G.; Gao, J.; Rega, N.; Zheng, G.; Liang, W.; Hada, M.; Ehara, M.; Toyota, K.; Fukuda, R.; Hasegawa, J.; Ishida, M.; Nakajima, T.; Honda, Y.; Kitao, O.; Nakai, H.; Vreven, T.; Throssell, K.; Montgomery Jr., J. A.; Peralta, J. E.; Ogliaro, F.; Bearpark, M. J.; Heyd, J. J.; Brothers, E. N.; Kudin, K. N.; Staroverov, V. N.; Keith, T. A.; Kobayashi, R.; Normand, J.; Raghavachari, K.; Rendell, A. P.; Burant, J. C.; Iyengar, S. S.; Tomasi, J.; Cossi, M.; Millam, J. M.;

Klene, M.; Adamo, C.; Cammi, R.; Ochterski, J. W.; Martin, R. L.; Morokuma, K.; Farkas, O.; Foresman, J. B.; Fox, D. J. *Gaussian 16 Rev. B.01*; Wallingford, CT, USA, 2016.

(327) Becke, A. D. Density-functional Thermochemistry. I. The Effect of the Exchange-only Gradient Correction. *The Journal of Chemical Physics* **1992**, *96* (3), 2155–2160. https://doi.org/10.1063/1.462066.

(328) Grimme, S.; Ehrlich, S.; Goerigk, L. Effect of the Damping Function in Dispersion Corrected Density Functional Theory. *Journal of Computational Chemistry* **2011**, *32* (7), 1456–1465. https://doi.org/10.1002/jcc.21759.

(329) Dunning, T. H., Jr. Gaussian Basis Sets for Use in Correlated Molecular Calculations. I. The Atoms Boron through Neon and Hydrogen. *The Journal of Chemical Physics* **1989**, *90* (2), 1007–1023. https://doi.org/10.1063/1.456153.

(330) Marenich, A. V.; Cramer, C. J.; Truhlar, D. G. Universal Solvation Model Based on Solute Electron Density and on a Continuum Model of the Solvent Defined by the Bulk Dielectric Constant and Atomic Surface Tensions. *The Journal of Physical Chemistry B* **2009**, *113* (18), 6378–6396. https://doi.org/10.1021/jp810292n.

(331) Dennington, R.; Keith, T. A.; Millam, J. M. *GaussView*, 6.1.1.; Semichem Inc.: Shawnee Mission, KS, 2016.

(332) Humphrey, W.; Dalke, A.; Schulten, K. VMD: Visual Molecular Dynamics. *Journal of Molecular Graphics* **1996**, *14* (1), 33–38. https://doi.org/10.1016/0263-7855(96)00018-5.

(333) Anacker, T.; Friedrich, J. New Accurate Benchmark Energies for Large Water Clusters: DFT Is Better than Expected. *Journal of Computational Chemistry* **2014**, *35* (8), 634–643. https://doi.org/10.1002/jcc.23539.

(334) Aghevlian, S.; Boyle, A. J.; Reilly, R. M. Radioimmunotherapy of Cancer with High Linear Energy Transfer (LET) Radiation Delivered by Radionuclides Emitting α-Particles or Auger Electrons. *Advanced Drug Delivery Reviews* **2017**, *109*, 102–118. https://doi.org/10.1016/j.addr.2015.12.003.

(335) Milenic, D. E.; Brady, E. D.; Brechbiel, M. W. Antibody-Targeted Radiation Cancer Therapy. *Nature Reviews Drug Discovery* **2004**, *3* (6), 488–499. https://doi.org/10.1038/nrd1413.

(336) Larson, S. M.; Carrasquillo, J. A.; Cheung, N.-K. V.; Press, O. W. Radioimmunotherapy of Human Tumours. *Nature Reviews Cancer* **2015**, *15* (6), 347–360. https://doi.org/10.1038/nrc3925.

(337) Sarrett, S. M.; Keinänen, O.; Dayts, E. J.; Dewaele-Le Roi, G.; Rodriguez, C.; Carnazza, K. E.; Zeglis, B. M. Inverse Electron Demand Diels–Alder Click Chemistry for Pretargeted PET Imaging and Radioimmunotherapy. *Nature Protocols* **2021**, *16* (7), 3348–3381. https://doi.org/10.1038/s41596-021-00540-2.

(338) Kelly, M. P.; Lee, F.-T.; Tahtis, K.; Power, B. E.; Smyth, F. E.; Brechbiel, M. W.; Hudson, P. J.; Scott, A. M. Tumor Targeting by a Multivalent Single-Chain Fv (scFv) Anti-Lewis Y Antibody Construct. *Cancer Biotherapy and Radiopharmaceuticals* **2008**, *23* (4), 411–424. https://doi.org/10.1089/cbr.2007.0450.

(339) Gestin, J. F.; Loussouarn, A.; Bardies, M.; Gautherot, E.; Gruaz-Guyon, A.; Saı-Maurel, C.; Barbet, J.; Curtet, C.; Chatal, J. F.; Faivre-Chauvet, A. Two-Step Targeting of Xenografted Colon Carcinoma Using a Bispecific Antibody and 188Re-Labeled Bivalent Hapten: Biodistribution and Dosimetry Studies. *Journal of Nuclear Medicine 42* (1), 146–153.

(340) Cook, B. E.; Adumeau, P.; Membreno, R.; Carnazza, K. E.; Brand, C.; Reiner, T.; Agnew, B. J.; Lewis, J. S.; Zeglis, B. M. Pretargeted PET Imaging Using a Site-Specifically Labeled Immunoconjugate. **2016**. https://doi.org/10.1021/acs.bioconjchem.6b00235.

(341) García-Vázquez, R.; Jørgensen, J. T.; Bratteby, K. E.; Shalgunov, V.; Hvass, L.; Herth, M. M.; Kjær, A.; Battisti, U. M. Development of 18F-Labeled Bispyridyl Tetrazines for In Vivo Pretargeted PET Imaging. *Pharmaceuticals* **2022**, *15* (2), 245. https://doi.org/10.3390/ph15020245.

(342) Breitz, H. B.; Weiden, P. L.; Beaumier, P. L.; Axworthy, D. B.; Seiler, C.; Su, F.-M.; Graves, S.; Bryan, K.; Reno, J. M. Clinical Optimization of Pretargeted Radioimmunotherapy with Antibody-Streptavidin Conjugate and 90Y-DOTA-Biotin. *Journal of Nuclear Medicine* **2000**, *41* (1), 131–140.

(343) Lesch, H. P.; Kaikkonen, M. U.; Pikkarainen, J. T.; Ylä-Herttuala, S. Avidin-Biotin Technology in Targeted Therapy. *Expert opinion on drug delivery* **2010**, *7* (5), 551–564. https://doi.org/10.1517/17425241003677749.

(344) Rondon, A.; Degoul, F. Antibody Pretargeting Based on Bioorthogonal Click Chemistry for Cancer Imaging and Targeted Radionuclide Therapy. *Bioconjugate Chemistry* **2020**, *31* (2), 159–173. https://doi.org/10.1021/acs.bioconjchem.9b00761.

(345) Poty, S.; Carter, L. M.; Mandleywala, K.; Membreno, R.; Abdel-Atti, D.; Ragupathi, A.; Scholz, W. W.; Zeglis, B. M.; Lewis, J. S. Leveraging Bioorthogonal Click Chemistry to Improve 225Ac-Radioimmunotherapy of Pancreatic Ductal Adenocarcinoma. *Clinical Cancer Research* **2019**, *25* (2), 868–880. https://doi.org/10.1158/1078-0432.CCR-18-1650.

(346) Keinänen, O.; Fung, K.; Brennan, J. M.; Zia, N.; Harris, M.; van Dam, E.; Biggin, C.; Hedt, A.; Stoner, J.; Donnelly, P. S.; Lewis, J. S.; Zeglis, B. M. Harnessing 64Cu/67Cu for a Theranostic Approach to Pretargeted Radioimmunotherapy. *Proceedings of the National Academy of Sciences* **2020**, *117* (45), 28316–28327. https://doi.org/10.1073/PNAS.2009960117.

(347) Zeglis, B. M.; Brand, C.; Abdel-Atti, D.; Carnazza, K. E.; Cook, B. E.; Carlin, S.; Reiner, T.; Lewis, J. S. Optimization of a Pretargeted Strategy for the PET Imaging of Colorectal Carcinoma via the Modulation of Radioligand Pharmacokinetics. *Molecular Pharmaceutics* **2015**, *12* (10), 3575–3587. https://doi.org/10.1021/acs.molpharmaceut.5b00294.

(348) Moon, H.; Jung, Y.; Kim, Y.; Kim, B. W.; Choi, J. G.; Kim, N. H.; Oh, M. S.; Park, S.; Kim, B. M.; Kim, D. High Stability of a Donor−Acceptor Type Oxazepine-Containing Fluorophore and Its Applications in Cellular Imaging and Two-Photon Deep Tissue Imaging. *Organic Letters* **2019**, *21*, 3891–3894. https://doi.org/10.1021/acs.orglett.9b00784.

(349) McDonagh, A. W.; McNeil, B. L.; Rousseau, J.; Roberts, R. J.; Merkens, H.; Yang, H.; Bénard, F.; Ramogida, C. F. Development of a Multi Faceted Platform Containing a Tetrazine, Fluorophore and Chelator: Synthesis, Characterization, Radiolabeling, and Immuno-SPECT Imaging. *European Journal of Nuclear Medicine and Molecular Imaging Radiopharmacy and Chemistry* **2022**, *7* (12). https://doi.org/10.1186/s41181-022-00164-1.

(350) Lee, W.; Bobba, K. N.; Kim, J. Y.; Park, H.; Bhise, A.; Kim, W.; Lee, K.; Rajkumar, S.; Nam, B.; Lee, K. C.; Lee, S. H.; Ko, S.; Lee, H. J.; Jung, S. T.; Yoo, J. A Short PEG Linker Alters the *in Vivo* Pharmacokinetics of Trastuzumab to Yield High-Contrast Immuno-PET Images. *Journal of Materials Chemistry B* **2021**, *9* (13), 2993–2997. https://doi.org/10.1039/D0TB02911D.

(351) Sharma, S. K.; Glaser, J. M.; Edwards, K. J.; Khozeimeh Sarbisheh, E.; Salih, A. K.; Lewis, J. S.; Price, E. W. A Systematic Evaluation of Antibody Modification and 89Zr-Radiolabeling for Optimized Immuno-PET. *Bioconjugate Chemistry* **2021**, *32* (7), 1177–1191. https://doi.org/10.1021/acs.bioconjchem.0c00087.

(352) Damerow, H.; Hübner, R.; Judmann, B.; Schirrmacher, R.; Wängler, B.; Fricker, G.; Wängler, C. Side-by-Side Comparison of Five Chelators for 89Zr-Labeling of Biomolecules: Investigation of Chemical/Radiochemical Properties and Complex Stability. *Cancers* **2021**, *13* (24), 6349. https://doi.org/10.3390/cancers13246349.

Appendix.

Supplementary figures and data

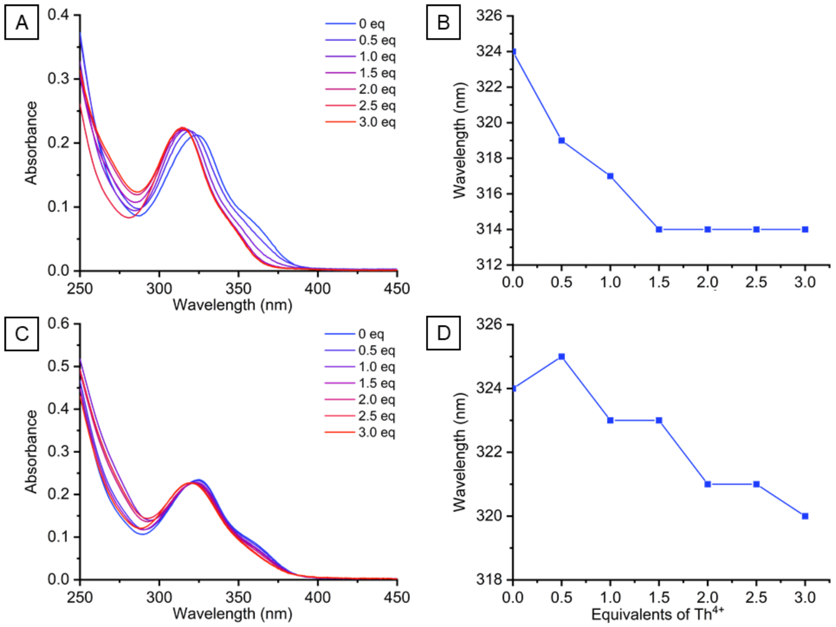

Figure A.1. UV-vis spectroscopic titration of Tb^{3+} (A) and Th^{4+} (C) with HOPO-O_{10} and a profile of the peak wavelength as a function of the equivalents of Tb^{3+} (B) and Th^{4+} (D) added.

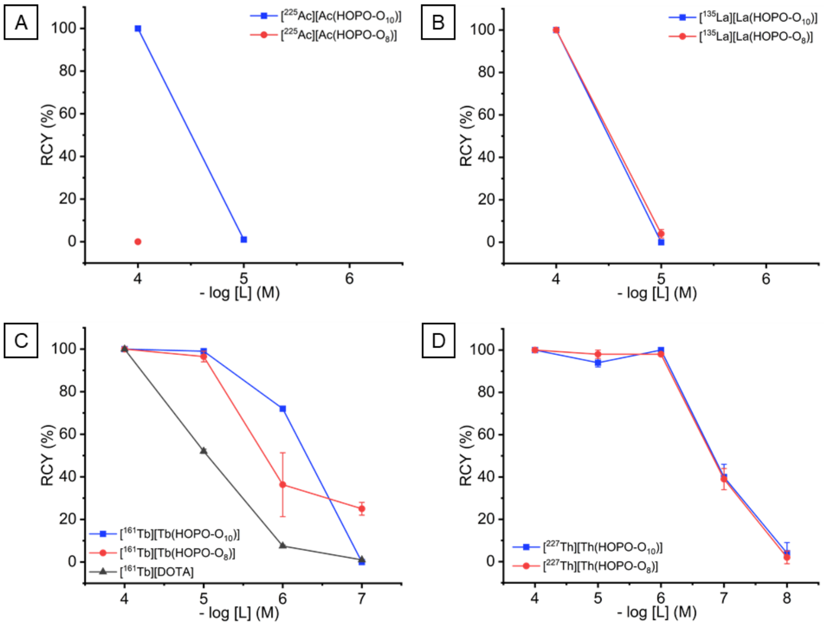

Figure A.2. Concentration-dependant radiolabeling plots of HOPO-O$_{10}$ (blue squares) and HOPO-O$_8$ (red dots) with [^{225}Ac]Ac^{3+} (100 kBq) in 0.5 M NH$_4$OAc pH 6 at 80 °C in 15 min (top left), [^{135}La]La^{3+} (600 kBq) in 0.5 M NH$_4$OAc pH 6 at 80 °C in 15 min (top right), [^{161}Tb]Tb^{3+} (91 kBq) in 0.5 M NH$_4$OAc pH 6 at 80 °C in 15 min including DOTA (bottom left), and [^{227}Th]Th^{4+} (1 kBq) in 0.5 M NH$_4$OAc pH 5 at 80 °C in 15 min (bottom right). n = 3 for each data point, except for [^{227}Th]Th^{4+} where n = 2.

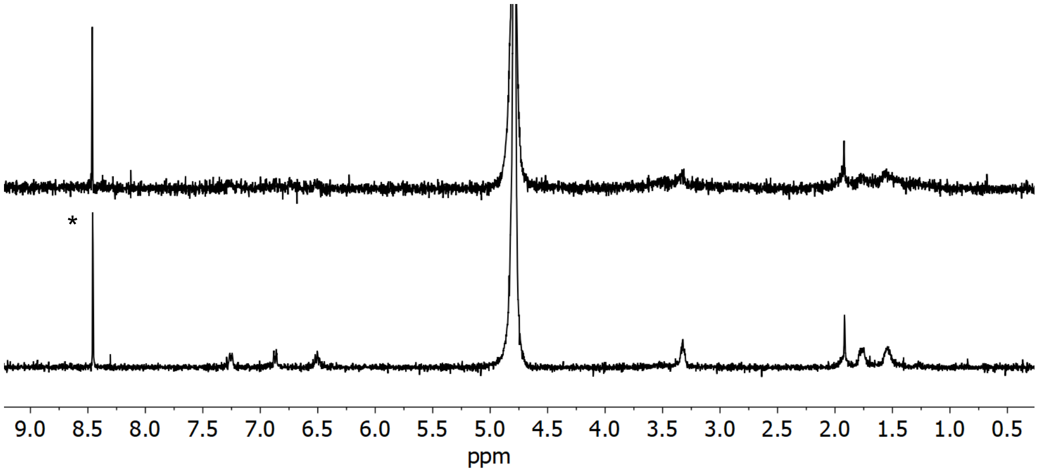

Figure A.3. ^{1}H NMR stability studies of CAM-O$_6$-C4 at time = 0 h (bottom) and 12 h (top) (400 MHz, D$_2$O, 298 K, 1 mM). *formic acid

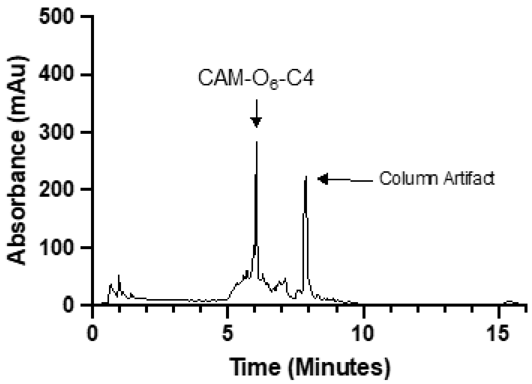

Figure A.4. LC-MS characterization of Ti-CAM-O_6-C4.

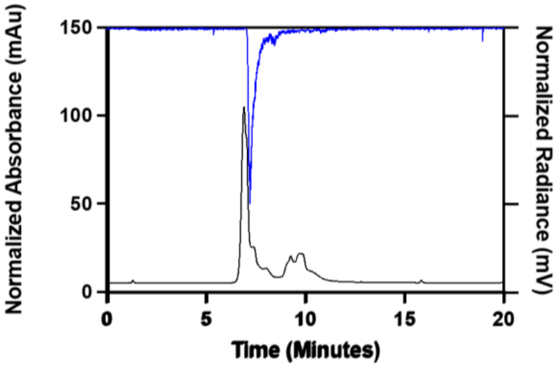

Figure A.5. HPLC characterization [^{45}Ti]Ti-TREN-CAM. The black trace corresponds to the UV profile and the blue to the radioactive measurement

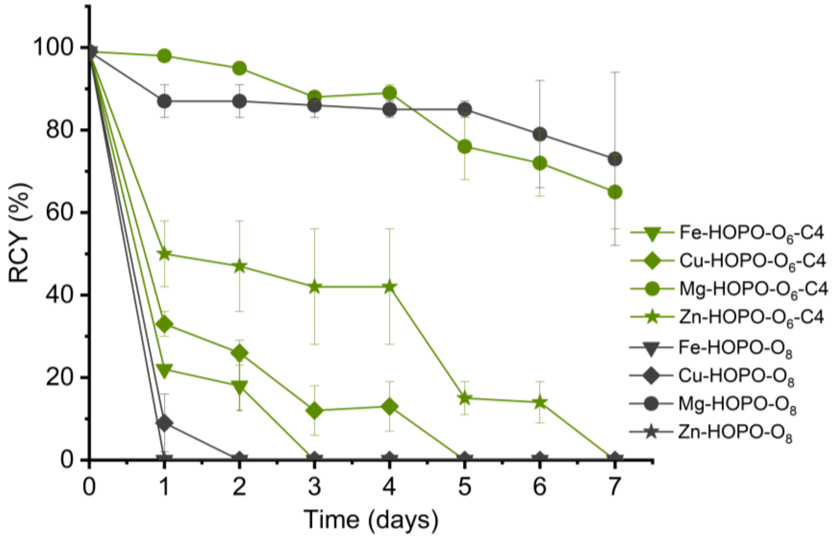

Figure A.6. Stability studies of [^{47}Sc]Sc-HOPO-O_6-C4 (green) and [^{47}Sc]Sc-HOPO-O_8 (grey) at 100 μM of Fe^{3+} (inverse triangle), Cu^{2+} (diamond), Mg^{2+} (circle), and Zn^{2+} (star) over 7 days.

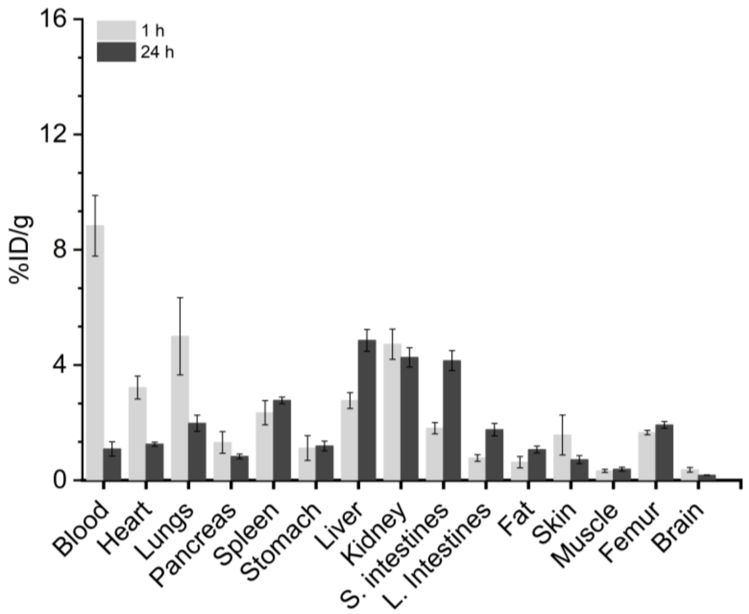

Figure A.7. Ex-vivo biodistribution studies of ~ 296 kBq [^{47}Sc]ScCl$_3$ in healthy mice at 1 h (n = 4) and 24 h (n = 3).

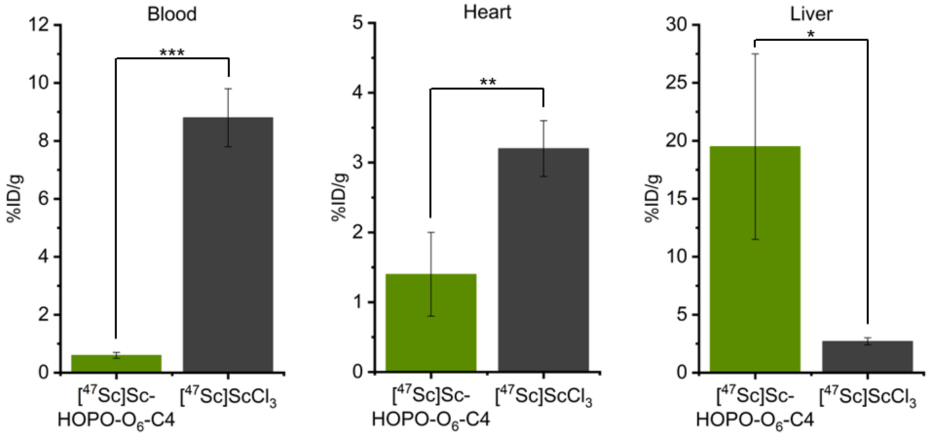

Figure A.8. Ex vivo biodistribution studies of [^{47}Sc]Sc-HOPO-O6-C4 (green) and [^{47}Sc]ScCl$_3$ on selected organs at 1 h time point (n = 4). Statistical analysis by t-test, * $p < 0.05$, ** $p < 0.01$, *** $p < 0.001$.

Table A.9. Summary of the radiolabeling conditions, radiochemical yields, and apparent molar activity calculations of [^{47}Sc]Sc-DOTA and [^{47}Sc]Sc-HOPO-O$_6$-C4.

		DOTA						**HOPO-O$_6$-C4**			
mass (µg)	**mol**	**A (kBq)**	**B (kBq)**	**C (kBq)**		**mass (µg)**	**mol**	**A (kBq)**	**B (kBq)**	**C (kBq)**	
23.750	0.0587	888	888	851		23.750	0.0362	740	851	814	
4.948	0.0122	814	777	851		4.948	0.00755	814	888	888	
0.271	0.000671	777	814	777		0.271	0.000414	851	851	851	
0.054	0.000134	740	851	814		0.054	0.0000827	814	777	814	
0.011	0.0000269	888	740	777		0.011	0.0000165	814	814	777	
		RCY (%)	**RCY (%)**	**RCY (%)**				**RCY (%)**	**RCY (%)**	**RCY (%)**	
		100	100	100				100	100	100	
		100	100	100				88	85	88	
		100	100	100				52	50	51	
		53	55	54				5	4	5	
		10	15	13				0	0	0	
					Average (MBq/µmol)						**Average (MBq/µmol)**
Apparent Molar Activity		7782	7498	7517	7599 ± 129			1543	1544	1570	1565 ± 17

Table A.10. Ex vivo biodistribution studies of ~ 185 kBq of [^{47}Sc]Sc-HOPO-O_6-C4 and ~ 296 kBq of [^{47}Sc]$ScCl_3$ and in healthy mice at 10 min, 30 min, 1 h (n = 4), and 24 h (n = 3) expressed as %ID/g.

	10 min	30 min	1 h		24 h	
	[^{47}Sc]Sc-HOPO-O_6-C4	[^{47}Sc]Sc-HOPO-O_6-C4	[^{47}Sc]Sc-HOPO-O_6-C4	[^{47}Sc]$ScCl_3$	[^{47}Sc]Sc-HOPO-O_6-C4	[^{47}Sc]$ScCl_3$
Blood (µL)	1.3 ± 0.3	0.6 ± 0.1	0.7 ± 0.1	8.8 ± 1.1	0.1 ± 0.0	1.1 ± 0.2
Heart	2.0 ± 0.2	1.7 ±0.2	1.4 ± 0.6	3.2 ± 0.4	0.8 ± 0.0	1.3 ± 0.1
Lungs	4.7 ± 0.7	3.0 ±1.2	2.5 ± 1.4	5.0 ± 1.3	0.4 ± 0.0	2.0 ± 0.3
Pancreas	0.9 ± 0.5	0.7 ±0.5	0.9 ± 0.6	1.3 ± 0.4	0.6 ± 0.2	0.8 ± 0.1
Spleen	2.5 ± 0.6	1.9 ±1.1	2.6 ± 0.7	2.3 ± 0.4	3.6 ± 1.6	2.8 ± 0.1
Stomach	1.0 ± 0.4	1.5 ± 0.7	0.5 ± 0.3	1.1 ± 0.4	1.0 ± 0.2	1.2 ± 0.2
Liver	17.2 ± 1.9	13.0 ±5.4	19.5 ± 8.0	2.8 ± 0.3	18.3 ± 5.0	4.9 ± 0.4
Kidney	3.1 ± 0.5	2.4 ± 0.3	2.9 ± 1.0	4.7 ± 0.5	2.8 ± 0.3	4.3 ± 0.3
Small intestine	0.8 ± 0.4	3.4 ± 2.4	3.1 ± 2.1	1.8 ± 0.2	1.2 ± 0.2	4.2 ± 0.2
Large intestine	3.3 ± 1.1	1.3 ± 0.9	2.2 ± 1.5	0.8 ± 0.1	1.4 ± 0.1	1.8 ± 0.1
Fat	1.1 ± 0.5	0.2 ± 0.1	1.1 ± 0.6	0.6 ± 0.2	0.6 ± 0.3	1.1 ± 0.1
Skin	0.9 ± 0.3	1.0 ± 0.4	1.0 ± 0.1	1.6 ± 0.7	3.2 ± 0.2	0.7 ± 0.1
Muscle	4.5 ± 1.1	0.2 ± 0.2	0.3 ± 0.2	0.3 ± 0.1	0.3 ± 0.1	0.4 ± 0.1
Femur	1.3 ± 0.6	0.7 ± 0.4	0.8 ± 0.3	1.7 ± 0.1	0.6 ± 0.3	1.9 ± 0.1
Brain	0.2 ± 0.0	0.2 ±0.1	0.2 ± 0.0	0.4 ± 0.1	0.1 ± 0.0	0.2 ± 0.0
Gallbladder	14.6 ± 4.6	14.2 ± 6.6	17.5 ± 4.9	No data	20.5 ± 14.9	No data
Tail	0.9 ± 7.0	1.9 ± 1.8	5.0 ± 3.0	No data	1.3 ± 1.0	No data

Table A.11. SUV mean values (g/mL) for selected organs of [^{161}Tb]Tb-HOPO-O$_8$-Tzmb (6.06-6.2 MBq) in mice bearing SKOV tumors xenografts over 6 days (n = 2 except for tumor where n = 1).

	1 h	4 h	24 h	48 h	122 h	144 h
Heart	4.37±0.02	3.23±0.32	1.77±0.07	1.53±0.26	1.10±0.09	0.97±0.02
Lungs	1.84±0.14	1.85±0.02	0.94±0.23	0.75±0.19	0.43±0.01	0.59±0.08
Liver	7.12±0.05	7.25±0.09	5.54±0.18	5.09±0.01	4.22±0.33	4.32±0.01
Bladder	1.98±0.13	1.63±0.28	0.96±0.23	0.61±0.06	0.22±0.14	0.14±0.03
Spleen	5.03±0.69	5.6±0.742	5.88±0.56	5.79±0.52	6.11±0.89	6.35±0.74
Joint	0.79±0.11	1.0±0.059	1.43±0.03	1.53±0.06	1.47±0.05	1.59±0.01
Bone	0.21±0.01	0.39±0.02	0.34±0.08	0.33±0.03	0.22±0.02	0.27±0.03
Tumor	0.21	0.58	2.01	2.26	4.35	5.41

Table A.12. SUV values (g/mL) for selected organs of [^{161}Tb]TbCl$_3$ (6.0 MBq) in mice bearing SKOV tumors xenografts at 3 and 24 h (n = 1).

	3 h	24 h
Heart	0.29	0.17
Lungs	0.30	0.07
Liver	6.75	5.9
Bladder	1.98	0.44
Spleen	4.37	4.72
Joint	2.01	9.04
Bone	7.17	0.07
Tumor	0	0

Table A.13. Ex-vivo biodistribution analysis of [^{161}Tb]Tb-HOPO-O$_8$-Tzmb (3.9-6.2 MBq) and [^{161}Tb]TbCl$_3$ (1.0-3.9 MBq) in Nu/J mice bearing SKOV3 tumor xenografts at 144 h expressed as %ID/g.

Organ	[^{161}Tb]Tb-HOPO-O$_8$-Tzmb	[^{161}Tb]TbCl$_3$
Blood	5.2 ± 0.5	0.1 ± 0.0
Urine	0.9 ± 0.2	1.3 ± 0.1
Feces	0.3 ± 0.1	0.4 ± 0.2
Brain	0.1 ± 0.0	0.0 ± 0.0
Tumor	13.5 ± 0.5	0.3 ± 0.3
Muscle	0.3 ± 0.3	0.1 ± 0.0
Bone	3.0 ± 0.5	14.7 ± 1.3
Bladder	1.8 ± 0.3	0.5 ± 0.1
Spleen	113.1 ± 36.1	31.1 ± 13.0
Pancreas	0.6 ± 0.1	0.2 ± 0.0
Ovaries + uterus	2.6 ± 0.7	0.5 ± 0.0
Kidneys	2.2 ± 0.2	4.7 ± 0.5
Adrenal glands	1.9 ± 0.2	1.3 ± 0.2
Liver	14.4 ± 1.5	29.0 ± 4.0
Heart	1.5 ± 0.1	1.0 ± 0.1
Lungs	3.3 ± 0.4	1.2 ± 0.3
Small intestine	2.6 ± 0.5	0.8 ± 0.1
Large intestine	1.1 ± 0.1	0.8 ± 0.1
Tail	1.7 ± 0.1	12.6 ± 6.9
Stomach	1.0 ± 0.1	15.0 ± 0.1
Joint	2.7 ± 1.0	No data

Table A.14. Ex-vivo biodistribution analysis of [^{89}Zr]Zr-HOPO-O$_8$-Tzmb (2.3-6.6 MBq) and in Nu/J mice bearing SKOV3 tumor xenografts at 120 h expressed as %ID/g.

Organ	[^{89}Zr]Zr-HOPO-O$_8$-Tzmb
Blood	3.1 ± 1.4
Urine	1.5 ± 0.4
Feces	0.6 ± 0.1
Brain	0.1 ± 0.0
Tumor	17.0 ± 12.4
Muscle	0.2 ± 0.1
Bone	0.9 ± 0.9
Bladder	1.6 ± 0.7
Spleen	18.1 ± 3.0
Pancreas	0.4 ± 0.1
Kidneys	2.9 ± 0.4
Liver	22.0 ± 2.4
Heart	1.1 ± 0.4
Lungs	2.1 ± 0.8
Small intestine	1.5 ± 0.6
Large intestine	0.9 ± 0.3
Tail	1.4 ± 0.9
Stomach	0.7 ± 0.2
Joint	1.1 ± 0.4